

Prospects of Finding New Fundamental Physics and Upgrade Studies with the ATLAS detector at the LHC

Inauguraldissertation

der Philosophisch-naturwissenschaftlichen Fakultät
der Universität Bern

vorgelegt von

Meghranjana Chatterjee

von Kolkata, India

Leiter der Arbeit:

Prof. Dr. Michele Weber

Albert Einstein Center for Fundamental Physics
Laboratorium für Hochenergiephysik
Physikalisches Institut



This work is licensed under the
[Creative Commons Attribution-NonCommercial-ShareAlike 4.0](https://creativecommons.org/licenses/by-nc-sa/4.0/)
[International License](https://creativecommons.org/licenses/by-nc-sa/4.0/).

Prospects of Finding New Fundamental Physics and Upgrade Studies with the ATLAS detector at the LHC

Inauguraldissertation

der Philosophisch-naturwissenschaftlichen Fakultät
der Universität Bern

vorgelegt von

Meghranjana Chatterjee

von Kolkata, India

Leiter der Arbeit:

Prof. Dr. Michele Weber

Albert Einstein Center for Fundamental Physics
Laboratorium für Hochenergiephysik
Physikalisches Institut

Von der philosophisch-naturwissenschaftlichen Fakultät angenommen.

Bern, 16. October 2023

Der Dekan
Prof. Dr. Marco Herwegh

Abstract

This thesis presents the work done to develop and qualify the Pixel Data Transmission Chain of the Inner Tracker (ITk) of the ATLAS experiment. To meet High Luminosity - Large Hadron Collider (HL-LHC) conditions, the ATLAS Inner Detector will adopt an all-silicon tracker with high-speed, radiation-resistant data transmission, of which a key stage is the electrical-to-optical component called optoboard. The optoboard is the fundamental component of the optosystem, which is responsible for the recovery, aggregation and electrical-optical conversion of all ITk Pixel data links. This thesis describes the design of the optosystem and the key components of the ITk Pixel data transmission chain, namely, the GBCR which restores the data that is attenuated after electrical transmission from the modules, the lpGBT which multiplexes and de-multiplexes the outgoing and incoming signal and the VTRx+ which is responsible for the electrical-to-optical conversion using a 850 nm laser diode. Functionality tests were performed to validate the design of the optoboard and to analyse and qualify the signal over the electrical part of the ITk Pixel data transmission chain to ensure that the the transmitted data is not distorted or lost and the required specifications fulfilled. Overall, the ITk Pixel electrical data transmission chain from the pixel modules to the optoboard is able to satisfy the requirements of $\text{BER} < 10^{-12}$ for a signal loss < 20 dB with lowest observed total jitter of ~ 110 ps. Furthermore, the Optosystem and the ITk Pixel Data Transmission Chain has successfully passed the final design review and is scheduled to be installed in ATLAS in the next long shutdown in 2026-2028. This thesis also documents the results of the analysis which searches for 3rd generation squarks with final states consisting of top and bottom quarks and missing transverse energy ($E_{\text{T}}^{\text{miss}}$) using the ATLAS detector at the Large Hadron Collider (LHC). The Standard Model (SM) of Particle Physics accurately predicts observed experimental outcomes related to the fundamental constituents of matter. However, there are still many unanswered questions. Supersymmetry (SUSY) is an extension of the SM that aims to fill these gaps by predicting a super partner particle for each particle in the SM. This analysis has been performed earlier using Run 1 and 36 fb^{-1} of Run 2 data. This time a dedicated search is performed using the full LHC Run 2 data of 139 fb^{-1} at $\sqrt{s} = 13 \text{ TeV}$ to look for the pair production of 3rd generation squarks decaying asymmetrically into a $\text{tb} + E_{\text{T}}^{\text{miss}}$ signature resulting in 1 lepton, 2 b -jets and $E_{\text{T}}^{\text{miss}}$ final state. The analysis was divided into bulk and compressed signal regions based on the mass difference between the top quark and $\tilde{\chi}_1^0$. The author's work had been focused on the developing and validating the entire signal grid and defining and analysing the bulk region. In this signal region, this search has placed expected exclusion limits on $m_{\tilde{t}/\tilde{b}}$ upto 980 GeV for $m_{\tilde{\chi}_1^0} = 110 \text{ GeV}$ assuming $\Delta m(\tilde{\chi}_1^0, \tilde{\chi}_1^\pm) = 1 \text{ GeV}$. This search increases the limit by $\sim 150 \text{ GeV}$ and 60 GeV when compared to the one lepton region and the combined $\text{bb} + E_{\text{T}}^{\text{miss}}$ and $\text{tb} + E_{\text{T}}^{\text{miss}}$ observed exclusion contours of the previous version of the analysis.

Acknowledgements

To my grandfather Shri A.M. Banerjee and my parents

I am extremely grateful to Anna Macchiolo and Marko Milovanović firstly for always mentoring me and encouraging me to apply for the then open position at in the University of Bern ATLAS team. They were absolutely spot on and knew that I would love the group and the city. It was the 10th of September, 2018 when my interview took place here in Bern. And I will be ever grateful to Michele and the entire Bern Team for giving me the best birthday gift ever, albeit two days later. While being a part of the team at Bern, living through one of most difficult phases experienced the world over and found incredible support in every way - in work and life, from my supervisor Michele, my post-Docs Antonello, Niklaus, John, Isidre, Laura, Aaron and since very recently Silke and all my team mates Yves, with whom I shared my office in the first year of my PhD and bequeathed me his Young Boys Bern mug, Tom who had been the first person to take me around the LHEP ATLAS lab, Armin, who is just "wow" and has been my first friend, philosopher and guide in the group in Bern, Lea, who always checks on me, Roman, whose eternal calmness is inspirational and Daniele, who seemed to miss me the most when I worked from home. I very thankful to Camilla, Roger, Marco and Gianfranco without whom LHEP wouldn't be the same and certainly my thesis would have to cross extra hurdles to reach its successful completion. An extremely special thanks goes to Ursula and Marcella, our LHEP secretaries who have been there to help me out not only with every paperwork but has always had a kind ear to listen and share in every little reason of joy or sorrow. Friends outside ExWi cannot be left behind. My heartfelt thanks to Katyayani, Shripriya, Harleen, Disha, Anupama, Karthik, Arzoo, Palash and Mohana for the continuous support and managing to uplift my spirits every single time - my home away from home. I cannot forget the remote yet consistent support, love and belief of Shree and Mrs. Dipti Das. Therefore WhatsApp too deserves a vote of thanks! These people have been my pillars of strength. Strange as it might seem, a vote of thanks must go to Mr. Ratan Tata, whose person, life, works and interviews helped me immensely while writing my thesis which a vexing phase as most PhD students would agree, and slowly and steadily it was done. Lastly and most importantly I would like to thank my grandfather Shri A.M. Banerjee and my parents, Swati and Uttam Chatterjee by dedicating this thesis to them. My grandfather knew and had faith in me and my parents have truly been the wind beneath my wings. Without their blessings, belief and support this accomplishment would not have been possible.

“For all that has been – thanks. For all that shall be – yes.”

-Dag Hammarskjöld

Contents

Abstract	v
Acknowledgements	vii
Introduction	1
1 Theoretical Overview: Standard Model and Supersymmetry	5
1.1 From Atoms to Quarks	5
1.2 The Standard Model of Particle Physics	6
1.3 Limitations of the Standard Model	11
1.4 Supersymmetry: An elegant solution	15
1.4.1 Solution to Hierarchy Problem and Unification	15
1.4.2 Particle Content of Minimal Supersymmetric Standard Model (MSSM)	16
1.4.3 R-parity	18
1.4.4 Supersymmetric Mass Eigenstates	18
1.4.5 Spontaneous Supersymmetry Breaking	19
1.4.6 The Phenomenological MSSM (pMSSM)	20
2 The Large Hadron Collider and the ATLAS experiment	21
2.1 The Large Hadron Collider (LHC):	21
2.1.1 The LHC experiments	22
2.1.2 Luminosity	23
2.1.3 Performance overview and Pile-up	24
2.2 The ATLAS Detector	25
2.2.1 The Coordinate System	25
2.2.2 The Inner Detector	27
2.2.3 The Calorimeter Systems	29

2.2.4	The Muon Spectrometer	31
2.2.5	Forward Detectors	34
2.3	The ATLAS Trigger and Data Acquisition	34
2.4	Particle Reconstruction in ATLAS	35
2.4.1	Tracks and Vertices	36
2.4.2	Electrons	39
2.4.3	Photons	39
2.4.4	Muons	40
2.4.5	Jets	40
2.4.6	Missing Transverse Momentum	43
3	Upgrade of the ATLAS ITk Data Transmission Chain for the HL-LHC	45
3.1	The High Luminosity LHC	46
3.2	ATLAS ITk System	47
3.3	ATLAS ITk Pixel Data Transmission System	52
3.4	The Optosystem	54
3.4.1	Overview of the optosystem	54
3.4.2	Key components of Optoboards	58
3.5	Concepts of Link Performance and Signal Quality Tests	65
3.5.1	Jitter Analysis and Eye Diagram	65
3.5.2	Bit Error Ratio Tests	67
3.5.3	Transmission losses using Vector Network Analyser	68
3.6	Preliminary Data Transmission Chain Test Setup and Results	69
3.6.1	Loopback tests conducted using the Xilinx Integrated Bit Error Rate Test (IBERT) in this Xilinx KC705 FPGAs	70
3.6.2	Jitter analysis of the electrical transmission chain using Xilinx KC705 FPGA generated PRBS over transmission chain: KC705/RD53B CDR, 1 m flex, 6 m twinAx and GBCR1	74
3.6.3	Irradiation studies of 6 m twinAx cables	75
3.6.4	Signal loss/gain of each electrical component after replacement of GBCR1 with GBCR2	78
3.6.5	Measurements with optoboard V0	78
3.6.6	Optimisation of GBCR2 and lpGBT register settings	84
3.6.7	BER and jitter analysis conducted over the entire uplink chain with replacement of optoboard V0 with V1	86

4	Search for Supersymmetry in events with $tb+E_T^{\text{miss}}$ final state	91
4.1	Analysis Motivation	91
4.1.1	Signal Phenomenology	92
4.1.2	Previous $tb+E_T^{\text{miss}}$ Run 2 Analysis at 36.1 fb^{-1}	93
4.1.3	Signal grid and kinematic studies	94
4.2	Analysis Strategy	100
4.2.1	Data and simulated event samples	100
4.2.2	Event reconstruction	102
4.2.3	Discriminating variables	104
4.2.4	Region definitions	107
4.3	Systematic Uncertainties	118
4.4	Results and interpretation	121
	Conclusions	137
	Bibliography	141
	Declaration of Consent	159

Introduction

Particle physics delves into the most fundamental inquiries about nature and the reality we inhabit, seeking to unveil the composition of matter itself. It aims to decipher the governing laws of the universe and unveil the essential building blocks that constitute it. Since the beginning of the 20th century, the dynamic interaction between theoretical and experimental facets of particle physics has played a pivotal role in its advancement. The interplay between theoretical predictions and experimental validations has challenged both sides to push the boundaries of knowledge. The Standard Model (SM) [1–5] has emerged as the culmination of these efforts, encapsulating our current comprehension of elementary particles and the forces driving their interactions.

The SM has been rigorously validated through numerous precise examinations and was completed with the landmark discovery of the Higgs boson at the Large Hadron Collider (LHC) [6] by the collaborative efforts of ATLAS and CMS in 2012 [7,8]. While it has provided profound insights, the SM falls short in explaining key observations. For instance, it does not account for the elusive phenomena of dark matter and dark energy, and it can only explain three out of the four fundamental forces. Furthermore, it grapples with the fundamental mystery of why our universe predominantly comprises matter and not anti-matter. Adding to these enigmas, the SM encounters the Hierarchy Problem [9,10] when assumed to hold up to the Planck scale. This challenge necessitates extensive fine-tuning to maintain the Higgs boson’s mass at the observed 125.1 GeV [11], a departure from the principle of naturalness [12–14].

Intensive exploration is underway to probe Beyond the Standard Model (BSM) physics, striving to expand the existing framework. CERN, notably through experiments at the LHC, spearheads a robust research programme to either validate or challenge concepts like supersymmetry (SUSY) and other BSM theories. The second data collection phase of the LHC, known as Run 2, concluded in December 2018, marking a pivotal step in the endeavour. This period witnessed a notable increase in the center-of-mass energy from 8 TeV to 13 TeV, enabling enhanced searches for BSM particles and pushing the limits of discovery sensitivity, ultimately yielding unprecedented mass exclusion boundaries.

Among the myriad of BSM theories aimed at extending the established SM framework, SUSY [15–21] stands out as particularly noteworthy. Built upon the foundational principle of symmetries that played a pivotal role in constructing the SM, this theory introduces an intrinsic symmetry bridging fermions and bosons. The potential ramifications of such a theory hold significant allure, possibly offering resolutions to several lingering questions within the SM, especially concerning the technical hierarchy problem. By assuming that fermions and bosons exhibit identical couplings to the Higgs, the fermionic and bosonic contributions combine in a neat cancellation and prevent the divergences in Higgs bo-

son mass at any given energy scale. This cancellation leaves only the bare Higgs mass. Given that the Yukawa couplings are proportional to the particle mass, the more massive particles exert the most substantial influence. Consequently, the superpartners of third-generation quarks - namely, the top (\tilde{t}) and bottom (\tilde{b}) squarks are of key importance.

While the theoretical foundation is robust, concrete evidence in support of this BSM theory has remained elusive. Exploration at the LHC has effectively ruled out numerous SUSY models, constraining their masses to approximately ~ 1 TeV or higher [22, 23]. However, the scope of SUSY is far from being eliminated, primarily due to the fact that only exceedingly basic interpretations of it have been explored thus far.

This thesis reports an exploration into the search for the pair production of the lightest SUSY counterparts to the top and bottom-quarks, utilising a dataset of 139 fb^{-1} from LHC Run 2 of proton-proton collisions at a center-of-mass energy of 13 TeV obtained from the ATLAS detector. This study focuses on final states characterised by one charged lepton, two b -jets, and missing transverse momentum E_T^{miss} . The analysis looking for the same final state was performed previously using partial Run 2 dataset of 36 fb^{-1} , where the bottom squark mass of upto 880 GeV was excluded. This meant that lightest SUSY particles can exist after 880 GeV [24]. Increased statistics from the full 139 fb^{-1} dataset, meant that there was a greater probability of finding new physics beyond the set mass limit or definitely increasing the present exclusion limits. To identify the desired process while effectively distinguishing it from plausible SM processes mimicking the same final state, a set of kinematic and phenomenological criteria is implemented. This discerning approach aims to isolate the targeted signal while mitigating background contamination. Precise modelling techniques are harnessed to ascertain the expected number of events originating from each distinct SM background process. A notable excess between observed data events and the expected outcomes from these backgrounds could potentially point towards the presence of novel physics phenomena.

During the current Run 3 of the LHC, around 300 fb^{-1} of proton-proton collision data at energies of 13–14 TeV will be generated until 2024. However, a substantially larger amount of integrated luminosity is required for achieving greater precision in SM measurements like the Higgs self-coupling and detecting more intricate and rare BSM signatures. This is the main motivation behind the High-Luminosity LHC (HL-LHC) initiative [25] which would enhance the LHC's capabilities by accumulating integrated luminosities of up to 4000 fb^{-1} . This augmentation, for instance, facilitates the exploration of top squarks with masses up to 1.25 TeV and the establishment of Higgs boson couplings at precision levels of around one percent [26]. The increase in luminosity will cause a greater number of proton-proton collisions leading to extremely harsh radiation environment. In response to the intensification of collision signatures and augmented radiation-induced harm, enhancements within the LHC experiments themselves are also imperative.

In accordance with the challenges that the High-Luminosity upgrade of the LHC poses, the current Inner Detector of the ATLAS experiment will be replaced with an all-silicon Inner Tracker (ITk) [27, 28] consisting of an inner Pixel and an outer Strip detector. The ITk incorporates not only novel sensing components but also an entirely revamped readout system. Given the increase in the simultaneous proton-proton collisions, the ITk data-taking will have to provide high-speed and radiation-hard data transmission. To fully utilise the space available inside the detector and to prevent loss of data, the data from multiple pixel modules is combined into single optical signals. This combination

and optical-to-electrical conversion are done using optoboards which consist of different components to meet the said requirements. The ITk Pixel data transmission transmits data electrically inside of the ITk at data rates of 1.28 Gbps, followed by the optical transmission at speeds of 10.24 Gbps through fibres out of the ATLAS detector to the counting room [29]. For my thesis, I planned to qualify the electrical signal from the sensor electronic prototypes to the optoboard using the initial prototypes, thereby building the first ITk Pixel data transmission chain prototype for the Bern ATLAS group. I further worked on optimising the configurations of the different electrical components connected over the transmission chain by the means of eye diagrams, signal loss and bit error rate measurements. Each component and the overall optoboard prototype was characterised to enhance the performance and meet the requirements of the ITk Pixel data transmission chain. I also did preliminary irradiation studies on the electrical cables to study the signal quality pre- and post-irradiation.

The description of the SM and introduction of SUSY is in Chapter 1. The overview of the LHC and ATLAS is provided in Chapter 2. Chapter 3 provides a description of the High-Luminosity programme of the LHC and the associated upgrade of the ATLAS detector. The chapter further presents my work on qualification of the optoboard and the ITk Pixel data transmission chain. Finally, Chapter 4 documents the analysis searching for 3rd generation squarks decaying asymmetrically into a $t\bar{b} + E_T^{\text{miss}}$ signature resulting in 1 lepton, 2 b -jets and E_T^{miss} final state using a dataset of 139 fb^{-1} .

Chapter 1

Theoretical Overview: Standard Model and Supersymmetry

This chapter provides an overview of the fundamental components of the Standard Model of particle physics leading to a comprehensive understanding of the fundamental particles and forces. However, the chapter also highlights certain limitations and unanswered questions within the Standard Model, such as the Higgs hierarchy problem and the mysterious nature of dark matter. To address these issues, the concept of supersymmetry is introduced as a potential solution. Supersymmetry proposes the existence of additional particles that could provide answers to the unresolved questions and offer a more complete description of the universe. By exploring supersymmetry, the chapter aims to present a possible avenue for extending the Standard Model and addressing its limitations.

1.1 From Atoms to Quarks

Centuries ago, the question of the smallest building blocks of matter emerged, leading to the remarkable discovery of the atom and revolutionising particle physics throughout the 20th century. Atoms consist of negatively charged electrons (e^-) orbiting a central nucleus composed of positively charged protons (p^+) and electrically neutral neutrons (n). The electromagnetic force, a manifestation of Quantum Electrodynamics (QED) at low energies, binds the electrons and nucleus together. However, protons and neutrons are not fundamental particles themselves. They are composite particles, bound states of even smaller entities known as quarks. The proton consists of two valence up quarks (u) and one valence down quark (d), while the neutron comprises one valence up quark and two valence down quarks.

The strong interaction, described by Quantum Chromodynamics (QCD), governs the behaviour of these quarks and is responsible for the formation of hadrons, such as protons and neutrons. It is the residual effect of the strong force that enables the formation of atomic nuclei. The varying combination of protons, neutrons, and electrons, along with the quantisation enforced by quantum mechanics, gives rise to the diverse elements observed in the periodic table.

The weak interaction, one of the fundamental forces in particle physics, is responsible for

processes like nuclear decay and acts on all the elementary particles. And gravity, the fourth and final fundamental force, although negligible at the atomic scale, governs the larger-scale structure of the universe.

The majority of matter consists of three particles: the electron, electron-neutrino (ν_e), and the up and down quarks. Together, they constitute the first generation of matter.

However, as we explore higher-energy regimes achievable through particle colliders, additional complexity emerges, leading to the discovery of more fundamental particles. The Standard Model of particle physics elegantly describes the known fundamental particles and the forces that govern their interactions. It categorises these particles into two types: fermions and bosons. Fermions have half-integer spin, follow Fermi-Dirac statistics, and adhere to the Pauli Exclusion Principle. Bosons, on the other hand, have integer spin and follow Bose-Einstein statistics.

1.2 The Standard Model of Particle Physics

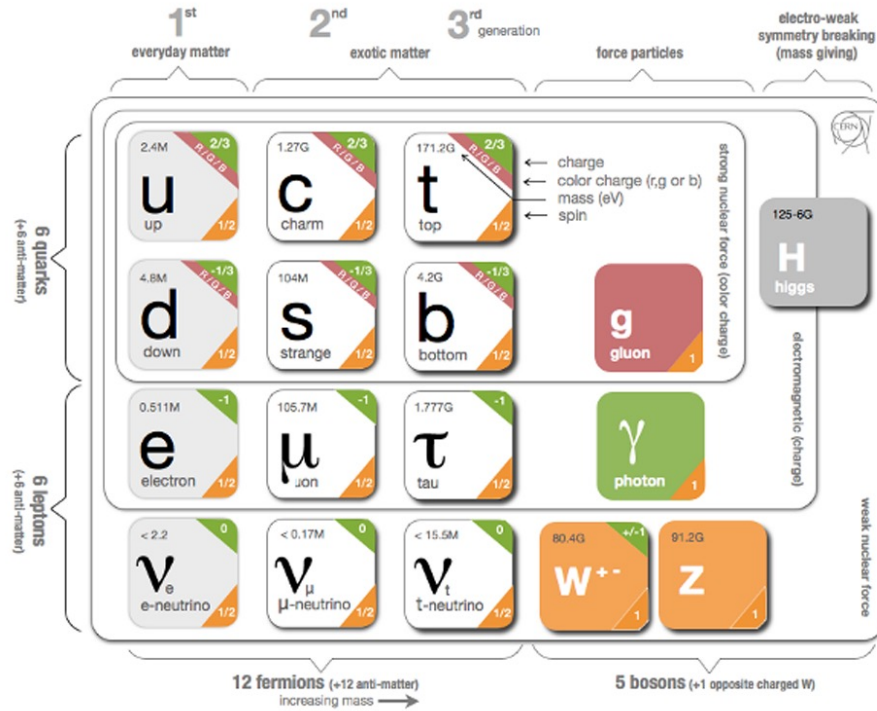


Figure 1.1: The Standard Model of particle physics. Figure has been taken from Reference [30].

The Standard Model (SM) is a concise theory that describes the interactions between fermionic particles and three of the four fundamental forces: the strong force, electromagnetic force, and weak force. However, the incorporation of gravity into the SM remains an unresolved challenge. Constructing the SM involves several fundamental components: the Dirac equation of relativistic quantum mechanics, which describes the dynamics of free fermions; Quantum Field Theory (QFT), which mathematically describes particles and their interactions; local gauge invariance, which governs how these interactions man-

ifest in nature; the Higgs mechanism of electroweak symmetry breaking, responsible for generating particle masses; and the extensive experimental data that played a crucial role in developing this theory [31].

Table 1.1 presents the fermionic and bosonic constituents of the SM, respectively. Fermions in the SM can be categorised as quarks, which can interact via the strong force, and leptons, which cannot. These particles further divide into three generations, with the first generation comprising the electron, electron-neutrino, up quark, and down quark. The particles in the second and third generations are unstable and decay into lighter particles, often observed in high-energy collisions. Each generation consists of two doublets, one for leptons and one for quarks. In the lepton doublet, an electrically charged particle (e , μ , τ) is paired with its corresponding electrically neutral lepton-neutrino (ν_e , ν_μ , ν_τ). Each of these fundamental particles have their corresponding antiparticles with same properties except for the electric charge which is opposite to its particle counterpart. Quantum Electrodynamics (QED) mathematically formulates these interactions, enabling particles with electric charge to interact through this force. QED provides a quantum description of matter-light interactions and is the counterpart to classical electrodynamics [32, 33].

Table 1.1: Summary of the SM particle content and the three fundamental interactions described by the SM with the corresponding mediators, charges and range.

Fermions						
Generation	Name	Symbol	Spin	Charge [e]	Mass	
I	Up-quark	u	1/2	+2/3	2.2 MeV	
	Down-quark	d	1/2	-1/3	4.7 MeV	
	Electron-neutrino	ν_e	1/2	0	<2 eV	
	Electron	e^-	1/2	-1	0.511 MeV	
II	Charm-quark	c	1/2	+2/3	1.27 GeV	
	Strange-quark	s	1/2	-1/3	96 MeV	
	Muon-neutrino	ν_μ	1/2	0	<0.19 eV	
	Muon	μ^-	1/2	-1	105.7 MeV	
III	Top-quark	t	1/2	+2/3	172.9 GeV	
	Bottom-quark	b	1/2	-1/3	4.18 GeV	
	Tau-neutrino	ν_τ	1/2	0	<18.2 eV	
	Tau	τ^-	1/2	-1	1776.8 MeV	
Gauge Bosons						
Interaction	Name	Symbol	Spin	Charge Type	Mass [GeV]	Range [m]
Strong	Gluon	g	1	electrical	0	10^{-15}
	Photon	γ	1	colour	0	∞
Weak	W-boson	W^\pm	1	weak isospin	80.4	10^{-18}
	Z-boson	Z^0	1	weak isospin	91.2	10^{-18}
Higgs Boson						
Name		Symbol	Spin	Charge [e]	Mass [GeV]	
Higgs boson		h	0	0	125.1	

The quark doublet consists of up-type quarks (u , c , t) with an electromagnetic charge of +2/3 and down-type quarks (d , s , b) with an electromagnetic charge of -1/3. Quarks also possess another conserved quantum property known as colour charge [34]. Quantum Chromodynamics (QCD) mathematically formulates this interaction, allowing particles with colour charge to interact through the strong force. Quarks can exist in red, green, or blue colour states; however, experimental evidence indicates that coloured particles do not exist freely in nature, and this is known as the colour confinement of quarks. This results in quarks existing only in bound, colourless states called hadrons. This colour

confinement phenomenon arises due to the dependence of the QCD coupling strength on the momentum transfer of the interaction, denoted as Q^2 . The QCD coupling constant, g_s , represented as $\alpha_s = g_s/4\pi$ as shown in Equation (1.1).

$$\alpha_s(Q^2) = \frac{g_s^2(Q^2)}{4\pi} = \frac{1}{\beta_0 \ln(\frac{Q^2}{\Lambda_{QCD}^2})}, \quad \text{where } \beta_0 = \frac{11n_c - 2n_f}{12\pi} \quad (1.1)$$

Here, Λ_{QCD}^2 is the energy scale at which the non-perturbative dynamics of QCD dominate, β_0 is calculated using the number of colours n_c which is 3 and the number of active flavours n_f with mass below Q .

In Figure 1.2, experimental measurements of the QCD coupling constant are depicted as a function of the momentum transfer. At low energies and large distances, where the momentum transfer approaches the QCD scale (Λ_{QCD}^2), the strength of the QCD coupling increases. This behaviour can be understood by considering an effective potential between two quarks. Empirical observations show that the potential follows a $1/r$ behaviour at short distances and an almost linearly rising potential at larger distances [11]. As distances increase, the energy required for further separation becomes high enough that it becomes energetically favourable to produce new particles from the vacuum. Consequently, this leads to the formation of new colour-neutral hadrons: mesons (quark-antiquark pairs with the colour - anti-colour charge) or baryons (bound states of three quarks or antiquarks with differing colours, where the proton is a commonly encountered example, composed of uud).

At high values of Q^2 i.e. small distances, the QCD coupling constant decreases, and the quarks are characterised as quasi-free. This phenomenon is known as asymptotic freedom, and it allows perturbative computation of QCD calculations. Hence, bare quarks and gluons are not directly observable in nature. Instead, they have the ability to emit additional gluons and radiate energy until reaching an energy scale where confinement takes place, leading to the initiation of the hadronisation process. This phenomenon is experimentally observed as a concentrated flow of hadrons, commonly referred to as a jet.

In the realm of particle physics, fermions are the building blocks of matter, while bosons mediate interactions between them. Each fundamental force within the framework of the Standard Model is accompanied by a distinct boson that acts as the mediator for interactions among fermions through that specific force. During these interactions, fermions exchange the associated boson with one another transmitting the respective force.

The electroweak interaction holds significant importance within the framework of the Standard Model. Initially, the weak and electromagnetic interactions were treated as separate forces, each with their respective theories. The electromagnetic interaction was effectively described by Quantum Electrodynamics (QED), while the weak interaction was initially captured by an effective theory called the Fermi theory or Quantum Flavour Dynamics. This Fermi theory successfully accounted for charged current interactions as point-like interactions, particularly at low energies. However, as energies approached the electroweak scale at approximately 100 GeV, the limitations of the Fermi theory became apparent. Experimental evidence unveiled that only left-handed chirality particles participated in charged current interactions, leading to the introduction of the weak isospin

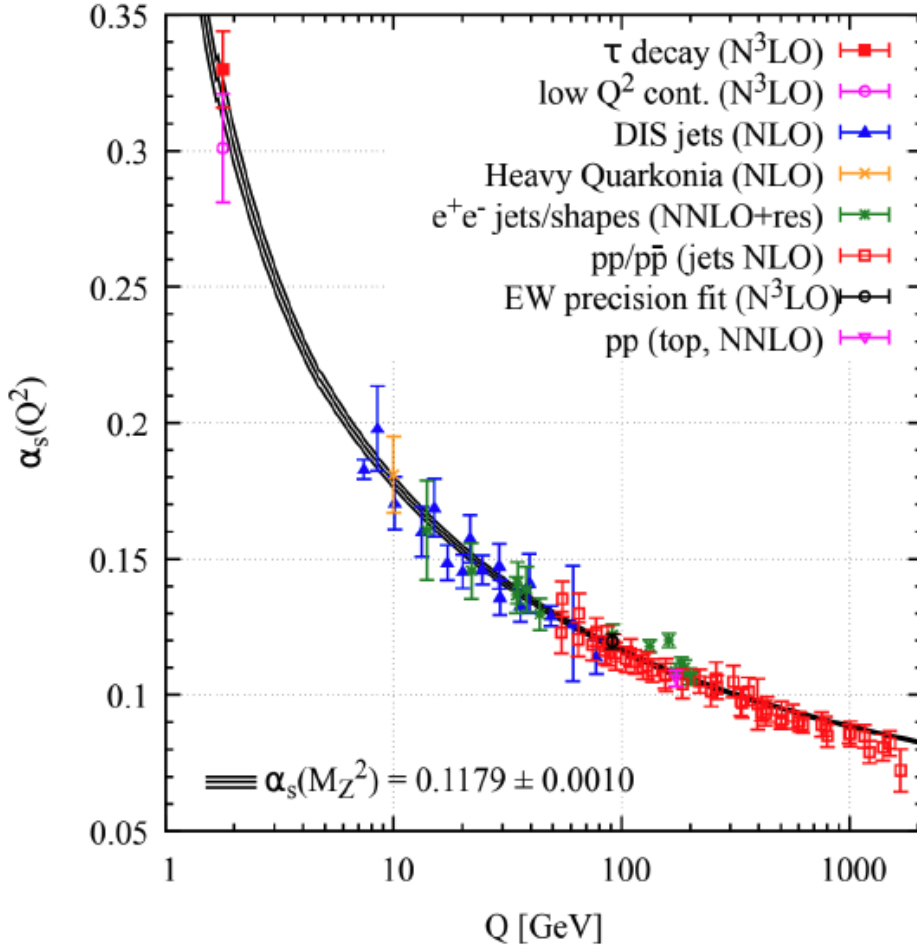


Figure 1.2: Theoretical predictions and experimental measurements of the QCD coupling constant α_s as a function of the momentum transfer Q^2 of a process. Figure has been taken from [35].

quantum number, denoted as T [36]. This discovery marked a crucial step in understanding the nature of the weak interaction. The distinct role of left-handed fermions in charged current interactions paved the way for a deeper unification of the weak and electromagnetic forces within the electroweak theory. Specifically, the forces couple to the third component of weak isospin, T_3 . Left-handed fermions are grouped into doublets with $T = 1/2$ and $T_3 = \pm 1/2$. Right-handed fermions form a singlet with $T = 0$ and $T_3 = 0$, thus not interacting via charged current interactions. The right-handed neutrino is not accounted for in the current formulation of the Standard Model. This is due to the fact that it has not been experimentally detected thus far. Theoretical predictions suggest that the right-handed neutrino primarily interacts through gravity, with negligible interactions through the other fundamental forces described by the Standard Model. As a result, the right-handed neutrino's absence in the model is based on experimental observations with no theoretical exclusions regarding its minimal involvement in other particle interactions. In order to describe the electromagnetic interaction, which interacts with both left-handed and right-handed particles, the concept of hypercharge Y_W is introduced. It is defined as $Q = T_3 + Y_W/2$, where Q represents the electric charge. An

important aspect of this unification is that the weak component of the Standard Model couples exclusively to the left-handed weak isospin doublets. On the other hand, the electromagnetic component has the ability to act on both left-handed and right-handed components. Glashow, Salam, and Weinberg proposed this unification of the electromagnetic and weak forces as the electroweak interaction [2, 3, 5, 36].

Symmetry plays a fundamental role in the Standard Model, and it is guided by Noether's theorem, which states that for every conserved symmetry, there exists a corresponding conserved quantity. The mathematical framework of the Standard Model is built upon this principle and is expressed through the formalism of Quantum Field Theory (QFT) [37]. By embracing symmetry, the Standard Model provides a powerful tool for understanding the fundamental interactions and particles that make up our universe. In the Standard Model, all fundamental particles are described as excitations of quantum fields that permeate all points in space-time. Fermions, such as quarks and leptons, are represented by fermion fields denoted as $\psi(x)$ and known as Dirac-spinors. On the other hand, gauge bosons, which mediate the fundamental forces, are described by vector fields denoted as $A_\mu(x)$, where μ represents the spacetime index. The Standard Model is constructed by incorporating local gauge invariance to account for the three fundamental forces. This involves introducing additional bosonic gauge fields that interact with fermions, giving rise to the fundamental interactions observed in nature. Local gauge invariance ensures that these interactions remain invariant under local gauge transformations. The number of bosonic gauge fields required corresponds to the number of generators in the symmetry group associated with each force. In other words, the number of physical bosons associated with a particular interaction corresponds to the number of bosonic gauge fields that need to be introduced in the theory. By incorporating local gauge invariance and the appropriate number of gauge fields, the Standard Model successfully describes the interactions between fermions and bosons.

As a consequence, the Standard Model can be expressed as a Quantum Field Theory (QFT) that incorporates an underlying symmetry given by $SU(3)_C \otimes SU(2)_L \otimes U(1)_Y$. The $SU(3)_C$ corresponds to the strong force or colour interaction, the $SU(2)_L$ corresponds to the weak isospin interaction, and the $U(1)_Y$ corresponds to the hypercharge interaction.

The gauge group $SU(3)_C$ corresponds to Quantum Chromodynamics (QCD) and describes the strong interaction. The mediator of the strong force are the gluons, which are electrically neutral and massless bosons. Gluons themselves possess colour charge. The total number of gluons is related to the number of colour charges in QCD. Since there are three "colours" (red, green, and blue) and three corresponding "anticolours" (antired, antigreen, and antiblue), each gluon can carry a combination of a colour and an anticolour charge. Thus there are nine possible combinations. As one combination is the colourless state, which does not interact strongly, it leaves a total of eight active gluons. Quarks, being fermions with colour charge, are the only particles that interact via the strong force and couple to gluons.

The combination of the weak and electromagnetic forces resulted in the development of the electroweak interaction, which is described by the symmetry group $SU(2)_L \otimes U(1)_Y$. Here, the subscripts L and Y refer to weak-isospin and hypercharge, respectively. This interaction is mediated by four gauge bosons: W_1, W_2, W_3 for $SU(2)_L$, and B for $U(1)_Y$. The W_i triplet and the B boson combine to form the physical bosons: the photon

(γ), the Z^0 boson, and the W^\pm bosons. The photon, being a massless and electrically neutral boson, serves as the mediator of the electromagnetic interaction. It interacts with electrically charged particles, allowing for electromagnetic interactions between quarks and charged leptons. The W^\pm bosons are charged and have mass. They mediate the weak charged current interaction. On the other hand, the Z^0 boson is electrically neutral and also possesses mass. It serves as the mediator for the weak neutral current interaction. It is worth noting that, as per gauge invariance, the mediators of fundamental interactions are typically expected to be massless. However, unlike the photon and gluon, the W and Z bosons do have mass. This massiveness of the W and Z bosons results in the weak force being limited in range, making it a short-range force compared to the electromagnetic force mediated by the massless photon.

To explain the non-zero masses of the W^\pm and Z^0 , the Standard Model incorporates a complex scalar field called the Higgs field, which incorporates the Brout-Englert-Higgs mechanism. This mechanism is responsible for generating the masses of the electroweak bosons through the process of spontaneous symmetry breaking in the electroweak sector [38–40]. The Higgs field is present throughout the universe and interacts with particles, providing mass to these particles. The Higgs boson, associated with the Higgs field, is a unique boson within the Standard Model. It is the only known fundamental scalar particle (with spin zero) and is not associated with any of the fundamental forces. Instead, it represents an excitation of the Higgs field. The strength of the interaction between fermions and the Higgs boson, known as Yukawa couplings, is directly proportional to the fermion’s mass.

To summarise, the Standard Model of particle physics based on experimental observations and theoretical predictions is a concise theory of interactions between the fermionic particles and three of the four fundamental forces: the strong force, electromagnetic and the weak force. It has demonstrated remarkable success and has been extensively validated through numerous experiments spanning a wide range of energy scales. Measurements conducted by the general purpose experiments, the Compact Muon Solenoid (CMS) and the A Large Toroidal Lhc ApparatuS (ATLAS) experiments at the Large Hadron Collider (LHC) have confirmed the SM’s predictions across multiple orders of magnitude in production cross-section [41]. Despite its achievements, the SM is recognised as an incomplete theory, functioning more as an effective field theory that accurately describes phenomena at low energies as it is unable to adequately explain certain observable phenomena. For example, the inclusion of gravity is an, as yet unresolved challenge. Therefore the SM is widely considered to be a subset of a more comprehensive framework, indicating the presence of physics beyond the Standard Model (BSM).

1.3 Limitations of the Standard Model

This section provides an overview of the unresolved questions within the Standard Model, with a specific emphasis on the problems that can potentially be addressed through Supersymmetry. A brief explanation is provided regarding how Supersymmetry offers potential solutions to these issues. However, a more comprehensive exploration of Supersymmetry is reserved for the subsequent sections.

Some of the challenges facing the standard model of particle physics are:

Dark Matter

The SM describes only about 4% of the content of the universe that is made up of the “ordinary” matter while the rest is observed from experimental measurements to be composed of dark matter (27%) and dark energy (68%) [42]. Measurements of the orbital speeds of stars in galaxies showed significant discrepancies as their rotational velocities do not follow the radial dependency expected from the mass of its ordinary matter (stars, gas, etc.) as seen in Figure 1.3. There is an observed linear dependence of the mass of the galaxy with respect to the radial distance $\propto r$ of the galaxy instead of the expected $\propto r^{-\frac{1}{2}}$ [43]. Thus it can be inferred that a significant proportion of the mass of a galaxy is non-luminous and referred to as dark matter and assuming its distribution from the galaxy’s centre out to its halo provides a solution to the afore-mentioned problem. Based on experimental constraints, a dark matter particle must possess greater mass than the weakly interacting particles in the SM, such as neutrinos. This ensures that the dark matter particle is non-relativistic, and able to form the large scale structures responsible for observed galactic structures. Such a weakly interacting massive particle or particles also known in short as *WIMP* would primarily have to interact with the gravitational force.

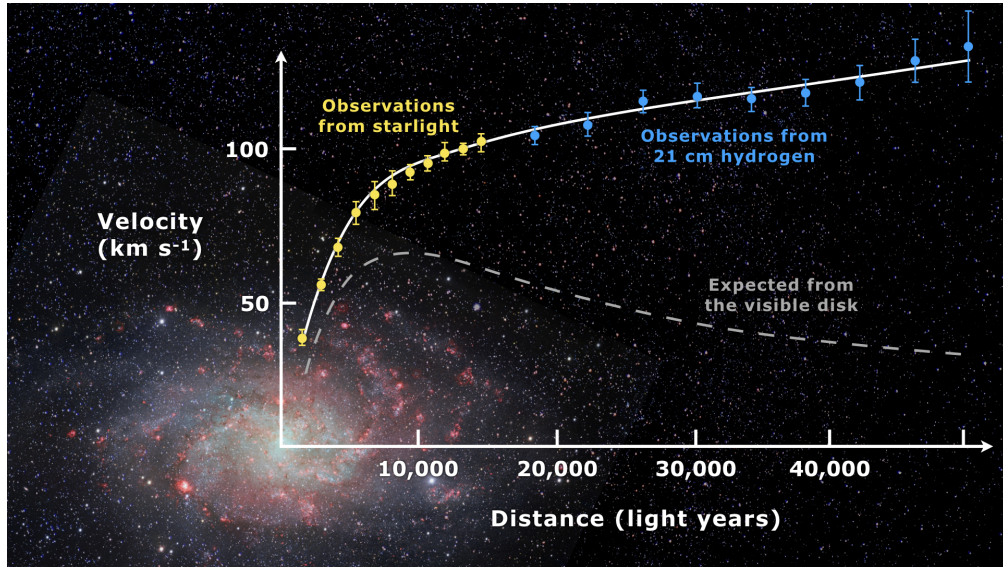


Figure 1.3: The figure shows the rotation curve of spiral galaxy Messier 33 (yellow and blue points with error bars), and a predicted one from distribution of the luminous matter (grey line). This discrepancy between the two curves can be accounted for by adding a dark matter halo surrounding the galaxy. Figure has been taken from Reference [44].

Matter Anti-matter Asymmetry

Another limitation of SM is its inability to conclusively explain the matter-antimatter asymmetry of the universe. The Big Bang should have created equal amounts of matter and antimatter in the early universe, however as the universe expanded and cooled comparatively, there is not much antimatter to be found. Baryogenesis refers to this process in the early universe that led to the creation of an excess of baryons (protons and neutrons) over antibaryons (antiprotons and antineutrons), resulting in the predominance of matter over antimatter in the universe we observe today. Matter and antimatter particles are always produced as a pair and when they come across each other, they annihilate each

other. In the course of the first fractions of a second of the Big Bang i.e. a picosecond (10^{-12}) of cosmic time, the hot and dense universe was filled with particle-antiparticle pairs popping in and out of existence. So, if matter and antimatter are created and destroyed together, theoretically the universe should still contain the same amount of matter and antimatter. According to the SM, this baryon asymmetry can be explained through certain processes that violate the conservation of baryon number, such as the violation of CP-symmetry. One of the most well-known baryogenesis mechanisms is the electroweak baryogenesis, which involves interactions between particles and forces during the electroweak epoch, a period of the universe's history when the electromagnetic and weak nuclear forces were unified. Another proposed mechanism is the leptogenesis, where the asymmetry is generated in the decays of heavy right-handed neutrinos, indirectly affecting the baryon number. This is still an active area of research and has not been conclusively verified.

Grand Unified Theory (GUT)

One of the most important shortcomings of the SM is that it does not include the gravitational force. A first step to include gravity is the *Grand Unified Theory (GUT)* which combines the electromagnetic, weak and strong forces into a single force at high enough energy scale. The scale at which this is predicted to occur is referred to as the scale of Grand Unified Theories and is in the order of $E_{GUT} \approx 10^{16}$ GeV [45].

In the context of GUTs, gravity is not included in the unification process because it is significantly weaker compared to the other three forces, and its behaviour is very different from the other forces. The other three forces can be unified at high energies (close to the Planck scale), but gravity becomes much weaker at these energies, making it difficult to fit it into the same framework as the other forces. The quest to unify gravity with the other fundamental forces is a major goal in theoretical physics. The search for a theory that combines General Relativity and Quantum Mechanics is known as "Quantum Gravity." Several approaches and candidate theories, such as string theory and loop quantum gravity, have been proposed to achieve this unification. However, achieving a consistent and experimentally verified theory of quantum gravity remains one of the most significant challenges in modern physics.

If the couplings as currently described by the SM are extrapolated to higher energies, it is seen that these three forces do not converge at the same point as seen in the dashed lines of the Figure 1.5. However, the apparent approximate unification of gauge couplings at E_{GUT} is an interesting observation by addition of new particles as seen in the solid lines of Figure 1.5, and it can be interpreted in two ways. First, it might be just a coincidence or accident, and there might not be any deeper underlying theory explaining it. Alternatively, it could be considered a strong hint in favour of grand unified theories (GUTs) or superstring models. Both GUT and superstring models go beyond the SM and attempt to unify the fundamental forces of nature at high energy scales, below the Planck scale.

Hierarchy Problem

The concept of naturalness is one that expects the parameters of a theory to take relative values of order one. A problem with respect is the very small ratio between the Electroweak and Planck scale $E_{EW}/E_{planck} \approx 10^{-17}$ where $E_{EW} \approx 10^2$ and $E_{planck} \approx 10^{19}$ [21].

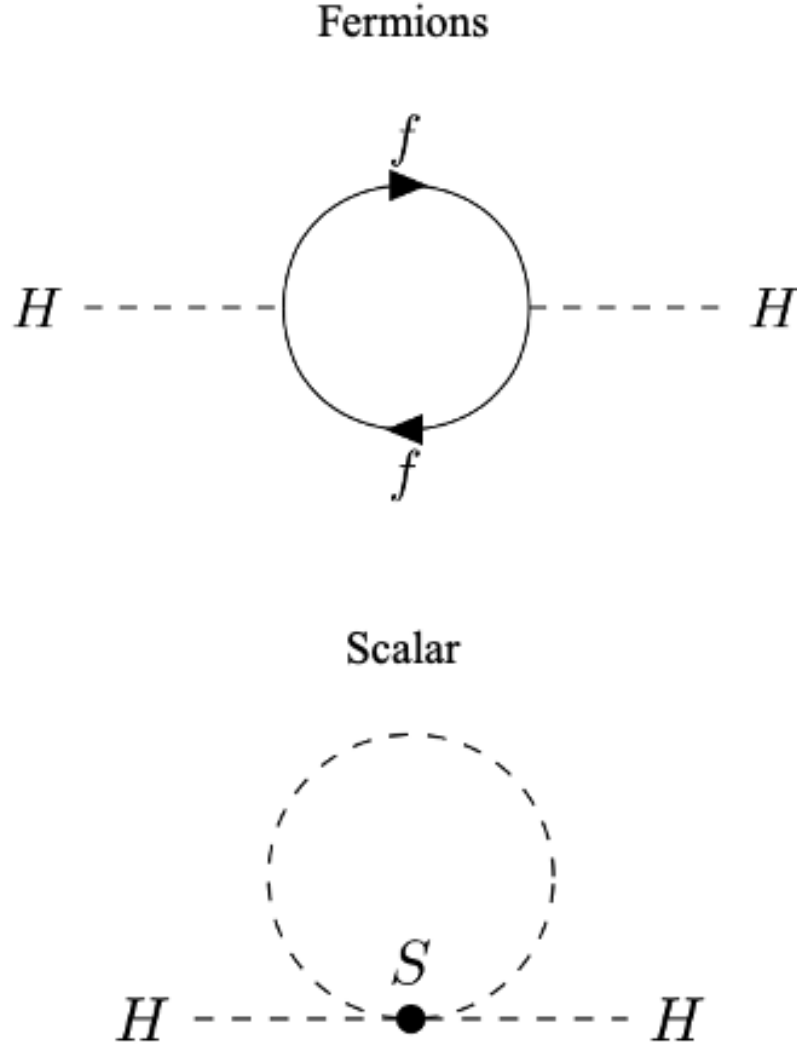


Figure 1.4: First order loop corrections to the Higgs mass. The loop for a fermion and a scalar are shown on the top and bottom respectively.

This poses an unresolved issue regarding the mass of the Higgs boson. The mass of the Higgs boson is measured to be $m_H = 125.1 \text{ GeV}$ [35]. This measured m_H is a sum of the bare mass term $m_{H,0}$ and quantum loop corrections Δm_H arising due to particles interacting with the Higgs field. The Δm_H has significant contributions from massive fermions like the top quark due to its strong coupling to the Higgs boson. Further, to regulate the loop integral an energy cutoff scale Λ is introduced. At energies typical of the electroweak scale, these corrections are negligible, however, if the Planck scale is considered to be the energy cutoff scale, then the quadratic divergences to the Higgs mass become an issue. Therefore, the corrections from the top quark interacting with the Higgs boson at the Planck scale will be much higher than the observed value of m_H . This is an important evidence that there must exist new physics between the electroweak and Planck scale that introduces a cancellation of these divergent corrections to the Higgs

boson mass and can account for the discrepancy in theoretical and observed mass of the Higgs boson.

$$m_H^2 = m_{H,0}^2 + \Delta m_{H,fermions}^2 + \Delta m_{H,bosons}^2 \approx m_{H,0}^2 - \sum_{fermions} \frac{|\lambda_f|^2}{8\pi^2} (\Lambda^2 + \dots), \quad (1.2)$$

Here λ_f is the Yukawa coupling of a fermion.

1.4 Supersymmetry: An elegant solution

This section introduces *Supersymmetry (SUSY)* as one of most promising Beyond the Standard Model (BSM) theories that overcomes the limitations of the SM. SUSY is an extension of the SM that introduces an underlying symmetry between fermions and bosons. The operator Q transforms fermions to bosons and vice versa (cite SUSY primer):

$$Q|Boson\rangle \propto |Fermion\rangle, \quad Q|Fermion\rangle \propto |Boson\rangle. \quad (1.3)$$

This new symmetry introduces a group orthogonal to the SM that can be expressed as $SU(3)_C \otimes SU(2)_L \otimes U(1)_Y \otimes SUSY$. According to Supersymmetry every SM particle has a SUSY superpartner such that for every SM fermion (boson) there is a SUSY boson (fermion). Due to orthogonality the mass and quantum numbers remain unchanged for the SUSY superpartner. However, these superpartners differ from their corresponding SM particles in terms of their spin by half a unit.

1.4.1 Solution to Hierarchy Problem and Unification

These additional particles provide an inherent solution to the Hierarchy Problem. As previously discussed the technical hierarchy problem arises from loop corrections to the Higgs mass causing significant divergences. However, with the inclusion of the SUSY particles, for each SM correction term there is an analogous supersymmetric contribution. The correction to the mass of the Higgs boson arising from the coupling of a fermion to the Higgs is presented in Equation (1.2). The new contributions arising due to the scalar SUSY particles is shown in Equation (1.4).

$$\Delta m_H^2 \approx \frac{\lambda_s}{16\pi^2} \left[\Lambda^2 - 2m_s^2 \ln\left(\frac{\Lambda}{m_s}\right) + \dots \right] \quad (1.4)$$

Here Δm_H is the correction to the physical Higgs boson mass and λ_s is the Yukawa coupling of a scalar of mass m_s . Assuming that the fermions and bosons couple to the Higgs in the same manner, i.e. $\lambda_s = |\lambda_f|^2$, then the contributions from the fermions and bosons interacting with the Higgs would cancel each other and prevent the divergences in Higgs boson mass at any given energy scale, leaving only the bare Higgs mass.

As previously discussed, the particles with the highest Yukawa couplings which itself is directly proportional to the masses of the particles, contribute most significantly to the loop corrections to the Higgs mass. Therefore the heaviest particles have the significant contributions. This implies that the SUSY counterparts to the third generation quarks,

the top \tilde{t} and bottom \tilde{b} squarks, are of key importance and should be close to the SM partners.

Another beneficial aspect of SUSY is that it leads naturally to the unification of the strong and electroweak forces as can be seen in Figure 1.5. It is observed from the plot that the evolution of the SM couplings as a function of energy does not converge (dashed line), which contradicts the prediction that there is a GUT scale where the forces unify. However with the addition of sparticles results in extra contributions to the renormalisation of the couplings such that at very high energies the couplings converge (solid line), suggesting the unification of the forces.

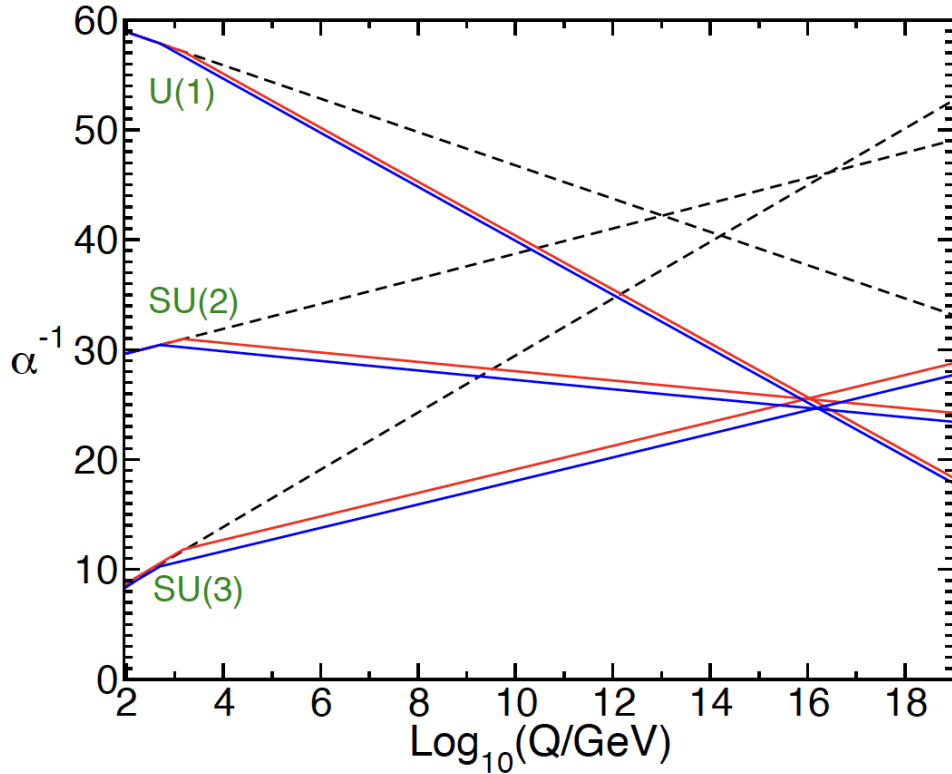


Figure 1.5: Evolution of the couplings in the SM (dashed) and SUSY (solid). Figure has been taken from [21].

1.4.2 Particle Content of Minimal Supersymmetric Standard Model (MSSM)

We can place the observed SM particles and their hypothetical superpartners into a *supermultiplet* which can be either scalar or vector in nature known as *chiral multiplet* and *gauge multiplet* respectively. The chiral multiplet consists of spin $\frac{1}{2}$ SM fermions and spin 0 SUSY partners. Since there are three generations of SM fermions there are three generations of chiral multiplets. Because the SM fermions are chiral spinors, they have two degrees of freedom that must be accounted for in the bosonic SUSY sector. Therefore each fermion has one scalar superpartner for the left-handed chirality \tilde{f}_L and another for the right-handed chirality \tilde{f}_R . The superpartners also experience the same

gauge interactions as their SM counterparts. The SUSY counterparts of the fermions have a prefix "s" due to their scalar nature for e.g. the *stop* (\tilde{t}) quark which is the SUSY counterpart of the top quark (t).

Name	Symbol	Supermultiplet		$SU(3)_C, SU(2)_L, U(1)_Y$
		spin 0	spin $\frac{1}{2}$	
squarks, quarks (one per generation)	Q	$(\tilde{u}_L \ \tilde{d}_L)$	$(u_L \ d_L)$	$(3, 3, \frac{1}{6})$
	\bar{u}	\tilde{u}_R^*	u_R^\dagger	$(\bar{3}, 1, -\frac{2}{3})$
	\bar{d}	\tilde{d}_R^*	d_R^\dagger	$(\bar{3}, 1, \frac{1}{3})$
sleptons and leptons (one per generation)	L	$(\tilde{\nu} \ \tilde{e}_L)$	$(\nu \ e_L)$	$(1, 2, -\frac{1}{2})$
	\bar{e}	\tilde{e}_R^*	e_R^\dagger	$(1, 1, 1)$
Higgs and Higgsinos	H_u	$(H_u^+ \ H_u^0)$	$(\tilde{H}_u^+ \ \tilde{H}_u^0)$	$(1, 2, +\frac{1}{2})$
	H_d	$(H_d^0 \ H_d^-)$	$(\tilde{H}_d^0 \ \tilde{H}_d^-)$	$(1, 2, -\frac{1}{2})$

Table 1.2: Chiral multiplets in the Minimal Supersymmetric SM (MSSM). This table contains the eigenstates after the supersymmetric transformation and do not represent the mass eigenstates [21]. The symbol for each of the chiral supermultiplets as a whole are indicated in the second column. Thus, for example, Q stands for the $SU(2)_L$ -doublet chiral supermultiplet containing \tilde{u}_L, u_L (with weak isospin component $T_3 = 1/2$), and \tilde{d}_L, d_L (with $T_3 = -1/2$), while \bar{u} represents the $SU(2)_L$ -singlet supermultiplet $\tilde{u}_R^*, u_R^\dagger$. Here, the fifth and final column describes of how different particles and their superpartners transform under the gauge groups $SU(3)_C$ (colour charge), $SU(2)_L$ (weak isospin), and $U(1)_Y$ (hypercharge).

In Table 1.2, the squarks and quarks transform as triplets under $SU(3)_C$, doublets under $SU(2)_L$ and the sleptons and leptons indicate that they are singlets under $SU(3)_C$, doublets under $SU(2)_L$. The electric charge under U is calculated by using $Q = T_3 + Y_W/2$, where Q represents the electric charge, T_3 is the weak isospin and Y_W is the hypercharge as mentioned in Section 1.2.

The SM Higgs boson and its superpartners also form chiral supermultiplets. The SM contains one Higgs doublet and as a consequence of charge conservation after the inclusion of SUSY, the SM sector is extended by adding two more Higgs doublets. The SUSY counterpart of the Higgs has a weak hypercharge of $Y = \pm \frac{1}{2}$ where the Higgs supermultiplet with $Y = +\frac{1}{2}$ gives mass to the up-type quarks and $Y = -\frac{1}{2}$ to the down-type quarks. Thus four gauge eigenstates are introduced from these two doublets: H_u^0, H_u^+ and H_d^0, H_d^- , which then mix to form the mass eigenstates: h^0, H^0, A^0 and H^\pm , where h^0 is the SM Higgs boson. Of this extended Higgs sector, it is the gauge eigenstates that are placed into a supermultiplet with their superpartners and are referred to as Higgsinos: $\tilde{H}_u^0, \tilde{H}_u^+, \tilde{H}_d^0, \tilde{H}_d^-$.

The gauge multiplets consist of the SM vector or gauge bosons and the SUSY counterparts are known as gauginos. As such all the supersymmetric particles in the gauge multiplet has a suffix '-ino' like a gluon's SUSY partner is called gluino. The spin 1 gauge bosons associated with the electroweak symmetry are the W_1, W_2, W_3 and B and the superpartners to these are referred to as winos and bino and are denoted as $\tilde{W}_1, \tilde{W}_2, \tilde{W}_3$ and \tilde{B} . As shown in Table ??luinos, which is an octet representation of $SU(3)_C$,

transforms as a singlet under $SU(2)_L$ and has zero hypercharge under $U(1)_Y$, the winos and W bosons transform as a singlet under $SU(3)_C$, belong to a triplet under $SU(2)_L$, and have zero hypercharge under $U(1)_Y$ and both bino and the B boson are singlets under $SU(3)_C$ and $SU(2)_L$, and they both have zero hypercharge under $U(1)_Y$.

Name	Supermultiplet		$SU(3)_C, SU(2)_L, U(1)_Y$
	spin $\frac{1}{2}$	spin 1	
gluinos and gluons	\tilde{g}	g	(8, 1, 0)
winos and W bosons	$\tilde{W}^\pm \tilde{W}^0$	$W^\pm W^0$	(1, 3, 0)
bino and B boson	\tilde{B}^0	B^0	(1, 1, 0)

Table 1.3: Gauge supermultiplets in the Minimal Supersymmetric SM (MSSM). This table contains the eigenstates after the supersymmetric transformation and do not represent the mass eigenstates [21].

These chiral and gauge supermultiplets have been summarised in Tables 1.2 and 1.3 respectively and provides an overview of the particle content of a phenomenologically viable extension of the SM, where the minimal content required to form a consistent theory is known as the Minimal Supersymmetric SM (MSSM) [46, 47].

1.4.3 R-parity

Despite solving the SM limitations, SUSY with its increased particle content introduces a coupling that would lead to a proton decay within seconds, whereas stringent limits exist on the proton lifetime set through experiment [48]. However, this issue too can be resolved by establishing a new symmetry known as *R-parity* [49] and defined as follows:

$$R = (-1)^{3(B-L)+2S} \quad (1.5)$$

where B, L and S are the baryon number, lepton number and spin respectively. R-parity is assumed to be conserved in all interactions. SM particles have an R-parity of $R = +1$ and all supersymmetric particles have $R = -1$. This implies that supersymmetric particles are only produced in pairs in order to conserve this quantum number, and as supersymmetric particles are unstable they eventually decay into lighter sparticles where the *Lightest Supersymmetric Particle* or *LSP*, is stable as it cannot decay any further thereby conserving R-parity. As such the LSP is also a very good candidate for dark matter. In R-parity conserving SUSY models, the lightest neutralino $\tilde{\chi}_1^0$ is electrically neutral and would interact solely via the gravitational interaction - behaving like a WIMP, and so is an attractive non-baryonic candidate for dark matter [50]. For this thesis, the $\tilde{\chi}_1^0$ is assumed to be the LSP.

1.4.4 Supersymmetric Mass Eigenstates

The SUSY particles undergo mixing of states just like the SM electroweak gauge bosons and quark flavours. This has been summarised in Table 1.4.

The neutral electroweak gauginos - bino and neutral wino and neutral higgsinos mix to form neutral particles known as the neutralinos, $\tilde{\chi}_{1-4}^0$. Likewise the charged winos and higgsinos also mix into mass eigenstates called charginos, $\tilde{\chi}_1^\pm$ and $\tilde{\chi}_2^\pm$. The amount of mixing between the binos, winos and higgsinos is driven by the bino mass M_1 , the wino mass parameter M_2 and the higgsino mass parameter μ . Also for the sfermion sector consisting of squarks and sleptons the mixing only happens for the third generation particles as the amount of mixing is proportional to the mass of the corresponding SM particle. Accordingly, the top and bottom squark gauge eigenstates, which are the superpartners of the left and right handed top and bottom, mix into $\tilde{t}_1, \tilde{t}_2, \tilde{b}_1, \tilde{b}_2$ where \tilde{t}_1 and \tilde{b}_1 are the lighter mass eigenstates by convention.

Name	Spin	R-parity	Gauge Eigenstates				Mass eigenstates			
Higgs boson	0	1	H_u^0	H_d^0	H_u^+	H_d^-	h^0	H^0	A^0	H^\pm
squarks	0	-1	\tilde{u}_L	\tilde{u}_R	\tilde{d}_L	\tilde{d}_R	(same)			
			\tilde{s}_L	\tilde{s}_R	\tilde{c}_L	\tilde{c}_R	(same)			
			\tilde{t}_L	\tilde{t}_R	\tilde{b}_L	\tilde{b}_R	\tilde{t}_1	\tilde{t}_2	\tilde{b}_1	\tilde{b}_2
sleptons	0	-1	\tilde{e}_L	\tilde{e}_R	$\tilde{\nu}_e$		(same)			
			$\tilde{\mu}_L$	$\tilde{\mu}_R$	$\tilde{\nu}_\mu$		(same)			
			$\tilde{\tau}_L$	$\tilde{\tau}_R$	$\tilde{\nu}_\tau$		$\tilde{\tau}_1$	$\tilde{\tau}_2$	$\tilde{\nu}_\tau$	
neutralinos	$\frac{1}{2}$	-1	B^0	W^0	H_u^0	H_d^0	$\tilde{\chi}_1^0$	$\tilde{\chi}_2^0$	$\tilde{\chi}_3^0$	$\tilde{\chi}_4^0$
charginos	$\frac{1}{2}$	-1	\tilde{W}^\pm	\tilde{H}_u^\pm	\tilde{H}_d^\pm		$\tilde{\chi}_1^\pm$	$\tilde{\chi}_2^\pm$		
gluino	$\frac{1}{2}$	-1			\tilde{g}				(same)	

Table 1.4: Gauge and mass eigenstates of the supersymmetric particles and the extended Higgs sector [21].

1.4.5 Spontaneous Supersymmetry Breaking

Despite the formalism of SUSY which theoretically reconciles the mass eigenstates of the sparticles, it is important to note that none of these sparticles have been observed. If SUSY was a perfect symmetry, then for e.g. a selectron \tilde{e} would have already been discovered with a mass equal to that of the SM electron e at the EW scale. Therefore, SUSY must be a broken symmetry and hence any supersymmetric model which aims to provide a realistic description of nature must contain a breaking mechanism, consequently leading to the supersymmetric partners being heavier than their SM partners.

The breaking mechanism must be broken spontaneously, but softly, so that the neat cancellation effect of the loop corrections to the Higgs boson mass remains. "Soft breaking" means that the effects of the breaking on the particle masses and interactions are mild and do not introduce large corrections that would disrupt the cancellation of quantum loop corrections to the Higgs boson mass as it plays a crucial role in the SM and SUSY theories. Quantum loop corrections involving particles (such as top quarks and gauge bosons) in the theory can significantly affect the Higgs boson mass. In order for the theory to be consistent, and maintain the cancellation of loop corrections, these corrections must be carefully balanced to avoid extreme fine-tuning. Therefore, soft breaking ensures that the high-energy (hence highly divergent) processes would continue to respect the

symmetry, while the low energy-processes would violate it and would cause loop corrections to the Higgs mass [51]. As a consequence of this kind of a breaking mechanism, the lightest supersymmetric particles are likely to have masses not much larger than the TeV scale [21]. Therefore we expect the masses of the top and bottom squarks to be close to that of their SM partners and accordingly maintains naturalness.

1.4.6 The Phenomenological MSSM (pMSSM)

The result of the soft SUSY breaking is that it introduces free parameters in addition to the 19 of the SM [52] to set the masses separately. By constraining a minimal model with experimental and theoretical constraints, it can be reduced to just 19 free parameters. This 19-parameter known as the ‘*phenomenological*’ *MSSM*, or *pMSSM* [53–55] provides a simpler framework that allows for phenomenological testing in experiments searching for these particles in the EW scale. The parameters describing the pMSSM are presented in Table 1.5.

Parameter	Description
$ M_1 , M_2 , M_3 $	Bino, Wino, Gluino mass parameter
$M_{\tilde{q}}, M_{\tilde{u}_R}, M_{\tilde{d}_R}, M_{\tilde{l}}, M_{\tilde{e}_R}$	1 st and 2 nd generation sfermion masses
$M_{\tilde{Q}}, M_{\tilde{t}_R}, M_{\tilde{b}_R}, M_{\tilde{L}}, M_{\tilde{\tau}_R}$	3 rd generation sfermion masses
A_t, A_b, A_τ	3 rd gen. trilinear couplings
μ	Higgsino/ Higgs mass parameter
$\tan\beta$	Ratio of Higgs vacuum expectation values
M_A	Pseudo-scalar Higgs boson mass

Table 1.5: Overview of the parameters of the pMSSM [21].

In conclusion SUSY predicts a set of new particles that aid in overcoming the shortcomings of the SM and when the argument for naturalness is considered these particles should begin to appear close to the EW scale, placing them within reach of current experimental high energy particle physics technologies.

Chapter 2

The Large Hadron Collider and the ATLAS experiment

Particle colliders are necessary for the expansion of our knowledge of the fundamental interactions in nature. The Large Hadron Collider (LHC) [6] is the largest particle collider built at present with a circumference of approximately 27 km. The LHC has been running since the September 10th, 2008. This chapter aims to describe this large accelerator complex and its experiments by providing an overview of the LHC and the ATLAS detector here based upon all the information that have been already very well documented [6, 56, 57].

2.1 The Large Hadron Collider (LHC):

The LHC is located at CERN in Geneva, Switzerland. It is installed around the Swiss-French border in the existing tunnel of the Large Electron Positron (LEP) collider which is approximately 100 m underground. The LHC was designed to accelerate proton beams to centre-of-mass-energies up to 14 TeV and heavy ions up to 2.8 TeV per nucleon and luminosities of $10^{34} \text{ cm}^{-2} \text{ s}^{-1}$ and $10^{27} \text{ cm}^{-2} \text{ s}^{-1}$, respectively.

Before being injected into the two LHC rings the protons are accelerated gradually at several steps. Figure 2.1 is a schematic representation of the accelerator complex. Any circular accelerator requires electric fields for acceleration in the longitudinal direction of the beam and magnetic fields in the transverse direction of the beam that keeps the particles on a circumference. In the LHC, the accelerating electric fields come in the form of Radio Frequency (RF) cavities. First, the protons are produced from negative hydrogen ions (H-) and accelerated to an energy of 160 MeV in the LINAC 4. After LINAC 4, these protons enter the Booster followed by the Proton Synchrotron (PS) where these protons are prepared in LHC bunch structures and the energy of the protons reaches 1.4 GeV and 25 GeV, respectively. The penultimate stage consists of the protons passing through the Super Proton Synchrotron (SPS), which accelerates them to energies of 450 GeV before the final injection into the LHC beam pipes. At full load there are in total 2808 bunches with each bunch containing $\sim 10^{11}$ protons per beam [6]. These bunches are not evenly spaced around the circumference of the ring but are grouped together in “trains”, the structure of which is called the “LHC filling scheme”. The

bunches are injected into two beam pipes and injected and accelerated to a centre of mass energy of 13 TeV. These proton beams are then bent by a magnetic field of 8.3 T generated by superconducting dipole magnets. And quadrupole magnets are used to focus the beam and direct them to the four collision points with a collision rate of 40 MHz.

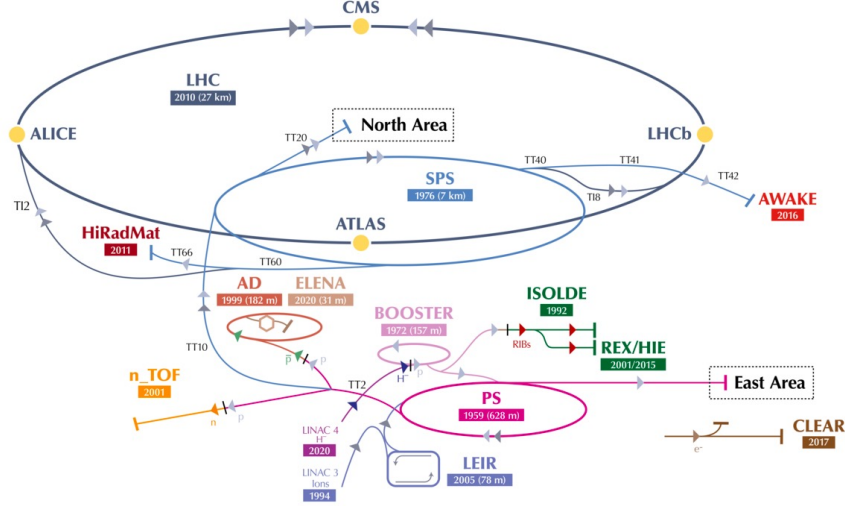


Figure 2.1: The LHC accelerator complex at CERN [56]. For pp collisions protons enter LINAC4 on this figure, followed by the Booster, Proton Synchrotron (PS) and the Super Proton Synchrotron (SPS) before finally arriving at the LHC.

2.1.1 The LHC experiments

There are four main large experiments which are located on each of the collision points around the LHC. Two of them, the ATLAS [57] (A Large Toroidal Lhc ApparatuS) and the CMS [58] (Compact Muon Solenoid) are general-purpose experiments. The main aim of these two experiments is to cover a wide range of physics searches and measurements. The other two experiments are: ALICE [59] (A Large Ion Colliding Experiment), which is dedicated to heavy-ion physics and focuses on studying QCD interactions at extreme energy densities and temperatures, and LHCb [60] which is an asymmetric detector built to record collision data in the forward direction only and specialises in the measurement of flavour physics that can appear in the interactions of hadrons containing mostly a bottom quark and charm and strange quarks. The LHC also has some smaller experiments situated around the LHC. Three of these smaller experiments are TOTEM (TOTal Elastic and diffractive cross-section Measurement) [61], LHCf (LHC forward) [62], MoEDAL (Monopole and Exotics Detector At the LHC) [63]. TOTEM consists of four detector pairs placed very close to the beam pipe at either side of the CMS detector and aims to study the products of inelastic collisions. MoEDAL is located close to the LHCb and is primarily designed to look for magnetic monopoles. The LHCf detector is similar in design to the MoEDAL counterpart and its detectors are placed on both sides of the ATLAS detector at 140 m from the collision point. Also, a new experiment called the FASER [64] (ForwArd Search ExpeRiment), is installed 480 m from the collision point of ATLAS, close to the beam axis, with the two main purposes of studying the

interactions of high-energy neutrinos and searching for elementary particles that couple weakly with matter. The SND@LHC (Scattering and Neutrino Detector) [65] is another an autonomous and compact scientific venture, designed to undertake pioneering neutrino measurements within an uncharted pseudo-rapidity range of $7.2 < \eta < 8.4$, a realm that complements the pursuits of other LHC experiments. Also situated 480 m downstream from ATLAS IP1, this experiment employs a distinctive amalgam of methodologies. Its detector configuration features an 800 kg assemblage of tungsten plates serving as a target mass, interspersed with emulsion and electronic trackers and a calorimeter and a muon system. This innovative framework adeptly discerns all three neutrino flavours, thus unveiling an unprecedented avenue for delving into heavy flavour production physics at the LHC. Notably, this is an unexplored domain for ATLAS, CMS, and LHCb. The intrinsic value of this sector is further accentuated, as it bears relevance to future circular colliders and the prediction of exceptionally high-energy atmospheric neutrinos.

2.1.2 Luminosity

The LHC luminosity is an important gauge of the operational efficiency of the accelerator. It relates the number of events, $\frac{dN}{dt}$ with the cross-section σ for a particular process. This connection between the instantaneous luminosity and the rate of events and the cross-section of a specific process is expressed by the following Equation (2.1):

$$\frac{dN}{dt} = \sigma \mathcal{L}. \quad (2.1)$$

For any collider, the instantaneous luminosity \mathcal{L} can be generally described with Equation (2.2), where N_b , is the number of bunches, n_p , is the number of protons in each of the two interacting bunches assuming they both have the same number of particles, A , is the area where the bunches overlap and f_{rev} , is the frequency of revolution in the LHC ring.

$$\mathcal{L} = \frac{N_b n_p^2}{A} f_{rev} \quad (2.2)$$

The integrated luminosity L which is used to describe a the luminosity over a period of time is obtained by integrating both sides of Equation (2.1):

$$N = \sigma L, \quad L = \int \mathcal{L} dt. \quad (2.3)$$

Integrated luminosity L is given in units of inverse cross-section, where typically the unit of cross-section is the barn ($1 \text{ b} = 10^{-28} \text{ m}^2 = 10^{-24} \text{ cm}^2$). Also, from Equation (2.3) it can be deduced that for a process with small σ , increasing the luminosity, increases the probability of finding that rare process.

2.1.3 Performance overview and Pile-up

After the proton beams are injected into the LHC, they are accelerated to the desired energy and collisions are initiated as soon as the beams are stable. These collisions last for several hours and during this time all the LHC experiments collect data from the pp collisions. The quality of beams degrades over time and the luminosity decreases. Once the luminosity falls below a certain level the beams are dumped and the magnets are readapted for a new fill. From the start of filling the LHC rings with the proton beams to dumping them, is known as a "fill".

The LHC operates at a stretch for a few years known as "LHC Runs" and before it is shut down for maintenance and upgrades known as "Long Shutdowns". There have been two LHC Runs and two Long Shutdowns and the new Run 3 has begun and has been collecting data since August 2022 as shown in Figure 2.2

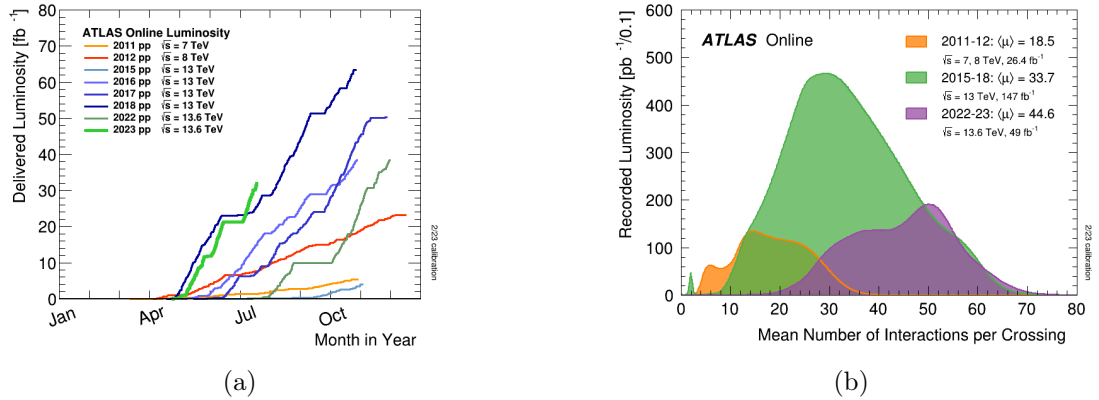


Figure 2.2: The plots show the delivered luminosity during Run 1, Run 2 and Run 3 [66] on the left and the distribution of the average number of interactions per crossing $\langle \mu \rangle$ on the right [67].

The analysis work in this thesis utilises the full LHC Run 2 data collected between 2015 to 2018. In the course of Run 2, the LHC reached an integrated luminosity of 160 fb^{-1} and exceeded its designed luminosity in 2018 by reaching the highest peak instantaneous luminosity of $2.1 \times 10^{34} \text{ cm}^{-2} \text{ s}^{-1}$.

Increasing luminosities i.e. the number of interactions per bunch crossing adversely affects the data collected by the experiments as there is an increase in the "pile-up" as shown in Figure 2.2b. Pile-up constitutes any interactions that contaminate the event we are interested in. Sometimes, the detector while recording an event also reads contributions from other bunch crossings such as the previous or following ones. These other interactions are called "out-of-time pile-up". Another type of pile-up known as "in-time pile-up" is caused by the multiple pp interactions in a single bunch crossing. The most energetic of these pp interactions is called the hard-scatter interaction followed by the other interactions in the same bunch crossing.

2.2 The ATLAS Detector

ATLAS is a cylindrical multi-purpose detector located on the LHC ring at one of the collision points. The detector weighs 7000 tonnes and measures 44m in length and 25m in height. The cylindrical shape of the detector along with its forward-backward symmetry is designed to capture particle interactions in all directions around the collision point. The detector is composed of broadly three sub-detectors designed to detect the different signatures left by the different particles arising from high-energy pp collisions in the LHC.

A complete diagram showing the overall design of the detector and its components is shown in Figure 2.3.

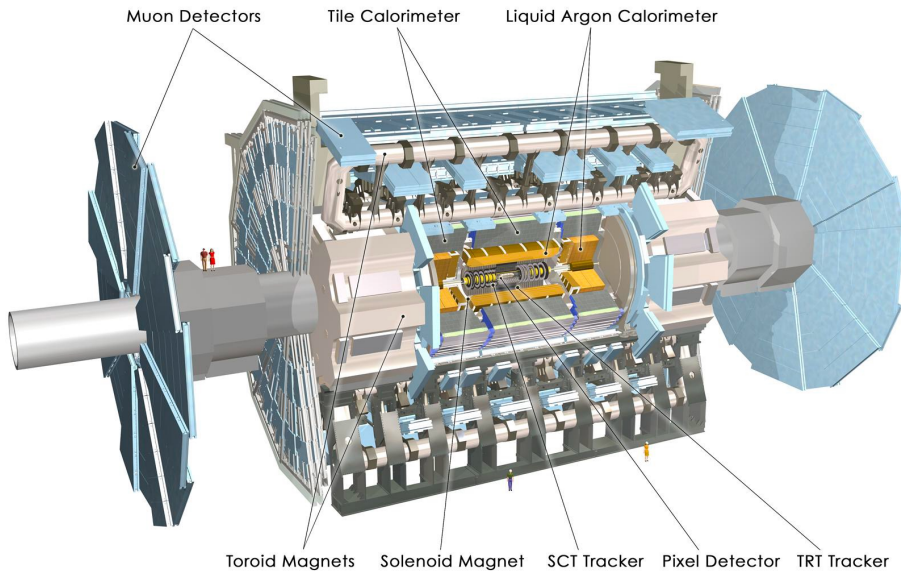


Figure 2.3: A computer generated image of the ATLAS experiment with cut out sections to show the layout of all the subsystems. Figure has been taken from Reference [68].

2.2.1 The Coordinate System

The coordinate system originates from the collision or interaction point (IP). The z -axis is aligned along the beamline, the x -axis points towards the centre of the LHC and the y -axis upwards, creating a right-handed coordinate system. The two sides of the detector are called "A-side" and "C-side" for positive and negative values of the z -axis, respectively. From the coordinate system the azimuthal angle ϕ and polar angle θ are also obtained. The ϕ , is measured in the transverse $x - y$ plane with respect to the positive x -axis and the θ , is measured relative to the positive z -axis. Like the $x - y$ plane is known as the transverse plane, the $y - z$ plane forms the longitudinal plane.

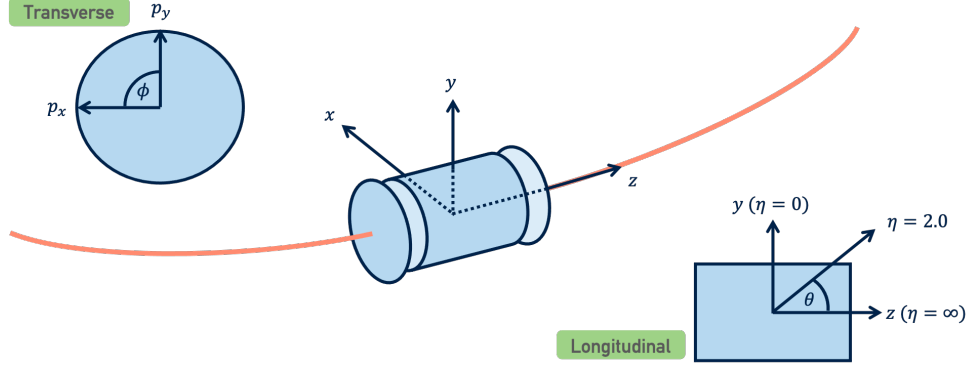


Figure 2.4: A simplistic schematic of the ATLAS experiment where the red sweeping line indicates the LHC beamline and the Cartesian coordinate system is overlaid on the barrel of the experiment. Two important planes are shown; the transverse plane (top left) and the longitudinal plane (bottom right). The transverse plane shows the two components of momentum as well as the azimuthal angle, the longitudinal shows some examples of the pseudo-rapidity, η [69].

As it is not possible to know the exact momentum of the colliding partons along the z -axis, the Lorentz invariant quantities are used for the measurements. To this end, a kinematic variable called "rapidity" (y) is defined in Equation (2.4):

$$y = \frac{1}{2} \ln \left(\frac{E + p_z}{E - p_z} \right). \quad (2.4)$$

The difference between the rapidity of two particles, Δy , is invariant under longitudinal Lorentz boosts, providing a solution to challenges related to parton momentum measurement. Therefore, variables such as transverse momentum is defined as shown in Equation (2.5):

$$p_T = \sqrt{p_x^2 + p_y^2}. \quad (2.5)$$

The sum of the transverse momenta of all the particles in the collision must also be zero, due to momentum conservation. This is used to detect the invisible particles whose collective momenta is the negative vector sum of the momenta of all visible particles inside the detector. Like the transverse momentum, another variable called pseudorapidity (η) is defined as shown in Equation (2.6):

$$\eta = -\ln[\tan(\theta/2)]. \quad (2.6)$$

For particles with momentum close to its energy, the rapidity can be approximated to

the pseudorapidity.

In the $\eta - \phi$ coordinate space the distance between objects ΔR , with (η_1, ϕ_1) and (η_2, ϕ_2) , is:

$$\Delta R_{12} = \sqrt{(\Delta\eta_{12})^2 + (\Delta\phi_{12})^2} = \sqrt{(\eta_1 - \eta_2)^2 + (\phi_1 - \phi_2)^2}. \quad (2.7)$$

2.2.2 The Inner Detector

The inner detector (ID) tracking system is the innermost sub detector of the ATLAS detector. It consists of three subsystems that employ different particle detection techniques: the pixel detector (PD), the semiconductor tracker (SCT) and the transition radiation tracker (TRT) as shown in Figure 2.5. The ID is divided into three regions, the central barrel region and two endcaps. The ID is designed to detect charged particles by reconstructing the trajectories of charged particles passing through with excellent momentum resolution and determine the positions of the interaction vertices of these particles with $|\eta| < 2.5$ [57]. The ID is embedded in a 2 T magnetic field produced by a superconducting solenoid magnet which "bends" these charged particles.

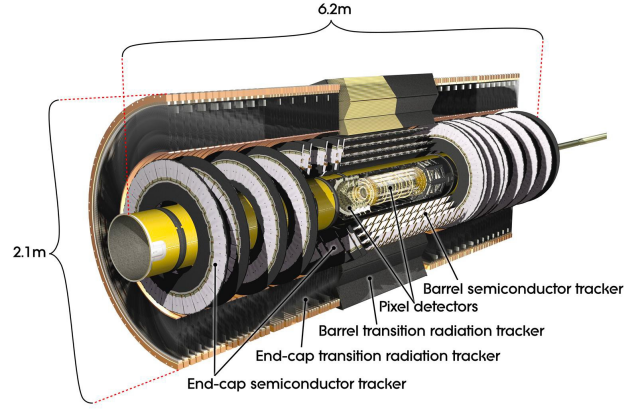
It is important to use as little material as possible in the ID to reduce secondary scattering from the incident particles interacting with detector material. Also, the ID has to be extremely radiation-hard being so close to the IP.

Silicon Pixel Detector

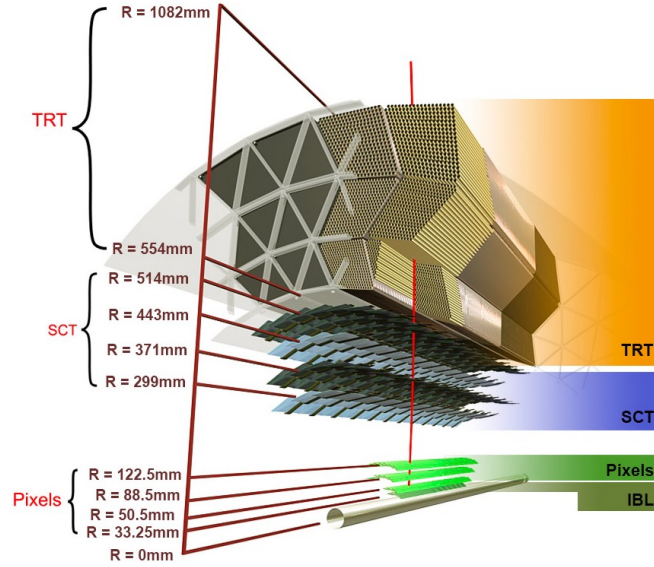
The pixel detector is the ID subsystem closest to the IP. The innermost layer of the detector is the insertable B-layer (IBL) [70], which is located at a radial distance of 33 mm from the z -axis and inserted during the first long shutdown (LS1) to maintain and improve the tracking performance of the detector. The pixel detector consists of 1744 modules arranged in three barrel layers and two endcaps each with three disc layers. Each of these modules are made up of 16 front-end chips each with 2880 electronic channels that are connected to the trigger and data acquisition system. The pixels on the sensors have a minimum size of $50 \times 400 \mu\text{m}^2$ and constitutes of reverse bias diodes. When a charged particle passes through one of these pixel sensors already under application of an external electric field, and depleted of its free charge carriers, it generates electrons and holes that moves in opposite directions. Simply put, a "hit" is registered if this induced current over a cluster of pixels is greater than a certain threshold and read out as binary decision of "1" and otherwise "0" by the front-end electronics of the modules made of the sensors+front-end electronics. The operational temperature of these sensors is below 0°C and the applied bias voltage is 150 V and increases over the operational period of the LHC runs. This lessens the adverse effects of the long term high radiation environment. The pixel detector (PD) provides a wide pseudo-rapidity coverage of $\eta \leq 3$.

Semiconductor Tracker

The next subsystem of the ID is the silicon Semi-Conductor Tracker (SCT). This detector subsystem is composed of four layers in the barrel region (BR) and nine disks in the endcap (EC) region. A p-in-n strip technology is employed. So the SCT is made of micro-strips that are 6 or 12 cm long and have a pitch of $80 \mu\text{m}$. There are two sets of strips: one aligned parallel to the beam axis and the other askew by 40 mrad stereo angle



(a)



(b)

Figure 2.5: (a) Computer generated image of the complete inner detector [57] and (b) a 3D drawing of the sensors and structural elements of the ID barrel region with a 10 GeV track with a red line traversing the beam-pipe, the IBL, pixel, SCT and TRT layers at $\eta = 0.3$.

with respect to the first layer. This allows for two-dimensional position measurement. The resulting spatial resolution achieved by the SCT is $17 \mu\text{m}$ in $(R-\phi)$ and $580 \mu\text{m}$ in z or R in both BR and EC.

Transition Radiation Tracker

The outermost part of the ID is the Transition Radiation Tracker (TRT). It is made of polyamide drift tubes or "straws" that are 4 mm in diameter with one $31 \mu\text{m}$ gold-plated tungsten anode wire running through its centre. Each straw is filled with a gas mixture of 70% Xenon, 27% carbon dioxide and 3% molecular oxygen. There is a potential difference of 1.5 kV between the wall of the straw and the central anode wire [71]. The TRT provides track measurements with spatial resolution to $120 \mu\text{m}$ per straw in the $(R-$

ϕ) and a pseudo-rapidity coverage of $\eta \leq 2$. When a charged particle passes through the TRT it ionises the gas mixture leaving a trail of free electrons and ions. The negatively charged electrons drift in the electric field to the central anode wire where they are amplified and read out as a signal. In between each straws, an inhomogeneous material is placed that causes a fundamental process of light emission and occurs whenever a charged particle moves across this region. This is known as transition radiation. The intensity of the emitted radiation depends on the $\beta = \text{velocity of particle} / \text{speed of light}$, of the traversing particle, with particles with lower mass emitting more transition radiation photons. As a result, the energy deposits from electrons which are the highest can be distinguished from other particles, such as pions.

2.2.3 The Calorimeter Systems

After the ID and the solenoid magnet lie the calorimeter systems. These measure the energy of incident particles by completely absorbing them within the calorimeter's volume. Unlike the ID, the calorimeters can measure the energies of both charged and neutral particles. Also, the calorimeters cannot measure the energy of very weakly interacting particles such as neutrinos and high p_T muons that traverse through the calorimetry system. It covers a range of $|\eta| < 4.9$ and is completely geometrically symmetric in ϕ . There are two types of calorimeters in the ATLAS calorimeter subsystem placed in three locations - Electromagnetic Calorimeter (ECal), the Hadronic Calorimeter (HCal), and the Forward Calorimeters (FCal), as shown in Figure 2.6.

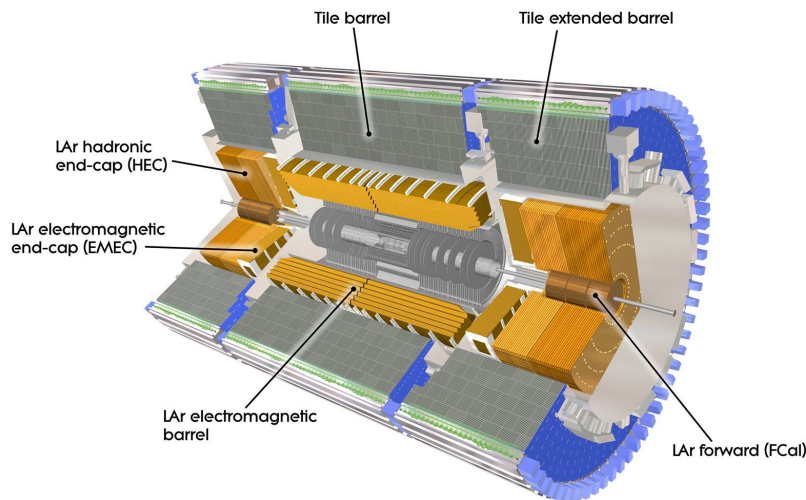


Figure 2.6: Schematic view of the ATLAS Calorimeter system [57].

The entire calorimetry system is 12.2 m long with an outer radius of 4.25 m. All the calorimeters are sampling calorimeters, i.e. they are segmented in the transverse plane and in ϕ by using alternating layers of high-density passive material, which produces particle showers and active material, which is used for particle identification and determination of the particle energy flow direction. In case of the ECal, the magnitude of the measured signal from the showers is proportional to the energy of the incident particles, in the case of electrons, positrons and photons. The HCal is used for the reconstruction

of jets and indirectly the missing transverse momentum. An important feature of the calorimeters is the depth as it must contain the showers and prevent these particles from reaching the muon detector. For the ECal, this depth is calculated in terms of the radiation length X_0 which is the mean length into the material at which the energy of an electron is reduced by a factor $1/e$ via bremsstrahlung. While for the HCal, the depth is estimated in terms of the interaction length λ , which is the mean distance a hadron travels into the material before it interacts inelastically with a nucleus. The ECal has a total depth $> 22 X_0$ in the barrel and $24 X_0$ in the endcaps and the HCal has 9.7λ in the barrel and 10λ in the endcaps. Also, the calorimeter subsystem covers the entire ϕ range and pseudo-rapidity $|\eta| < 4.9$. When juxtaposed with the shower length with respect to energy deposition, the ECal and HCal configurations play a significant role. The substantial depths of the ECal and HCal contribute to efficient shower development and energy absorption, thereby facilitating accurate measurement and reconstruction of particle energies within the detector.

Electromagnetic Calorimeter

The ECal has two sections, the ElectroMagnetic Barrel (EMB) and the ElectroMagnetic End-Caps (EMEC) with $|\eta| < 1.47$ and $1.47 < |\eta| < 3.2$, respectively [57]. The layers and the cell segmentation for a barrel module is shown in Figure 2.7a.

The EMB consists of two half-barrel calorimeters and two coaxial wheel calorimeters which are located on either side of the forward regions. The active and passive materials used are liquid argon (LAr) and lead, respectively, at low temperatures. This allows for good detector performance and high radiation resistance. To maintain the ECal operation requirements, it is placed within three independent cryostats. To collect the charge output, lead absorber plates are interleaved with kapton electrodes which are arranged in an accordion geometry to avoid dead zones and minimise the electronic dead-time. The region covered by $|\eta| < 2.5$, covered both by the ID and ECal is very important for precision measurements and constitutes of three longitudinal layers. The first layer is finely segmented into strip cells to improve the measurement in the $|\eta|$ -direction. The second layer is made of square tower cells that collect the largest fraction of energy obtained from an electromagnetic shower. And the third layer cells collect the remaining tails of the electromagnetic shower and is therefore twice the size of the cells in the second layer. The middle and outer cells of the LAr calorimeters feature a fine granularity of 0.0245×0.025 and 0.0245×0.05 in $(\phi - \eta)$, respectively. This high level of detail is particularly advantageous for distinguishing between electrons and photons, especially when they originate from neutral and charged pions. These pions are among the most commonly produced particles in the LHC experiments. The EMEC is structurally similar to the EMB except that it is rotated in the radial direction instead of the axial direction as in the case of the EMB. Also, between the ID and the ECal exists a presampling calorimeter ($|\eta| < 1.8$), which estimates the energy loss of electrons and photons from their interactions with the preceding material. It is made of 1.1 cm thick layer of LAr in the barrel and 0.5 cm in the endcap region.

Though using LAr calorimeters comes with many advantages such as detector uniformity, linear response, radiation hardness, and high granularity, it also has some drawbacks including poor stochastic term resolution which is a property of sampling calorimeters, challenging cryogenics and slow charge collection time. Slow charge collection happens as the LAr calorimeters operating at an applied voltage of 2 kV, the charge collected takes

~ 450 ns compared to the 25 ns LHC bunch crossing. This slow extraction of physics signals and triggering of the detector is then adjusted by employing a technique called "Time Calibration" that samples these signals every 25 ns. This approach creates an ideal pulse shape as illustrated in Figure 2.7b.

The combined energy resolution in the ECal is shown in Equation (2.8),

$$\frac{\sigma_E}{E} = \frac{10\%}{\sqrt{E}} \oplus 0.7\% \quad (2.8)$$

where, \oplus denotes quadrature sum.

Hadronic Calorimeter

The HCal is located right outside the ECal and constitutes the the Tile Calorimeter (TileCal), the Hadronic End-Cap Calorimeter (HEC) and the Forward Calorimeter (FCal). The TileCal is a sampling calorimeter with an inner radius of 2.28 m, and an outer radius of 4.25 m, that employs steel as the absorber material and scintillating tiles as the active material. It comprises a central barrel covering a region of $|\eta| < 1.0$ and two extended barrels covering over $0.8 < |\eta| < 1.7$. Like the ECal, the TileCal is made of three layers with different depths. The central barrel layers have respective thicknesses of 1.5λ , 4.1λ and 1.8λ , and the other barrels have the corresponding depths of 1.5λ , 2.6λ , and 3.3λ . The HEC comprises two wheels at each end of the detector that is segmented into two longitudinal sections and covers a region of $1.5 < |\eta| < 3.2$ which overlaps with both the tile and forward calorimetry regions. It employs copper plates as an absorber and LAr as the active material. The resolution of the barrel and endcap calorimeters is given by Equation (2.9):

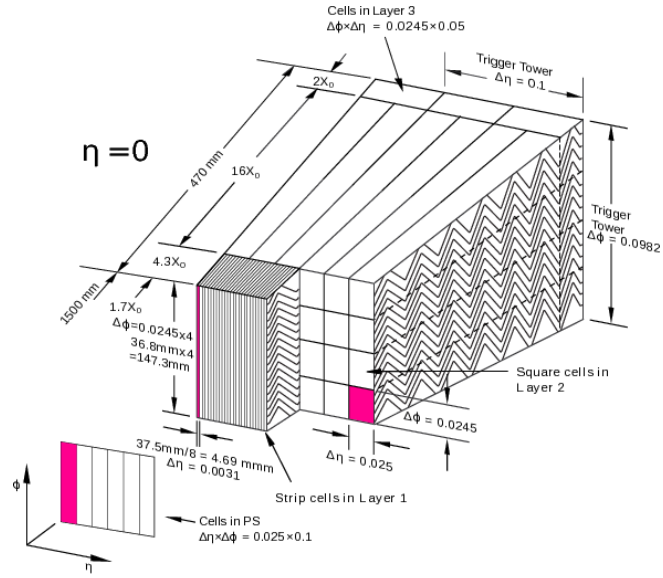
$$\frac{\sigma_E}{E} = \frac{50\%}{\sqrt{E}} \oplus 3\%. \quad (2.9)$$

The FCal consists of three layers per endcap covering a region of $3.1 < |\eta| < 4.9$. The first layer designed for electromagnetic measurements, is closest to the interaction point and employs copper as the absorber material. The other two layers are designed to estimate mainly the hadronic activity and use tungsten instead. The active material employed for all the layers in the FCal is LAr. A brass layer is present after the FCal to intercept any remnants of the hadronic shower. The FCal energy resolution can be calculated using Equation (2.10):

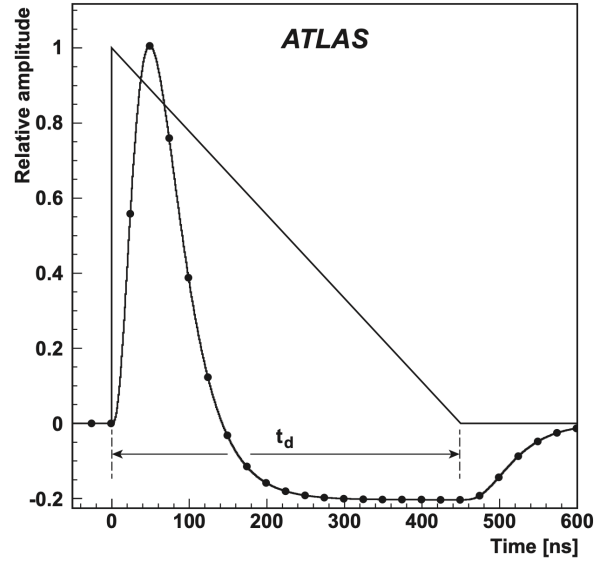
$$\frac{\sigma_E}{E} = \frac{100\%}{\sqrt{E}} \oplus 10\%. \quad (2.10)$$

2.2.4 The Muon Spectrometer

The Muon Spectrometer (MS) is the outermost part of the detector, typically reached by muons as all the other particles have already been absorbed in the calorimeters. The MS comprises high-precision tracking chambers that have separate trigger chambers for fast signal processing. Figure 2.8 represents the MS and its parts schematically. The



(a)



(b)

Figure 2.7: (a) Schematic view of the ATLAS Calorimeter system and (b) the idealised pulse shape for signal extraction. Figures have been taken from Reference [57].

MS operates by bending the muons in the bending plane ($\eta - z$) and taking precise positional measurements. The most important part of the MS are the superconducting toroid magnets which provide the required magnetic field for the measurement of the momentum of the traversing muons. The MS magnetic system consists of three magnets: one large one in the barrel region and two in the endcaps on either side of the detector, covering $|\eta| < 1.4$ and $1.6 < |\eta| < 2.7$, respectively. Each of these magnets have eight coils. The coils on the barrel magnet have their individual cryostat and the endcap ones have a common cryostat with 0.5 T and 1 T magnetic fields, respectively instead. Also, in the barrel, the tracking chambers are placed in three cylindrical layers around the beam axis and in the endcaps, three wheels are placed perpendicular to the beam axis 7.4 m, 10.8 m and 21.5 m from the interaction point.

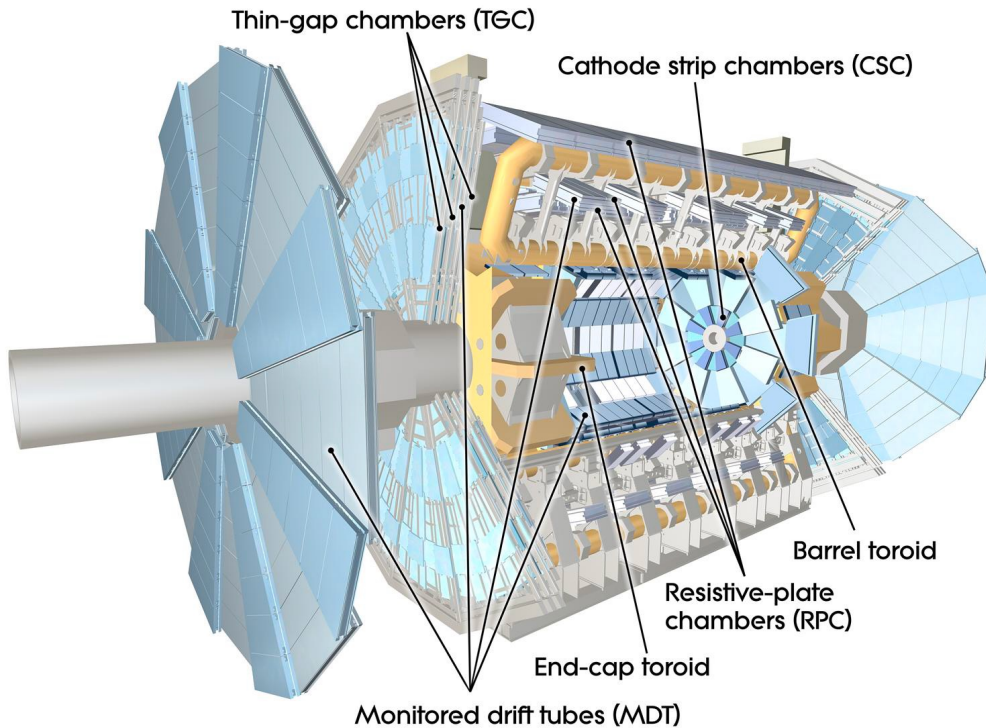


Figure 2.8: Schematic view of the ATLAS Muon spectrometer [57].

The muon system comprises four different gas detectors that provide both time and spatial information. These gas detectors operate on a similar principle to silicon detectors but utilise ionising gas instead of doped semiconductors to generate signals [72].

For high-precision tracking information within the range $|\eta| < 2.7$, Monitored Drift Tubes (MDTs) are utilised. The MDTs have a relatively low counting rate of 250 Hzcm^{-2} . During Run 2, Cathode Strip Chambers (CSCs) were used in the inner layers with a higher counting rate of 1000 Hzcm^{-2} . However, in the second long shutdown, the CSCs in the Small Wheels (part of the forward muon tracking system) were completely replaced with New Small Wheels [73]. The New Small Wheels employ two technologies: small-strip Thin Gap Chambers (sTGC) and Micromegas detectors (MM).

In addition to the tracking detectors, two other types of detectors, namely Resistive Plate Chambers (RPCs) and Thin Gap Chambers (TGCs), are utilised for fast trigger signal generation in event selection. RPCs are employed in the barrel region, while TGCs cover

the end-caps, providing trigger signals within a pseudorapidity range up to $|\eta| < 2.4$.

2.2.5 Forward Detectors

In addition to the main ATLAS detector systems described before, smaller sets of detectors are located that measures particle properties at very high absolute values of pseudorapidity along with additional beam information in the very forward region. These detectors are listed as follows:

- The Luminosity Cherenkov Integrating Detector-2 (LUCID-2) [74], is the main detector used for luminosity monitoring during Run 2 in the ATLAS experiment. It comprises two detectors located around the beam-pipe on either ends of the ATLAS detector at ~ 17 m from the IP. This detector estimates the luminosity by detecting Cherenkov light signals from charged particles from the debris of inelastic proton-proton collisions and also provides online monitoring of instantaneous luminosity.
- The Zero-Degree Calorimeter (ZDC) [75] has two modules placed at a distance of ± 140 m from the ATLAS IP. It is a sampling calorimeter which is made of alternating layers of quartz rods, the active medium and tungsten plates, the absorber medium. The ZDC can detect neutral particles at $|\eta| \geq 8.2$, that is crucial in case of heavy-ion collisions. In case of pp collisions it is employed for tagging minimum-bias events.
- The ATLAS Forward Proton (AFP) [76] is made of two parts located on either side of the detector at 204 m and 217 m with respect to the ATLAS IP and extends the physics reach of the ATLAS detector by detecting and measuring properties of the extremely forward protons. However, the AFP mostly targets to study diffractive processes where one or both protons remain intact after the collision.
- The Absolute Luminosity For ATLAS (ALFA) detector [77] is placed at a distance of ± 240 m from the IP. It is made up of scintillating fibre trackers placed in four Roman pots stations that is adjustable and very close to the beam (~ 1 mm). The ALFA is mainly used to estimate the total pp cross-section and the luminosity, by measuring the proton scattering at very small angles.
- The design purpose of the Beam Conditions Monitor (BCM) made of radiation hard pCVD diamond sensors are to protect the detector from damage from abnormal beam conditions and measure the instantaneous luminosity. These sensors are installed in the pixel detector very close to the IP.

The AFP, ALPHA and LUCID are being used in Run 3.

2.3 The ATLAS Trigger and Data Acquisition

The frequency of the pp collisions occurring every 25 ns is 40 MHz. This leads to a high quantity of data to be stored and subsequently analysed. Therefore, interesting events have to be selected and stored using the Trigger and Data Acquisition System (TDAQ). The TDAQ in Run 2 consists of two systems: the Level-1 Trigger (L1) and the High

Level Trigger (HLT) [78].

The Level 1 Trigger The Level 1 (L1) trigger is a hardware-based trigger system plays a crucial role in the data selection process. It takes input from the sub-detectors and performs an initial set of selections based on preliminary object reconstruction. The L1 trigger system is divided into three components: L1Calo, which operates on calorimeter information; L1Muon, which utilises the muon spectrometer; and L1Topo, which applies more complex analysis to jets, electrons, taus, and muons following L1Calo processing. After the L1 trigger components process and identify objects of interest, the data is then sent to the Central Trigger Processor (CTP). This initial stage significantly reduces the data rate from the initial 40 MHz to 100 kHz. Once this reduction is achieved, the selected events are passed on to the High-Level Trigger (HLT) for further analysis and decision-making.

The High Level Trigger The high-level trigger (HLT) in the ATLAS experiment is designed to access the complete readout from the detector at the L1 trigger rate. Unlike the hardware-based L1 trigger, the high-level trigger operates using software algorithms, enabling more intricate selections and criteria to be applied. By employing advanced object reconstruction techniques, the rate of selected events is further reduced from the L1 rate of 100 kHz to approximately 1 kHz. Events that are selected by the L1 trigger undergo immediate processing through event buffering facilitated by the Read-Out System (ROS). The high-level trigger itself consists of a farm comprising 2800 CPUs, which execute offline-like event reconstruction on the complete detector readout, including partial track reconstruction (as depicted in Figure 2.9). Following the high-level trigger selection, the chosen events are categorised into different data streams. These events are then sent to local storage for processing at a Tier-0 facility. The Main Physics Stream, which serves as the primary data used for physics analysis, is further divided into distinct categories based on the physics objects present in the event, such as b-jets, electrons, muons, and so on. Additionally, an Express stream is utilised to swiftly reconstruct the data using offline data processing techniques. This stream dedicates a small portion of the bandwidth to assess data quality and provide calibration information.

2.4 Particle Reconstruction in ATLAS

The primary objective of the ATLAS experiment is to utilise the electrical signals obtained from the detector to reconstruct all stable and interacting particles generated in a given pp collision. By identifying these candidate objects, a wide range of Standard Model processes and potentially interactions beyond the Standard Model can be investigated. Once the reconstruction process is finalised, physicists possess a dataset consisting of events that contain "physics objects." This section will provide a comprehensive overview of the process involved in constructing these objects.

Figure 2.10 illustrates the interactions of various particles with the ATLAS detector. Dashed lines in the diagram represent particles that do not interact with a specific portion of the detector, whereas solid lines indicate particles that do interact with that particular region.

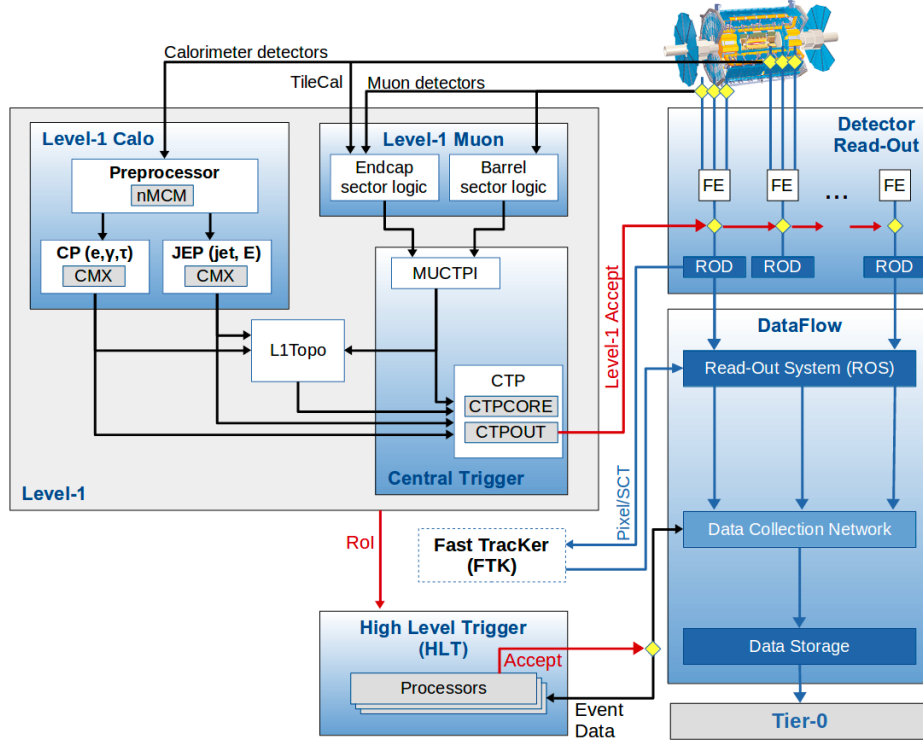


Figure 2.9: Diagram of the ATLAS Trigger and Data Acquisition System in Run 2 taken from reference [78].

2.4.1 Tracks and Vertices

Tracks in the ATLAS detector are defined relative to a reference point, typically the beamspot where proton-proton collisions occur. These tracks are characterised by a set of track parameters: d_0 , z_0 , ϕ , θ , and q/p . The transverse impact parameter, d_0 , represents the closest point in the transverse plane to the reference position, while z_0 is the longitudinal impact parameter, similar to d_0 but in the longitudinal plane. The angles ϕ and θ denote the azimuthal and polar angles, respectively, and q/p is the charge of the reconstructed track q divided by the track momentum p .

The track reconstruction process starts in the innermost pixel layer using an "inside-out" approach. A track seed, formed by three space points in unique layers of the pixel or SCT sub-detectors of the Inner Detector (ID), is sought by the track reconstruction algorithm (see Figure 2.11a). Once these track candidates pass various quality cuts such as momentum and number of hits, they become part of the track collection. The tracks are then extended into the Transition Radiation Tracker (TRT) through classical track extrapolation. If successful, the track is said to have a TRT extension. Another step involves forming tracks from the TRT in regions seeded by the electromagnetic calorimeter. These tracks are subsequently extended inwards towards the SCT and pixel detectors. TRT tracks without any silicon hits are retained for photon reconstruction as discussed later in Section 2.4.3. The TRT hits are shown in Figure 2.11b. All these tracks constitute the final reconstructed track collection [80].

The resulting track collection is used to identify the primary interaction in a bunch

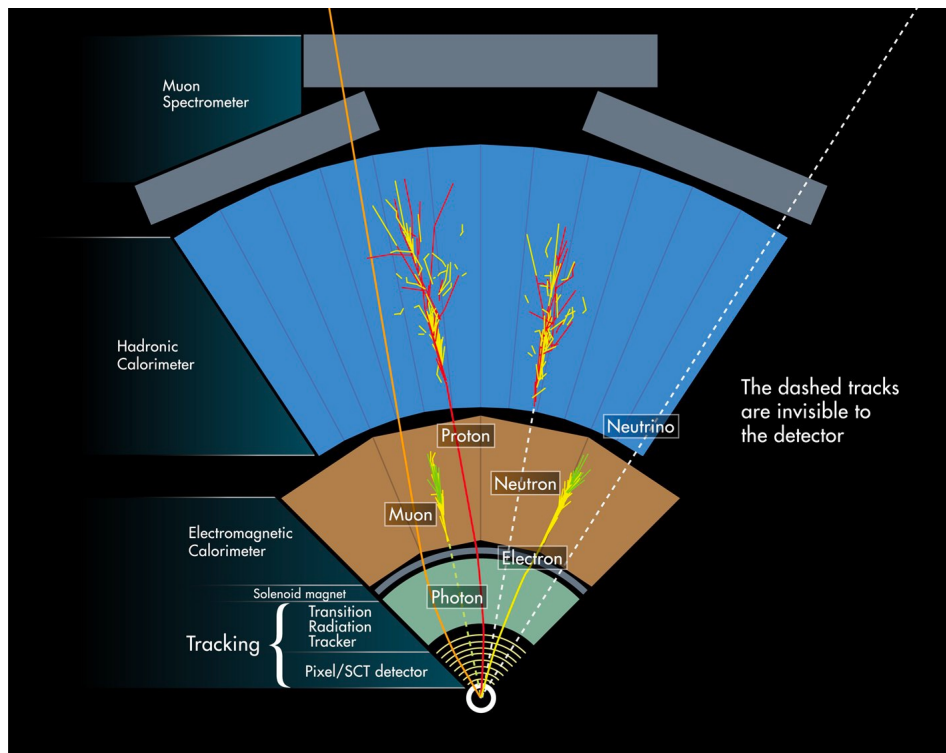


Figure 2.10: The diagram displays a single "slice" of the detector in the transverse plane, revealing each of the sub-detectors as they extend outward from the beam-pipe. The sub-detectors visible in the illustration include the Inner Detector (ID), the electromagnetic calorimeter (ECal), the hadronic calorimeter (HCal), and the muon spectrometer (MS). This has been taken from reference [79].

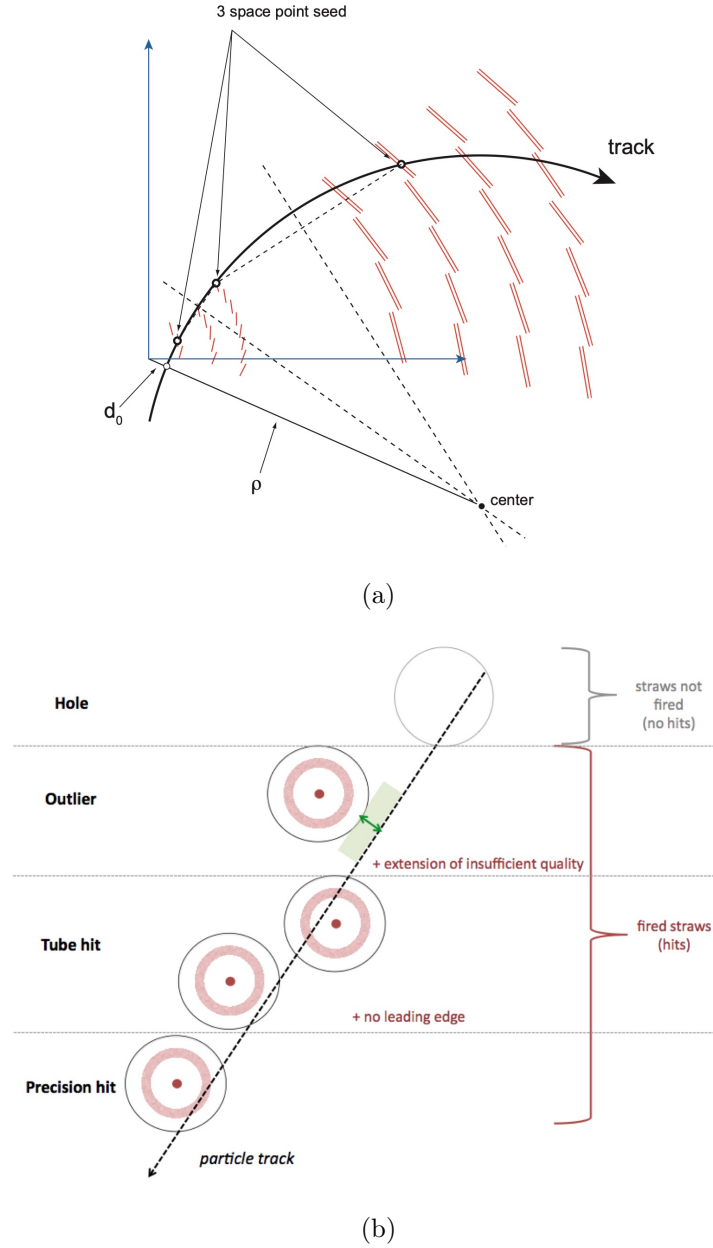


Figure 2.11: Schematic representation of (a) the process of the track seeding method in ATLAS where ρ is the radius of the circle determined from the track [82] and (b) the definition of TRT hits [80].

crossing with the highest energy. This is accomplished by defining primary vertices (PVs) through vertex finding and vertex fitting processes [81]. The PV with the highest $\sum p_T^2$ of associated tracks is more likely to be the location where the interesting physics phenomena occurred. All other vertices are known as pile-up vertices.

2.4.2 Electrons

The reconstruction of electrons in ATLAS involves combining information from the EM calorimeter and tracks from the Inner Detector (ID). The trajectory of the tracks is projected to the calorimeter, where a calorimeter cluster is expected to be found. ATLAS adopts the topo-clustering approach as the standard method for reconstructing electrons, photons, and hadronic jets. This clustering algorithm groups adjacent cells in the calorimeter to form three-dimensional clusters, which ideally represent the energy and direction of the incident particles. The primary criterion for clustering the cells is the cell energy significance, defined as the measured cell energy divided by the expected cell noise [83] as shown in Equation (2.11).

$$\zeta_{cell}^{EM} = \frac{E_{cell}^{EM}}{\sigma_{noise cell}^{EM}} \quad (2.11)$$

The algorithm follows these steps:

1. Clustering begins from a seed cell in the calorimeter, which has an energy significance above a threshold value S , $|\zeta_{cell}^{EM}| > S$. For Run 2, the threshold was set at $S = 4$.
2. The cluster expands by adding neighbouring cells that satisfy a growth control threshold (N) such that $|\zeta_{cell}^{EM}| > N$, with $N = 2$ for Run 2.
3. The cluster boundaries are determined by adding cells that meet a principal cell filter threshold (P) such that $|\zeta_{cell}^{EM}| > P$, set at $P = 0$ for Run 2.

This approach is commonly referred to as the *4-2-0 ATLAS topo-clustering* algorithm [84]. Clusters with a longitudinal and lateral shower profile consistent with that of an electromagnetic (EM) shower are selected to form regions-of-interest (ROIs). Standard track reconstruction is performed in the Inner Detector, and these tracks are matched to the ROIs, taking into account the effects of bremsstrahlung in the detector, to seed a supercluster [84]. The super-clustering method, introduced in 2017, replaced a previous "sliding-window" technique [85].

The reconstructed electrons then undergo calibration using regression boosted decision trees (BDT) trained to correct the energies of the uncalibrated electron candidates [86]. To ensure high purity of electrons, a set of quality requirements, known as "working points," are applied. These working points are defined using a likelihood discriminant and include "Loose", "Medium", and "Tight" quality working points. Isolation working points are also defined by comparing the energy in a cone or region around the electron to the energy of the electron itself [84].

2.4.3 Photons

The reconstruction of photons in ATLAS follows a similar procedure to that of electrons. The topo-clusters for photons are seeded in a similar manner [86], but there are differences in how tracking information is utilised. To seed a photon supercluster, the topocluster must have a slightly higher transverse energy (E_T) threshold of $E_T > 1.5 \text{ GeV}$ [84]. There are two main types of photon reconstruction:

1. **Converted photons:** In this case, the photon interacts with the material in the Inner Detector, resulting in the production of charged particles (electrons or positrons) that leave tracks in the ID modules. These conversions can be single or double-track conversions [85].
2. **Unconverted photons:** Here, the photon does not undergo conversion and appears solely as an energy deposit in the EM calorimeter [85].

The calibration procedure for photons is similar to that of electrons, and the working points for photon identification are constructed in a similar manner [84].

2.4.4 Muons

Muons in ATLAS are reconstructed using signals from the Inner Detector (ID) and the Muon Spectrometer (MS) independently. The reconstruction of muons in the ID follows the same procedure as for other tracks, as described in section 2.4.1. Tracks reconstructed in both the MS and ID are then combined to form the final collection of muons. To achieve high precision in momentum and resolution for muons, corrections are applied. These correction factors are determined by studying Z boson decays to e^+e^- and J/ψ meson decays to e^+e^- in both data and Monte Carlo simulations.

After the muons are reconstructed, various selection criteria can be applied to ensure the purity of the muon sample, similar to the selection process for electrons. These quality requirements are designed to identify signal muons while rejecting those originating from background processes such as the decay of hadronic particles like kaons or pions. The quality of the tracks used to reconstruct the muon, both in the ID and MS, is utilised to define a set of quality working points [87].

2.4.5 Jets

In high-energy collisions, quarks and gluons undergo hadronisation, resulting in a stream of colour-neutral hadrons. These hadrons leave detectable signals in the Inner Detector (ID) and calorimeters, which are used to construct jets. Jets provide valuable information about the initial quark or gluon, including their energy and direction.

The process of jet construction begins with clustering the hadronic energy deposits in the Hadronic Calorimeter (HCal) into structures called topo-clusters [83, 88, 89]. The topological clustering algorithm groups HCal cells based on the amount of energy they contain above the total noise level. It starts by identifying seed cells that significantly exceed the noise level (signal-to-noise ratio $> 4\sigma$) and iteratively adds neighbouring cells with high energy deposits ($> 2\sigma$). Adjacent cells are combined while ensuring no overlaps between topo-clusters using a cluster-splitting algorithm. The resulting clusters are treated as massless objects and used to create a four-vector originating from the primary vertex, with the energy associated with it equal to the sum of the topo-cluster cells.

To construct jets, the topo-clusters and ID tracks are combined using the Particle Flow (PF) algorithm [90], resulting in Particle Flow Objects (PFOs) used in jet formation. The PF algorithm first addresses overlaps between momentum measurements in the ID

and energy measurements in the calorimeters. It then matches individual topo-clusters to well-measured tracks, creating a track/topo-cluster system. The track is used to estimate the average expected energy deposit ($\langle E_{dep} \rangle$) in the calorimeter, which is compared with the actual energy of the topo-cluster. If necessary, additional topo-clusters are added to the track/topo-cluster system. The energy in these added topo-clusters is subtracted cell-by-cell using $\langle E_{dep} \rangle$, leaving behind remnants that are removed if their energy matches the expected fluctuations in the energy shower.

PFOs are formed by combining tracks matched to the primary vertex ($|z_0 \sin\theta| < 2 \text{ mm}$) with energy-subtracted topo-clusters. The topo-clusters then serve as inputs to the anti- k_t algorithm clustering algorithm [91]. This algorithm belongs to a group of sequential recombination algorithms that use distances (d_{ij}) between clusters i and j , as well as between a cluster i and the beam ($d_{i\beta}$), to construct jets in a sequential manner. These distances are defined as in Equations (2.12), (2.13) with R representing the desired radius of the jets.

$$d_{ij} = \min \left(p_{T,i}^{2p}, p_{T,j}^{2p} \right) \frac{\Delta R_{i,j}^2}{R^2} \quad (2.12)$$

$$d_{i\beta} = p_{T,i}^{2p} \quad (2.13)$$

The algorithm follows these steps:

- Calculate all distances d_{ij} and d_i .
- If the smallest distance d_i corresponds to a cluster, define that cluster as a jet and remove it from subsequent calculations.
- If the smallest distance d_{ij} corresponds to clusters i and j , replace them with a new combined cluster.

This procedure repeats until all clusters have been combined or classified as jets. The anti- k_t algorithm, with $p = 1$, starts with the most energetic clusters and gradually combines them with neighbouring low-energetic clusters. This approach ensures that the constructed jets remain infra-red and collinear safe, meaning that the emission of soft gluons and collinear splitting of a parton do not significantly alter the properties of the jets [92].

As the topo-clusters are initially calibrated at the electromagnetic (EM) scale [90], a jet calibration is necessary to obtain the jet energies at the hadronic scale. The Jet Energy Scale calibration [93] corrects the energy scale of the jets by comparing them to simulated truth jets. This calibration accounts for variations in the jet energy due to factors such as incorrect jet origin, pile-up, dependence on the flavour of the original parton, and η (a parameter) [89]. Additionally, the calibration of the associated jet energy resolution is performed.

To further suppress pile-up-induced jets, the Jet Vertex Tagger (JVT) algorithm [94] is employed. JVT combines the Jet Vertex Fraction, which represents the fraction of total momentum from tracks originating from the primary vertex, with the number of primary vertices in the event using a multivariate approach. Applying a selection based on the

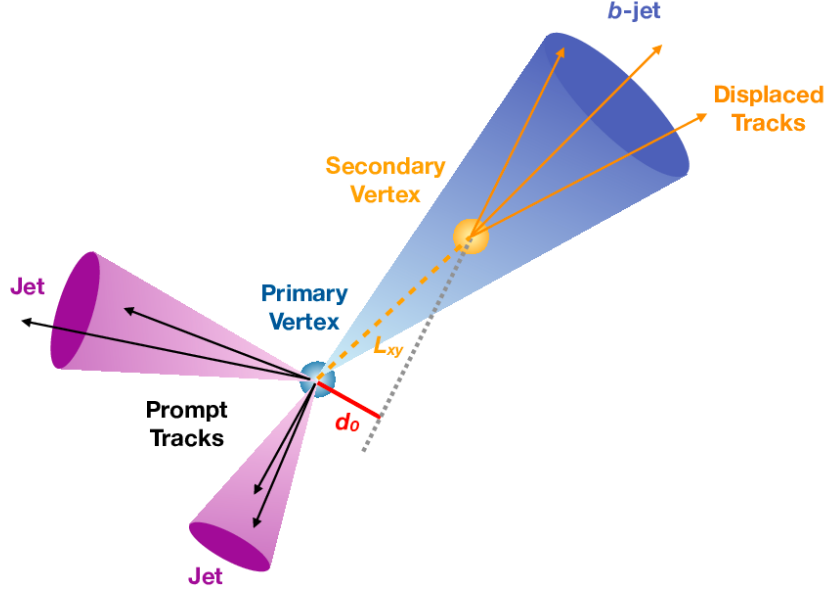


Figure 2.12: Example of the production of two light jets and a b -jet in the transverse plane. Taken from reference [98].

JVT improves the rejection of pile-up events while maintaining a consistent efficiency with respect to the number of primary vertices.

It is worth noting that jets can also be constructed from sources other than pp -collisions, including beam-induced backgrounds (BIB) caused by proton losses away from the interaction point, cosmic-ray showers, and calorimeter noise. Prior to analysis, it is crucial to remove such jets. This is achieved by applying quality criteria that consider variables such as the signal pulse shape in the LAr calorimeters, as well as track-based and energy ratio-based variables [95].

b-tagged Jets

The accurate identification of jets originating from the hadronisation of a b -quark such as a B-meson, known as b -jets, is of great significance in this thesis. These B-mesons decay in a proper time of approximately 1.5 ps, where the proper time is the time as measured in the rest frame of the particle. This short lifetime results in their travel distance of a few millimetres before decaying, creating a secondary vertex, as depicted in Figure 2.12. and can be distinguished by specific features, such as displaced vertices and secondary semi-leptonic decay products. Thus, the jet can be tagged as a b -jet [96, 97]. The identification of b -jets involves two steps: low-level algorithms and high-level algorithms, aimed at enhancing efficiency.

In the first step, the low-level algorithms utilise the tracks associated with a jet and their impact parameters to assess if they originate from a secondary vertex. Several low-level algorithms are employed, including:

- IP2D and IP3D, which are impact parameter (IP) based algorithms utilising information about the impact parameter of the tracks associated with the jets [99].
- The SV1 algorithm, which focuses on reconstructing the secondary vertex [100].
- The JetFitter algorithm, which reconstructs the complete decay chain of b and c -hadrons [101].

The outputs of these low-level algorithms serve as inputs for the high-level algorithms. ATLAS employs two main high-level algorithms: MV2 and DL1. MV2 utilises a Boosted Decision Tree (BDT) approach, while DL1 utilises a Deep Neural Network (DNN) [102]. DL1 incorporates the same inputs as MV2, along with input from the JetFitter algorithm, thereby improving the rejection of c -jets and light-flavour jets compared to MV2.

The performance of these algorithms is evaluated based on their efficiency and their ability to discriminate against light-flavour and c -jets. The b -tagging efficiency represents the probability of correctly identifying a b -jet using the algorithm. The mistag rate, on the other hand, refers to the probability of erroneously tagging a c -jet or light-flavour jet as a b -jet. The b -tagging efficiency is estimated separately from simulations and collision data, and a Scale Factor (SF) is determined as the ratio between data and simulation. This SF is used to weight simulated events on a per-jet basis. To estimate the b -tagging efficiency and mistag rates in data, $t\bar{t}$ events with two opposite sign leptons and two jets in the final state are employed. The efficiencies and mistag rates for the MV2 algorithm can be found in references [103, 104]. Typically, the b -tagging efficiency using the MV2 algorithm in the ATLAS experiment at the LHC is reported to be around 77% for b -jets, for a drop of 20% in the light-flavoured jet (i.e. jets originating from up, down, or strange quarks) rejection [97].

2.4.6 Missing Transverse Momentum

In pp collisions, the partons involved in the hard interaction predominantly carry momentum along the beam axis (z -axis) and possess nearly zero momentum in the transverse plane. According to momentum conservation principles, the vector sum of the transverse momenta of all collision products should be zero. However, any deviation from this is missing transverse momentum, which is denoted as $\mathbf{E}_T^{\text{miss}}$ and represents the negative of the vector sum. The reconstruction of $\mathbf{E}_T^{\text{miss}}$ commences after the reconstruction and calibration of previously mentioned objects such as jets, photons, and leptons. Since these objects are reconstructed independently, some energy deposits or associated tracks can be utilised by multiple objects. Therefore, a step to remove any overlaps is performed before estimating the $\mathbf{E}_T^{\text{miss}}$.

The reconstructed high p_T physics objects, including electrons, muons, hadronic decaying visible electrons, photons, and jets, collectively known as the "hard-term" of $\mathbf{E}_T^{\text{miss}}$, constitute the objects involved in the hard interaction. Conversely, tracks originating from the primary vertex (PV) that are not associated with any of the "hard" objects constitute the "soft" component. The soft term plays a crucial role in estimating the scale and resolution of $\mathbf{E}_T^{\text{miss}}$, especially in events with a low number of hard objects. It is reconstructed by utilising tracks from the Inner Detector (ID) associated with the PV.

So the total missing transverse momentum vector ($\mathbf{E}_T^{\text{miss}}$) can be calculated [105] as the

sum of these terms as:

$$\mathbf{E}_T^{\text{miss}} = - \underbrace{\sum_{i \in \text{Hard Objects}} \mathbf{p}_T^i}_{\mathbf{E}_T^{\text{miss, Hard}}} - \underbrace{\sum_{i \in \text{Soft Signals}} \mathbf{p}_T^i}_{\mathbf{E}_T^{\text{miss, Soft}}} . \quad (2.14)$$

$$\mathbf{E}_T^{\text{miss}} = - \underbrace{\sum_{\text{Selected Electrons}} \mathbf{p}_T^e}_{\mathbf{E}_T^{\text{miss, e}}} - \underbrace{\sum_{\text{Selected Muons}} \mathbf{p}_T^\mu}_{\mathbf{E}_T^{\text{miss, } \mu}} - \underbrace{\sum_{\text{Selected Jets}} \mathbf{p}_T^{\text{jets}}}_{\mathbf{E}_T^{\text{miss, jet}}} - \underbrace{\sum_{\text{Unused Tracks}} \mathbf{p}_T^{\text{soft}}}_{\mathbf{E}_T^{\text{miss, Soft}}} . \quad (2.15)$$

Hard Term
Soft Term

Chapter 3

Upgrade of the ATLAS ITk Data Transmission Chain for the HL-LHC

The High-Luminosity Large Hadron Collider (HL-LHC) is an upgrade to the existing LHC accelerator complex and detectors of associated experiments positioned around the collision points. The HL-LHC upgrade objective is to increase the integrated luminosity of the LHC by a factor of 5 to 7 compared to its current design luminosity. This will consequently provide scientists with a much larger number of collisions to study, enabling more SM precision measurements and expand the reach of BSM studies and the potential discovery of new particles or phenomena. This upgrade of the LHC is scheduled to take place in 2026–2028 in the Long Shutdown 3 (LS3) as presented in Figure 3.1. The first phase of the HL-LHC upgrade is expected to take place between 2026 and 2027 and the LHC will undergo modifications to increase its luminosity. Then 2027-2028 onwards further modifications and improvements to the accelerator and its experiments.

In order to achieve the desired increase in luminosity, the HL-LHC upgrade plan includes several key enhancements. One of the primary focuses is the replacement of the existing LHC superconducting focusing magnets with new superconducting focusing magnets capable of generating stronger magnetic fields. These upgraded magnets will enable tighter focusing of the particle beams, resulting in a higher particle density and more frequent collisions. Additionally, the installation of new radio frequency (RF) cavities is planned to accelerate and control the proton beams effectively. These RF cavities play a crucial role in maintaining beam stability and optimising its performance. Furthermore, the HL-LHC upgrade will incorporate crab cavities, which have the capability to tilt the particle beams and maximise the chances of head-on collisions. This innovative approach further contributes to increasing the overall luminosity of the collider. These upgrades collectively aim to significantly enhance the performance of the HL-LHC, enabling higher collision rates and greater precision in data collection.

In response to the challenges presented by the High-Luminosity upgrade of the LHC, the ATLAS detector must also undergo significant upgrades. This chapter focuses on the replacement of the current Inner Detector of the ATLAS experiment with the all-silicon Inner Tracker (ITk). The ITk features advanced capabilities such as high-speed and radiation-hard data transmission. A crucial component of this upgrade is the electrical-to-optical conversion stage, known as the optoboard, which combines multiple electrical

signals into an optical signal. This chapter provides an overview of the HL-LHC project and the ITk, highlighting their importance in advancing the capabilities of the ATLAS detector. It then delves into the details of the ITk Pixel data transmission chain, with a specific focus on the optosystem and its various components. The author's work in this area involves validating the preliminary versions of the optoboard design through functionality tests. Additionally, an analysis of the signal quality is performed both before and after irradiation to ensure accurate propagation of transmitted data through the entire chain. Through this upgrade and validation process, the ATLAS experiment aims to enhance its ability to handle the increased luminosity and radiation environment of the HL-LHC. The advancements in the ITk Pixel data transmission chain, including the optosystem, play a crucial role in maintaining the accuracy and reliability of the detector's measurements during high-energy collisions.

3.1 The High Luminosity LHC

To increase the luminosity to reach the design luminosity of the HL-LHC, the injection chain must undergo upgrades [106].

The replacement of the LINAC 2 by LINAC 4 is part of the overall plan to prepare the LHC for the HL-LHC project that has already been done during the LS2 [107]. The improved beam quality and intensity provided by LINAC 4 also contributes to the overall improved performance of the LHC during the present Run 3. The LINAC 4 accelerates negative hydrogen ions (H^-) to an energy of 160 MeV while the LINAC 2 accelerated protons from a source to an energy of 50 MeV. In the LINAC 4, these ions are then stripped of their electrons to produce proton beams that are further accelerated in subsequent stages of the accelerator complex before being injected into the LHC for high-energy collisions. In the injector chain, the Proton Synchrotron Booster (PSB) is also upgraded to provide a beam energy of 2 GeV instead of 1.4 GeV. Furthermore, the PS and SPS will also be upgraded to cope with the increased injection energy and beam current.

Another major upgrade to the LHC consists of replacement of the current focusing superconducting magnets at the interaction points with new triplet quadrupole magnets placed at the ATLAS and CMS IPs. These new focusing magnets are made from a compound of niobium-tin (Nb3Sn), which exhibits superconductivity at very low temperatures. Nb3Sn has a higher critical magnetic field than other superconducting materials, such as niobium-titanium (NbTi). This higher critical magnetic field of Nb3Sn allows for stronger magnetic focusing. These new magnets will provide a magnetic field of 11–12 T from the current magnetic field of 8.33 T and reduce the β^* function at the IPs. These new magnets aid in increasing the peak instantaneous luminosity and requires a larger crossing angle to keep the two beams separate when sharing a common beam pipe which consequently reduces the instantaneous luminosity (\mathcal{L}). To address this, the HL-LHC will employ RF crab cavities to generate a transverse electric field that rotates each of the bunches by half the crossing angle to ensure a head-on collision. The HL-LHC is expected to deliver $\mathcal{L} = 7.5 \times 10^{34} \text{ cm}^{-2} \text{ s}^{-1}$ that is almost 3 times the LHC Run 2 instantaneous luminosity \mathcal{L} . This would imply an increase in the pile-up in the general purpose detectors to up to $\langle \mu \rangle = 200$. The increased luminosity level should allow the delivery of 300 - 350 fb⁻¹ per year i.e. as many pp collisions per year as the current

LHC has since its first decade of operation, resulting in a total integrated luminosity of $L = 3000 - 4000 \text{ fb}^{-1}$.

The HL-LHC plans to use a luminosity levelling scheme that will limit \mathcal{L} to $5 \times 10^{34} \text{ cm}^{-2} \text{ s}^{-1}$ by utilising techniques such as the Beam-Beam Compensation (BBC) which involves using an additional beam or an external force to counteract the effects of the opposing beam, thereby reducing the beam-beam interaction and maintaining the luminosity at a desired level. However, even with these added measures, the expected pile-up conditions and radiation doses will be much higher than at the LHC. And tracking all the particles produced from an average of 200 simultaneous pp interactions cannot be managed by the current tracking detectors in the LHC experiments. Also, an increased integrated luminosity (L) will cause more radiation damage and would consequently degrade the performance of the present detectors very fast. As such the LHC experiments have to be upgraded as well.

The following section provides an overview of the largest detector component of the High-Lumi upgrade of the ATLAS detector - the replacement of the current ID with an all-silicon ITk that will take place during LS3.



Figure 3.1: Current timeline of the LHC and HL-LHC programs. The installation of the HL-LHC mainly takes place in the LS3 in 2026-2028. At the same time, ATLAS and CMS will undergo their HL upgrades. Taken from reference [108].

3.2 ATLAS ITk System

The HL-LHC upgrade will require improvements to the ATLAS Inner Tracker (ITk) [27, 28] to handle the increased collision rate and maintain the high-quality tracking capabilities.

The main goals for the HL-LHC upgrade of the ATLAS ITk are:

1. Increased radiation hardness: The ITk needs to withstand the higher radiation

- levels generated by the increased collision rate. To achieve this, new radiation-tolerant materials and electronics will be used in the construction of the detector.
2. Improved granularity: The ITk will have a higher number of modules additional tracking layers for tracking with smaller pixel sizes and strip pitches in comparison to the pixel and strip detectors in the current ID, resulting in improved spatial resolution. This enhanced granularity will provide better tracking of charged particles, allowing for more precise measurements of their momentum and charge.
 3. Enhanced timing capabilities: The ITk will also have improved timing capabilities to enable more accurate identification of particle tracks and better reconstruction of particle decay vertices. This will be achieved by reducing the timing uncertainty of the detector modules.
 4. Reduced material budget: Minimising the material budget in the ITk is crucial to reduce multiple scattering and improve particle trajectory measurements. By using lightweight materials and optimising the detector layout, the ITk achieves lower material density and thus less scattering. This is crucial to reduce the scattering and energy loss of particles passing through the detector, which can degrade the measurement accuracy.

To meet these goals, the ITk will incorporate new technologies, such as advanced silicon sensors, improved readout electronics, and innovative cooling systems and the design of the ITk needs to fulfil among others these requirements [27]:

- Full detector coverage for tracks with $p_T > 1$ GeV originating from a region of $|z| < 15$ cm and $r < 2$ mm.
- Reconstruction of tracks from the primary vertex up to $|\eta| < 4$.
- Efficient tracking performance comparable or better than in the ID in HL-LHC pile-up conditions of $\langle \mu \rangle \simeq 200$.
- Radiation resistant for the expected 10 years of operation with $\mathcal{L} \leq 7.5 \times 10^{34} \text{ cm}^{-2} \text{ s}^{-1}$ with replacement of innermost components after 5 years.

The ATLAS ITk comprises a strip detector [27] in the outermost layers and a pixel detector [28] in the innermost layers closer to the IP as shown in Figure 3.2. It is an all-silicon tracker without a TRT-like sub-detector.

The strip detector covers the pseudorapidity region of $\eta < 2.7$. It consists of four barrel layers and six end-cap rings on each side of the barrel located at $385 \text{ mm} < r < 1000 \text{ mm}$ and upto $|z| < 2850 \text{ mm}$. The strip detector uses double modules with a pitch, which refers to the distance between adjacent strips in the detector module, of $69 - 85 \mu\text{m}$ in the $r - \phi$ plane. The pitch of these strip sensors is comparable to the current SCT. However, unlike the SCT, the strip detector has 10x the number of channels to cover the entire volume.

The pixel detector of the ITk further consists of three sub-systems: the Inner System (IS), the Outer Barrel (OB) and two Outer Endcaps (OEs). In the region closest to the IP, known as the low z region, the modules, which consist of a sensors and corresponding electronics, of the ITk pixel detector are positioned on specialised support structures called staves. These staves are arranged parallel to the beam pipe and are grouped

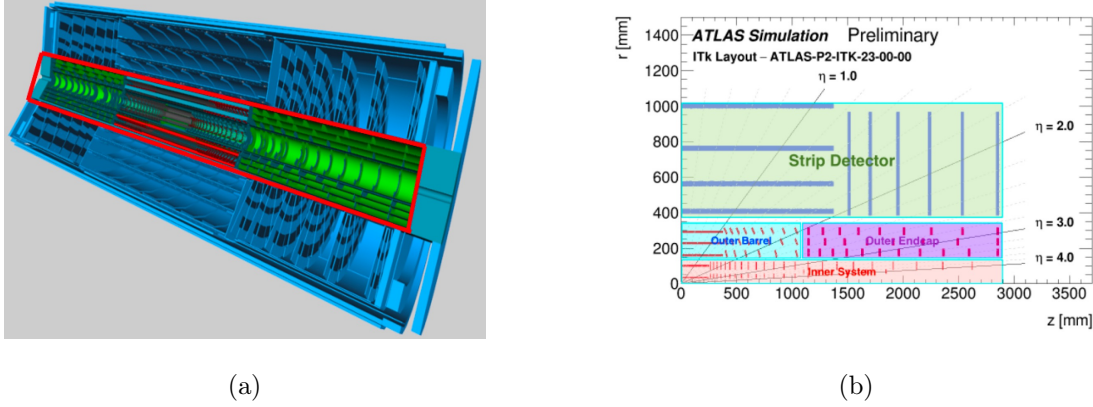


Figure 3.2: This shows the ATLAS ITk layout. Figure shows (a) the strip detector in blue and pixel detector marked by the red rectangle [28] and (b) shows the pixel and strip detector quadrants η coverage with the three individual sub-systems [109].

together in layers to form the barrel section of the detector. On the other hand, in the higher z region, the modules are mounted on rings that are perpendicular to the beam pipe, forming the endcaps of the detector.

The staves and rings have local support systems. They provide mechanical stability to the detector, ensuring its proper alignment and positioning. Additionally, they play a role in temperature control, helping to maintain the sensors at cool operating temperatures. Furthermore, these support structures facilitate the routing of electrical services to and from the modules. The parameters of all local supports are listed in Table 3.1 for the staves and in Table 3.2 for the rings.

Table 3.1: Parameters for the ITk pixel flat barrel and inclined rings in reference [110]. The number of sensors per row refers to a complete stave in the central, flat part of the barrel where sensors are placed parallel to the beam line. The number of inclined rings refers to both sides of the detector. Triplets consist of three connected read-out chips, each associated with a $2 \times 2 \text{ cm}^2$ sensor, while 'quad' modules are made of four connected read-out chips associated with a single $4 \times 4 \text{ cm}^2$ sensor.

Barrel Layer	Radius [mm]	Rows of Sensors	Flat Barrel $ z $ [mm]	Flat Sensors per Row	Inclined Rings $ z $ [mm]	Inclined Rings	Module Type
0	34	12	0-245	24	-	-	triplets
1	99	20	0-245	12	-	-	quads
2	160	32	0-372	18	380-1035	2 x 6	quads
3	228	44	0-372	18	380-1035	2 x 8	quads
4	291	56	0-372	18	380-1035	2 x 9	quads

The IS is made of a barrel and an endcap section and follows a quarter-shell integration structure. Each of the quarter shells have a barrel section with the staves and rings as local support structures. It also has an endcap section with flavours of rings to support the pixel modules. The barrel section is made of the two innermost barrel layers in region $|z| < 250 \text{ mm}$ and the corresponding innermost end-cap rings, making up the endcap sections. These innermost layers provide the coverage of the ITk of upto $\eta < 4$. As the IS is the closest to the IP, it faces the largest amount of radiation as shown in Figure 3.3 and is therefore designed to be replaceable once the radiation tolerance of the

Table 3.2: The parameters of one end-cap of the ATLAS ITk pixel system in the ITk design as in Reference [110]. The radius indicated in the table shows the distance between the closest sensor of a ring to the beam pipe. It is expected that particles coming from $z = +15$ cm will leave between one to four hits in each of the endcaps layers with each layer comprising multiple rings. Here, the layers 0 to 1 belong to the IS. The number of rings refers to both sides of the detector.

Ring Layer	Radius [mm]	z [mm]	Rings	Sensors per Ring	Module Type
0	33.20	263-1142	2 x 15	18	triplets
0.5	58.70	1103-1846	2 x 6	30	triplets
1	80.00	263-2621	2 x 23	20	quads
2	154.50	1145.5-2850	2 x 11	32	quads
3	214.55	1145.5-2850	2 x 8	44	quads
4	274.60	1145.5-2850	2 x 9	52	quads

IS is exceeded. This happens around $L = 2000 fb^{-1}$. The total irradiation dose for each of the ITk Pixel data transmission components is also listed in Table 3.3.

Table 3.3: The radiation levels expected for each of the ITk pixel detector services [29].

Pixel Detector Section	TID	
	Expected dose without safety factor (Mrad)	Dose including 1.5 safety factor (Mrad)
IS Type-0 L0 cables	830	1245
IS Type-0 L1 cables	380	570
IS Type-1 cables	305	457.5
OB Type-0/Type-1 cables	162	243
OE Type-0 cables	352	528
OE Type-1 cables	216	324
TwinAx cables	305	457.5
IS PP1 and Type-2	124	185
OS PP1 and Type-2	47	70.5
Optopanel	10	15
PP2 and Type-3 cables	0.05	0.075
PP3	0.01	0.015

The OB layout consists of two different sections, flat and inclined, at $|z| < 400$ mm. The staves of the OB are 2m in length. The local supports in the flat section are known as "longerons" while those in the inclined section are known as "inclined rings". This arrangement ensures the hermeticity of the ITk while simultaneously reducing the number of required modules. Furthermore, it minimises the amount of material needed by the OB, thus improving the tracking performance.

In the case of the OE, the local supports are carbon-based half-ring structures with an embedded titanium pipe. The OE comprises the layers 2 – 4 rings and their placement is also optimised to ensure hermeticity. Both sides of the half-rings will be loaded with the pixel modules along with a flex PCB known as the Patch Panel 0 (PP0) to route power and monitor the command or signals to and from each modules.

The ITk pixel modules employ a hybrid technology, where the silicon sensors are bump-

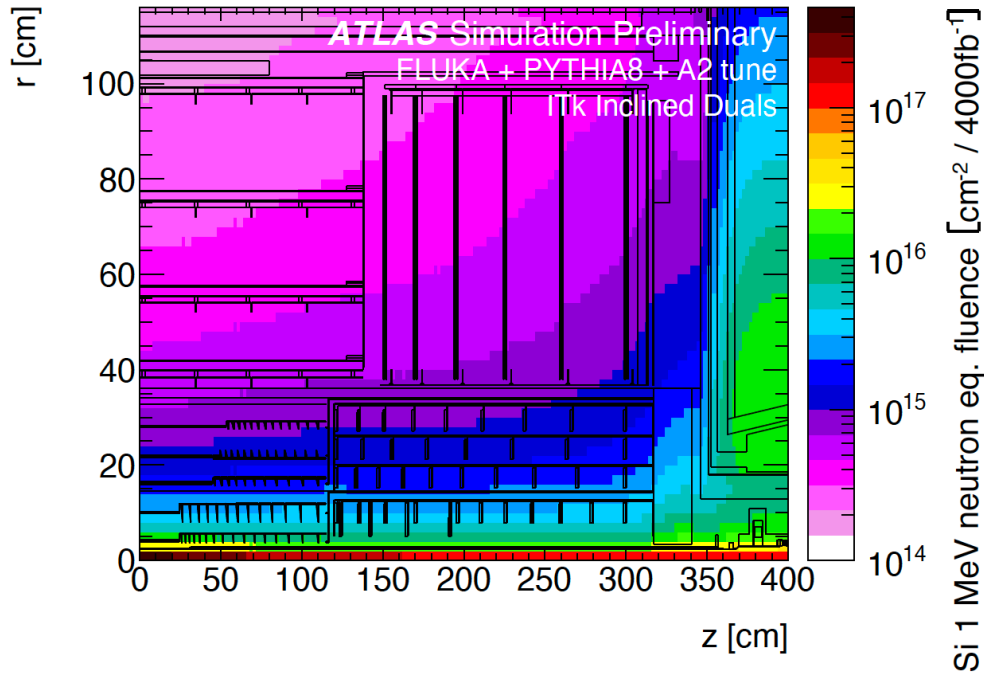


Figure 3.3: Distribution of the non-ionising energy loss in units of 1 MeV neutron equivalent fluence for $L = 4000 \text{ fb}^{-1}$ in the ITk. Here, "Si 1 MeV neutron equivalent fluence" refers to a measure of the amount of energy deposited by neutrons with an energy of 1 MeV in a silicon (Si) material, scaled to be equivalent to the effects of a certain fluence (number of neutrons passing through per unit area). This plot is taken from reference [111]. The simulation here is done using FLUKA [112] on the ITk layout as described in reference [28].

bonded to the readout ASICs developed by the RD53 collaboration [113] and are based on the 65 nm technology. Extensive optimisation studies [114] were conducted using pixel module prototypes by the ATLAS collaboration to determine which sensor technology is to be used in which part of the detector. From the studies it was concluded that the best compromise between performance, yield and cost is achieved by having planar pixel sensors in layers 1 to 4, with $100 \mu\text{m}$ thick sensors in layer 1 and $150 \mu\text{m}$ thick sensors in layers 2, 3 and 4 and 3D silicon pixel sensors in layer 0 due to their higher radiation resistance. In a 3D silicon pixel sensor, the pixels are fabricated on thin columns of silicon that extend into the bulk of the substrate. This creates a three-dimensional structure where the sensitive volume is not restricted to the surface as in planar sensors. These sensors exhibit enhanced radiation resilience due to the closely spaced implanted electrodes. This configuration necessitates a lower bias voltage, resulting in reduced leakage current and subsequently demanding less cooling. This design also serves to mitigate charge trapping effects. Furthermore, the depletion voltage remains lower compared to planar sensors, even under high irradiation doses. A crucial advantage is that the sensor thickness required for signal generation and the electrode spacing are independent, enabling the production of thicker and more radiation-resistant sensors. The layer 0 also employs two different pixel geometries to have a better resolution. $50 \times 50 \mu\text{m}^2$ and $25 \times 100 \mu\text{m}^2$ pixel sensors are used on the rings and in the central staves, respectively.

To enhance the pixel readout capabilities, a new generation of front-end chips with smaller pixels and increased bandwidth has been developed, as part of the RD53 collaboration. This collaboration has led to the creation of the RD53A prototype readout chip, specifically designed for the ATLAS Experiment. Subsequent development has resulted in the RD53B, also known as ITkPixv1. The final chip, ITkPix, has a size of approximately $(2 \times 2) \text{ cm}^2$, allowing four FEs to read out a sensor area of roughly $(4 \times 4) \text{ cm}^2$, encompassing 307,200 pixels. The ITkPixv1 supports up to four data channels [115] with a nominal bandwidth of $4 \times 1.28 \text{ Gbps}$. Furthermore, it offers enhanced radiation tolerance, capable of withstanding at least $500 \text{ Mrad} = 5 \text{ MGy}$ [28].

The pixel system will be powered using a serial powering scheme [116] where up to thirteen pixel modules will be powered in the longest chain in the OEs. The use of the serial powering significantly reduces the material budget by reducing the number of cables required for powering. A Monitor Of the Pixel System (MOPS) chip will be employed to monitor the temperature and the voltage drop in every module. The electrical signals will be transmitted at 1.28 Gbps from the module through electrical cables to the opto-electrical conversion system outside of the pixel detector. This custom-designed system known as "optosystem", designed and tested by the ATLAS team at University of Bern will equalise and aggregate the signals to 10.24 Gbps and convert the electrical signals to optical signals.

The combined performance of the ITk Pixel and Strip detectors ensure that charged particles with $p_T \geq 1 \text{ GeV}$ leave at least 9 hits in a silicon layer with $\eta < 4$, as shown in Figure 3.4. This is a major improvement when compared to the current ID with $\eta < 2.5$ [117], that takes into account a maximum of 8 hits. Also, the expected tracking performance of the ITk is shown in Figure 3.5. It is seen that the track reconstruction efficiency is on par with that of Run 2 and an average pile-up that is 5x higher. Also it is observed that the fake rate is reduced by one order of magnitude due to the higher number of hits featured in the ITk [28].

$$\langle \mu \rangle = 200$$

Thus, the ITk we are building meets the design requirements.

3.3 ATLAS ITk Pixel Data Transmission System

The ITk Pixel data transmission chain has three stages as shown in Figure 3.6:

1. Modules to Optosystem: The front-ends (FEs) of the ITkPix modules transmit the detector data (uplink) and receive the command+trigger (downlink) via electrical signals with twin-axial (twinAx) cables described in the following sections.
2. Optosystem: The Optosystem's heart is the Optoboard where the electrical-optical conversion along with the (de)-serialising of data and command+trigger between front-end and back-end, where the back-end consists of Front End Link Exchange (FELIX) [119] servers, occurs.
3. Optosystem to backend: The FELIX backend servers receive the data and transmit the command+trigger for the front-end modules through optical fibres.

Furthermore, the readout system has to fulfil the following set of requirements:

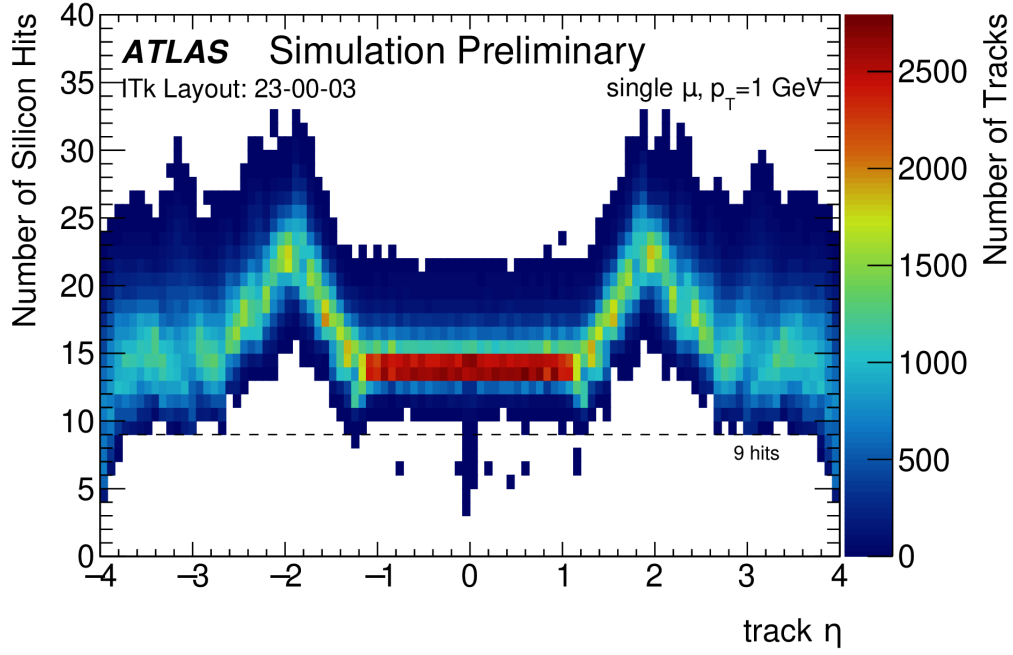


Figure 3.4: Number of silicon hits in the ITk as a function of η for muons with p_T of 1 GeV. This plot is taken from reference [110].

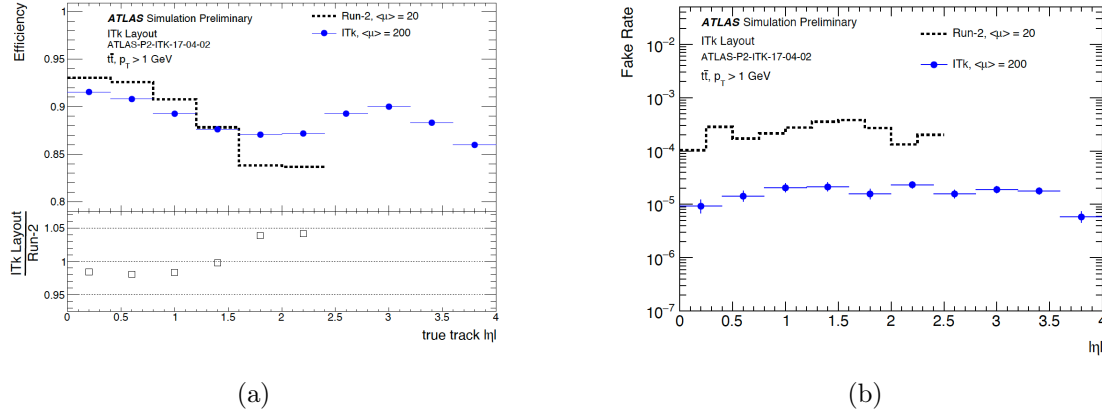


Figure 3.5: The plots show a comparison of (a) the track reconstruction efficiency and (b) fake rate to the Run 2 reconstruction performance with an average pile-up of $\langle \mu \rangle = 20$ and the ITk with $\langle \mu \rangle = 200$ as a function of η for hard-scatter tracks with $p_T = 1$ GeV using simulated $t\bar{t}$ events. These are taken from reference [118].

- Ensuring dependable transmission of data and command+trigger signals through the uplinks and downlinks, respectively, between the front-end (FE) components and FELIX at the necessary bandwidths.
- Small contribution to material budget to reduce negative effects from multiple scattering from particle interaction with the detector.
- Power consumption < 10 kW, complying with the ITk cooling plan.
- Readout components that are radiation tolerant taking into consideration $L = 4000 \text{ fb}^{-1}$ and 2000 fb^{-1} for the IS.

- Satisfy the ITk Grounding and Shielding (GS) policy [28].

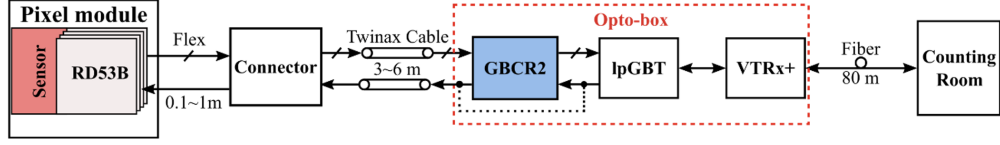


Figure 3.6: Overview of the interfaces for the data transmission [120].

The FEs are configured and triggered via 160 Mbps electrical downlink signals and send their data via 1.28 Gbps electrical uplink signals. These electrical signals employ low-voltage differential signalling, transmitting their signals using twin-axial cables with p- and n-polarities i.e. employing Low Voltage Differential Signaling (LVDS) technique [121]. These two polarities have currents flowing in opposite directions, thus cancelling the EM fields. This makes the transmitted signals less susceptible to the environment. The data arriving on the uplink is encoded using the 64b/66b Aurora protocol [28, 122]. These electrical up- and downlinks, consisting of AWG34 twinAx cables running up to 6 meters, are accompanied by power and monitoring lines. They are routed along a flexible printed circuit board (PCB) henceforth referred to as a flex, until they reach the PP0 PCB, which is mounted on the local support structure. The PP0 is the single point of contact for the electrical lines from the modules to the PP0 to the backend housed outside of ATLAS via the optosystem.

The backend FELIX system is located outside of the ATLAS detector in the USA15 service cavern. Therefore, the optical links or fibres going to the FELIX from the optosystem have lengths of upto $\sim 100 - 150$ m. The optical links are used here instead of the electrical links as the distance from the detector to backend would result in signal loss via attenuation of the electrical signals over the copper cables. Using optical fibres results in a much smaller signal loss and higher bandwidth capabilities.

The optosystem, placed in between the FEs and the backend, has evolved drastically since the ITk Pixel Technical Design Report (see Reference [28]), as the overall layout of the Pixel data transmission system changed. At the time the author worked on the data transmission chain, it was the first preliminary setup using the first prototypes to validate the concept of the ITk Pixel data transmission chain and the results additionally aided in designing the newer prototypes and optimising the performance of this chain.

3.4 The Optosystem

This section provides the technical overview of the system itself and describes the main components of an optoboard.

3.4.1 Overview of the optosystem

The optosystems are located outside the ITk, onto the ITk end-plates at $|z| = 3500$ mm and $r = 1450 - 2450$ mm, some of which are shown in Figure 3.7. The optosystem has to fulfil requirements such as aggregation and opto-electrical conversion of all up- and

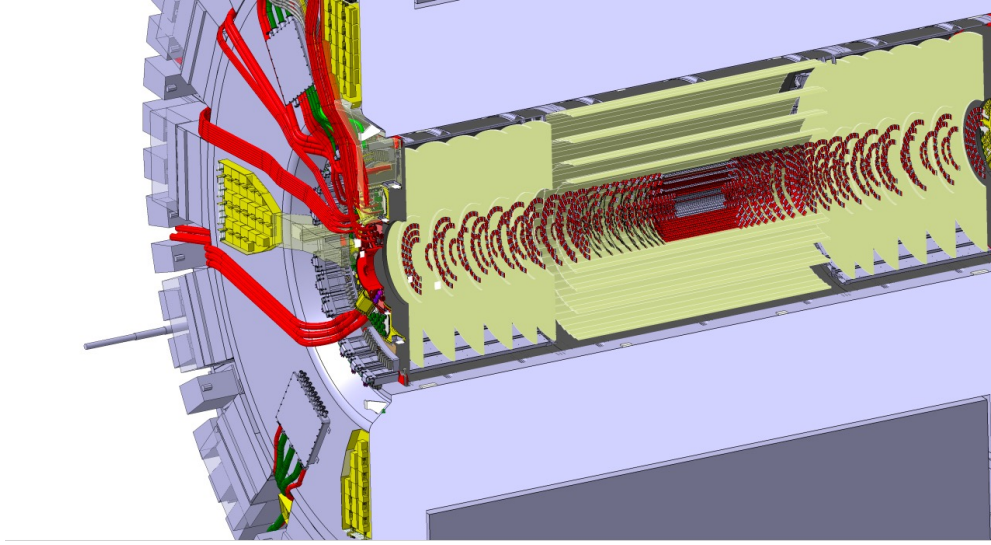


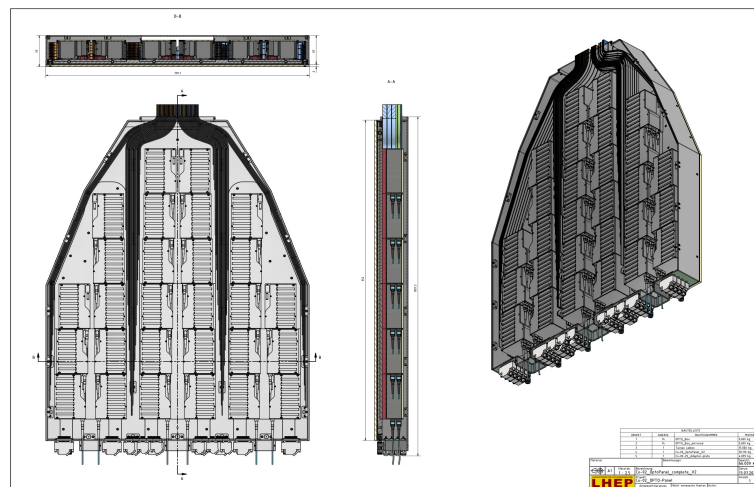
Figure 3.7: A CAD drawing showing the locations of the Optopanel, in yellow, relative to the ITk detector. The ITk Pixel detector is shown at the centre of the volume in red.

downlinks, ensure a Bit Error Rate (BER) $< 10^{-12}$ over the complete transmission chain, tolerance to radiation levels at the ITk end-plates of 50 kGy and 7×10^{14} MeV n_{eq}/cm^2 [123] with applied safety factor, efficient cooling and powering and monitoring of all the components and ease of access for replacement of components and compact design to fit on the ITk end-plate.

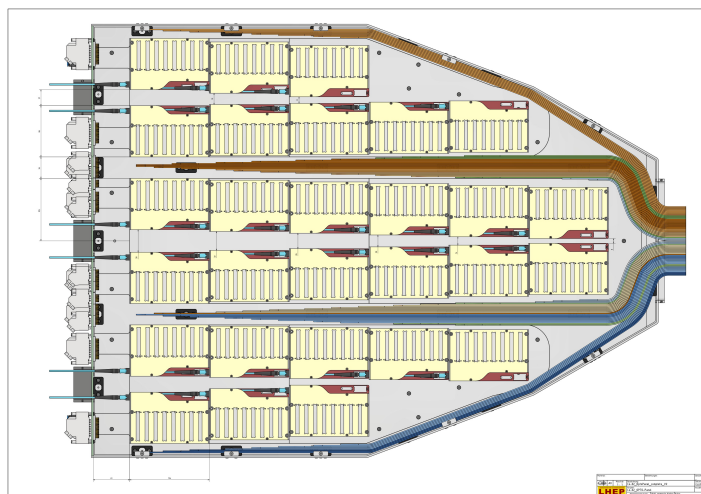
The optoboards are hosted in a mechanical structure known as an optobox, with ≤ 8 optoboards residing inside an optobox. The number of optoboards depends on the number of e-links coming from a particular sub-detector of the ITk Pixel detector: the IS, the OB and the OE.

The twinAx cables carrying electrical signals reach the optoboxes containing the optoboards using termination boards. Twenty-eight optoboxes make one optopanel and there are four optopanel at each side of the ATLAS detector, totalling eight panels dedicated to the readout and control of the ATLAS ITk Pixel detector. The bundles of twinAx cables consisting of upto 24 uplinks and 8 downlinks are soldered onto a cable termination PCB, which is linked to a single optoboard via a connector. These bundles are further wrapped by a shield to extend the Faraday cage of the ITk to the optosystem.

The grounding and shielding constraints of the ITk are carefully followed, ensuring the integrity of the Faraday cage within the optopanel. This is achieved through the use of appropriate measures, such as the outer walls depicted in Figure 3.8a, which serve as a Faraday cage. Additionally, the black plastic spacers, extending from the base of the cooling plate, ensure isolation between the cooling plate and the base plate. These measures, along with the enclosing walls and lid, contribute to maintaining the required shielding and grounding characteristics of the optopanel. Further complying with the grounding and shielding requirements of the ITk, the openings for the fibres on one side and twinAx cable opening on the other side, have protruding flanges to ensure the integrity of the Faraday cage. The narrow end of the optopanel is designed to receive the twinAx cables carrying the electrical signals from the ITk Pixel modules.



(a)



(b)

Figure 3.8: The final prototype design of the optopanel (a) in CAD drawing and (b) showing the routing of the twinAx cable in more detail and coloured by subsystem: blue for the IS, green showing the OB and orange representing the EC.

Figure 3.9 shows a small scale version of a working prototype of an optopanel, containing only one optobox which hosts multiple optoboards. Each of these optoboards has the capacity to serialise upto 24×1.28 Gbps electrical twinAx cables to 4×10.24 Gbps fibres and de-serialise command and clock control from 2.56 Gbps fibres to upto 8×160 Mbps twinAx cables.

Each optobox consists of a power board and connector board, respectively, for powering of the optoboards. The power board consists of upto five bPOL12V DCDC converters that receive a voltage of around 10 V from the power supplies and output 2.5 V. As one bPOL12V can have a maximum output current of 4 A [124], it can only provide power to two to a maximum of three optoboards when fully loaded. The power board also has the MOPS for monitoring of the bPOL12V output voltages. The power supplied to an optobox is disabled when and if it reaches very high temperature. This is monitored

using two negative temperature coefficient (NTC) thermistors on the power and connector boards directly linked to the interlock system. The connector board as the name suggest connects the optoboards with the power board and ensures the correct mapping of the five bPOL12V to the eight optoboards, based on the ITk Pixel SP chain.

The VTRx+ module (described in following Section 3.4.2) receives its required 2.5 V supply voltage for the VCSELs directly from the Power Board [125, 126]. On the other hand, the lpGBTs, GBCRs, and VTRx+ components require a 1.2 V supply voltage, which is generated by a dedicated bPOL2V5 DCDC converter. This converter is situated on a separate small PCB that is mounted on the optoboard. By employing this arrangement, the necessary supply voltages for different components are efficiently generated and distributed as per their specific requirements.

Each optobox utilises around 8 W of power when fully configured and operational, and results in a significant amount of thermal energy generated by a complete optopanel. In order to dissipate this, three cooling pipes are placed on a cooling plate within the optopanel using a perfluorohexane cooling fluid provided by the ATLAS services at 16 °C or 289.15 K.

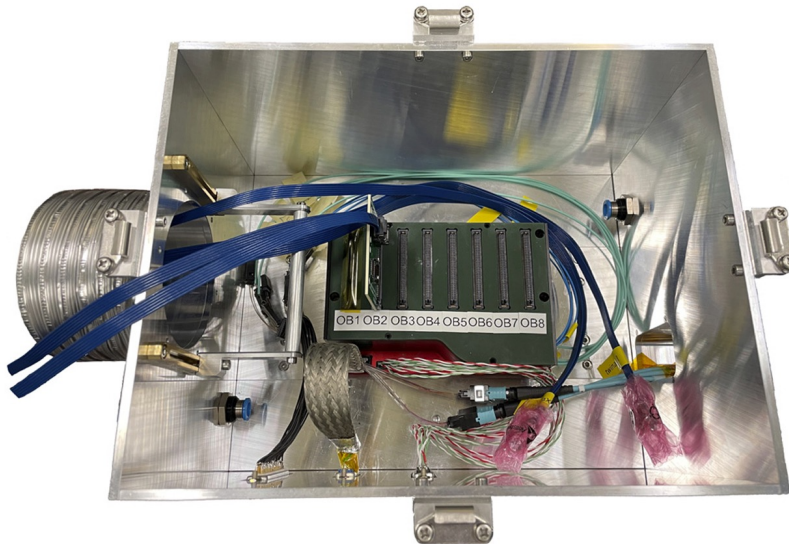


Figure 3.9: The optobox Prototype Panel for the Outer Barrel system test. It is a final design of the optobox which contains seven optoboards, their respective ERM8 connector is visible above the optoboard (OBn) labels. On the left side the entry of the electrical twinAx cables (blue) can be seen. They end at an adaptor PCB that was produced for the Outer Barrel system test. On the right side one can see the outlet of the fibres (mint) going towards the back-end (FELIX). Power and DCS are handled inside the panel through feed-through connectors on the bottom wall of the panel.

The optosystem's basic component is a PCB called optoboard that hosts the one VTRx+, four lpGBT and four GBCR ASICs that aggregate the electrical links and subsequently convert them to optical signals for transmission to the ATLAS back-end system (FELIX) via fibre optical cables on the uplink and converting the optical signals to electrical and distribution of these clock and command signals to the pixel modules. Each GBCR has an associated lpGBT that aggregates the six 1.28 Gbps uplinks into a single high-speed signal. The lpGBTs on the uplink after aggregating the signals operate at 10.24 Gbps

using FEC12 that can correct 24 consecutive bits. Out of the 4 lpGBTs, one of them is an lpGBT "master" i.e. operates as a transceiver that distributes the 2.56 Gbps downlink signal into the 160 Mbps e-links and the other three work as transmitters only and are referred to as lpGBT "slave". The lpGBT master clock data recovery (CDR) unit recovers a clock from the incoming high speed downlink data that synchronises with its internal oscillator. This recovered clock is used to check the received downlink frames, generate 1.28 GHz e-clocks or electrical clocks, are used to synchronise and regulate the timing of digital circuits or systems for operating the GBCRs using the retiming mode and provide a 40 MHz reference clock to the other three lpGBTs. The lpGBT master is configured using information sent over the IC field contained in the downlink data frame and the other components - lpGBT slaves and the GBCRs (and VTRx+ is also possible) via I²C control of the lpGBT master. The optical signals are transmitted via optical fibres to and from the ATLAS counting rooms for processing by the FELIX cards.

The first prototype known as optoboard V0, only has 1 VTRx+ and 1 lpGBT. The next version, optoboard V1 had 1 VTRx+, 4 lpGBTs and 4 GBCRs as shown in Figure 3.10a. The latest and final version of the prototype is optoboard V3, shown in Figure 3.10b. In comparison V1, on the downlink direction, the GBCRs on optoboard V3 are bypassed with the lpGBT handles the downlink pre-emphasis strength. From the bottom view the full number of GBCRs and lpGBTs can be seen, up to four of each can be hosted on the optoboard V3 PCB. This number of ASICs is determined by the number of e-links arriving from the modules of a particular sub-system and therefore can be lower than 4. It also has a hole in the PCB that allows for the direct thermal contact of the bPOL2V5 to the cooling L-profile.

3.4.2 Key components of Optoboards

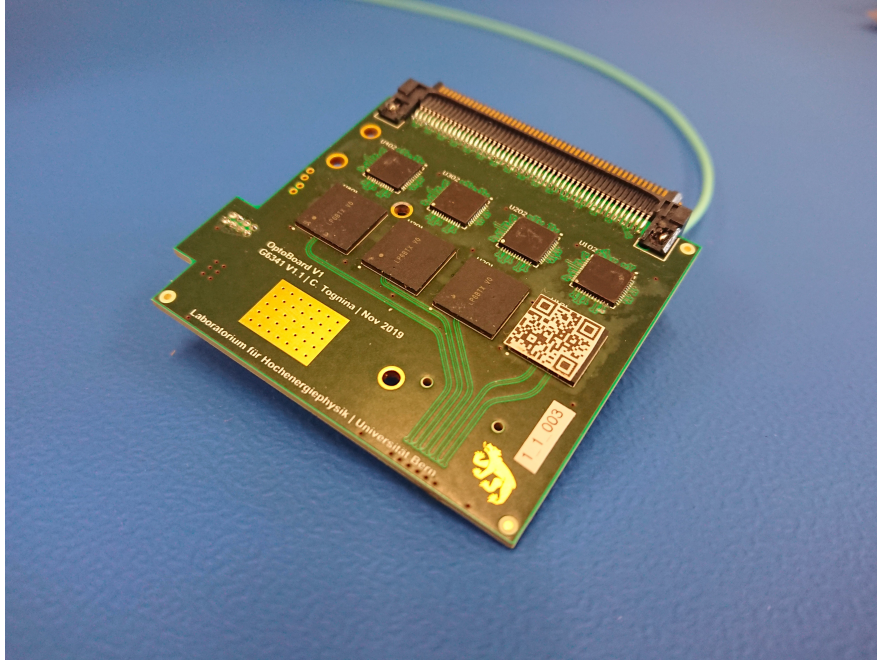
This sub-section describes the key ASICs of an optoboard in more detail.

Versatile Link⁺ Transceiver

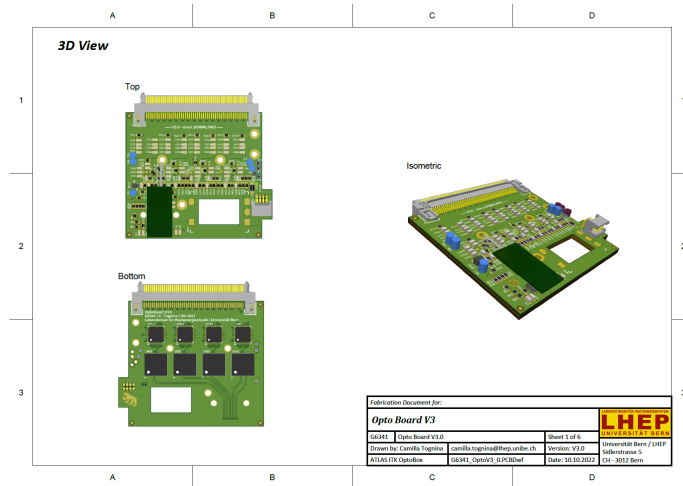
The Versatile Link⁺ or the VL+ [127], is a bi-directional multi-gigabit per second optical physical data transmission system designed to perform efficiently in the HL-LHC environments. It comprises three parts: an on detector transceiver (VTRx+), passive optical components and commercial off-the-shelf back-end transmitters/receivers, as shown in Figure 3.11. This device transmits uplinks at a speed of upto 10.24 Gbps and downlinks upto 2.56 Gbps and can resist a total ionising dose (TID) of 1 MGy. Also, the VL+ operates at wavelengths of 850 nm. Table 3.4 lists all the specifications associated to this VL+ project. The specifications take into account the minimum, maximum and nominal values of important parameters such as the bit rates, the bit error, temperature, optical link length, TID tolerance and NIEL (Non-Ionising Energy Loss) tolerance which refers to the ability of a material or device to withstand the effects of non-ionising radiation-induced damage.

The VTRx+ module [128] has a dimension of 20 x 10 mm². It is made of four parts and contains custom developed qualified parts as transmitter (Tx), receiver (Rx) and transceiver (TRx) that are interconnected on a PCB:

1. There is a p-in-n doped diode (PIN diode) that generates an electrical pulse from the incoming Rx optical signal.



(a)



(b)

Figure 3.10: The figure displays (a) an image depicting the rear side of the optoboard V1 prototype and (b) a design representation of the optoboard V3 prototype, illustrating the arrangement of its different components - the larger ASICs are the four lpGBTs, the smaller ASICs are the four GBCR2s and the small PCB to host the bPOL2V5.

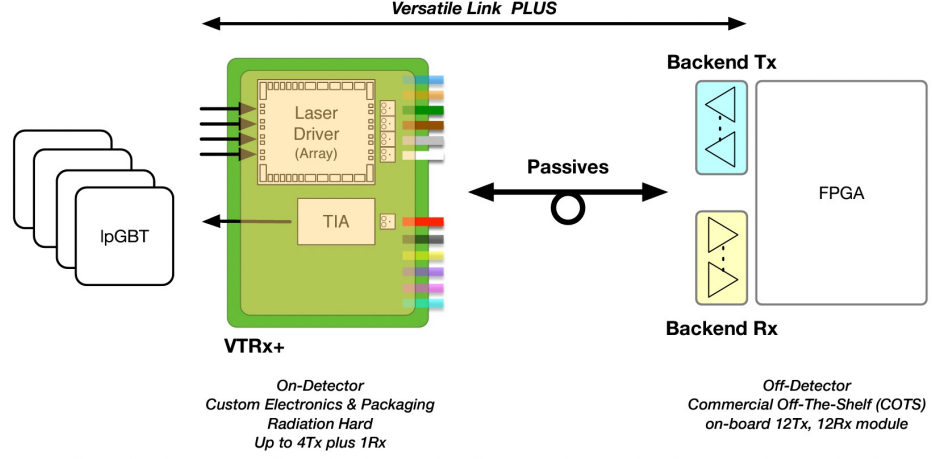


Figure 3.11: Versatile Link⁺ architecture showing the components of the VL⁺ : VTRx⁺ transceiver, passives, and commercial backend optical transmitters (Tx) and receivers (Rx) taken from reference [127].

Table 3.4: Specifications of the Versatile Link⁺ system.

Parameter	Min.	Typ.	Max.	Unit
Uplink bit rate			10.24	Gbps
Downlink bit rate			2.56	Gbps
BER			10^{-12}	
Link Length		50	150	m
TID tolerance			1	MGy
NIEL tolerance			10^{15}	neutrons/cm ²
Hadron tolerance			10^{15}	neutrons/cm ²
VTRx+ temperature	-35		60	⁰ C
Passives in-detector temperature	-35		60	⁰ C

2. The GBTIA [129] then amplifies the Rx electrical signal from the PIN diode.
3. The module is equipped with an LDQ10 laser diode driver [130], which is responsible for generating the necessary currents for the vertical-cavity surface-emitting lasers (VCSELs) used for transmitting optical signals. The LDQ10 driver allows for the configuration of various parameters such as bias and modulation currents, as well as pre-emphasis, through an I2C [131] interface. This interface enables convenient and flexible control and adjustment of the laser diode driver settings.
4. Finally, an array of four VCSELs transforms the LDQ10 electrical signals into an optical signal.

The signal attenuation and power budget of the VL⁺ project including both standard and extended grade of radiation tolerance is summarised in Table 3.5. It also takes into consideration effects of attenuation across 80 to 100 m of optical fibres along with radiation damage to these fibres and other effects.

Table 3.5: Power budget of the complete VL+ extended grade chain between the on-detector transmitter and receiver (VTx+ and VRx+) and the corresponding back-end components (Rx and Tx). Adapted from Reference [127].

Property	Uplink	Downlink
	VTx+ \rightarrow Rx (10.24 Gbps)	Tx+ \rightarrow VRx+ (2.56 Gbps)
Tx Optical Modulation Amplitude (OMA) [dBm]	>-5.2	>-1.6
Rx sensitivity [dBm]	<-12.5	<13.1
Power budget [dB]	>7.3	>11.5
Margin [dB]	>0.9	>1.975

Low-power Gigabit Transceiver

The Low-power Gigabit Transceiver (lpGBT) [132, 133] is a radiation tolerant ASIC that can be used to implement multipurpose high speed bidirectional electrical links for aggregation and monitoring in high-radiation environment of high-energy physics experiments such as the HL-LHC. This ASIC is controlled with a back-end firmware running on a Field-Programmable Gate Array (FPGA) like the FELIX system for the ITk. In the tests done and shown using the lpGBT in this chapter, a KC705 FPGA board with customised lpGBT firmware [134, 135] was used.

The lpGBT can either be operated with an external reference clock or by the using its clock data recovery (CDR) circuit, which synchronises its internal oscillator to the clock extracted from the incoming data. The ASIC supports 2.56 Gbps links in the downlink direction and 5.12 or 10.24 Gbps links in the uplink direction, depending on the selected operation mode. The 2.56 Gbps downlink is then further deserialised into individual e-links at data rates of 80, 160 or 320 Mbps. The structure of one lpGBT-FPGA encoded downlink frame, i.e., a structured format in which the data is organised and transmitted using encoding techniques, transmitting at a frequency of 40 MHz is shown in Figure 3.12b. Out of the 64 bits of a downlink data frame, 32 bits are used for the data (D field), while the other 32 bits are used for internal control (IC) data to configure the lpGBT, the external control (EC) to configure other lpGBTs to support master-slave operation and the Forward Error Correction (FEC field). FEC employs Reed-Solomon Codes [133, 136] technique which permits the detection and correction of up to 12 consecutive bit errors in the data. The data within the downlink frame is processed through two important steps: interleaving and scrambling. Interleaving involves arranging the bits within a frame in a specific order, while scrambling involves replacing bits to achieve DC balance, ensuring an equal number of '1's and '0's in the data before transmission. The uplink operated at either 5.12 or 10.24 Gbps is aggregated with incoming uplink e-links at data rates between 0.16 and 1.28 Gbps. For the ITk Pixel data transmission chain and the tests shown in the following section the uplink data stream at 1.28 Gbps is used. The structure of the uplink data frame is similar to that of the downlink. However, it has a total of 128 or 256 bits for data rates of 5.12 or 10.24 Gbps, respectively, because of the larger D and FEC fields. The uplink data frame employs either FEC5 or FEC12 encoding schemes for 5.12 or 10.24 Gbps modes respectively. The IC and EC fields are made of the associated responses to the downlink IC and EC commands. Also, like the downlink, the uplink data is scrambled and interleaved before leaving the lpGBT.

Furthermore, this ASIC has General Purpose Input Output (GPIO) pins, I²C control, analogue-to-digital converters (ADC) and clock outputs to configure, monitor and com-

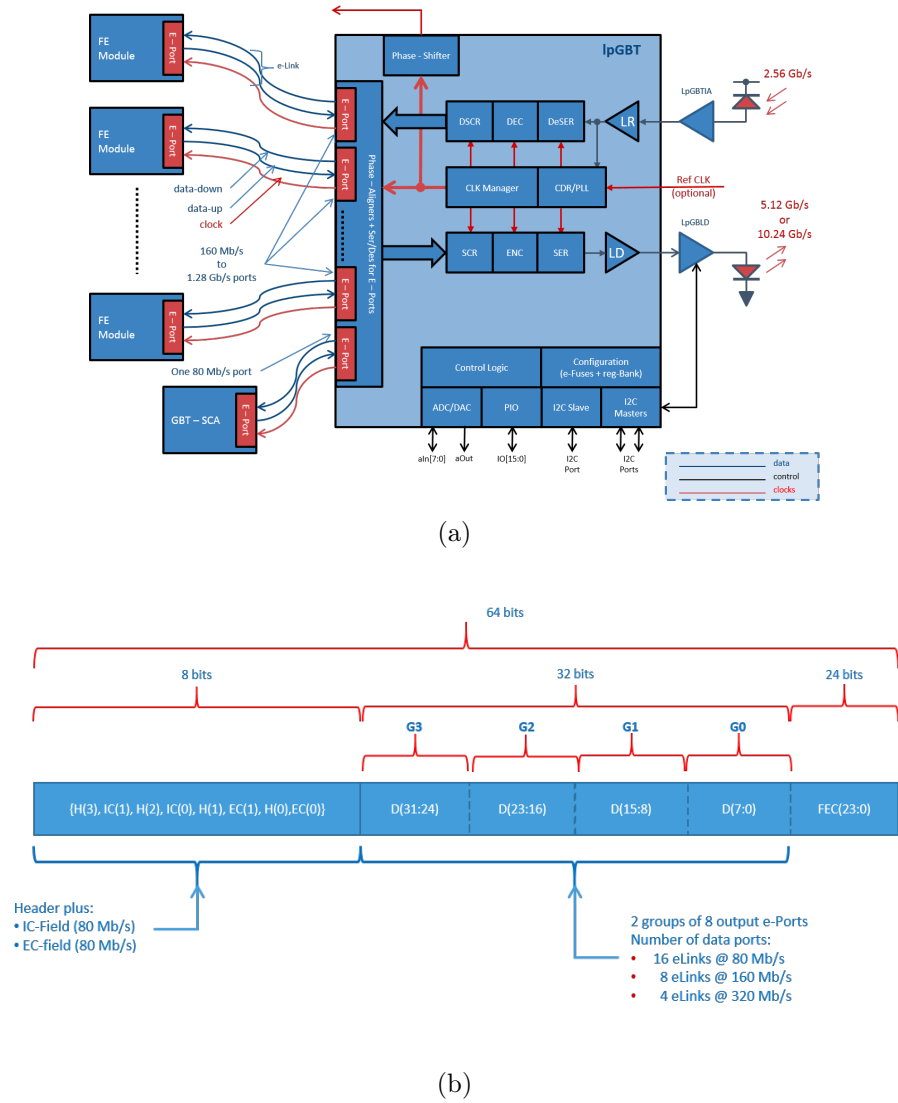


Figure 3.12: Structure of the lpGBT (a) architecture and (b) downlink frame [133].

municate with other components such as other lpGBTs and the Giga-bit Cable Receivers (GBCRs).

Giga-bit Cable Receiver

The third key component is the Giga-bit Cable Receiver (GBCR). In the ITk pixel data transmission chain, each pixel module has a pixel sensor and three or four RD53B chips [137–139] in parallel that transmits the data from the FEs at 1.28 Gbps per channel to a lpGBT via a GBCR. Due to space constraints close to the IP and radiation tolerance specifications of the lpGBT and VTRx+, these ASICs are to be located a few meters from the pixel modules. From the pixel modules the data is electrically transmitted via a flex of 0.1 m to 1 m followed by AWG34 twinAx cable of ≤ 6 m which leads to about 20 - 25 dB signal loss at a data rate of 1.28 Gbps i.e. a frequency of 0.64 MHz. Thus, the RD53B's output signal is completely embedded in the noise, necessitating compensation of the signal loss for the lpGBT to recognise and process the signal. A GBCR is used to

recover the signal's high-frequency loss. An initial prototype ASIC called GBCR1 [?, 140] was used for the initial data transmission scheme in which it receives 4 uplink channels each functioning at 5.12 Gbps. An updated prototype ASIC called GBCR2 [141] was then designed to meet requirements of the current baseline scheme, in which it receives six uplink channels each functioning at 1.28 Gbps.

The design of the GBCR2 employs the 65 nm CMOS technology with a single power supply of 1.2 V and a dimension of $1 \times 2 \text{ mm}^2$. The GBCR2 features seven uplink channels, which consist of six channels for data transmission and one channel for testing purposes, mirroring the configuration of the lpGBT. In addition, this prototype introduces the option of utilising two downlink channels operating at a speed of 160 Mbps from the lpGBT to the RD53B. These downlink channels incorporate integrated pre-emphasis functionality to compensate for situations where the pre-emphasis provided by the lpGBT is insufficient to drive the command and trigger signals to the RD53B effectively. This feature helps reduce jitter on the downlink, consequently minimising jitter on the uplink channels as well since the uplink clock is recovered from the Clock and Data Recovery (CDR) unit of the RD53B [142]. The GBCR ensures compliance with the ITk pixel data transmission chain requirement of an uplink BER $1 < 10^{-12}$. The incoming signal from the RD53B is equalised and can optionally be retimed using a phase-adjustable e-clock operating at 1.28 GHz provided by the lpGBT and received by the GBCR2 phase shifter. All seven uplink channels share the same phase shifter. The equalised or retimed data is then directed to the electrical receiver (eRx) of the lpGBT. The lpGBT I²C master is utilised for configuring both the uplink and downlink channels, as well as the phase shifter.

Each uplink channel comprises:

- *Passive attenuator*: It is adjustable with 1/3, 2/3, and 1 of the signal and targets avoiding the saturation of the equaliser.
- *Equaliser*: The long electrical cables attenuate the high-frequency components of the signal more than the low frequency ones causing significant Inter-Symbol Interference (ISI) jitter i.e. the distortion or variation in the timing of received symbols or bits in a communication system caused by the presence of multiple symbols overlapping in time. Therefore the equaliser acts as a high-pass filter and degrades the low-frequency components thereby compensating for the high-frequency loss. The equaliser is designed for a cable lengths of 1 m flex and 6 m twinAx cable i.e. 7 m long electrical transmission cable. The equaliser settings can be optimised by configuring the middle and high frequency settings where 80 to 200 MHz, 200-400 MHz and 400 MHz to 1.3 GHz are the low, medium and high frequency ranges. Each uplink channel has its individual equaliser comprising three identical high, medium and low frequency Continuous-Time Linear Equalisers (CTLEs). All 3 CTLEs together provides up to 30 dB peaking strength defined as the amount of amplification or boost applied to specific frequency components of a signal by the CTLE to the signal. And the power consumption of the entire equaliser is $\sim 0.84 \text{ mW}$ per uplink channel.
- *Limiting Amplifier (LA)*: It amplifies the equaliser's output signal to saturation for the output driver. It includes a DC-offset-cancellation circuit to remove the DC offset due to the mismatch between the LA and the equalisers.

- *Retiming logic*: As afore-mentioned, the uplink channels can be operated in either retiming or non-retiming mode. In the retiming mode, the equalized signal undergoes further minimization of jitter by being retimed. This process involves utilizing a phase shifter that receives a 1.28 GHz e-clock from the lpGBT. The phase shifter generates phase-adjustable clocks for each uplink channel's retiming logic, which samples the uplink data at precise intervals. On the other hand, in the non-retiming mode, the retiming logic is bypassed, and the phase shifter is disabled. Also in this mode, the phase delay of each uplink channel can be independently configured through the I²C interface.
- *Current-Mode Logic (CML) driver*: This driver is responsible for transmitting the recovered data to the lpGBT.

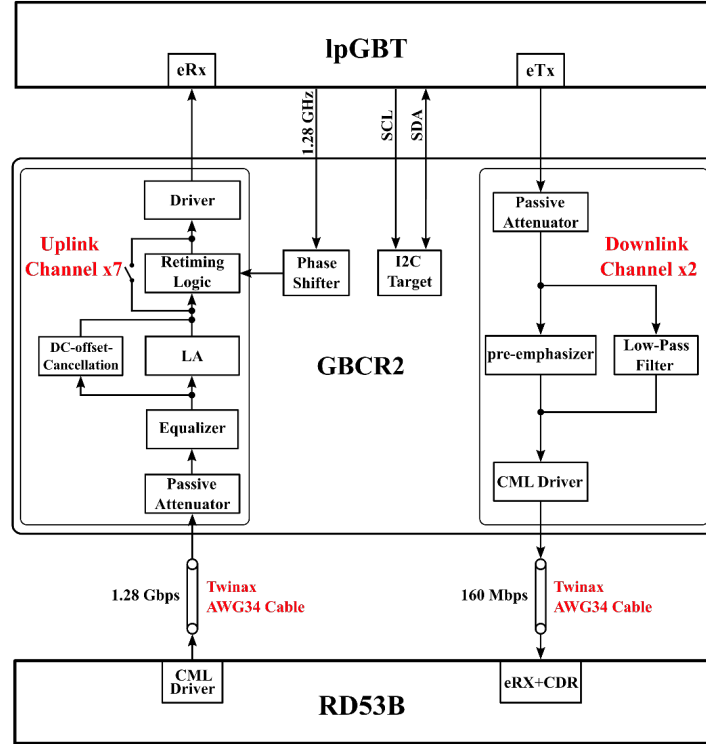


Figure 3.13: The GBCR2 architecture taken from Reference [120]. The downlink channels in the GBCR2 are not bypassed as in the next updated versions of the optoboard and overall data transmission. These channels are configured in its optimal settings as described by the GBCR2 team.

In the uplink channels, the total jitter of the output signal is 129.1 ps (peak-peak) and 79.3 ps (peak-peak) and the total power consumption is 109.1 mW and 127.7 mW below the specification of 174 mW, in the non retiming and retiming modes, respectively. The power consumption of the two downlink channels is < 53 mW [120].

In this thesis, optoboard prototype versions V0 and V1 have been tested and the results are shown in Section 3.6. The next section explains some theoretical concepts underlying the tests done to qualify the data transmission chain.

3.5 Concepts of Link Performance and Signal Quality Tests

The quality of the data transmission chain and validating whether it meets the required specifications are done using jitter analysis, bit error ratios and measuring the signal attenuation.

3.5.1 Jitter Analysis and Eye Diagram

Jitter is a short-term variation in the timing of a digital signal from its nominal value. There are two main types of jitter, random jitter and deterministic jitter. Random jitter is unbounded, which means that its value continues to increase with increasing duration of measurement. It is associated with stochastic processes like noise. Deterministic jitter is bounded, and its amplitude is limited with increasing observation time. The description of these different types of jitter is based on the Tektronix primer for jitter characterisation [143].

Time-domain jitter types of interest are period jitter, cycle-to-cycle jitter, time interval error (TIE) and total jitter(TJ).

Jitter that repeats in a cyclic fashion is called periodic jitter. It is defined as the deviation in cycle time of a signal with respect to the ideal period over a random number of cycles, preferably between 1000 to 10000 cycles. Peak-to-peak period jitter is defined as the difference between the highest and the lowest period value from the sample size used for the measurement. The period jitter, is illustrated by the measurements P1, P2 and P3 in Figure 3.14 and shows that this jitter measures the period of each clock cycle in the waveform.

Cycle-to-cycle jitter is defined as the variation in cycle time of a signal between adjacent cycles over a random sample of adjacent cycle pairs. The number of cycles selected for this measurement should range between 1000 to 10000 to have ample confidence in the measurement. Cycle-to-cycle jitter is usually specified as the greater of the absolute values of the highest positive or negative variation value in cycle time between adjacent cycles. For example, if the largest positive cycle-to-cycle variation is 62 ps and the largest negative cycle-to-cycle variation is -65 ps, the overall cycle-to-cycle jitter is commonly specified to be 65 ps. The cycle-cycle jitter is also indicated by C2 and C3 in Figure 3.14.

Figure 3.14 also shows the time interval error indicated by the measurements TIE1 through TIE4. This type of jitter measures how far each active edge of the clock varies from its ideal position. The TIE is obtained by integrating the period jitter, after first subtracting the ideal clock period from each measured period. This jitter measurement is important as it shows the collective effect from a small amount of period jitter over time. Once the TIE reaches ± 0.5 unit intervals, the eye of the eye diagram, explained later in this section, is closed and a receiver circuit will experience bit errors.

TJ is another time-domain jitter specification commonly used in Serial IO applications that is derived from the TIE measurement. It is measured at a specified BER for the serial IO link and combines the effect of random and deterministic jitter components. It predicts a peak-to-peak jitter that will only be exceeded with a probability equal to the BER. Real-time oscilloscopes such as the Textronic 2 GHz oscilloscope typically include jitter analysis software tools that decompose TJ into random (RJ) and deterministic jitter

(DJ) components. The relationship between TJ, RJ and DJ is shown in Equation (3.1) where n is the application BER multiplier which in case of 10^{-12} is 14.26 [144]:

$$TJ_{pk-pk} = DJ_{pk-pk} + n \times RJ(rms). \quad (3.1)$$

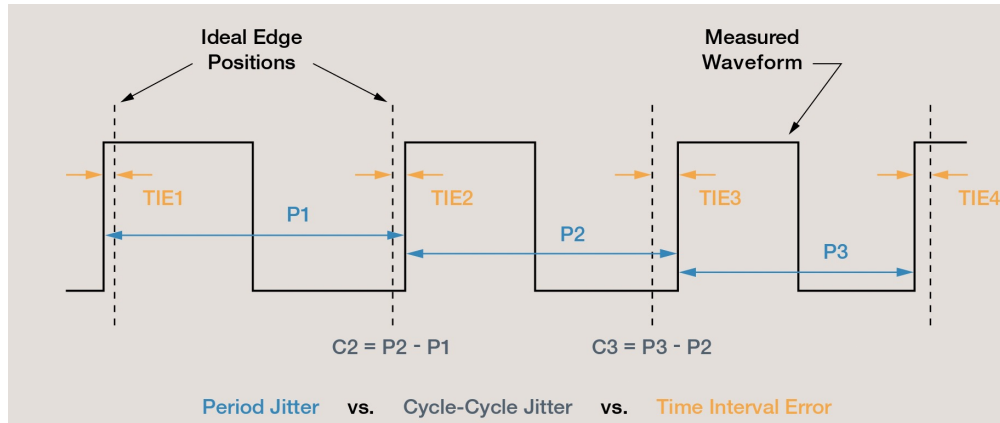


Figure 3.14: The different types of jitter measurements taken from Reference [143].

All of the methods discussed so far rely on edge locations only. An eye diagram is a graphical representation of a digital signal's quality and integrity. An eye diagram is created by superimposing multiple digital signal periods on top of each other, with the horizontal axis representing time and the vertical axis representing signal amplitude, as shown in Figure 3.15a. If the waveform is repeatable, a sampling scope may be used to build an eye diagram from individual samples taken at random delays on many waveforms. The resulting pattern resembles an "eye" shape, hence the name. In practice, eye diagrams are typically either monochrome or colour scaled to indicate the density of waveform samples at any given point of the display.

The eye diagram typically consists of three main components:

Vertical Opening: The vertical opening of the eye diagram represents the signal's voltage levels. It shows the amplitude range over which the receiver can reliably distinguish between high and low signal levels. A wider opening indicates better signal quality and a larger voltage margin for reliable detection.

Horizontal Width: The horizontal width of the eye diagram corresponds to the time duration of a single bit period. It represents the timing uncertainty or jitter in the received signal. A narrower width indicates less jitter and better timing synchronisation.

Noise and Distortions: The eye diagram also reveals the presence of noise, ISI, and other signal distortions. These are represented by variations in the eye's edges, blurring, or overlapping of the eye pattern. These distortions can degrade the signal quality and impact the receiver's ability to accurately detect and interpret the transmitted data.

By examining the eye diagram, one can gain valuable insights into the performance of

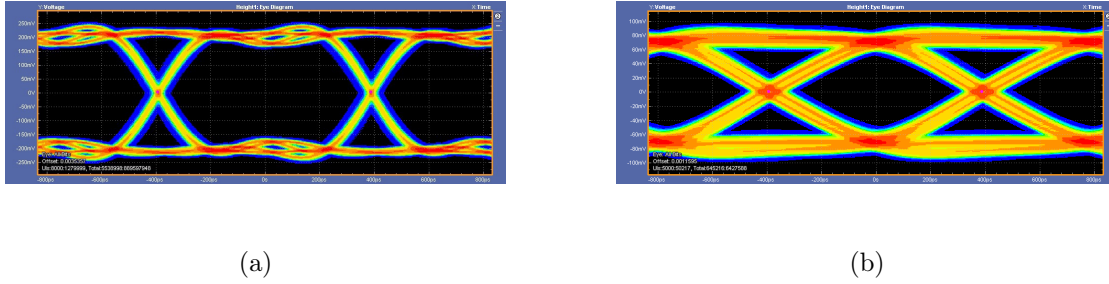


Figure 3.15: Comparing eye diagrams of RD53B CDR uplink in (a) to that of RD53B CDR + 1 m flex + 6 m twinAx cable in (b). The more closed the "eye" the higher the jitter.

the communication system. One can assess the impact of various impairments, such as noise, timing errors, crosstalk, and signal distortions. This information can be used to optimise the system's design, diagnose problems, and make necessary adjustments to improve overall signal quality and reliability and ensure high-quality data transmission and reception.

For all the data transmission validation tests, TIE and TJ were considered along with the associated eye diagrams.

3.5.2 Bit Error Ratio Tests

A bit error ratio (BER) test is a common method used to assess the quality of digital communication systems by measuring the error rate of received bits.

In a BER test, a known pattern of bits, usually a pseudorandom bit sequence (PRBS), is transmitted through the communication system under test. The receiver then compares the received bits with the expected pattern and counts the number of bit errors. The BER is calculated by dividing the number of bit errors by the total number of transmitted bits. It is usually expressed as a ratio, such as 10^{-6} (1 error bit per million transmitted bits). This measured ratio is affected by many factors including: signal to noise, distortion, and jitter.

$$\text{BER} = \frac{N_{\text{err}}}{N_{\text{bits}}} \quad (3.2)$$

The BER test provides insights into the system's performance by quantifying the level of errors occurring during data transmission. It helps identify potential issues, such as noise, interference, channel impairments, or problems with equipment or components. By measuring the BER at different points in the system or under different conditions, one can pinpoint problem areas and take appropriate corrective measures.

For most transmission chains, BER is expected to be less than a predefined threshold. For the ITk Pixel data transmission chain, the specified BER threshold is 10^{-12} . The number of bits required to accomplish this will only depend on the required confidence level and BER threshold. In numerous scenarios, precise measurement of the BER may not be

essential; instead, the measurement can be terminated if the BER value is unequivocally below or above a specific threshold. For instance, during a qualification test, the crucial requirement is to verify that the device being tested operates with a BER surpassing 10^{-12} and the exact BER value, becomes less significant in this context. The certainty of such an assertion can be conveyed through the concept of a confidence level (CL). The CL of a BER measurement can be calculated using statistical methods statistical methods based on the binomial distribution function and Poisson theorem as shown in Equation (3.3).

$$N = \frac{1}{BER} \left[-\ln(1 - CL) + \ln \sum_{k=0}^E \left(\frac{(N \times BER)^k}{k!} \right) \right] \text{ or} \quad (3.3)$$

$$CL = 1 - e^{-N \times BER} \times \sum_{k=0}^E \frac{(N \times BER)^k}{k!}$$

Here, N stands for the number of bits transmitted, BER is the required BER to qualify the transmission chain for example 10^{-12} and E is the total number of errors detected. In case, $E = 0$, the second term in this equation is equal to zero. Therefore, for a specified BER of 10^{-12} and a required typical confidence level of 95%, the required number of bits to test without any errors is 3×10^{12} . Once these many bits have been tested without error, it ensures that the $BER < 10^{-12}$.

3.5.3 Transmission losses using Vector Network Analyser

A vector network analyser (VNA) is a test instrument used to measure the electrical characteristics of high-frequency and microwave devices, circuits, and systems. A VNA operates based on the principle of scattering parameters (S-parameters), which describe the relationship between the incident and reflected waves at different ports of a device under test (DUT). By measuring and analysing these S-parameters, a VNA can provide valuable information about the DUT's impedance, gain, insertion loss, return loss, phase shift, and other electrical characteristics.

S-parameters, also known as scattering parameters, describe the relationship between the input and output signals of a device under test (DUT), which in this case are the electrical cables and ASICs (GBCR2), in terms of amplitude and phase. The S-parameters of a DUT define the amplitude and phase of the incident and reflected waves at each port of the device.

The VNA generates a stimulus signal and measures the response of the DUT at different frequencies. The measurement setup involves connecting the DUT to the network analyser using coaxial cables or other appropriate transmission lines. Before taking measurements, the VNA is calibrated to remove any systematic errors introduced by the test setup. The DUTs such as twinAx cables and GBCR2 is connected one at a time to the network analyser, with each port properly terminated to match the characteristic impedance of 50Ω . The network analyser then sweeps through a range of frequencies of interest while measuring the response of the DUT. At each frequency point, the network analyser measures the S-parameters such as amplitude and phase of the incident and reflected waves.

Therefore, the measured S-parameter matrix describes the changes in the reflected and transmitted waves with respect to the incident wave at an N-port PCB component, where N is the number of ports. These parameters are defined in terms of transmission and reflection coefficients. The most common S-parameters are S_{11} , S_{12} , S_{21} , and S_{22} , which represent the scattering parameters for the forward and reverse waves at the input and output ports, respectively. Each parameter is represented as a complex number, including magnitude and phase information.

For a two-port transmission line or device under test (DUT), these four S-parameters are shown in Figure 3.16:

- S_{11} and S_{22} = Reflected/Input [dB]
- S_{12} and S_{21} = Transmitted/Input [dB]

Hence, S_{21} is the measure of the transmitted signal from port 2 relative to the input entering port 1 while S_{11} is the measure of the reflected signal from port 1 relative to the input entering port 1. For all the tests conducted using the VNA as shown later in Figures 3.20 and 3.22, the S_{21} parameter was measured.

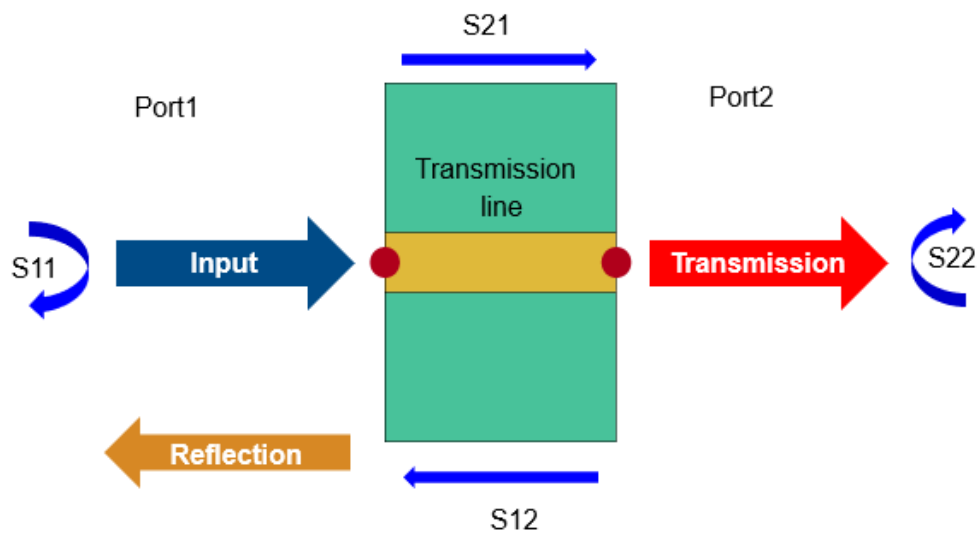


Figure 3.16: A two-port device with four S-parameters.

3.6 Preliminary Data Transmission Chain Test Setup and Results

The ITk pixel data transmission chain was validated adding one component at a time, using the testing methods described in Section 3.5.

3.6.1 Loopback tests conducted using the Xilinx Integrated Bit Error Rate Test (IBERT) in this Xilinx KC705 FPGAs

I developed the first test set up to test the GBCR1 along with a 6 m long twinAx cable using the KC705 field-programmable gate arrays (FPGA) board [145] to perform loopback tests.

The KC705 board features a Xilinx Kintex-7 FPGA, which provides a high-performance and programmable logic fabric. The FPGA offers a range of resources, including logic cells, memory blocks, and high-speed transceivers, making it suitable for a wide range of applications. The KC705 FPGA board can also be used for signal recovery in high-speed digital communication applications. To perform signal recovery on the KC705 board, the user would typically use the high-speed serial transceiver interfaces available on the board. These transceivers are designed to handle high-speed data transmission and provide features to aid in signal recovery. The KC705 board typically includes clock and data recovery circuitry within the high-speed serial transceivers. The CDR circuitry recovers the clock signal embedded in the received data stream and uses it to synchronise the data recovery process. It compensates for any timing variations or jitter introduced during transmission. Furthermore, depending on the specific application, additional signal conditioning techniques may be employed to improve signal integrity such as pre-emphasis, de-emphasis, retiming, and other methods to enhance the received signal quality. Signal recovery can also involve error detection and correction mechanisms like forward error correction.

I performed loopback tests over this chain using the Xilinx Integrated Bit Error Rate Test (IBERT) [146] feature available in this Xilinx FPGA and system-on-chips (SoCs) that allow for convenient on-chip testing and measurement of the BER of high-speed serial interfaces.

Some key aspects and capabilities of Xilinx IBERT which were employed for the measurements are:

- *On-Chip Test Pattern Generation and Detection:* IBERT provides an on-chip test pattern generator (TPG) and test pattern checker (TPC). The TPG generates a known test pattern, such as a pseudorandom bit sequence (PRBS), that is transmitted through the serial interface. The TPC receives the transmitted pattern and compares it with the expected pattern to calculate the BER.
- *Flexible Configuration:* IBERT allows configuration of various parameters to match the characteristics of the specific serial interface being tested. This includes selecting the data rate, configuring the pattern length, adjusting voltage levels, and specifying the number of lanes or channels. The tests I conducted used PRBS of 15 and 23 bit lengths and data rates of 1.28 GHz and 5.12 GHz.
- *Eye Scan and Jitter Analysis:* Advanced analysis features, such as eye diagrams that provide insights into the quality and margin of the received signal and jitter analysis, which allowed to measure and characterise timing variations and jitter components affecting the serial link under test were used.
- *Real-Time Monitoring and Debugging:* IBERT provides real-time monitoring capabilities of important link metrics such as BER, error counts, and link status enabling

efficient debugging and troubleshooting of issues affecting the serial communication link.

- *Integration with Vivado Design Suite:* IBERT is also integrated with Xilinx's Vivado Design Suite, which provides a comprehensive design environment for developing and testing FPGA-based systems. Vivado Design Suite allows users to configure and generate the necessary intellectual property (IP) cores and constraints for IBERT, as well as perform system-level simulations and analysis. The integrated Vivado Design Suite is particularly helpful as it provides built-in capabilities for generating and analysing eye diagrams as shown in Figure 3.18.

For the high-speed serial communication link under tests, the IBERT IP core is utilised in Vivado to generate the necessary test signals and capture the received data. The IBERT IP core is configured with the desired settings for the specific link, including data rate, pattern length, and equalisation options. With the IBERT IP core configured, the BERT is performed. Vivado also provides a graphical interface for setting up the test parameters, such as the number of samples, the test duration, and the desired test patterns. Once the bit error rate test is generated, it is run and the received data is captured. Vivado offers analysis tools that enable the selection of the captured data, specification of the number of Unit Intervals (UIs) to include in the eye diagram, and adjustment of various display options. Additionally, Vivado allows for the examination of key parameters of the eye diagram, such as the eye opening, voltage levels, and timing margins.

IBERT generates and sends over the chain Pseudo-Random Bit Sequences (PRBS) of various lengths. The KC705 board provides access to 16 GTX transceivers. One of these GTX is wired to SMA connectors (RX: J17, J18 TX: J19, J20) which are used in these loopback tests to send and receive the PRBS data over the transmission chain under test connected via SMA cables. The IBERT IP block compares the sent and received data and calculates the BER.

The GBCR1 registers were configured via I²C protocol using an Arduino microcontroller (hardware and software project). The GBCR equalisation parameters and other associated parameters were configured to its optimum settings as recommended by the GBCR1 developers. The suggested optimum settings for the GBCR1 equalisation parameters are shown in Figure 3.17.

Comparing the effect of different bit rates

I performed a comparison of the loopback tests using one device at a time between the design data rate of 1.28 Gbps and 5.12 Gbps for the ITk Pixel data transmission chain on the uplink and that of the GBCR1, respectively is shown in Table 3.6. It is seen that the higher the bit rate, the lower the eye opening UI%. Adding the twinAx cable considerably worsens the eye opening overall. However, adding GBCR1 to the chain after the twinAx, is seen to improve the eye opening UI%. The signal recovery by the GBCR1 combined with that of the KC705 is observed here to improve the eye opening and is the same for both the bit rates. The eye diagram obtained via the Vivado interface for a PRBS of 23 bits at 1.28 Gbps, sent from the KC705 through the 6 m twinAx cable to the GBCR1 and back to the KC705 via another 6 m twinAx cable is shown in Figure 3.18. The eye opening in UI is 81.4%. This initial tests confirmed that though the GBCR1 design frequency did not match the ITk requirements, the concept works and further

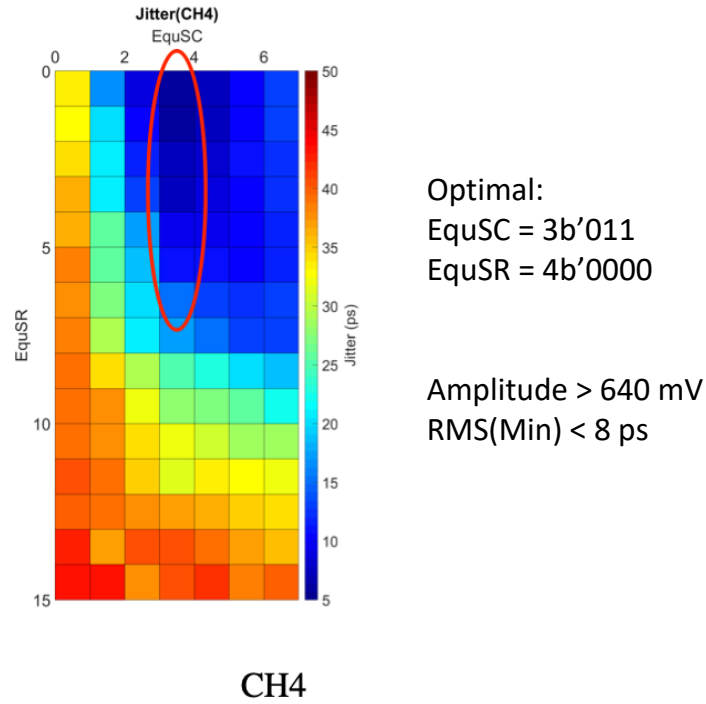


Figure 3.17: A 2D plot showing the GBCR1 equaliser (EQ) setting and the associated jitter in channel number 4. The EQ setting circled in red shows the optimal settings for the design frequency of 5.12 Gbps. Here the EquSC and EquSR are capacitor and resistor registers associated to optimising the equaliser.

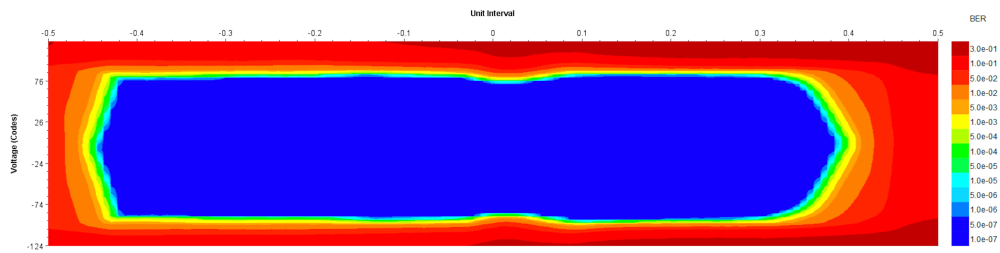


Figure 3.18: Loopback test using KC705 and Vivado interface along with a 6 m TwinAx cable and GBCR1.

tests could be carried out till the updated GBCR2 was available for tests.

Comparing direct powering vs. DCDC converter

Table 3.6: Comparing bitrates from loopback tests conducted using KC705 and Vivado interface

Devices/Bitrate	Eye opening (UI%) for PRBS23	
	1.28 Gbps	5.12 Gbps
KC705	79.84	66.67
KC705 + TwinAx (6 m)	65.89	36.36
KC705 + GBCR1	81.40	69.70
KC705 + TwinAx (6 m) + GBCR1	81.40	69.70

As mentioned in Section 3.4.1, the components on the optoboard such as the GBCR are not powered directly but via DCDC converters to provide an efficient solution for the distribution of power for each of these components. Loopback tests were performed to compare the effect on the performance of the transmission chain when the GBCR is directly powered versus powered via a DCDC converter, FEAST 1.2 V. The FEAST 1.2 V is also a single-phase synchronous buck DCDC converter like the bPOL2V5. The FEAST 1.2 V was used instead of the bPOL2V5 due to unavailability of the latter at the time of testing.

A synchronous buck converter, also known as a synchronous step-down converter, is a type of DCDC converter that is an enhanced version of the conventional buck converter. It offers improved efficiency compared to a standard buck converter by replacing the diode with a synchronous rectifier (typically a MOSFET) in the output path. The basic principle of a buck converter involves using a switching transistor, an inductor, a diode, and a capacitor to control the voltage output. The switching transistor (typically a MOSFET) is turned on and off at a high frequency by a control circuit, such as a pulse-width modulation (PWM) controller. When the transistor is turned on, current flows through the inductor, storing energy in its magnetic field. This is the "on" or "charging" phase. When the transistor is turned off, the inductor's magnetic field collapses, causing the stored energy to be released. The diode, known as the freewheeling diode or catch diode, allows the inductor current to continue flowing and charges the output capacitor. This is the "off" or "discharging" phase. By adjusting the duty cycle of the switching transistor (i.e., the ratio of on-time to off-time), the average voltage across the inductor and output capacitor can be controlled. This allows the buck converter to regulate the output voltage to a desired level, which is typically lower than the input voltage.

The FEAST DCDC converter needs to be enabled as the circuit is disabled by default and requires an application of a voltage above 850 mV to the designated enable pin in the FEAST circuit. Furthermore an input voltage of 5 V upto 12 V is provided directly via a power supply that converts this input voltage to 1.2 V that is used to then power the GBCR1. More information on the FEAST can be found in reference [147]. The performance of the transmission chain employing the FEAST instead of direct powering is comparable as shown in Table 3.7. Therefore, the next tests were carried out using direct powering.

Table 3.7: Comparing direct powering vs. FEAST 1.2V of GBCR1 from loopback tests conducted using KC705 and Vivado interface

Bitrate [Gbps] over KC705 + TwinAx (6 m) + GBCRv1	Eye opening (UI%) for PRBS23	
	Power supply	FEAST 1.2 V
1.28	81.40	82.17
5.12	69.70	66.67

3.6.2 Jitter analysis of the electrical transmission chain using Xilinx KC705 FPGA generated PRBS over transmission chain: KC705/RD53B CDR, 1 m flex, 6 m twinAx and GBCR1

Incorporation of 1 m flex

I conducted further tests with the 1 m flex added to the transmission chain. Jitter analysis was performed using a 2 GHz Tektronix oscilloscope instead of the Vivado interface. The KC705 provided the PRBS data through the chain via 1 m flex, 6 m twinAx cable. The results have been summarised in Table 3.8. It is seen that the jitter over the chain is ~ 200 ps measured at a measurement point right after the flex, which is quite high. The lpGBT requires the jitter to be ≤ 100 ps. The jitter after only the twinAx cable is very high and no open eye was observed. Adding GBCR1 helped to decrease the jitter despite not operating at the intended design frequency of 1.28 Gbps, when incorporated in the chain right after either the flex or the twinAx cables. The KC705 + TwinAx (6 m) + GBCR1 chain has a very high TIE in comparison to the TJ. Ideally the TJ \sim TIE. When TIE is $>$ or $<$ TJ, it was observed that it is caused by the DJ component in the TJ ($TJ = RJ + DJ$). As such, no pattern was detected on the oscilloscope which is composed of periodic jitter (PJ), data dependent jitter and bounded uncorrelated jitter (BUJ). The PJ leads to unstable clock-recovery in the PLL from the received PRBS to GBCR1 whose design frequency is not 1.28 Gbps but 5.12 Gbps. Therefore the TIE, which measures the deviation of the clock recovered from the received data to the ideal clock, is far more reliable in measurements conducted with GBCR1. The fact that no open eye was observed from the data transmitted over the maximum transmission length of 1 m flex and 6 m twinAx cable shows that the signal loss needs to be compensated and therefore there is a requirement of a GBCR designed to recover 1.28 Gbps uplink signals.

The measurements were also corroborated with a 16 GHz oscilloscope as measuring a 1.28 Gbps signal with a 2 GHz oscilloscope can some challenges due to the bandwidth limitations of the equipment. Also, a high sample rate i.e how frequently the oscilloscope samples the signal, was set $\sim 10,000$, to accurately capture the 1.28 Gbps signal's fast transitions in both the oscilloscopes.

Incorporation of RD53B CDR in place of KC705 FPGA board

I performed the next jitter tests also using a 2 GHz oscilloscope after including the RD53B CDR chip as the RD53B FE was not available for testing in place of the KC705 board.

The RD53B CDR chip was developed by the ATLAS group in Bonn as an independent test vehicle for the clock-data recovery circuit that would be integrated in the RD53B FE chip. The BDAQ53 board with Enclustra KX-2 FPGA module was also developed by the ATLAS group at the University of Bonn and used to configure the RD53B CDR chip, as

Table 3.8: Jitter tests using a 2 GHz oscilloscope incorporating 1 m flex in the KC705, 6 m TwinAx and GBCR1 in the transmission chain

Devices			Observed Jitter using 2 GHz oscilloscope	
			TJ [ps]	TIE pp [ps]
KC705 + Flex (1 m)			234	201
KC705 + TwinAx (6 m)			No open eye	
KC705 + GBCR1	CDR enabled	Pre-emphasis	52	47
		No pre-emphasis	49	48
	CDR disabled		487	238
KC705 + Flex (1 m) + GBCR1			64	60
KC705 + TwinAx (6 m) + GBCR1			97	1959
KC705 + Flex (1 m) + TwinAx (6 m)			No open eye	
KC705 + Flex (1 m) + TwinAx (6 m) + GBCR1			No open eye	

shown in Figure 3.19. The software part of the readout system is written in Python and heavily relies on Basil framework. A voltage of 1.2 V was directly provided to the RD53B CDR using a power supply. The BDAQ board itself could be either directly powered or powered from the PC via a USB cable. Once the chip was powered, a 160 Mbps training pattern (010101...) was sent to the command input of the chip. The command and configuration information was sent to the RD53B CDR via BDAQ FPGA display port cable. Then, once the voltage controlled oscillator (VCO) in the RD53B CDR circuit was locked, i.e stabilised, and produced a 1.28 GHz output clock, the RD53B CDR switched from its "startup" mode to normal operation. Here, the command sent over to the chip could be switched from the training pattern to PRBS pattern with 3, 5 or 7 bits. The configuration of the chip then released the reset of the linear-feedback shift register (LFSR), generating data for the serialiser (SER) and setting the output pattern to be either PRBS7 or PRBS15 (in this case PRBS15). The CML driver of the chip then drives this PRBS pattern through the uplink. A pre-emphasis circuitry implemented in the chip design ensures that the settings can be adjusted for each cable type and length individually for best results. The uplink was sent via connecting SMA cables to the flex and twinAx and GBCR to be then analysed on the oscilloscope.

Table 3.9 shows the jitter observed over the the different components of the transmission chain with the RD53B CDR sending the PRBS instead of the KC705. As mentioned earlier, the lpGBT specifications require the jitter ≤ 100 ps [148] at a BER of 10^{-12} . The uplink, tested right after the RD53B CDR, has a jitter of 100 ps. The RD53B CDR pre-emphasis on the uplink is required to observe an open eye with the 6 m twinAx cable in the transmission chain. Again, the TIE is more reliable than the TJ in the measurements conducted with the GBCR1 in the transmission chain. The observations from these measurements are comparable to those with the KC705 providing the PRBS pattern.

3.6.3 Irradiation studies of 6 m twinAx cables

Signal loss analysis

Given the potential exposure of the electrical cables to elevated radiation levels, as indicated in Table 3.3, I carried out preliminary evaluations to assess the integrity of the data transmission chain using irradiated twinAx cables. These cables are anticipated to en-

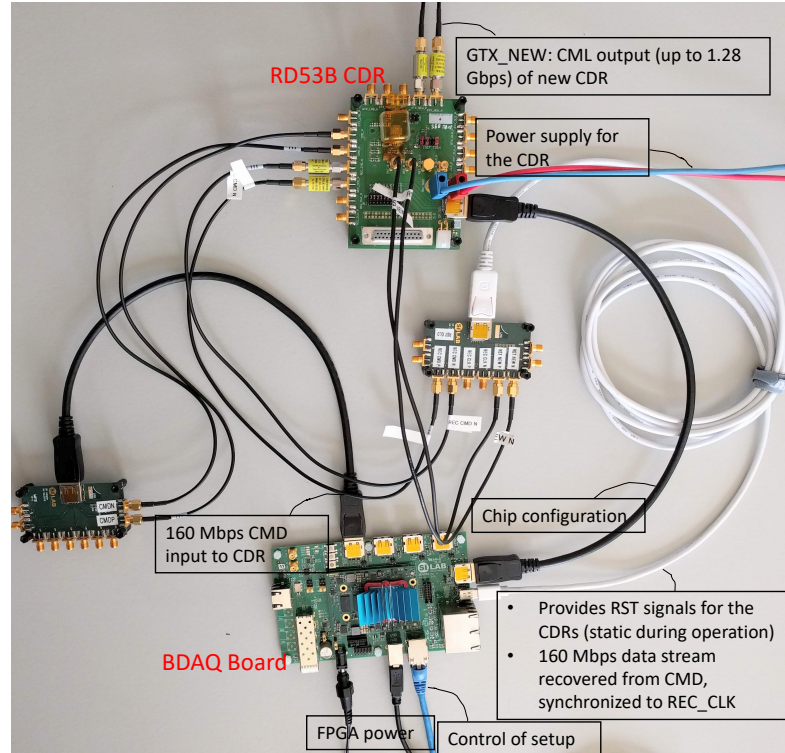
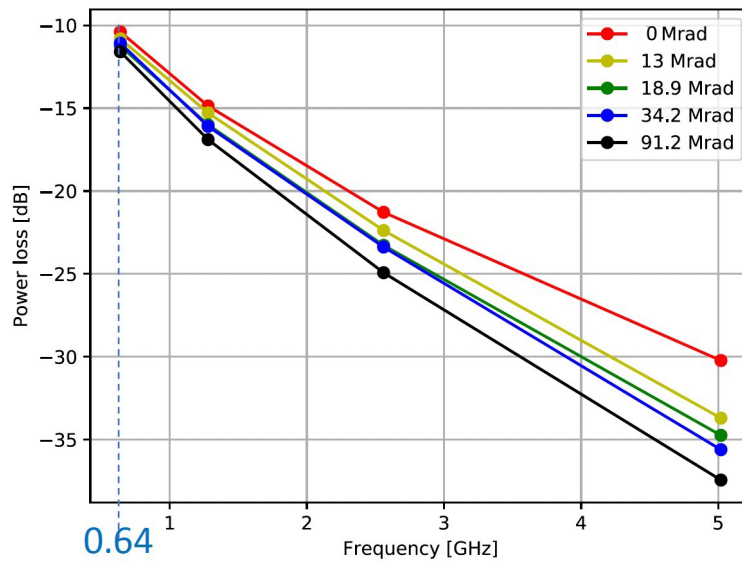


Figure 3.19: The RD53B CDR setup for configuration via BDAQ53 board and powering.

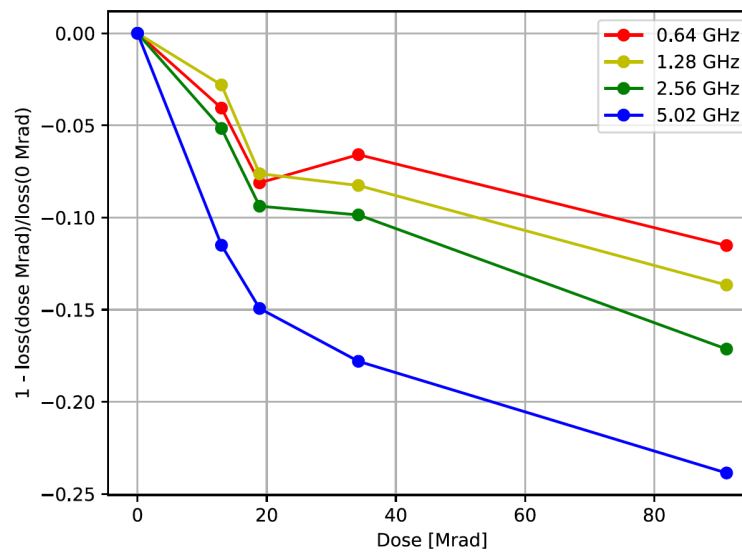
counter a radiation dose of approximately ~ 300 Mrad, and thus, their performance was examined for quality assurance. A 6 m twinAx cable was irradiated in steps and then the signal loss over the cable and subsequent jitter analysis was performed. Figure 3.20 shows the signal or power loss over the transmission chain as a function of the frequency. At a data rate of 1.28 Gbps, which corresponds to a frequency of 0.64 GHz, the power loss is negligible, measuring less than 1 dB when comparing the power loss at 13 Mrad to that at 91.2 Mrad. However, at higher frequencies, the power loss becomes more significant, and the signal experiences faster attenuation, particularly at elevated irradiation doses and frequencies. It is important to mention here that comparisons were made with 13 Mrad instead of 0 Mrad as these measurements were planned and accordingly conducted after the twinAx cable had already been irradiated to 13 Mrad.

Jitter analysis

Table 3.10 presents the jitter values at various stages of irradiation for a 6 m TwinAx cable transmitting a PRBS15 pattern through the uplink from the RD53B CDR. Interestingly, I observed that the jitter at 34.2 Mrad was greater than that at 91.2 Mrad, indicating that factors other than irradiation dose, such as suboptimal pre-emphasis settings on the RD53B CDR and environmental may have influenced the jitter behaviour. Generally upon repeating each measurement, the jitter was seen to be within ± 20 ps. However, it is evident that the overall trend is an increase in jitter with higher irradiation doses and with an increased number of electrical components in the transmission chain.



(a)



(b)

Figure 3.20: Electrical signal loss at different stages of irradiation of a 6 m TwinAx cable (a) against frequency [GHz] and (b) against dose [Mrad] including the interpolated insertion loss at 0 Mrad.

Table 3.9: Jitter tests using a 2 GHz oscilloscope incorporating RD53B CDR (PRBS15) in place of KC705 board in the test setup.

Devices				TJ [ps]	TIE pp [ps]	
RD53B CDR				100	93	
RD53B CDR + GBCR1				88	85	
RD53B CDR + Flex (1 m)				277	260	
RD53B CDR + Flex (1 m) + GBCR1				85	78	
RD53B CDR + TwinAx (6 m)		no pre-emp		No open eye		
		pre-emp		217	196	
RD53B CDR + TwinAx (6 m) + GBCR1		no pre-emp		83	248	
		pre-emp		147	220	
RD53B CDR + Flex (1 m) + TwinAx (6 m)		no pre-emp		No open eye		
		pre-emp		264	209	
RD53B CDR + Flex (1 m) + TwinAx (6 m) + GBCR1		pre-emp	EQ h'30	GBCR1 CDR on	875	456
				GBCR1 CDR off	782	406
			EQ h'00	GBCR1 CDR on	91	421

Table 3.10: Jitter measurements performed using a 2 GHz oscilloscope at various irradiation stages of a 6 m TwinAx cable using a PRBS15 pattern generated from the RD53B CDR.

Devices	Irradiation Dose [Mrad]							
	13		18.9		34.2		91.2	
	TJ [ps]	TIE [ps]	TJ [ps]	TIE [ps]	TJ [ps]	TIE [ps]	TJ [ps]	TIE [ps]
RD53B CDR + TwinAx (6 m)	217	196	218	198	320	309	239	223
RD53B CDR + Flex (1 m) + TwinAx (6 m)	264	209	340	262	267	225	270	221

3.6.4 Signal loss/gain of each electrical component after replacement of GBCR1 with GBCR2

Next I measured the signal loss on each of the electrical components in the transmission chain once the GBCR2 ASIC (designed to recover the uplink signals at a data rate of 1.28 Gbps) mounted on a PCB designed for lab testing was available. The measurements included ~ 3 m of SMA cables that were used to connect the components. Summing over the observed loss for each of the components, the total loss over the chain at 0.64 GHz without SMA cables is ~ -17 dB and with SMA cables is ~ -23 dB prior to incorporating the measurements for the GBCR2. The GBCR2 was configured with default settings and the adjustable resistances HFSR and MFSR associated to the high and medium frequency CTLEs set to 8 each as shown in Figure 3.21. It is seen that the GBCR2 has a gain of ~ 20 dB for an input signal with -20 dB insertion loss. Therefore, the GBCR2 with optimum equaliser configuration recovers the losses, as shown in Figure 3.22.

3.6.5 Measurements with optoboard V0

Next, I employed the optoboard V0 test setup to validate the interaction among the lpGBT, optical data transmission, and the customised firmware that includes the lpGBT-FPGA core operating on the KC705. Successful configuration of the lpGBT ASIC was achieved using the IC field of the high-speed optical link.

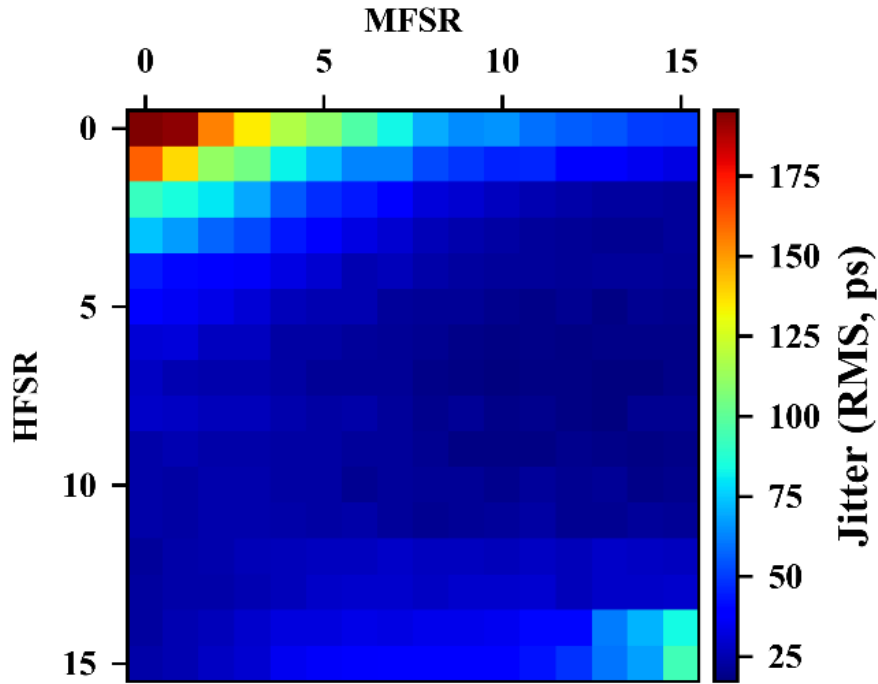


Figure 3.21: Jitter versus CTLE peaking parameters taken from Reference [120]. It is observed that the optimal values of MFSR and HFSR for the CTLE is around 8 - 10 for each.

This prototype comprises the VTRx+, one lpGBT and no GBCR. However, even with these components, it was sufficient for testing and confirming the fundamental operational principles of the optosystem i.e. conversion of the high-speed signals from optical to electrical, the configuration of the optosystem via the optical link, and the multiplexing of the e-links.

The VTRx+ and lpGBT V0 on the optoboard V0 were provided with 2.5 V and 1.2 V directly using power supplies and dedicated circuitry on the optoboard V0 PCB. Configuration of lpGBT V0 internal registers and I²C masters of lpGBT V0 was sent over optical downlink using the IC field in the lpGBT data frame from the KC705 FPGA hosting the customised lpGBT backend firmware. In addition to other information, this dataframe includes the lpGBT address, register address, and data that will be written/read. Then, using the Si5324 oscillator, which is a precision clock generator of the KC705 FPGA board to provide a reference clock at a frequency of 320 MHz, the GTX transceiver transmits the 2.56 Gbps downlink over the Small Form-factor Pluggable Plus (SFP+) transceiver on the KC705. The optical to electrical conversion is done by the VTRx+ and then the lpGBT V0 recovers both data and a 40 MHz clock from the downlink. The e-link signals of the lpGBT can be analysed using the Integrated Logic Analyser (ILA, [149]).

Demonstration of operational principle using the downlink

The first test I performed with the optoboard V0 was to effectively demonstrate the operational principle using the downlink. To this end, an increasing counter was injected

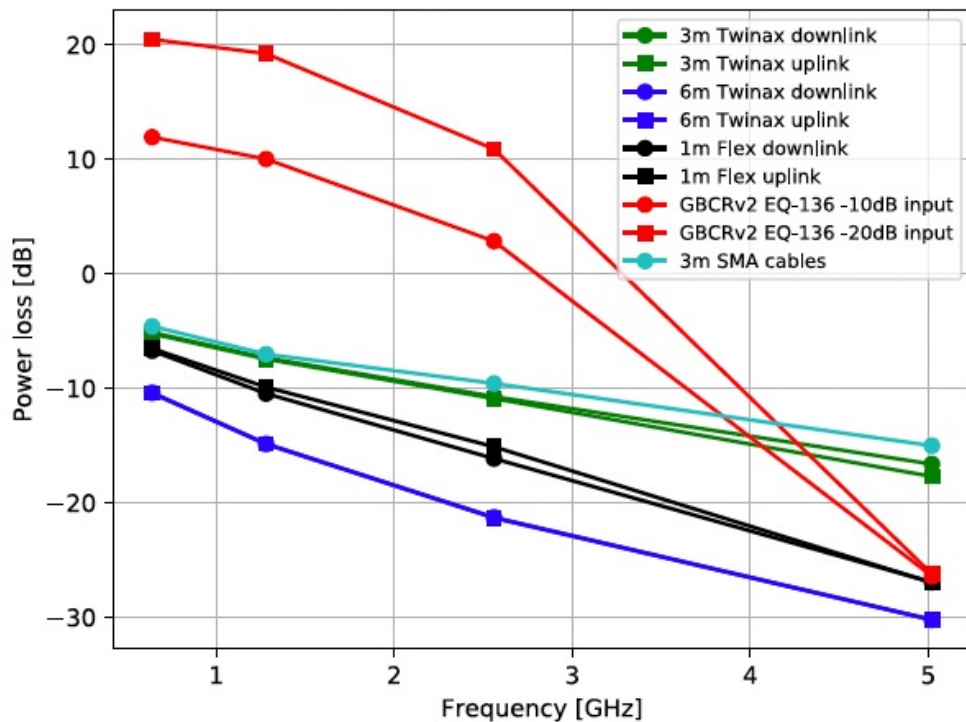


Figure 3.22: Electrical signal loss/gain of each electrical component. It is seen that the GBCR2 has a gain of ~ 20 dB for an input signal with -20 dB insertion loss. Therefore, the GBCR2 with optimum equaliser configuration recovers the losses over the transmission chain.

into one of the downlink data fields of the lpGBT-FPGA. By observing the resulting e-link signal after traversing the entire downlink chain (SFP+ – fiber – VTRx+ – lpGBT), the counter could be seen in the corresponding e-link, on the ILA and also on the oscilloscope as shown in Figure 3.23. This qualitative demonstration effectively showcased the operational principle of the Optosystem where the optical downlink was received and converted to electrical signals by the VTRx+ and then demultiplexed in the lpGBT.

BERT using internal lpGBT pattern checker/generator

I performed a BERT on the uplink using the internal lpGBT PRBS generator and pattern checker. The lpGBT test pattern checkers and generators have been schematically shown in Figure 3.24. The lpGBT transmitter can be programmed to transmit the following: a fixed pattern, PRBS sequence, clock sequence, or loop back incoming downlink frame. The data coming from each group of receiver ports of the lpGBT (ePortRx) can be replaced with test patterns. The test pattern generator generates 16 or 32 bits in each clock cycle when the chip operates in low or high speed mode respectively. When a fixed pattern is used to test the data transmission in fact a PRBS is transmitted over the high speed frame. Since the fixed pattern transmitted is DC balanced the receiver will have no problem locking to the incoming data stream. The lpGBT has one pattern checker which can monitor various points along the data path. This architecture implies that only one data stream can be checked at any given time. The duration of the measurement is expressed in the number of 40 MHz clock cycles and can be programmed accordingly. It should be noted, that the actual number of bits checked depends on the data source.

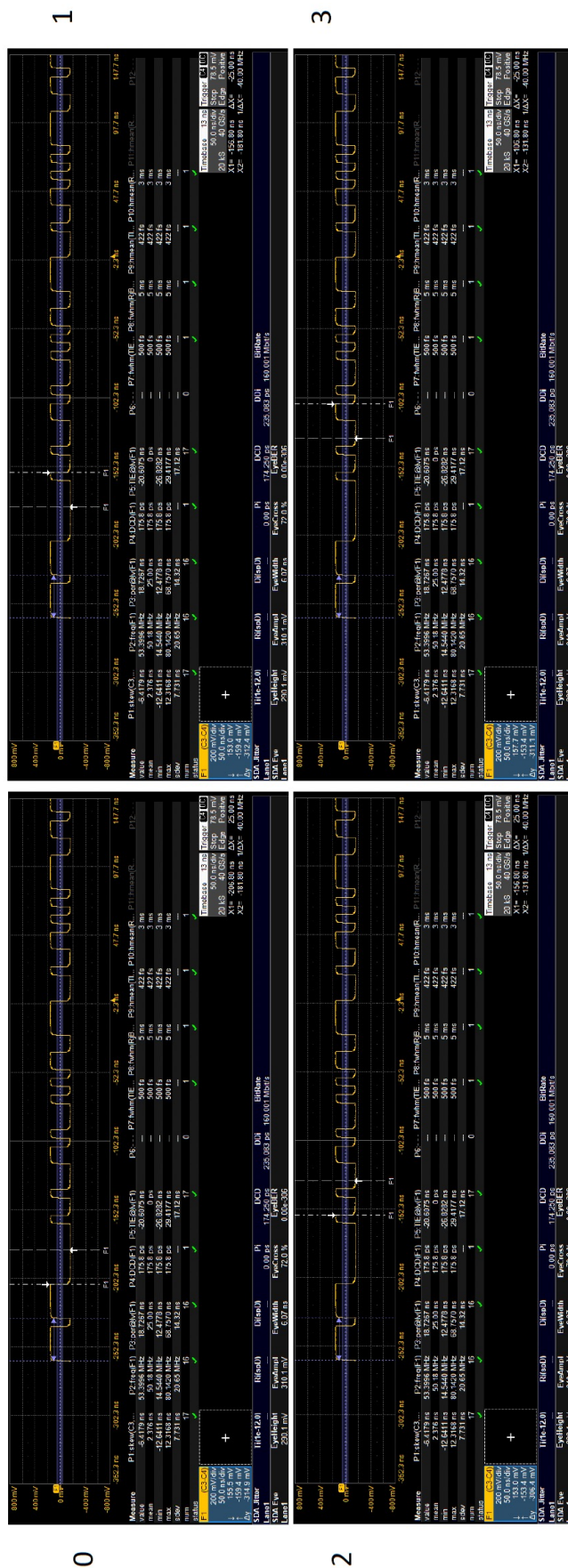


Figure 3.23: Downlink opto-electrical test for the optoboardv0 using 16 GHz oscilloscope. A counter is sent over the downlink using the lpGBT V0 firmware hosted in the customised KC705 board and then demultiplexed in the lpGBT V0. It is observed on the oscilloscope by connecting via SMA cables the corresponding output port (EO_00) of the SMA connector board of the optoboardv0.

For example, channel working at 80 Mbps produces only two bits per 40 MHz clock cycle, while channel working at 1.28 Gbps produces 32 bits per 40 MHz clock cycle.

As the lpGBT V0 had a known issue with its phase shifter such that it didn't lock when using PRBS7 generator with the highest clock frequency of 1.28 GHz, the internal downlink loopback test was conducted at an uplink data rate of 640 Mbps. This affects only test mode and not normal operation. The internal PRBS7 Generator of lpGBT was enabled and the bits were checked by Pattern Checker of the lpGBT internally. The test was conducted for ~ 14 mins (the highest offered by lpGBT internally i.e. 239 bits) and there was no observed bit errors.

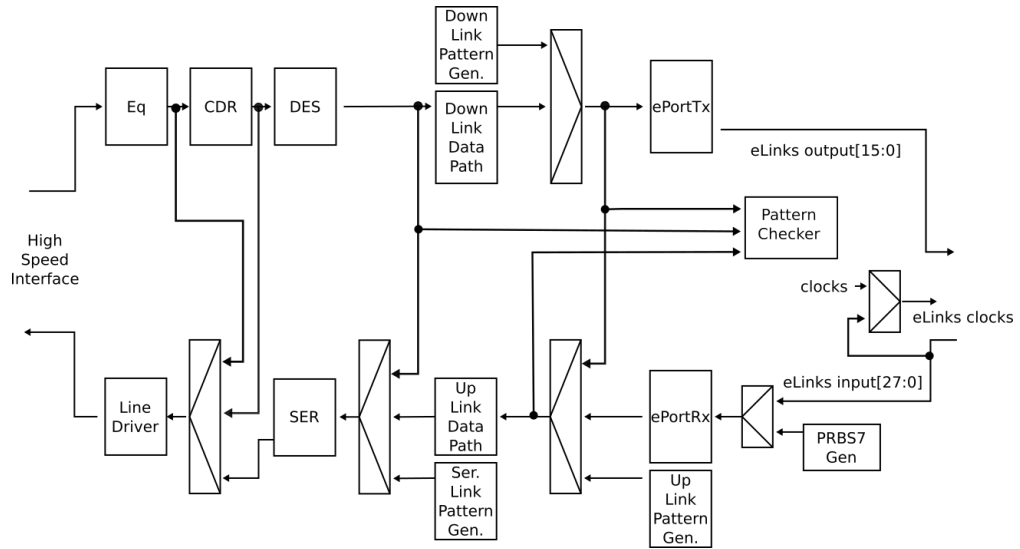


Figure 3.24: Schematics of the lpGBTv0 internal PRBS generator and pattern checker.

Master-slave functionality tests

As the Optoboard hosts 4 lpGBTs, it was important to test the concept of lpGBT "master-slave" functionality. The lpGBT successfully configured as a transceiver addressed informally as lpGBT "master" was used to generate 40 MHz output e-clocks as reference clocks for the three transmitter-only lpGBTs addressed informally as lpGBT "slaves". As the optoboard V0 hosts only 1 lpGBT ASIC, four optoboard V0s were connected in a daisy chain as shown in Figure 3.25, where one of the optoboards hosted the lpGBT configured as a master provided this 40 MHz reference clocks to the lpGBT slaves via SMA cables connected to an customised adapter PCB. The I²C master of the lpGBT facilitated the configuration of the lpGBT slaves via I²C protocol thereby confirming the fundamental principle of the optoboard in the optosystem.

I first tested the master-slave functionality concept by checking the frequency of the reference clock provided by the lpGBT master to the lpGBT slaves and the jitter on the clock observed from the lpGBT slave on the last optoboard v0 connected in the daisy chain. I noticed that the quality of the reference clock from lpGBTv0 slaves degrades with respect to position in daisy chain. And the lpGBT addressed as slave "003" was observed to have a lower eclock frequency of 39 MHz and a very high jitter.

In the next versions of the optoboards including the optoboard V1 used in some of the later tests presented in this thesis, were designed with direct lines from master to

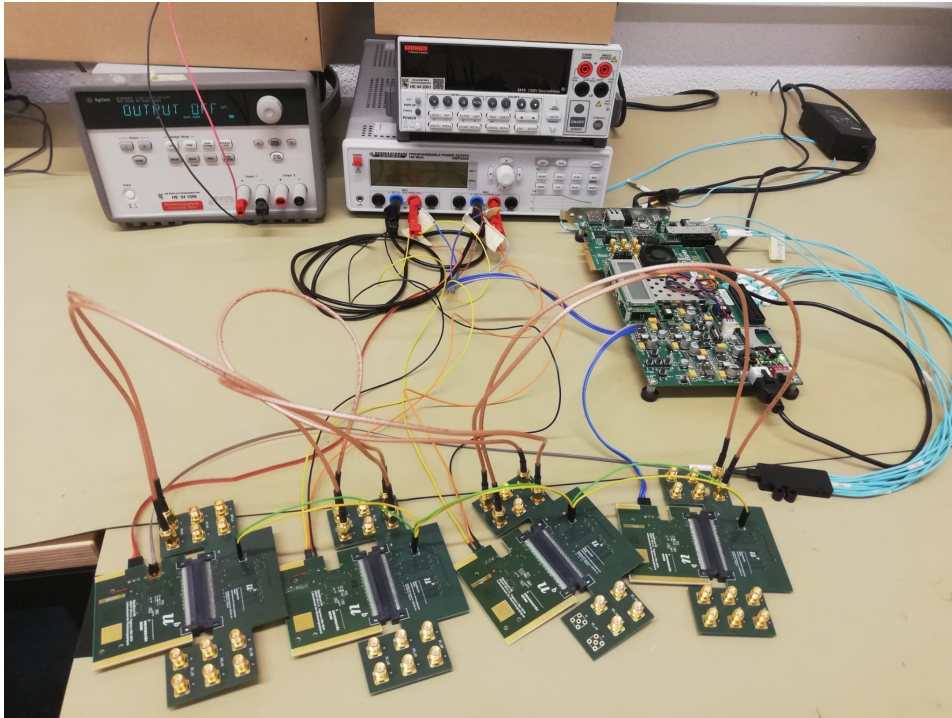


Figure 3.25: This is the optoboard V0 test set up for preliminary testing and lpGBT V0 master-slave functionality tests. The master optoboard V0 is on the extreme left with the lpGBT V0 configured as a master connected via daisy chain to the optoboard V0s with lpGBT V0s configured as slaves.

slave which further corroborated the working concept of the optosystem in the ITk pixel data transmission chain. And, I did not observe any issues e-clock frequency and jitter associated to the master-slave functionality of the lpGBT ASICS on the optoboard V1s that I tested.

A second test was conducted to validate the lpGBT master-slave communication concept using the internal BERT feature of the lpGBT. The BER was found to be less than 10^{-12} for all the lpGBTs, except for lpGBT slave 003. The other lpGBT slaves exhibited similar levels of jitter, approximately 200 ps, and operated at an e-clock frequency typically around 40 MHz. However, lpGBT slave 003 was observed to be malfunctioning with higher jitter and lower e-clock frequency and deemed defective.

Nevertheless, this test successfully confirmed the functional operation of the lpGBT master-slave functionality, demonstrating its viability and effectiveness.

Validation of working concept of ITk pixel data transmission chain using the optoboard V0

I performed an inclusive test using BERT to validate the working concept of ITk pixel data transmission chain using the optoboard V0. To this end I provided, a constant training pattern followed by PRBS7 pattern to the RD53B CDR by the lpGBT V0 master over the electrical downlink at 160 Mbps. Once the VCO of the RD53B CDR locked to the downlink pattern, it then generated a PRBS7 uplink pattern at 1.28 Gbps.

Table 3.11: LpGBTv0 master-slave functionality: Quality of the reference clock using jitter analysis

Daisy chain orientation M: lpGBTv0 master, 2: 2,3,4: lpGBTv0 slaves 002, 003, 004	lpGBTv0	Clock Frequency [MHz]	Total Jitter [ps]
M,2,4,3	master	40.0022	218
	slave 002	40.0038	186
	slave 004	40.0005	205
	slave 003	38.8315	3714
M,2,3,4	slave 003	39.9975	244
M,3,2,4	slave 003	40.0025	223

This uplink was then received both directly from the RD53B CDR and via 1 m flex, 6 m twinax and GBCR2 hosted on its customised PCB to be checked by the pattern checker inside the lpGBT. A total of 3×10^{12} bits were checked for each case and the no bit errors were observed.

Effect of downlink jitter on the uplink

It is expected that the quality of the downlink will affect the quality of the uplink. As such, I did comparison of the effect of downlink jitter on uplink as summarised in Table 3.12. The jitter on the uplink for optoboard V0 (OBv0) and OBv0 + 1 m flex + 6 m twinAx is comparable. Using the BDAQ board to send the downlink to the RD53B CDR instead of the lpGBT hosted on the OBv0 considerably reduces the uplink jitter. However, when testing retiming mode with the GBCRv2, it is necessary to send the downlink from the OBv0 to match the phase of the 1.28 GHz e-clock. Overall, the RD53B CDR is able to lock to the incoming downlink with jitter around 200 ps and the observed jitter on the generated uplink is lower than the jitter on the downlink.

Table 3.12: Comparing effect of downlink jitter on uplink generated by the RD53B CDR

Devices in downlink signal	Jitter (TJ) on downlink [ps]	Jitter (TJ) on RD53B CDR uplink [ps]
OBv0	194	141
OBv0 + TwinAx (6 m) + Flex (1 m)	216	142
BDAQ	163	119

3.6.6 Optimisation of GBCR2 and lpGBT register settings

Tests were done by me to optimise GBCR2 and lpGBT register settings to improve the performance of the data transmission chain.

Figure 3.26 shows the signal and jitter over RD53B CDR (with no added pre-emphasis) + 1 m Flex + 6 m TwinAx + GBCR2, with the GBCR2 configured in the default equaliser (EQ) mode. The received downlink was a PRBS5 pattern coming from the BDAQ board. The observed TJ is ~ 221 ps and TIE pp ~ 189 ps.

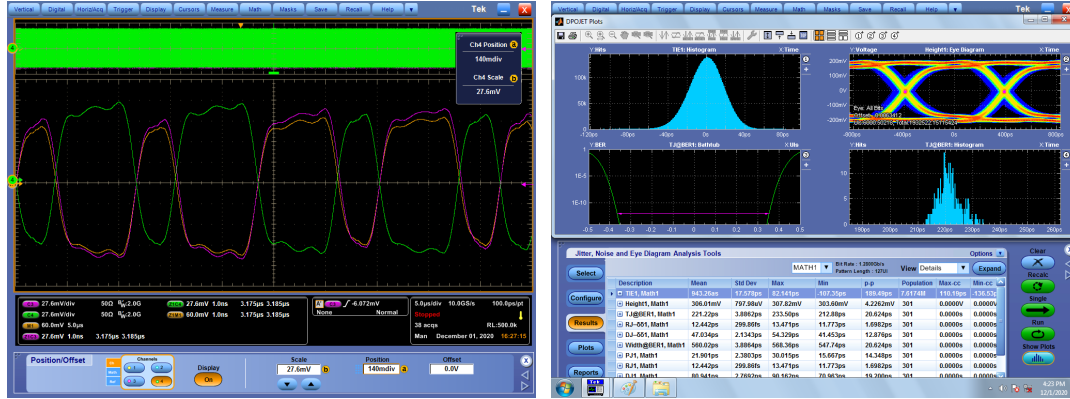


Figure 3.26: The signal and jitter over RD53B CDR (no pre-emphasis) + 1 m Flex + 6 m TwinAx + GBCRv2 (default EQ mode).

Then the Continuous Time Linear Equaliser (CTLE) parameters versus corresponding total jitter was measured. The CTLE parameters adjust peaking strength of middle frequency range from 250 to 450 MHz and high frequency range from 400 to 1300 MHz. The uplink channel was configured without attenuation. And it is seen that the output amplitude strengths have similar TJ measurements. The CTLE configuration d'136 in EQ mode i.e. the adjustable resistances HFSR and MFSR associated to the high and medium frequency CTLEs set to 8 each gives the lowest TJ ~ 205 ps as shown in Figure 3.27. Though the lpGBT is able to recover the incoming uplink signals with a jitter > 100 ps, with a BER $< 10^{-12}$, it is preferable to optimise the parameters further to reduce the jitter to 100 ps.

As the retiming mode is expected to further reduce the jitter, the next studies were conducted using the GBCR2.

A comparison between the 40 MHz and 1.28 GHz clock was done and the TIE pp observed was 114 ps and 117 ps, respectively. Therefore, the jitter on the eclocks are comparable. The next step was to optimise the settings of the 1.28 GHz e-clock using jitter analysis as shown in Table 3.13. It is observed that the jitter:

- lowers with decreasing drive strength
- is comparable for different pre-emphasis modes (disabled, self-timed, clock-timed)
- lowers with increasing pre-emphasis strength

A drive strength 2.0 mA was seen to have the lowest jitter. The jitter of the pre-emphasis modes are comparable. The pre-emphasis strengths and widths of 2.0 mA – 4.0 mA are also comparable. However the pre-emphasis width of 960 ps has a slightly lower jitter. So, the 1.28 GHz that would be provided to the GBCR2 for retiming was configured with

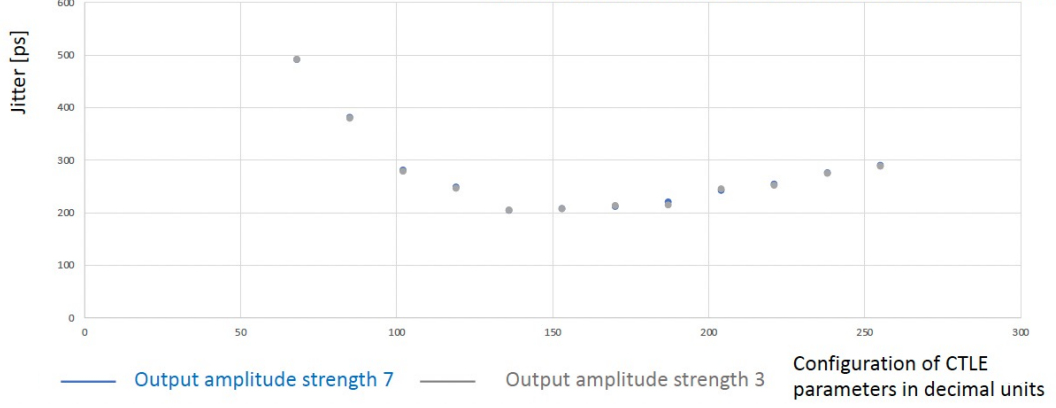


Figure 3.27: The jitter over RD53B CDR (no pre-emphasis) + 1 m Flex + 6 m TwinAx + GBCRv2 different EQ modes.

a drive strength 2.0 mA, pre-emphasis mode – clock timed, pre-emphasis strength 4.0 mA and observed TJ ~ 106 ps.

It is important to note in case of the retiming mode, the phase delay in GBCR2 is directly proportional to the Tbit where $T_{bit} = 1/\text{bit rate}$. The phase delay in GBCR2 increases by 1 if Tbit is increased by 1. In the lpGBT, the phase delay line covers more than one bit period i.e., $1.75 \times T_{bit}$ and in automatic mode during initialisation only phases 4 to 11 are allowed as shown in Figure 3.28.

3.6.7 BER and jitter analysis conducted over the entire uplink chain with replacement of optoboard V0 with V1

One of the first full data transmission test setup is shown in Figure 3.29 with the KC705 hosting the lpGBT-FPGA core, Optoboard V1 with one VTRx+, four lpGBTS and four GBCR2s, two 6 m twinAx cables for the down and uplink and the RD53B CDR with the BDAQ board. SMA cables are used to connect each of the components.

After optimisation of the multiple parameters of the different components - RD53B CDR, lpGBT V0 and GBCR2, jitter and BER tests were performed over the entire uplink chain with the GBCR2 in EQ mode as shown in Figure 3.30. The jitter and BER correlate as expected and the BER for good configurations of the devices is $< 10^{-12}$ (dark green areas).

I did this test using 3 m twinAx cables instead of 6 m twinAx cables. As expected, the CTLE configurations of the GBCR2 changes with the change in length of the electrical transmission chain. With a smaller electrical transmission length, more configurations with the desired BER $< 10^{-12}$ is available.

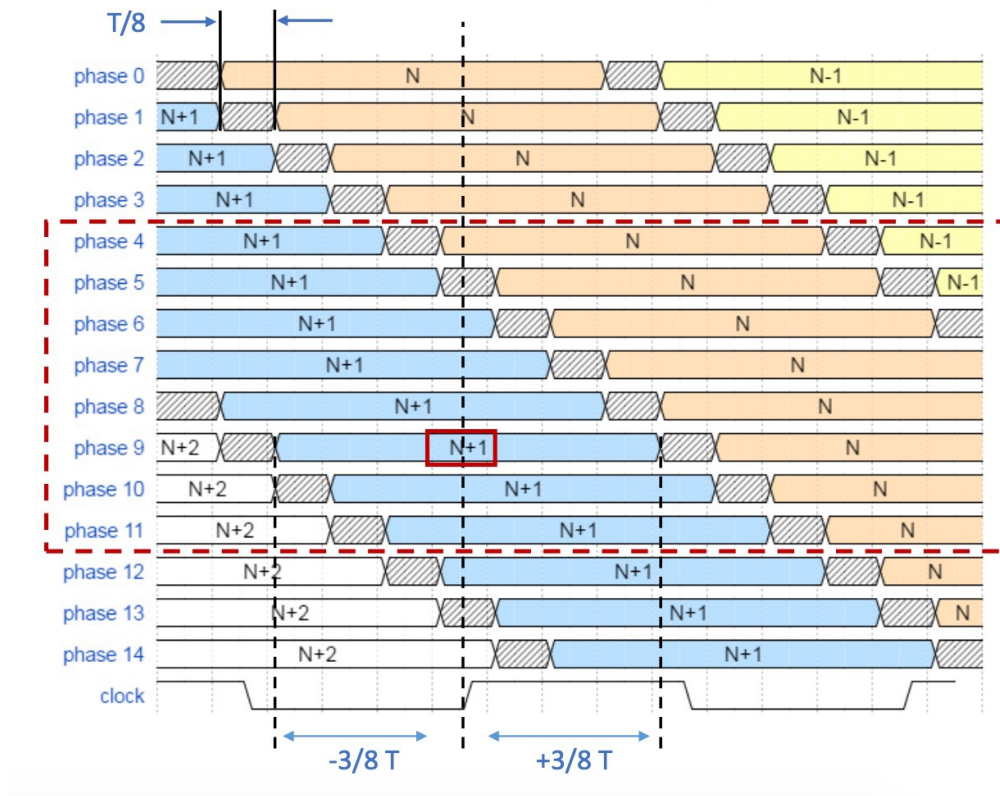


Figure 3.28: Schematically representing the phase delay between GBCRv2 and lpGBTv0.

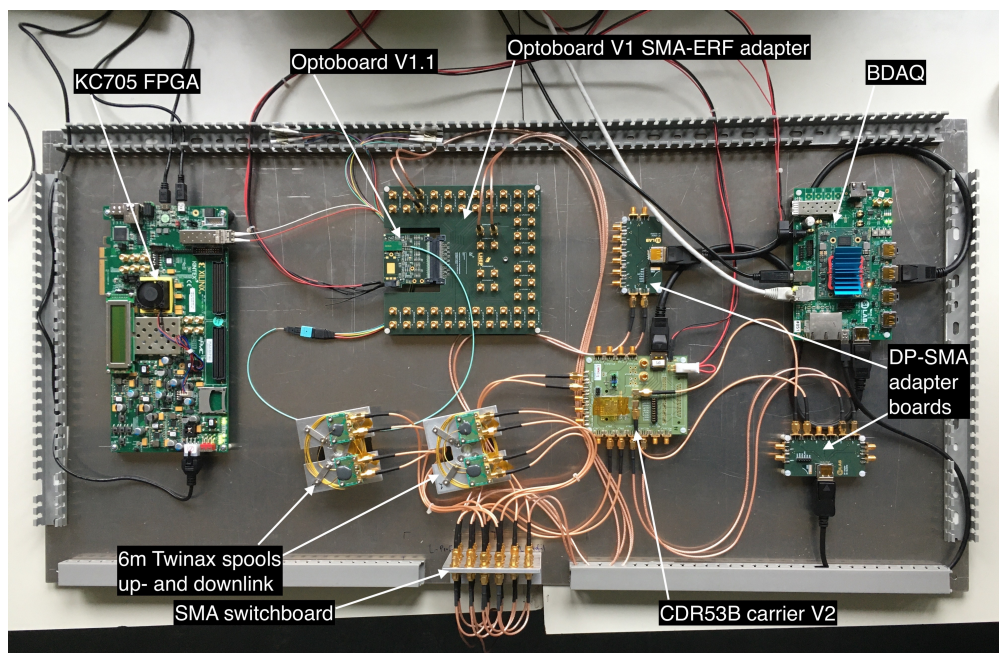


Figure 3.29: The Preliminary Data Transmission Test Setup at Bern.

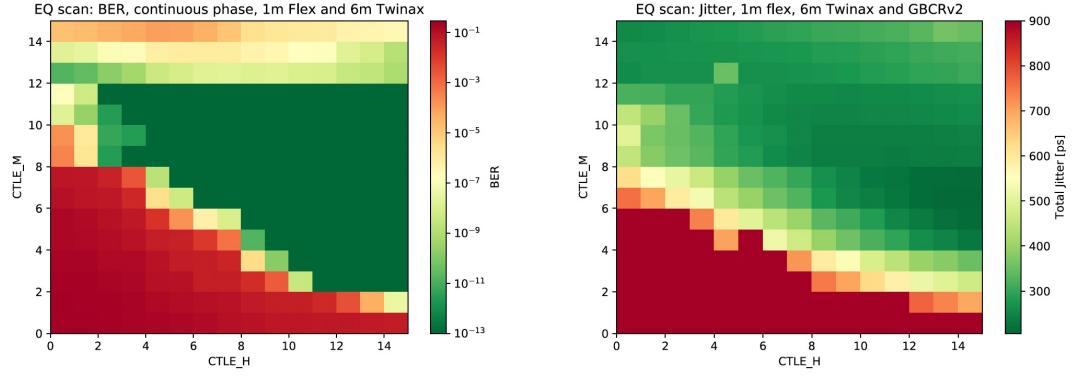


Figure 3.30: BER and jitter tests on the uplink with the entire transmission chain consisting of 1 m flex and 6 m twinAx with GBCR2 in Equaliser mode. The jitter and BER correlate as expected and the BER for certain configurations of the devices is $< 10^{-12}$ as demonstrated in the dark green areas.

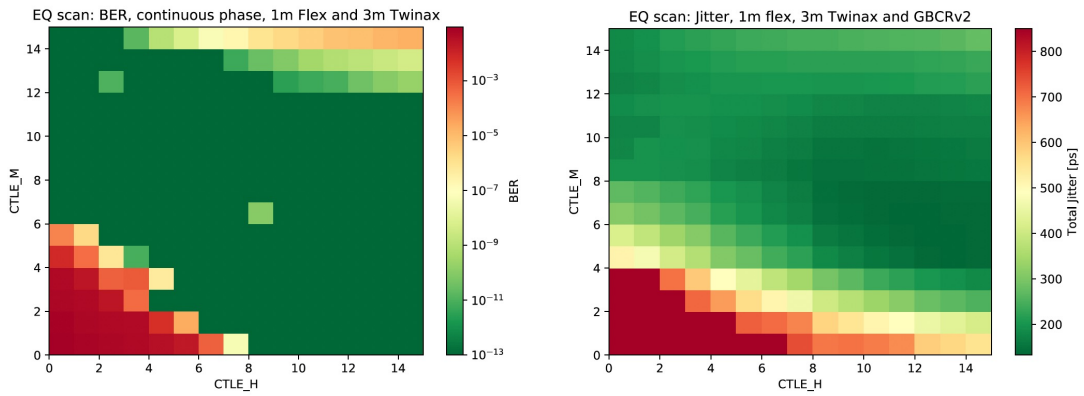
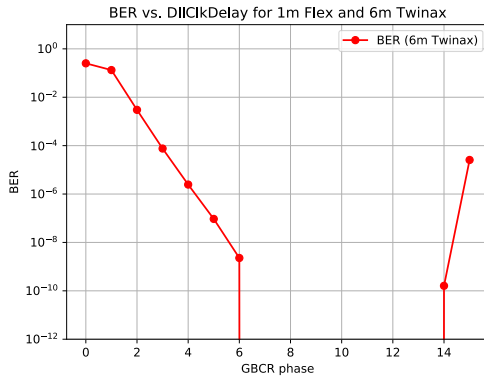


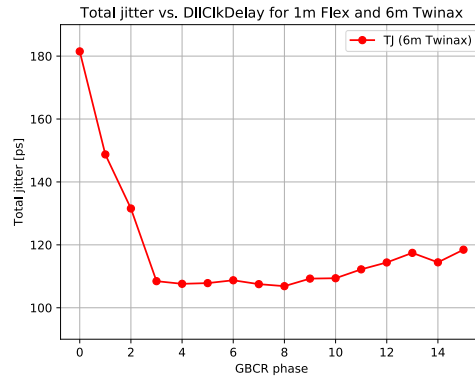
Figure 3.31: BER and jitter tests on the uplink with the entire transmission chain consisting of 1 m flex and 3 m twinAx with GBCRv2 in Equaliser mode.

Table 3.13: Comparing parameters of 1.28 GHz Eclk to optimise settings using jitter analysis (16 GHz oscilloscope)

lpGBTv0 1.28 GHz EClk Parameters		TJ [ps]
Drive strength [mA]	4.0	122.45
	3.0	120.60
	2.0	112.29
Pre-emphasis mode (Drive strength 2.0 mA)	Disdabled	112.29
	Self-timed	114.79
	Clock-timed	113.24
Pre-emphasis strengths [mA] (Drive strength 2.0 mA, clock-timed)	0.0	113.24
	1.0	112.74
	2.0	107.61
	3.0	107.23
	4.0	107.59
Pre-emphasis width [ps] (Drive strength 2.0 mA, clock-timed, pre-emphasis strength 4.0 mA)	120	107.59
	360	107.35
	720	106.39
	960	105.91



(a)



(b)

Figure 3.32: BER and jitter tests on the uplink with the entire transmission chain consisting of 1 m flex and 6 m twinAx with GBCR2 in retiming mode. It is seen that for the right phase alignment of data with GBCR2 and lpGBT V0, a lowest jitter ~ 110 ps with corresponding $\text{BER} < 10^{-12}$ is achieved.

The BER and jitter tests performed over the entire chain with GBCR2 in retiming mode is shown in Figure 3.32. In the Retiming mode (i.e. additional clock fed to GBCR2 from lpGBT V0 aside from recovered clock from data), for the right phase alignment of data with GBCR2 and lpGBT V0, a jitter ~ 100 ps that is within the lpGBT specifications is observed.

The phase difference depending on the electrical transmission chain length in the GBCR2 retime mode is shown in Figure 3.33. This demonstrates that depending on the length of the chain, the parameters must be set differently.

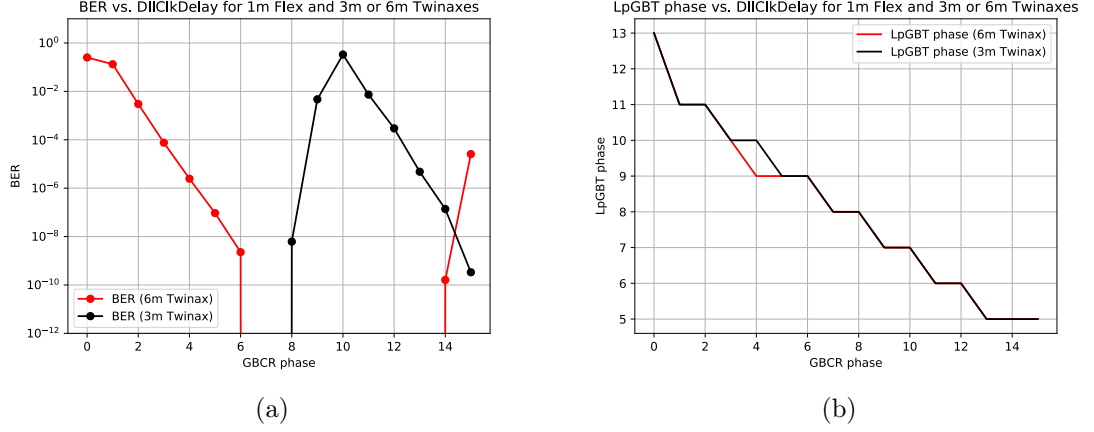


Figure 3.33: BER and phase difference tests on the uplink with the entire transmission chain consisting of 1 m flex and 3 m twinAx and 6 m twinax with GBCR2 in retiming mode respectively. The DLL phase difference between lpGBT V0 and GBCR2 depends on the length of the data transmission chain and consequently the configuration for the lowest BER. It shows that depending on the length of the chain, the parameters must be set

In conclusion, the ITk pixel data transmission chain setup using the initial prototypes, are able to meet the requirements of:

1. the loss in electrical signal on the uplink < 20 dB,
2. the bit error ratio $< 10^{-12}$ bits in most configurations.

It is also important to note that though the total jitter of ~ 110 ps in the retiming mode and ~ 200 ps in the equaliser mode have a jitter higher than the lpGBT specification of jitter within 100 ps, the data transmission chain exhibits the required BER $< 10^{-12}$. Hence, it can be safely concluded that the ITk pixel data transmission chain with jitter within 200 ps and < 20 dB signal loss over the uplink has a BER $< 10^{-12}$ and fulfils all the criteria.

With the working concept of the optoboard and the ITk pixel data transmission chain verified and parameters optimised, next tests out of the scope of this work done by me were performed by the Bern ATLAS team by incorporating the RD53B FE and then the final FE version known as ITkPix V2 and the FELIX system in place of the RD53B CDR and KC705 board. Also, further irradiation campaigns were done to irradiate all the cables and components on the optoboard and BER and jitter tests post irradiation were done. A final design review (FDR) of the ITk pixel data transmission chain has also taken place and very soon production of the optosystem and the overall transmission chain will begin.

Chapter 4

Search for Supersymmetry in events with $t\bar{b} + E_T^{\text{miss}}$ final state

Supersymmetry (SUSY) offers an extension to the Standard Model (SM) that addresses various issues left unanswered by the SM. These include the hierarchy problem, dark matter, and dark energy. SUSY accomplishes this by introducing partner particles for the known bosons and fermions in the SM. In R-parity conserving SUSY models, these SUSY particles are pair-produced and the lightest supersymmetric particle (LSP) which is considered to be the lightest neutralino ($\tilde{\chi}_1^0$) is stable, and is a proposed dark matter candidate.

All SM fermions have left and right-handed chiral components (f_L and f_R) and by extension in SUSY there are two additional scalar particles (\tilde{f}_L and \tilde{f}_R) for these fermions. From Naturalness considerations, the lighter states of the SUSY partners of 3rd generation SM quarks known as "*stops*" and "*sbottoms*" are favoured. The top squark (\tilde{t}) states mix to yield mass eigenstates \tilde{t}_1 and \tilde{t}_2 . Likewise the sbottom (\tilde{b}) states mix to yield \tilde{b}_1 and \tilde{b}_2 . By convention \tilde{t}_1 and \tilde{b}_1 are considered to be the lighter state. If we consider $\tilde{t}_1 \sim \tilde{t}_L$, then the \tilde{t}_1 is accompanied by a \tilde{b}_1 being close in mass due to Spontaneous Supersymmetry Breaking. These \tilde{b}_1 and \tilde{t}_1 could be pair-produced with relatively large cross-sections at the LHC as shown in Figure 4.10 later in Section 4.1.3.

This chapter provides an overview of the search for the pair production of \tilde{t} and \tilde{b} squarks decaying into final states comprising of a top quark, a bottom quark and E_T^{miss} .

The author's contribution to the analysis is the designing the signal grid and validating the signal points, defining the signal, control and validation regions for the bulk region or Region A of this analysis and associated statistical and systematic analysis. This is an ongoing analysis.

4.1 Analysis Motivation

Earlier versions of the analysis has been performed using Run 1 and part of Run 2 datasets using 20 fb^{-1} and 36.1 fb^{-1} of recorded data and at $\sqrt{s} = 8 \text{ TeV}$ and 13 TeV respectively. This analysis is performed again with the full Run 2 dataset of 139 fb^{-1} .

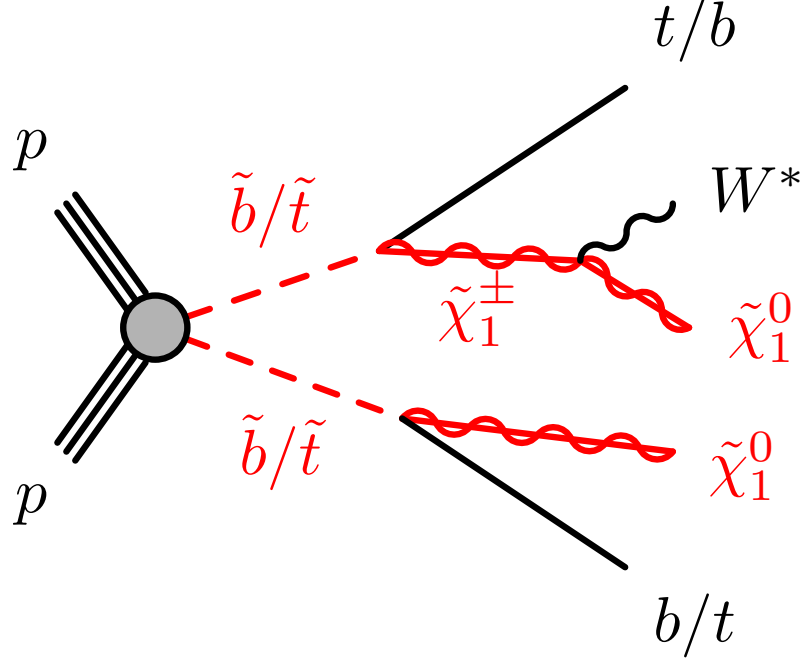


Figure 4.1: Diagram illustrating the signal scenario for the pair production of bottom and top squarks where one arm shows decays to a top or bottom quark and the lightest neutralino and the other other arm shows decays via an intermediate chargino to a top or bottom quark and the lightest neutralino. The mass difference $\Delta m(\tilde{\chi}_1^\pm, \tilde{\chi}_1^0)$ is small i.e. chosen to be 1 GeV, therefore the W boson from chargino decay is off-shell.

This increased data set combined with the latest object definitions and reconstruction techniques are utilised to improve the sensitivity to this unique and already well motivated supersymmetric signature.

4.1.1 Signal Phenomenology

For this search, simplified models based on the phenomenological minimal supersymmetric extension of the SM (pMSSM) [150–152] are considered. The signal scenario taken into account for this search is shown in Figure 4.1. The \tilde{t} or $\tilde{b} \rightarrow t + \tilde{\chi}_1^0$ and \tilde{t} or $\tilde{b} \rightarrow b + \tilde{\chi}_1^\pm$ decays are considered to be equally probable. The intermediate $\tilde{\chi}_1^\pm$ is assumed to be almost degenerate with the $\tilde{\chi}_1^0$ and decays to a $\tilde{\chi}_1^0$ and an off-shell W boson. The W boson is highly off-shell as the mass difference between the $\tilde{\chi}_1^\pm$ and $\tilde{\chi}_1^0$ is taken to be small and its decay products are therefore not detected. As such, the signature consists of a top quark, a bottom quark and $\tilde{\chi}_1^0$ s in the form of E_T^{miss} .

As the branching ratio (BR) for the \tilde{t} or $\tilde{b} \rightarrow t + \tilde{\chi}_1^0$ or $b + \tilde{\chi}_1^0$ is taken to be 50%, half of the decays proceed via this asymmetric decay mode with $tb + E_T^{\text{miss}}$ final states while the rest of the decays proceed symmetrically with 25% decaying to a $bb + E_T^{\text{miss}}$ final states and the other 25% decaying to a $tt + E_T^{\text{miss}}$ final states.

For our signature of $tb + E_T^{\text{miss}}$, the top quark decays semi-leptonically, so events with one charged lepton, two b-jets and E_T^{miss} are selected. Therefore for this final state,

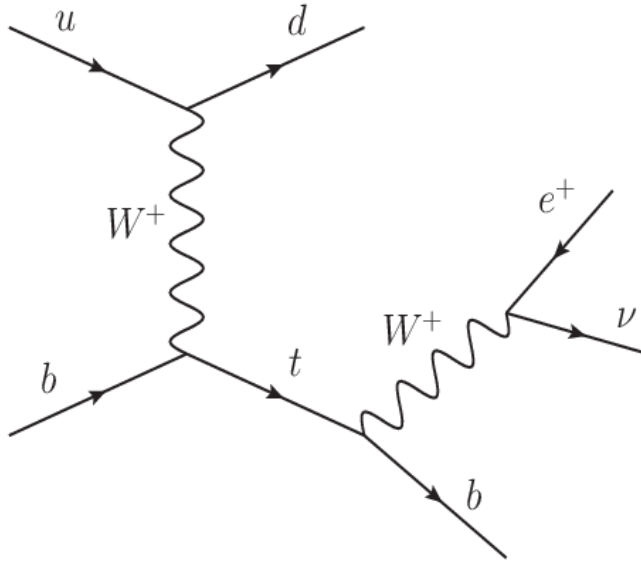


Figure 4.2: A t-channel single top quark production and its leptonic decay processes. Taken from Reference [153].

the main expected SM backgrounds come from single-top, $t\bar{t}$, W +jets, and $t\bar{t} + Z$. The expected dominant background is the single-top in this 1-lepton final state caused by a t-channel single-top. The W decays leptonically to a lepton (anti-lepton) and anti-neutrino (neutrino) as shown in Figure 4.2.

The $t\bar{t}$ background which was observed to be the dominant background in the previous analysis [24], is a well modelled background and therefore can be suppressed when designing the signal region is expected to have some contributions in this analysis as well. This is because, in $t\bar{t}$ events, the top quarks decay into bottom quarks and W bosons. One of these W bosons decay leptonically as in single-top background and the other hadronically. Some background contribution is also expected from the W +jets events. No contributions is expected from Z +jets process as a Z boson would decay to a lepton and anti-lepton pair or a neutrino and anti-neutrino pair thus not meeting the one-lepton criteria of our signal process. However, contributions from $t\bar{t} + Z$ processes are expected if the Z boson here decays invisibly and the the tops decay each to a bottom quark and W boson, out of which one W boson decays leptonically and the other hadronically.

4.1.2 Previous $tb + E_T^{\text{miss}}$ Run 2 Analysis at 36.1 fb^{-1}

This analysis had been originally based on a paper summarising ATLAS Run 1 searches for direct pair production of third-generation squarks at the Large Hadron Collider [154] and optimised for $\tilde{t} \tilde{t}^* \text{ or } \tilde{b} \tilde{b}^* \rightarrow \tilde{b} \tilde{\chi}_1^\pm + \tilde{t} \tilde{\chi}_1^0$ asymmetric decay using Run 1 and Run 2 data at 20 fb^{-1} and 36.1 fb^{-1} , respectively. For both searches the mass difference between the $\tilde{\chi}_1^\pm$ and $\tilde{\chi}_1^0$ is taken to be very small and the $\tilde{\chi}_1^\pm$ decays as $\tilde{\chi}_1^\pm \rightarrow W^* + \tilde{\chi}_1^0$.

The mass difference between the $\tilde{\chi}_1^\pm$ and $\tilde{\chi}_1^0$ was taken to be 5 GeV and 20 GeV for the search performed with 20 fb^{-1} of Run 1 data. From this search, \tilde{t} masses upto 560 GeV were excluded for $\tilde{\chi}_1^0$ masses of 110 GeV [155]. The $tb + E_T^{\text{miss}}$ final state was investigated

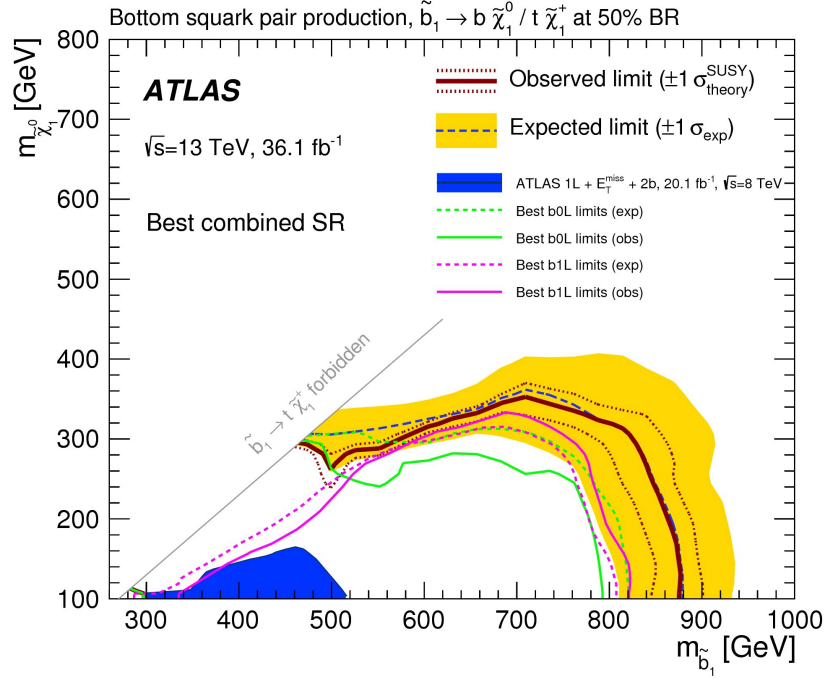


Figure 4.3: Observed and expected exclusion contours at 95% CL, along with the $\pm 1\sigma$ variation of the expected limit, in the $\tilde{b}_1 - \tilde{\chi}_1^0$ mass plane in combination with another SUSY search with pair-produced bottom quarks and E_T^{miss} [24]. The pink line denoting b1L-SRs is of interest for this full ATLAS Run 2 data set $tb + E_T^{\text{miss}}$ analysis for motivation as well as comparison.

again with the combined 2015 and 2016 Run 2 data of 36.1 fb^{-1} with a chosen mass difference of 1 GeV between the $\tilde{\chi}_1^\pm$ and $\tilde{\chi}_1^0$. This 1 GeV mass difference is also chosen for the full Run 2 analysis described in this section and is further explained in Section 4.1.3.

The analysis had been designed to be statistically combined with the $bb + E_T^{\text{miss}}$ analysis performed in 2016. The statistical combination of the analysis provides exclusion up to larger \tilde{t} or \tilde{b} masses. As seen from Figure 4.3, the combined exclusion excludes \tilde{t} or \tilde{b} masses up to 880 GeV for $\tilde{\chi}_1^0$ mass of 110 GeV, while the pink contour in the plot showing the 1-lepton observed limits, excludes \tilde{t} or \tilde{b} masses up to 820 GeV for the same $\tilde{\chi}_1^0$ mass [24].

4.1.3 Signal grid and kinematic studies

I conducted signal kinematic studies to optimise the sensitivity to these mixed-decay processes where one leg decays as $\tilde{t}/\tilde{b} \rightarrow t + \tilde{\chi}_1^0$ and the other as $\tilde{t}/\tilde{b} \rightarrow b + \tilde{\chi}_1^\pm$, where the $\tilde{\chi}_1^\pm$ subsequently decaying as $\tilde{\chi}_1^\pm \rightarrow W^* + \tilde{\chi}_1^0$.

Five MC generated samples using MadGraph with same \tilde{t} and $\tilde{\chi}_1^0$ masses and five different $\Delta m(\tilde{\chi}_1^0, \tilde{\chi}_1^\pm) = \{1, 5, 10, 20, 100\}$ GeV were produced to check effect of the different mass differences and the implementation of the off shell W decay. When the mass difference is 100 GeV, the W boson is on-shell and the generation of on-shell events is more likely

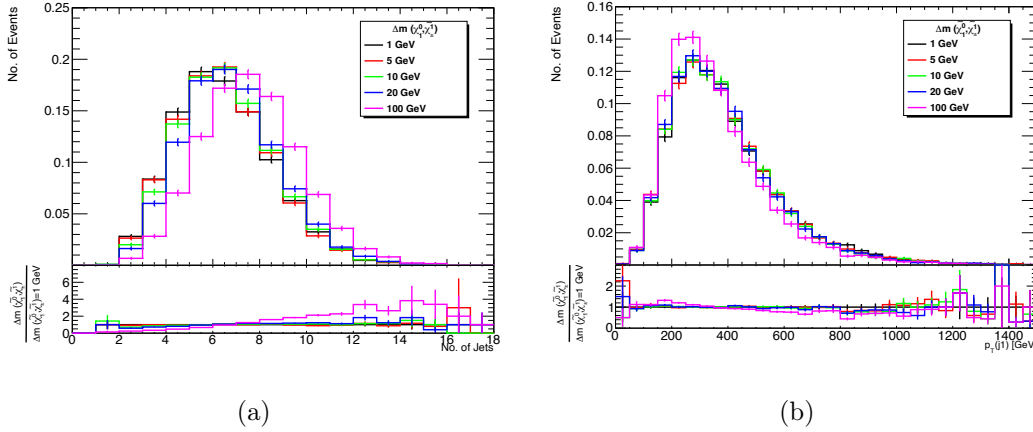


Figure 4.4: No. of jets vs. number of events (a) and leading jet p_T (b) for $m_{\tilde{t}} 900$ GeV and $m_{\tilde{\chi}_1^0} 400$ GeV.

with higher numbers of jets. From the Figure 4.4a, it is observed that for lower mass differences, the off-shell W decay generally has events with a lower number of jets, when compared to the on-shell decay with a mass difference of 100 GeV, suggesting the off-shell decay is working as expected. Additionally, as shown in Figure 4.4b, the jets originating from off-shell decays exhibit higher p_T , which aligns with expectations because in case of the 100 GeV mass difference, the generation of an on-shell W boson leaves lesser energy in comparison to the smaller mass difference scenarios for the associated jets. It is also seen that the histograms representing the small mass differences all fall within their respective statistical uncertainties. So, as long as the chosen mass difference is small, which ensures that the W-boson mass is off-shell, the kinematics remain unaffected. Thus, to maintain consistency with the previous iteration of the analysis and to keep the W boson off-shell, the chosen mass difference is $\Delta m(\tilde{\chi}_1^0, \tilde{\chi}_1^\pm) = 1$ GeV.

Next, the top quark decay distribution for all the \tilde{t} and $\tilde{\chi}_1^0$ signal points was plotted for verification, and as expected figure 4.6a shows that there is maximum number of events with 1 top quark i.e. $tb + E_T^{\text{miss}}$ events as the $BR = 0.5$. The number of events are distributed as per the set BR where 50% of the total events produced are $tb + E_T^{\text{miss}}$ events along with equal number of $bb + E_T^{\text{miss}}$ events and $tt + E_T^{\text{miss}}$ events which constitute 25% of the total events individually.

A E_T^{miss} characterisation of all the signal points were performed to check if E_T^{miss} cuts were required for any of the signal points. It was seen that for signal points where $\Delta m(\tilde{t}, \tilde{\chi}_1^0) < 300$ GeV which is the compressed region of the analysis, an E_T^{miss} filter is required as an E_T^{miss} trigger is used in the analysis. This E_T^{miss} characterisation pre- and post-application of the E_T^{miss} filter is shown in Figure 4.7. The efficiency of E_T^{miss} trigger is $\sim 100\%$ around $E_T^{\text{miss}} > 230$ GeV as shown in Figure 4.5. In the case of these signal points located in the compressed region, an E_T^{miss} filter with a threshold of 150 GeV is implemented. This filter guarantees that events with E_T^{miss} values close to the applied threshold are not excluded during the calculation of systematics.

Applying the E_T^{miss} filter affects the branching ratio of each of the decay modes and changes it from the desired $BR_{tb + E_T^{\text{miss}}} = 0.5$ and $BR_{bb + E_T^{\text{miss}}} = BR_{tt + E_T^{\text{miss}}} = 0.25$ as seen in Figure 4.6. The signal points that are generated without the E_T^{miss} filter, the BR

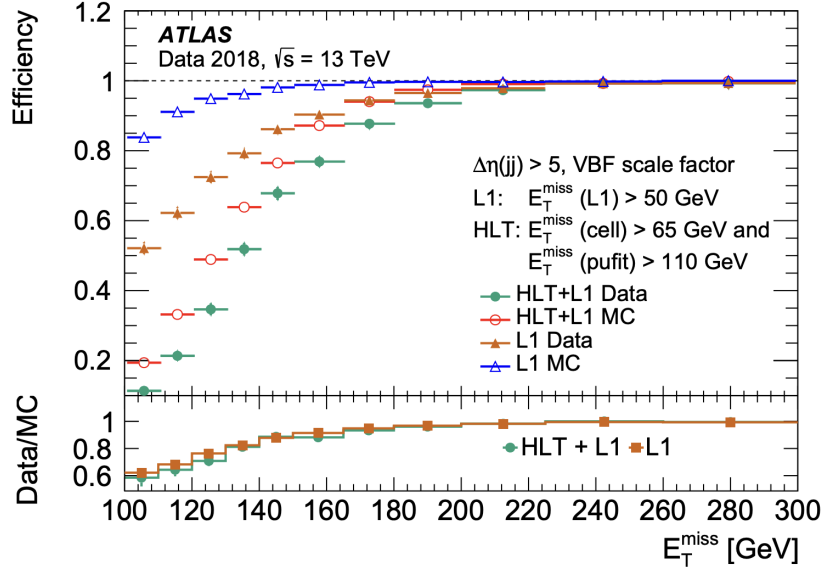


Figure 4.5: Performance of the missing transverse momentum triggers for the ATLAS detector during Run-2 data taking [156]. It is seen that the E_T^{miss} trigger efficiency is 100% at $E_T^{\text{miss}} > 230$ GeV.

is rescaled using Equation (4.1). Here, the desired branching ratio of $BR_{\tilde{t}/\tilde{b} \rightarrow b + \tilde{\chi}_1^\pm} = 0.5$ and $BR_{\tilde{t}/\tilde{b} \rightarrow t + \tilde{\chi}_1^0} = 0.5$ in the ideal scenario.

$$N_{\text{TOTAL}} = \frac{BR_{\tilde{t}/\tilde{b} \rightarrow b + \tilde{\chi}_1^\pm}^2 N_{bb}}{BR_{\tilde{t}/\tilde{b} \rightarrow b + \tilde{\chi}_1^\pm}^2} + \frac{BR_{\tilde{t}/\tilde{b} \rightarrow b + \tilde{\chi}_1^\pm} BR_{\tilde{t}/\tilde{b} \rightarrow t + \tilde{\chi}_1^0} N_{tb}}{BR_{\tilde{t}/\tilde{b} \rightarrow t + \tilde{\chi}_1^0} BR_{\tilde{t}/\tilde{b} \rightarrow b + \tilde{\chi}_1^\pm}} + \frac{BR_{\tilde{t}/\tilde{b} \rightarrow t + \tilde{\chi}_1^0}^2 N_{tt}}{BR_{\tilde{t}/\tilde{b} \rightarrow t + \tilde{\chi}_1^0}^2} \quad (4.1)$$

In case of the signal points with E_T^{miss} filter applied where the generated events for each of the three decay modes is not as desired, the Equation (4.1) can be modified as in Equation (4.2) to include rescaling factors $R_{bb} = \frac{N_{bb}}{N_{bb}(\text{filter})}$, $R_{tb} = \frac{N_{tb}}{N_{tb}(\text{filter})}$ and $R_{tt} = \frac{N_{tt}}{N_{tt}(\text{filter})}$.

$$N_{\text{TOTAL}} = R_{bb} \frac{BR_{\tilde{t}/\tilde{b} \rightarrow b + \tilde{\chi}_1^\pm}^2 N_{bb}}{BR_{\tilde{t}/\tilde{b} \rightarrow b + \tilde{\chi}_1^\pm}^2} + R_{tb} \frac{BR_{\tilde{t}/\tilde{b} \rightarrow b + \tilde{\chi}_1^\pm} BR_{\tilde{t}/\tilde{b} \rightarrow t + \tilde{\chi}_1^0} N_{tb}}{BR_{\tilde{t}/\tilde{b} \rightarrow t + \tilde{\chi}_1^0} BR_{\tilde{t}/\tilde{b} \rightarrow b + \tilde{\chi}_1^\pm}} + R_{tt} \frac{BR_{\tilde{t}/\tilde{b} \rightarrow t + \tilde{\chi}_1^0}^2 N_{tt}}{BR_{\tilde{t}/\tilde{b} \rightarrow t + \tilde{\chi}_1^0}^2} \quad (4.2)$$

After generation of the signal points, further validation of these points were done by plotting the leading jet p_T distribution shown in Figure 4.8. This distribution is observed to be continuous as expected with events in the compressed region signal point having the lowest leading jet p_T distribution.

To check if the produced samples were as expected, each of the mass points of the $tb + E_T^{\text{miss}}$ signal grid have been validated and the number of events in all these plots shown in Figures 4.4, 4.6, 4.7 and 4.8 have been normalised to 1.

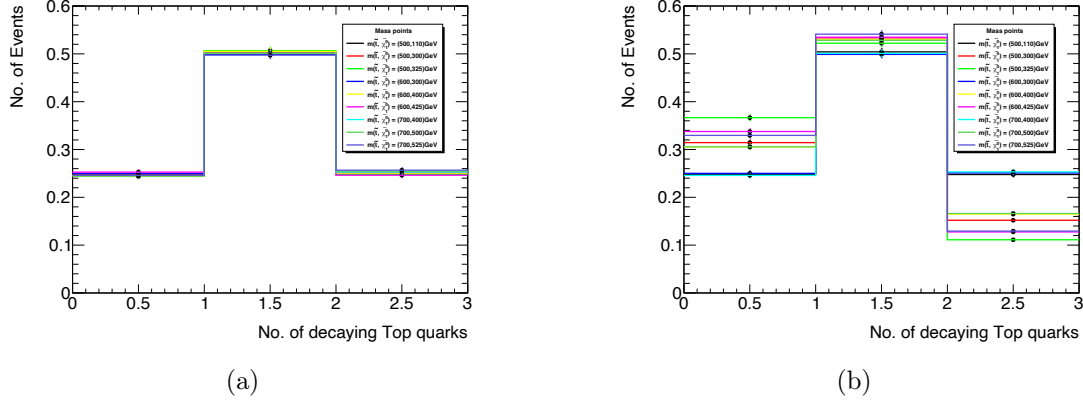


Figure 4.6: The Top quark decay distribution for some of the signal points. On the left hand side, the top quark decay distribution before application of the MET filter of 150 GeV and on the right hand side the top quark decay distribution after application of the E_T^{miss} filter. As the BR is set to 50% for $t\bar{b}+E_T^{\text{miss}}$ events, it is expected that events decaying to 1 top quark is 0.5 while to 2 and 0 top quarks is 0.25 as seen before application of the E_T^{miss} filter as the plots have been scaled to unity. Applying the E_T^{miss} filter for signal points that have a $\Delta m(\tilde{t}, \tilde{\chi}_1^0) < 300$ GeV, causes the BR of some of the $t\bar{t}+E_T^{\text{miss}}$ and $b\bar{b}+E_T^{\text{miss}}$ events to change and this re-weighting is corrected using equation (4.2).

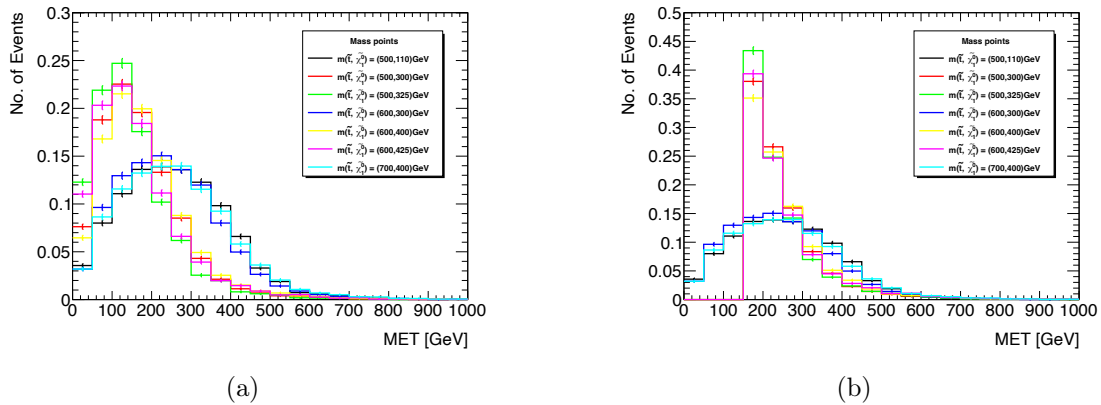


Figure 4.7: Some of the signal points without applying the E_T^{miss} (MET) filter of 150 GeV (a) and after applying the E_T^{miss} filter (b).

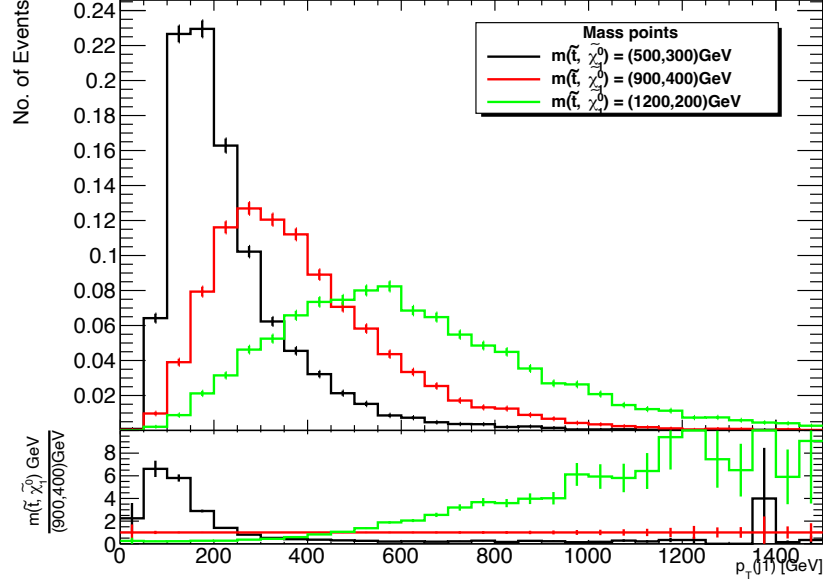


Figure 4.8: Leading Jet p_T of the representative points in compressed $m_{\tilde{t}} = 500$ GeV, $m_{\tilde{\chi}_1^0} = 300$ GeV, intermediate $m_{\tilde{t}} = 900$ GeV, $m_{\tilde{\chi}_1^0} = 400$ GeV and bulk $m_{\tilde{t}} = 1200$ GeV, $m_{\tilde{\chi}_1^0} = 200$ GeV regions.

The proposed $t\bar{b} + E_T^{\text{miss}}$ signal grid is shown in Figure 4.9. It has 1.59 million events per MC campaign and there are 3 such campaigns to have enough events for the analysis. The points along the diagonal is known as the compressed region with very small mass difference between \tilde{t} and $\tilde{\chi}_1^0$, the points with large mass difference between \tilde{t} and $\tilde{\chi}_1^0$ are known as the bulk region and the rest is known as the intermediate region. Figure 4.9a shows the proposed signal grid with the events generated per signal point. The number of events per signal point is chosen to ensure that the number of events at these points is not dominated by the statistical uncertainties.

The effective luminosity for a signal point is the ratio of number of events to be generated and the product of the cross-section of the \tilde{t} mass and filter efficiency for that signal point. Figure 4.9b shows the effective luminosity and Figure 4.9c shows the filter efficiency of each of the signal points. In case of all the points where the E_T^{miss} filter of 150 GeV is not applied, the filter efficiency is 1 as expected.

The SUSY cross-sections plot helped to decide the \tilde{t} mass upper limit. The cross-section for 1500 GeV and 1700 GeV is $0.257 \times 10^{-03} \pm 16.63\% \text{ pb}^{-1}$ and $0.796 \times 10^{-04} \pm 19.4\% \text{ pb}^{-1}$ respectively. Since number of expected events is a product of cross-section and integrated luminosity, for a \tilde{t} of mass of 1500 GeV and an integrated luminosity of 139 fb^{-1} , the approximate number of expected events is ~ 139 . In case of a \tilde{t} of mass of 1700 GeV and same integrated luminosity, the approximate number of expected events is 14. With an efficiency of a SUSY selection on the expected signal of about 20%, for a \tilde{t} mass of 1700 GeV the number of expected measured events that pass the selection is ~ 3 events. To achieve sufficient statistical significance and validate the analysis assumptions exclusions have to be made on the signal with more than 2 to 3 events. To this end, the \tilde{t} mass upper limit of 1500 GeV was decided upon.

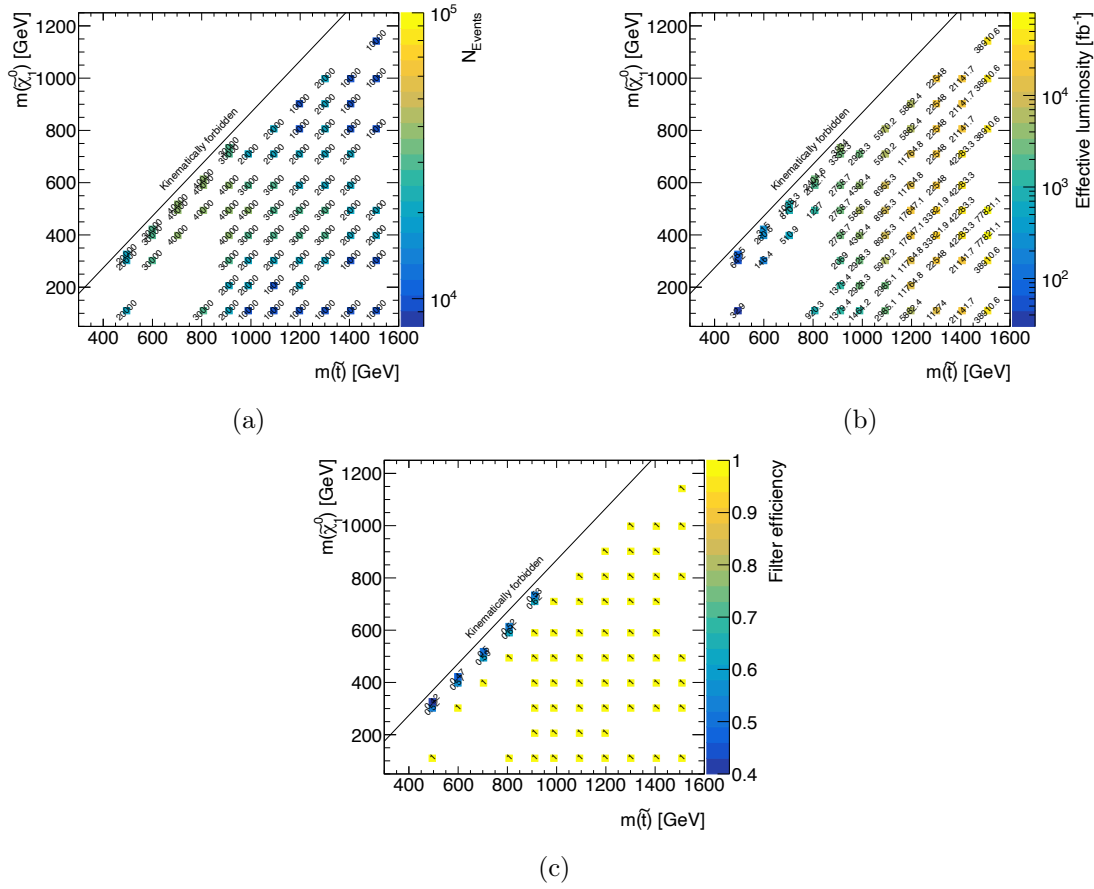


Figure 4.9: The signal grid with (a) the no. of events, (b) effective luminosity and (c) filter efficiency per signal point respectively. The total no. of events per MC campaign is 1.59M.

The other mass limits are taken based on the previous analysis. A lower limit of 500 GeV was placed on the \tilde{t} mass because the last analysis did not exclude the mass points around \tilde{t} mass of 500 GeV and $\tilde{\chi}_1^0$ mass ~ 350 GeV. Therefore this SUSY search should be sensitive to these points.

Furthermore, an upper limit of 1150 GeV was kept for the $\tilde{\chi}_1^0$ mass for 1200 GeV \tilde{t} mass onwards as there is a loss of sensitivity as the $\tilde{\chi}_1^0$ mass increases. This is due to the difference in kinematics of high $\tilde{\chi}_1^0$ and high \tilde{t} mass regions known as 'bulk and intermediate regions' to that of low $\tilde{\chi}_1^0$ and high \tilde{t} mass regions or the region where both the $\tilde{\chi}_1^0$ and \tilde{t} masses are similar i.e. along the diagonal known as 'compressed region'.

The final LEP exclusion ~ 102 GeV as shown in Figure 4.11 helped in setting the lower limit on the $\tilde{\chi}_1^\pm$ mass. The constraints placed by the LEP experiment on direct $\tilde{\chi}_1^\pm$ production provided the lower limit on the $\tilde{\chi}_1^\pm$ mass, chosen to be 110 GeV [158] taking into consideration both the final LEP exclusion limit and alignment with the earlier version of the analysis. This subsequently constrains the $\tilde{\chi}_1^0$ masses considered, based on the chosen mass splitting of 1 GeV.

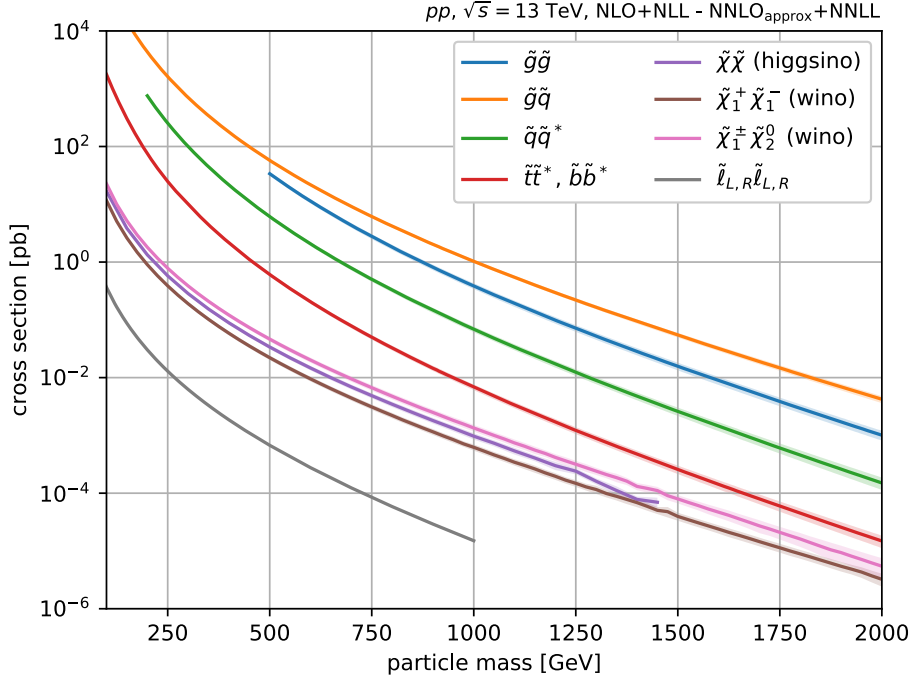


Figure 4.10: Plot illustrating the effect on cross-section of SUSY particles with increasing particle mass. It shows that with increasing particle mass, the cross-section decreases at a centre-of-mass energy of $\sqrt{s} = 13 \text{ TeV}$ [157].

4.2 Analysis Strategy

The analysis is divided into two kinematic regions - A and B. Region A consists of the signal points in the bulk and intermediate regions where $\Delta m(\tilde{t}, \tilde{\chi}_1^0) \geq 300 \text{ GeV}$ while Region B consists of the compressed region where $\Delta m(\tilde{t}, \tilde{\chi}_1^0) < 300 \text{ GeV}$ such that Δm is kinematically close to the mass of the top quark given $\tilde{t}/\bar{b} \rightarrow \tilde{\chi}_1^0 + b/t$ (see Figure 4.1).

A cut-and-count approach was used for this analysis using selections on physical variables to optimise and design the signal regions of this search. Furthermore, to enhance the sensitivity by combining with the $b\bar{b} + E_T^{\text{miss}}$ analysis which has 0-lepton regions, the regions in this analysis use 1-lepton selections to maintain orthogonality.

4.2.1 Data and simulated event samples

This analysis uses the full $\sqrt{s} = 13 \text{ TeV}$ Run 2 data, recorded between 2015 and 2018, with a total integrated luminosity of 139 fb^{-1} . Table 4.1 lists the SM backgrounds that are generated.

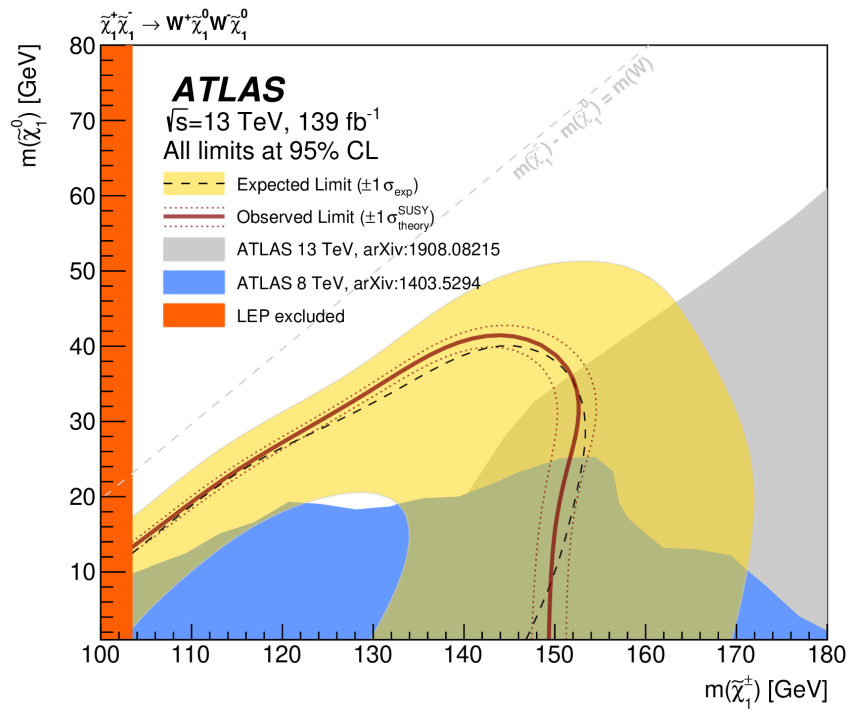


Figure 4.11: This plot has been taken from an ATLAS paper [159]. Constraints placed by LEP on direct $\tilde{\chi}_1^\pm$ production provide a chosen lower limit on the $\tilde{\chi}_1^\pm$ mass of 110 GeV, which in these scenarios also constrains the $\tilde{\chi}_1^0$ masses considered, dependent upon the mass splitting chosen as shown in the above plots.

Table 4.1: Overview of the nominal simulated background samples.

Process	Event generator
Z	Sherpa_221_NNPDF30NNLO [160, 161]
W	Sherpa_221_NNPDF30NNLO [160, 161]
single top	PowhegPythia8EvtGen_A14 [162], PhHerwig7EG_H7UE,aMcAtNloPythia8EvtGen_A14 [163]
$t\bar{t}$	PhPy8EG_A14 [162, 164]
diboson	Sherpa_222_NNPDF30NNLO, Sherpa_221_NNPDF30NNLO [160, 161]
$t\bar{t}Z$	aMcAtNloPythia8EvtGen_MEN30NLO_A14N23LO [165]
$t\bar{t}W$	aMcAtNloPythia8EvtGen_MEN30NLO_A14N23LO [165]
tZ	MadGraphPythia8EvtGen_A14
$t\bar{t}H$	PhPy8EG_A14NNPDF23_NNPDF30ME, PowhegPy8EG_A14NNPDF23_NNPDF30ME [166]

4.2.2 Event reconstruction

This search for pair production of \tilde{t} squarks is based on selections of events with two b-jets and large missing transverse momentum, with exactly one charged lepton in the final state. So the main physics objects used in this analysis are light leptons consisting of electrons, muons, jets and reconstructed E_T^{miss} . The light leptons and jets are known as "baseline" objects as selections on these objects or variables are required to satisfy the preliminary requirements which are then further processed using an "overlap removal" (OR) technique to prevent potential overlaps between these reconstructed objects.

Jets

Jet objects are reconstructed from three-dimensional energy clusters in the calorimeters using the anti- k_t jet algorithm with a radius parameter R of 0.4 [91] and clustered particle flow objects (PFO) [90]. These jets have to meet certain criteria to isolate jets from jets arising from non-collision sources or detector noise and any event containing such jets are then removed. These jets are categorised as "baseline" when these jets have a $p_T > 20$ GeV and $|\eta| < 2.8$. Other pile-up jets that arise from hard scatter, is removed using the Jet Vertex Tagger (JVT) [167]. If the jet has $JVT > 0.5$ or it has $p_T > 60$ GeV or $|\eta| > 2.4$, the jet is kept. Then the OR is applied to be further categorised as "signal" jets.

B-tagged Jets

Baseline jets are categorised as b-tagged using a multivariate algorithm [103] that utilises information about the impact parameters of inner detector tracks associated with the jets. This algorithm also takes into account secondary displaced vertices and the reconstructed flight paths of b-hadrons within the jet to determine the likelihood of the jet originating from a b-quark. For this analysis the jets are labelled as b-jets if they pass the "standard" 77% efficiency working point with $p_T > 20$ GeV, $|\eta| < 2.5$ and satisfy the standard JVT requirements as described before.

Light Leptons - electrons and muons

Electrons, muons and their respective antiparticles constitute light leptons. The electron candidates are reconstructed using the energy clusters in the electromagnetic calorimeter which are matched to a track in the inner detector (ID) and are required to satisfy a set of quality criteria termed as "loose" [168–170]. These candidates are termed "baseline" when along with the quality criteria, they satisfy the conditions $p_T > 10$ GeV, $|\eta| < 2.47$ and longitudinal impact parameter $z_0 \sin(\theta) < 0.5$ mm. These baseline electrons are used

to perform the lepton-jet overlap removal and in the lepton veto in the signal region.

Baseline muon candidates are similarly identified from ID tracks by matching with the Muon Spectrometer (MS) track. These candidates have to meet the requirements of $p_T > 10$ GeV, $|\eta| < 2.7$ and have $z_0 \sin(\theta) < 0.5$ mm [171].

These remaining baseline lepton candidates after performing overlap removal (described later) with baseline jets are used to define "signal" leptons. The signal electrons are required to satisfy "tight" quality criteria [172]. Further, to be classified as "signal" leptons, these leptons are matched to the primary vertex by requiring the transverse impact parameter $d_0/\sigma(d_0) < 5$ for electrons and $d_0/\sigma(d_0) < 3$ for muons [84, 171, 172].

Overlap Removal

A b -aware overlap removal (OR) is applied to these reconstructed baseline physics objects - the light leptons and jets defined above in order to avoid that reconstructed objects are double counted as two different physics objects. The procedure follows the "heavy flavour" overlap removal (OR) recommendation [172] and the sequence to resolve these overlapping physics objects are:

- If two electrons share a track then the object with lower p_T is rejected
- If a muon and an electron share their ID track then electron is rejected, unless the muon is a calo-muon, then the muon is rejected
- If a jet and an electron are within $\Delta R = \sqrt{\eta^2 + \phi^2} < 0.2$ and the jet is not a b -jet then the jet is removed
- If a jet and an electron are within $\Delta R < 0.4$ then the electron is removed
- If a jet and a muon are within $\Delta R < 0.2$ or the muon track is ghost associated to the jet then the jet is removed if it's number of tracks is lower than 3 and is the jet is not a b -jet.
- If a muon and a jet are within $\Delta R < 0.4$ then the muon is rejected.

Along with the OR technique, multiplicative scale factors are applied to simulated MC events to take into account the differences between data and simulation for reconstruction, identification and isolation efficiencies, and for the jet momentum scales and energy resolutions. Similar corrections are also applied to the probability of mis-tagging jets originating from the hard proton-proton scattering as pile-up jets with the Jet Vertex Tagger (JVT) discriminant which is described later in the chapter.

E_T^{miss}

E_T^{miss} is defined as the negative vector sum of the p_T of all the selected and calibrated physics objects i.e. the electrons, muons and jets in an event coming from the hard-scatter (HS) vertex and an extra soft term which comprises of all the detector signals associated to the HS but not with any of the pre-defined physics objects [173] as described also previously in Section 2.4.6. This soft term is calculated from inner detector tracks with p_T above 0.4 GeV matched to the primary vertex to make it more resistant to contamination from pile-up in comparison to the calorimeter based equivalent. The full E_T^{miss} calculation using the reconstructed objects is shown in Equation (2.15).

The default "Tight" working point is used for the E_T^{miss} reconstruction [172]. This applies extra restrictions on the jets entering the calculation. On top of the meeting the requirements for signal jets there is a transverse momentum condition of $p_T > 30$ GeV applied in the range $2.4 < |\eta| < 4.5$. A condition of $JVT > 0.5$ is also applied to jet with $p_T < 60$ GeV and $|\eta| < 2.4$. Tau and photon contributions are not included to the E_T^{miss} calculation, because they are not expected for the signal models targeted in this analysis.

Triggers

Two types of triggers are used for this analysis. E_T^{miss} (HLT- E_T^{miss} -triggers) trigger [174] is employed for all the regions with 1ℓ events and the single lepton trigger is employed for the 3ℓ control region of one of the dominant $t\bar{t}Z$ backgrounds where the pair of ℓ are used to mimic the E_T^{miss} from $t\bar{t}Z$ with an invisibly decaying Z boson.

Inferred from previous ATLAS analyses and studies conducted while constructing the signal grid and signal regions, a E_T^{miss} threshold > 250 GeV and a p_T threshold > 27 GeV for the leading- p_T leptons is used to ensure full trigger efficiency.

4.2.3 Discriminating variables

A set of discriminating variables are built from the kinematic quantities in order to define the signal regions and the corresponding control and validation regions. The purpose of these variables is to discriminate SUSY signature from the various SM background events in the signal region (SR) and to demonstrate effective modelling in the control (CRs) and validation regions (VRs).

The variables used in for this analysis are described below:

- **H_T [GeV]:** is defined as the scalar sum of the p_T of all the signal jets in an event. For SUSY signals with high p_T jets, the H_T variable is expected to peak at a larger value than the SM backgrounds.

$$H_T = \sum_i p_{T,i}. \quad (4.3)$$

- **Effective Mass [GeV]:** is defined as the scalar sum of the p_T of the leading n jets in an events which is the H_T variable and the E_T^{miss} as shown in the equation below.

$$m_{\text{eff}} = \sum_{i \leq n} (p_T^{\text{jet}})_i + E_T^{\text{miss}} = H_T + E_T^{\text{miss}}. \quad (4.4)$$

For this variable too, a selection on large values of m_{eff} improves the SUSY signal to SM background ratio.

- **Object Based E_T^{miss} Significance:** The E_T^{miss} significance is used to quantify E_T^{miss} contribution to the total hadronic activity in an event. For SUSY signals, the E_T^{miss} and H_T are expected to be very large and therefore E_T^{miss} significance is also expected to be very large. Furthermore, m_{eff} and E_T^{miss} significance are correlated as they are constructed using the E_T^{miss} and H_T variables. Selections on

the E_T^{miss} significance variable effectively reduces the multi-jet contributions with fake E_T^{miss} . The Object Based E_T^{miss} Significance is the dimensionless definition of the E_T^{miss} significance which encodes the resolution of each object involved in the calculation as shown in Equation (4.5), where σ_L is the longitudinal variance of the missing momentum vector and ρ_{LT} represents the covariance between longitudinal and transverse measurements..

$$\mathcal{S} = \frac{E_T^{\text{miss}}}{\sqrt{\sigma_L^2 (1 - \rho_{LT}^2)}} \quad (4.5)$$

- **$m_{\ell\ell}$** : the invariant mass of two leptons.
- **Transverse Mass**: is defined as shown in the following Equation (4.6).

$$m_T = \sqrt{2(p_T(l)E_T^{\text{miss}} - \vec{p}_T(l) \cdot \vec{E}_T^{\text{miss}})} \quad (4.6)$$

This variable is used to reconstruct the mass of a particle which decays to a particle that is detectable, for e.g. a lepton and to an undetectable particle. This variable is used in 1ℓ signal and control regions to suppress the $W + \text{jets}$ and $t\bar{t}$ backgrounds. The m_T for a W boson decay is calculated to be equal to the mass of the W boson m_W with the E_T^{miss} coming from the neutrino in the decay process. In SUSY scenarios, the E_T^{miss} contribution arises from neutralinos in the event by selecting $m_T > 90 - 120$ GeV.

- **$m_{T_j}^{\min}(\text{jet}_{1-4}, E_T^{\text{miss}})$** : is defined as the minimum transverse mass of the jets in an event and E_T^{miss} . This variable is used to reduce the $t\bar{t}$ backgrounds by selecting $m_{T_j}^{\min}(\text{jet}_{1-4}, E_T^{\text{miss}}) > 150$ GeV.
- **$m_{T_b}^{\min}(b\text{-jet}_{1-2}, E_T^{\text{miss}})$** : is defined as the minimum transverse mass of the b -jets in an event and E_T^{miss} .
- **$\Delta\phi^{\min}(\text{jet}_{1-4}, E_T^{\text{miss}})$** : is defined as the minimum $\Delta\phi$ between any of the four leading jets and the missing transverse momentum vector. Angular selections between E_T^{miss} and jets help in reducing the mis-measured QCD multi-jet backgrounds.
- **$m_{b\ell}^{\min}$** : the minimum invariant mass between the lepton and one of the two b -jets is defined as follows.

$$m_{b\ell}^{\min} = \min_{i=1,2} (m_{\ell b_i}) \quad (4.7)$$

$m_{b\ell}^{\min}$ is constrained by the top quark mass. Then the lepton and b -jet under consideration would be compatible with $t\bar{t}$ production and can be used to distinguish $t\bar{t}$ from single-top quarks coming from Wt - channel in 1ℓ regions.

- **N_{jet}** : the number of jets or "jet multiplicity" in an event.
- **$N_{b\text{-jet}}$** : the number of b -jets in an event or, " b -jet multiplicity".
- **N_{lep}** : the number of leptons in an event or, this can be the number of baseline or signal leptons and is marked accordingly.

- $\vec{p}_T(j_i)$: The transverse momentum of the i^{th} jet in the event.
- $\vec{p}_T(\ell_i)$: The transverse momentum of the i^{th} lepton in the event.
- **Asymmetric Transverse Mass, am_{T2}** : The am_{T2} [175, 176] is a specialisation of the m_T variable that reconstructs the masses of semi-invisibly decaying particles where both legs of the decay channels are not composed of the same particles.

In this analysis, the am_{T2} variable is used to reject the $t\bar{t}$ backgrounds where one of the top quark decays semi-leptonically. For the $t\bar{t}$ process, am_{T2} can be calculated as a function of 5 parameters. In a 1ℓ scenario, the visible particles in the $t\bar{t}$ decay consist of the two b -quarks or b -jets (b_1, b_2) and a light lepton (ℓ). This reduces the number of mass parameters involved by 1 because of the conventional m_T calculation where the lepton's mass is disregarded. As such, one invisible particle is involved in the decay process, specifically the neutrino arising from the leptonic decay of the W -boson. Consequently, the masses of the invisible particle is set to 0. So, in the case of the $t\bar{t}$, the am_{T2} function can be obtained from the following equation:

$$am_{T2} = am_{T2}(m_b, \vec{p}_T(b_1), \vec{p}_T(b_2), \vec{p}_T(\ell), \vec{p}_T^{\text{miss}}). \quad (4.8)$$

Also the above described $m_{b\ell}^{\text{min}}$ variable needs to be considered in this 1ℓ scenario when reconstructing the am_{T2} . The lepton in the top quark decay can be paired with either of the b -jets for this calculation and am_{T2} is calculated based on the following scenarios:

- If the $m_{b_1\ell}$ and $m_{b_2\ell}$ computed for both legs of the decay is > 170 GeV, neither of the two associated lepton and b -jet is compatible with the lepton and b -jet originating from a top decay, so the event is rejected and the am_{T2} is set to the overflow value as every control, validation and signal region requires $m_{b\ell} < 170$ GeV to suppress SM $t\bar{t}$ events.
- If one of the $m_{b_1\ell} < 170$ GeV and the other is $m_{b_2\ell} > 170$ GeV, then the am_{T2} is reconstructed using the the first b -jet (b_1).
- If one of the $m_{b_1\ell} > 170$ GeV and the other is $m_{b_2\ell} < 170$ GeV, then the am_{T2} is reconstructed using the the second b -jet (b_2).
- If the $m_{b_1\ell}$ and $m_{b_2\ell}$ are both < 170 GeV, the am_{T2} is calculated using both the b -jets as both $m_{b_1\ell}$ and $m_{b_2\ell}$ are compatible with the b -jet and lepton coming from a top quark decay.
- $m_{T2}^{\ell\ell}$: is the lepton-based stransverse mass which is constructed in the same way as am_{T2} , but assumes that both heavy particles decayed into a lepton and an invisible particle.
- $\Delta\phi_{\text{boost}}$: is the angle between E_T^{miss} and E_T^{miss}/I , which describes the azimuthal angle between the \vec{p}_T^{miss} vector and the $\vec{p}_T^{\text{miss}}/I$ vector, which is the vectorial sum of \vec{p}_T^{miss} and the transverse momenta vectors of the two leptons, $\vec{p}_T(\ell_1)$ and $\vec{p}_T(\ell_2)$ (also called lepton-corrected \vec{p}_T^{miss})

Therefore a selection of $am_{T2} > 175 \text{ GeV} \sim m_t$ is used to suppress the $t\bar{t}$ background and the signal to background ratio increases at higher values of am_{T2} .

4.2.4 Region definitions

This $t\bar{b} + E_T^{\text{miss}}$ search employs a general strategy of defining signal, control and validation regions using the kinematic variables defined above. The signal Regions (SRs) are defined based upon kinematic differences between SUSY signal and SM background. The SRs are optimised to maximise the discovery or exclusion significance for the SUSY model. The control regions (CRs) are defined to constrain the SM backgrounds in the SRs. The CRs are kinematically close but orthogonal to the SRs and are designed to contain events with only the specific background process considered as much as possible. The validation regions (VRs) are defined to validate the backgrounds in the SRs. And all these regions are orthogonal to each other.

Before defining a SR, a preliminary set of selections are made on the variables referred to as "Preselections" are applied such that they take the kinematics of the signal topology for the compressed, intermediate and bulk regions of the signal grid into consideration. These preselections are employed for initial SUSY signal, SM backgrounds and data to MC agreement or modelling studies. These preselections aim to remove all the data that do not have the intended physics signature yet inclusive enough that appropriate control and validation regions can be constructed.

All the events are required to pass the LHC Run 2 Event Cleaning (2015 and 2016) [177]. Offline event cleaning is required to remove any poorly measured events which affects the data quality and removes backgrounds that do not arise from the collisions in the beamline such as beam halo, cosmic ray particles incident on the detector and random coherent energy spikes in the calorimeter. To pass the the event cleaning criteria each of these events have to have at least one primary vertex with two reconstructed tracks, with $p_T > 500$ MeV measured by the ID [178]. Jets that come from the aforementioned unwanted processes are called "fake jets" and those coming from pp collisions are "good jets". The "good jets" are selected and the "fake jets" are rejected as per the "LooseBad" criteria as defined in [95]. Only "good jets" with an efficiency greater than 99.5% for jets with $p_T > 20$ GeV are selected. Also, some of the events in the early Run 2 were flagged and rejected when they were observed to have large amounts of transverse energy, particularly in the $|\eta|$ ranges of the Liquid-Argon (LAr) calorimeter caused by saturation of the EM calorimeter endcap and indicated by the measurement of unusual pulse shapes. Cosmic muons and reconstructed muons that are identified from events satisfying the $|z_0| > 1$ mm or $|d_0| > 0.2$ mm conditions and have a large error ($> 20\%$) on the momentum and consequently introduces high values of E_T^{miss} respectively are rejected by applying event cleaning.

As mentioned before in Section 4.1.1, the SUSY signature consists of E_T^{miss} and a top and a bottom quark coming from an asymmetric decay of a \tilde{b}/\tilde{t} pair production. The top quark further decays into a second bottom quark and a leptonically decaying W boson, resulting in a final state with two bottom quarks, one lepton and E_T^{miss} . Due to this signal topology, the preselection requires events with 2 b -jets and 1 baseline and signal lepton (e, μ). Also a selection of $E_T^{\text{miss}} > 250$ GeV is applied in order to be in the trigger plateau. A selection is additionally applied on the $p_T(\ell) > 10$ GeV to meet the criteria for lepton candidates as explained in Section 4.2.2.

The preselections that are applied for all the regions in this analysis are listed in Table 4.2 and Figure 4.12 shows the signal, and background distributions of some variables at

preselection level using the full Run 2 data. The lower panels of the preselections plots show the agreement of the data to the MC generated events. In general the data and MC are in agreement except at higher values of $m_{b\ell}^{\text{min}}$ due to the constraints of MC modelling of this variable.

Table 4.2: Preselection requirements used as a baseline selection for all regions in the analysis

Selection Criteria	Value
Trigger selection	Passed single lepton or E_T^{miss} Trigger
E_T^{miss}	$\geq 250.0 \text{ GeV}$
$n_{b\text{-jets}}$	$= 2$
$n_{\text{lep}(e,\mu)}$ <i>baseline</i>	$= 1$
$n_{\text{lep}(e,\mu)}$ <i>signal</i>	$= 1$
$p_T(\text{lep})$	$\geq 10.0 \text{ GeV}$

Signal Region A definition

This chapter and the author's work was focused on the bulk region which is referred to as signal region A (SRA). This region is analysed using a conventional cut and count type method. The SRA, is built to be sensitive to $tb + E_T^{\text{miss}}$ signals where the mass splitting $\Delta m(\tilde{t}/\tilde{b}, \tilde{\chi}_1^0)$ is large.

The optimisation of the SRA follows a strategy that attempts to maximise the discovery significance as defined in Equation (4.9) from reference [179], where s and b are the number of expected signal and background events and σ_b is the uncertainty on the background events. The statistical significance Z can be calculated using Equation (4.9) which helps in optimising the sensitivity of the SRs to the $tb + E_T^{\text{miss}}$ signal.

$$Z = \left(2(s+b) \ln \left[\frac{(s+b)(b+\sigma_b^2)}{b^2 + (s+b)\sigma_b^2} \right] - \frac{b^2}{\sigma_b^2} \ln \left[1 + \frac{\sigma_b^2 s}{b(b+\sigma_b^2)} \right] \right)^{1/2} \quad (4.9)$$

SRA utilises the kinematic variables described in Section 4.2.3 to isolate the signals from the SM background. Figure 4.13 shows the distributions of the most important SRA selection variables before the selection is applied, known as *n-1 plot*, that helps in deciding 'cuts' placed on the kinematic variables such that the SM backgrounds are strongly suppressed.

The final SRA selections are summarised in Table 4.3.

The distribution of two variables from SRA are shown in Figure 4.14 along with the calculated significance. The good sensitivity to the bulk region signals and the number of predicted events or yield are summarised in Table 4.4. It is observed that the main background composition of SRA is single top, followed by $t\bar{t}Z$.

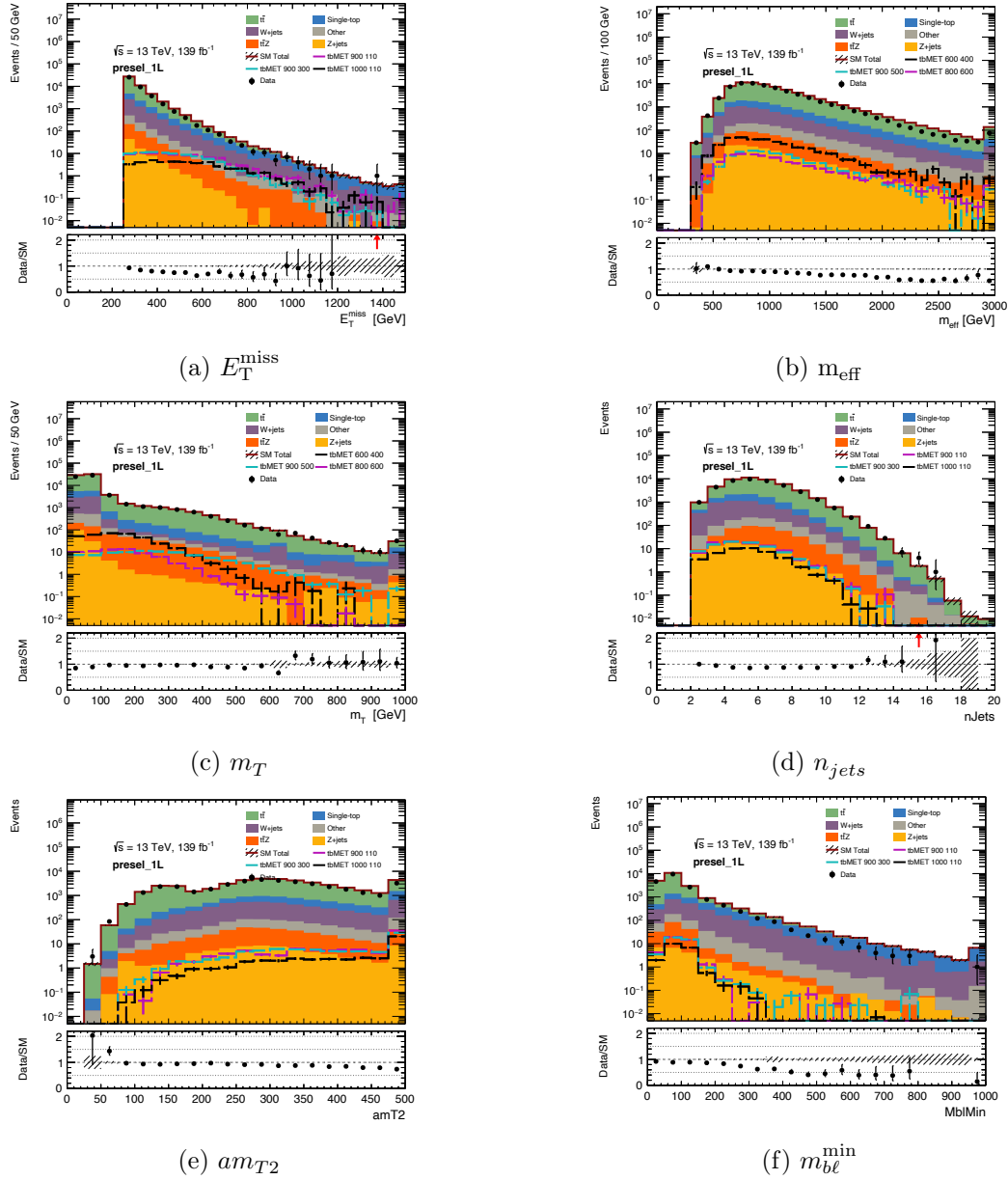


Figure 4.12: The preselection conditions from Table 4.2 are applied to plot all important variables used later on in this analysis. The E_T^{miss} , m_{eff} , m_T , the jet multiplicity, am_{T2} and m_{bl}^{min} have been shown here. The MC simulation is scaled to 139 fb^{-1} . The solid coloured histograms indicate the different SM background distributions with the hashed area representing the total statistical uncertainty. The lines show the distribution of three representative signal points. The lower panel displays the data over MC ratio for each bin. In general the data and MC are in agreement except at higher values of m_{bl}^{min} .

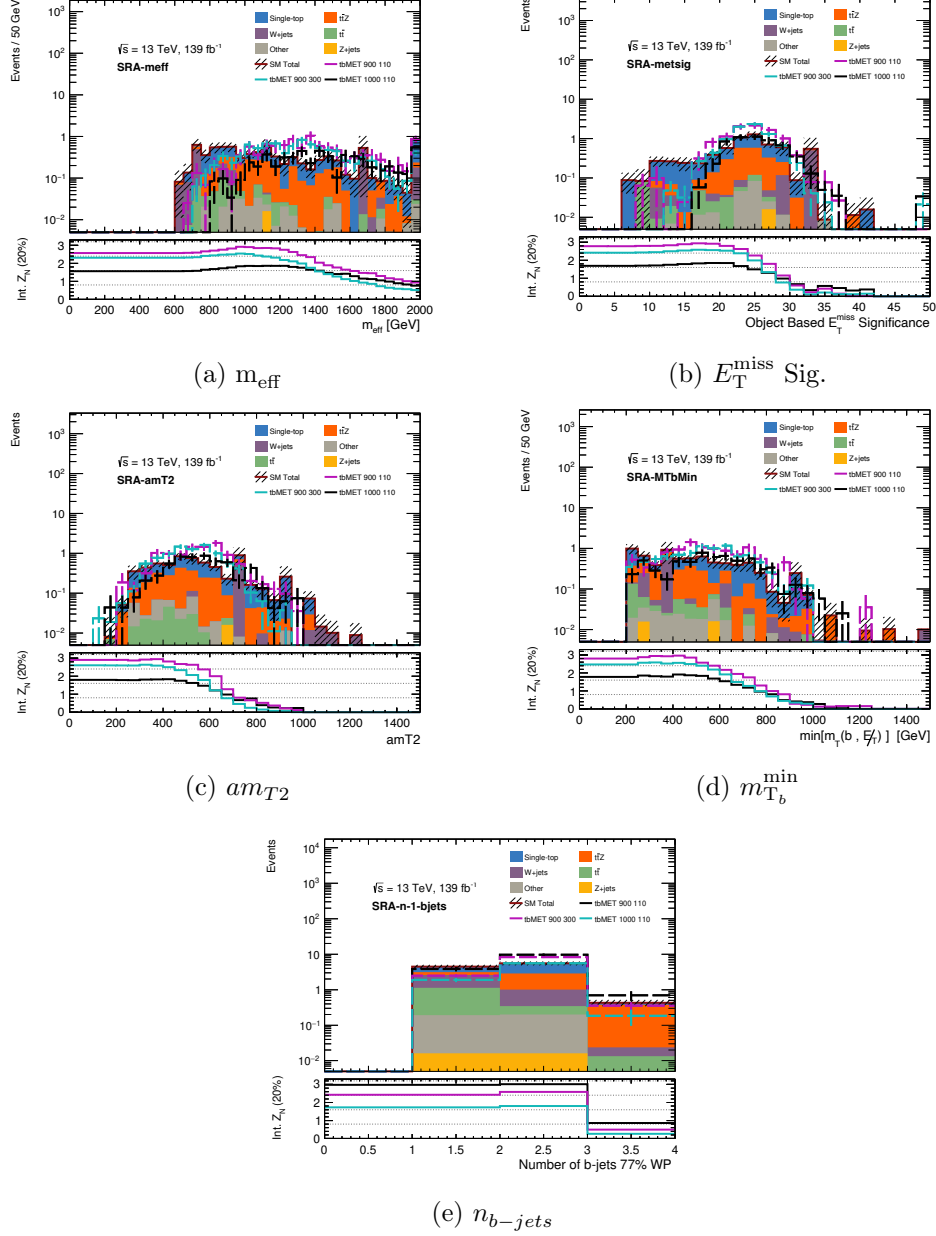


Figure 4.13: N-1 distributions for relevant variables in SRA motivating the chosen selections for the SRA. The variable plotted is the one removed from the SRA selections. The MC simulation is scaled to 139 fb^{-1} and a semi-log scale applied. The solid coloured histograms indicate the different SM background contributions. With the hashed area representing a total statistical uncertainty. The lines show the distributions from three different "representative" signal points. The lower panel displays the standard recommended ATLAS significance of each bin, Z_n , with a flat 20 % uncertainty applied.

Table 4.3: Definition of Signal Region A (SRA)

Selection	SRA
E_T^{miss} [GeV]	> 250.0
n_{lep} <i>baseline</i>	$== 1$
n_{lep} <i>signal</i>	$== 1$
$n_{\text{b-jets}}$	$== 2$
n_{jets} <i>signal</i>	≥ 2
leading- p_T jet	is b-tagged
$p_T(j_1)$ [GeV]	> 100.0
$p_T(j_2)$ [GeV]	> 100.0
$p_T(\ell_1)$ [GeV]	> 27.0
$\min[\Delta\phi(\text{jet}_{1-4}, E_T^{\text{miss}})]$	> 0.4
am_{T2} [GeV]	> 350.0
E_T^{miss} significance	> 16.0
H_T	> 300.0
$m_{T_j}^{\text{min}}$	> 200.0
m_{eff} [GeV]	> 1000.0
m_T [GeV]	> 200.0
m_{bl}^{min} [GeV]	< 170.0
$m_{T_b}^{\text{min}}$	> 300.0

Table 4.4: Composition of SRA, with both the SM background and three representative signal points for 139 fb^{-1} .

SRA	Yield
tbMET 900 110	9.71 ± 0.77
tbMET 900 300	8.31 ± 0.46
tbMET 1000 110	5.51 ± 0.44
Single-top	2.65 ± 0.37
$t\bar{t}Z$	1.86 ± 0.19
W+jets	0.67 ± 0.52
Other	0.18 ± 0.05
$t\bar{t}$	0.14 ± 0.04
Z+jets	0.02 ± 0.02
SM	5.52 ± 0.67

Table 4.5: Summary of CR selections for single top

Selection	CRA-st
E_T^{miss} [GeV]	> 250.0
n_{lep} <i>baseline</i>	$== 1$
n_{lep} <i>signal</i>	$== 1$
$n_{\text{b-jets}}$	$== 2$
n_{jets} <i>signal</i>	≥ 2
leading- p_T jet	is b-tagged
$p_T(j_1)$ [GeV]	> 100.0
$p_T(\ell_1)$ [GeV]	> 27.0
$\min[\Delta\phi(\text{jet}_{1-4}, E_T^{\text{miss}})]$	> 0.4
am_{T2} [GeV]	> 350.0
E_T^{miss} significance	$[13.0, 16.0]$
m_T [GeV]	> 90.0
m_{bl}^{min} [GeV]	< 170.0
$m_{T_b}^{\text{min}}$ [GeV]	> 200.0

Control Regions A definitions

The single top background which is the dominant background in SRA, is controlled using the selections listed in Table 4.5. The $m_{bl}^{\text{min}} < 170$ GeV is used as the modelling of the m_{bl}^{min} at higher values worsens and is not around 1. The $am_{T2} > 350$ GeV and $m_{T_b}^{\text{min}} > 200$ GeV selections helps in removing the $t\bar{t}$ background. Furthermore, the $m_T > 90.0$ GeV helps in removing $W + \text{jets}$. The selection on the E_T^{miss} significance between 13 and 16 not only aids in designing a pure single top CR (CRA-st) but also in maintaining the orthogonality of CRA-st to the SRA.

From the yields in Table 4.6 it is seen that the single top background has been well isolated and Figure 4.15 shows some of variables plotted in CRA-st. These distributions show the single top dominance and that the data to MC agreement is reasonable in this region.

The next dominant background in region A which is also observed in the compressed regions, is the $t\bar{t}Z$. To ensure a pure $t\bar{t}Z$ CR, a 3ℓ selection is applied and additionally a selection on the invariant mass between the two opposite sign and same flavour (OSSF) leptons is applied to target the Z -peak between 86.0 and 105.0 GeV. Also, the CR- $t\bar{t}Z$ uses the single-lepton trigger unlike the other 1ℓ regions discussed so far, which employ the E_T^{miss} -trigger [156]. Table 4.7 summarises the applied selections for the $t\bar{t}Z$ CR and Figure 4.16 shows that the $t\bar{t}Z$ background has been well isolated and the data to MC modelling is in agreement. The corresponding yields are reported Table 4.8.

Validation Region A definition

One validation region is defined for both single top and $t\bar{t}Z$ as summarised in Table 4.9. The designed VR has a similar SM background contribution in comparison to the SRA and motivates using these VR selections to validate the A Type fit particularly as it

Table 4.6: Data and Monte Carlo yields broken down by process in CRA-st for 139 fb^{-1} .

CRA-st	Yield
tbMET 900 110	1.18 ± 0.28
tbMET 900 300	1.13 ± 0.17
tbMET 1000 110	0.82 ± 0.17
Data	40.00 ± 6.32
Single-top	21.10 ± 1.09
$t\bar{t}$	11.42 ± 0.56
W+jets	8.05 ± 1.11
$t\bar{t}Z$	1.61 ± 0.20
Other	0.87 ± 0.13
Z+jets	0.23 ± 0.09
SM	43.28 ± 1.68
Data	40.00 ± 6.32

Table 4.7: Selections for $t\bar{t}Z$ control region.

Selection	CR- $t\bar{t}Z$
Trigger	1ℓ
n_{lep}	$==3$
n_{jets}	≥ 2
$n_{\text{b-jets}}$	$== 2$
$p_{\text{T}}(\ell_1) [\text{GeV}]$	27
$p_{\text{T}}(\ell_2) [\text{GeV}]$	10
$p_{\text{T}}(\ell_3) [\text{GeV}]$	10
$m_{\ell\ell} [\text{GeV}]$	[86,105]

Table 4.8: Data and Monte Carlo yields in $t\bar{t}Z$ control region for 139 fb^{-1} .

CR- $t\bar{t}Z$	Yield
tbMET 800 600	0.00 ± 0.00
tbMET 900 400	0.00 ± 0.00
tbMET 600 400	0.00 ± 0.00
Data	43.00 ± 6.56
$t\bar{t}Zq\bar{q}l$	30.64 ± 0.41
Other	9.65 ± 0.37
$t\bar{t}$	0.27 ± 0.12
Z+jets	0.13 ± 0.05
Single-top	0.01 ± 0.01
W+jets	0.00 ± 0.00
SM	40.70 ± 0.57
Data	43.00 ± 6.56

is very difficult to isolate the $t\bar{t}Z$ completely in a separate VR. The associated yield is tabularised in Table 4.10. Here the orthogonality with the signal and control regions of region A is maintained by requiring that the $am_{T2} < 350 \text{ GeV}$. Figure 4.17 shows that the two main backgrounds observed in SRA have been validated in the designed VR. Again it is seen that there is a good agreement in the yield of data and MC prediction with approximately half of the events coming from single top followed by $t\bar{t}$ and $t\bar{t}Z$.

Table 4.9: Summary of the selections that define VRA for the single top and $t\bar{t}Z$ background.

Selection	VRA-st
E_T^{miss} [GeV]	> 250.0
n_{lep} <i>baseline</i>	$== 1$
n_{lep} <i>signal</i>	$== 1$
$n_{b\text{-jets}}$	$== 2$
n_{jets} <i>signal</i>	≥ 2
leading- p_T jet	is b-tagged
$p_T(j_1)$ [GeV]	> 50.0
$p_T(\ell_1)$ [GeV]	> 27.0
$\min[\Delta\phi(\text{jet}_{1-4}, E_T^{\text{miss}})]$	> 0.4
am_{T2} [GeV]	< 350.0
m_T [GeV]	> 200.0
m_{bl}^{\min} [GeV]	< 170.0
m_{Tb}^{\min} [GeV]	> 270.0

Table 4.10: Data and Monte Carlo yields broken down by process in VRA-st for 139 fb^{-1} .

VRA-st	Yield
tbMET 900 300	8.11 ± 0.46
tbMET 900 110	7.55 ± 0.70
tbMET 1000 110	2.76 ± 0.31
Single-top	31.73 ± 1.91
$t\bar{t}$	15.63 ± 0.76
$t\bar{t}Z$	14.75 ± 0.57
Other	3.16 ± 0.21
W+jets	3.10 ± 0.72
Z+jets	0.26 ± 0.12
SM	68.62 ± 2.27
Data	65.00 ± 8.06

All the A regions maintain orthogonality with the B regions by requiring the leading jet to be a b -jet.

Signal Region B definition

The optimisation of the signal region B was performed by the $tb+E_T^{\text{miss}}$ analysis team and included in this thesis for completeness.

The SRB is tailored to encompass the "compressed" region, characterised by a small mass splitting of < 300 GeV between the mass of \tilde{t}/\tilde{b} and the $\tilde{\chi}_1^0$. Table 4.11 summarises the SRB selections and Figure 4.18 shows the effective mass and E_T^{miss} plotted for SRB. Also the background composition and the projected signal events in SRB are both summarised in Table 4.12. This yield table indicates a slightly higher number of expected events, both for signal and background, in SRB compared to SRA. However, the analysis's sensitivity to new physics remains robust, and notably, the composition of the dominant backgrounds is different to that of the SRA. The primary background source is attributed to $t\bar{t}Z$, followed by $t\bar{t}$ and single top events as seen in Table 4.12. As mentioned before, the $t\bar{t}Z$ background is shared between the two regions.

Table 4.11: Summary of the selections that define SRB along with the complimentary CR and VR for the $t\bar{t}$ background.

Selection	SRB	CRB-ttbar	VRB-ttbar
E_T^{miss} [GeV]	>400.0	>250.0	>250.0
n_{lep} <i>baseline</i>	$== 1$	$== 1$	$== 1$
n_{lep} <i>signal</i>	$== 1$	$== 1$	$== 1$
$n_{\text{b-jets}}$	$== 2$	$== 2$	$== 2$
n_{jets} <i>signal</i>	≥ 3	≥ 3	≥ 3
leading- p_T jet	not b-tagged	not b-tagged	not b-tagged
$p_T(j_1)$ [GeV]	> 200.0	> 200.0	> 200.0
$p_T(j_2)$ [GeV]	> 100.0	> 100.0	> 100.0
$p_T(\ell_1)$ [GeV]	> 10.0	> 10.0	> 10.0
$\min[\Delta\phi(\text{jet}_{1-4}, E_T^{\text{miss}})]$	> 0.4	> 0.4	> 0.4
am_{T2} [GeV]	> 280.0	> 280.0	> 280.0
E_T^{miss} significance	>15.0	≤ 15.0	≤ 15.0
m_{eff} [GeV]	>800.0	>800.0	>800.0
m_T [GeV]	> 150.0	[100,150]	> 150.0
m_{bl}^{min} [GeV]	< 170.0	< 170.0	< 170.0
$m_{T_b}^{\text{min}}$ [GeV]	>200.0	>120.0	>120.0

Control Regions B definitions

SRB has a high standard model contribution from $t\bar{t}$ processes, where the tops decay into b-quarks and W-bosons, of which one decays leptonically into one lepton and a neutrino, while the other decays hadronically. The selections for a dedicated $t\bar{t}$ CR are also summarised in Table 4.11, which require one lepton and similar kinematic variables as the SRB. The orthogonality to the SRB and VRB are ensured by choosing a window within the m_T variable. The CR- $t\bar{t}$ is shown in Figure 4.19 and the corresponding yields are reported in Table 4.13.

The $t\bar{t}Z$ CR selection is shared with region A and the relevant selections and yields are

Table 4.12: Composition of SRB with the expected SM backgrounds and three representative signal points.

SRB	Yield
tbMET 600 400	8.93 ± 1.45
tbMET 900 500	4.72 ± 0.41
tbMET 800 600	2.45 ± 0.27
ttZnunu	4.70 ± 0.38
$t\bar{t}$	4.15 ± 0.17
Single-top	2.34 ± 0.37
W+jets	1.77 ± 0.49
Other	0.88 ± 0.11
ttZqqll	0.10 ± 0.05
Z+jets	0.00 ± 0.00
SM	13.94 ± 0.75

Table 4.13: Yields in $t\bar{t}$ control region.

CR-ttbar	Yield
tbMET 600 400	1.85 ± 0.64
tbMET 800 600	0.28 ± 0.10
tbMET 900 400	0.17 ± 0.06
$t\bar{t}$	115.89 ± 2.02
Single-top	11.75 ± 1.11
W+jets	11.46 ± 1.39
Other	2.52 ± 0.27
$t\bar{t}Z$	1.99 ± 0.26
Z+jets	0.06 ± 0.04
SM	143.66 ± 2.71
Data	145.00 ± 12.04

shown in Tables 4.7,4.8 and Figure 4.16.

Validation Regions B definitions

The $t\bar{t}$ Validation Region is defined similarly to the $t\bar{t}$ control region. All selections are summarised in Table 4.11. The inverted m_T selection being greater than 150.0 GeV sets it kinematically closer to the SRB than the CR. The selection of number of jets was relaxed to be < 2 , to ensure high enough statistics in the VR. Table 4.14 summarises the yields and Figure 4.20 shows distributions of the $t\bar{t}$ validation region.

Since $t\bar{t}Z$ is the dominant background in the SRB, a more dedicated VR was designed for validation.

Inspired by a two-lepton $t\bar{t}Z$ enriched SR from the $tt + E_T^{\text{miss}} 2\ell$ analysis [180], a two-

Table 4.14: Yields in $t\bar{t}$ validation region.

VR-ttbar	Yield
tbMET 600 400	1.81 ± 0.62
tbMET 900 400	0.53 ± 0.11
tbMET 800 600	0.38 ± 0.10
$t\bar{t}$	19.75 ± 0.77
Single-top	3.78 ± 0.54
W+jets	1.71 ± 0.56
ttZnnu	1.62 ± 0.24
Other	0.84 ± 0.10
ttZqqll	0.23 ± 0.11
Z+jets	0.04 ± 0.02
SM	27.97 ± 1.13
Data	17.00 ± 4.12

lepton VR was defined for $t\bar{t}Z$. The selections are summarised in Table 4.15. The two most important variables in this region definition are the lepton-based transverse mass, $m_{T2}^{\ell\ell}$, and the angle between the original and lepton-correct E_T^{miss} , $\Delta\phi_{\text{boost}}$.

A three-lepton $t\bar{t}Z$ background is considered to affect the SRB in cases where the Z -boson decays invisibly into neutrinos contributing to E_T^{miss} , while the two tops decay semi-leptonically. Therefore, the two-lepton $t\bar{t}Z$ VR is expected to have a high contribution from $t\bar{t}Z$ events. The distributions in Figure 4.21 show variables in the two-lepton $t\bar{t}Z$ VR where the $t\bar{t}Z$ background is split into $t\bar{t}Z$ ($\nu\nu$) and $t\bar{t}Z$ ($llqq$) for further classification and evaluation of the targeted invisible Z -decay. In this region like the $t\bar{t}Z$ CR, a single-lepton trigger is used.

Table 4.15: Selections for ttZ validation region.

Selection	ttZ-VR
n_{lep}	$=2$
Leptons flavour	DF SF
$p_T(\ell_1)$ [GeV]	>25
$p_T(\ell_2)$ [GeV]	>20
$m_{\ell\ell}$ [GeV]	- $<70, >110$
$n_{\text{b-jets}}$	≥ 1
$ \Delta\phi_{\text{boost}} $ [rad]	<1.5
E_T^{miss} significance	>12
$m_{T2}^{\ell\ell}$	>110
E_T^{miss} [GeV]	>200

Finally, a summary of the complete Signal Regions A and B selections along with each of the contributing control and validation regions is presented in Table ??.

Table 4.16: Yield table for the two-lepton ttZ -VR.

VR- ttZ	Yield
tbMET 900 500	2.63 ± 0.28
tbMET 600 400	1.48 ± 0.58
tbMET 800 600	0.66 ± 0.14
$ttZ\nu\nu$	14.30 ± 0.56
$t\bar{t}$	11.52 ± 1.25
Other	10.26 ± 0.35
$ttZq\bar{q}ll$	7.30 ± 0.20
Single-top	3.90 ± 0.67
$Z + \text{jets}$	1.58 ± 0.26
$W + \text{jets}$	0.17 ± 0.14
SM	49.04 ± 1.60
Data	67.00 ± 8.19

4.3 Systematic Uncertainties

There are broadly two types of uncertainties - "detector" and "modelling". The detector uncertainties are related to the detector and reconstruction of the analysis objects like jets and leptons and applies on the signal and background while the modelling uncertainties arise from the modelling of SM and SUSY in the MC generated events depending on the MC generator. Systematics to the theoretical predictions are also considered on the signal.

Detector Uncertainties

The definition of the physics objects utilises p_T and η values taken from the reconstruction of these objects based on the data collected by the detector. Therefore taking into detector uncertainties is very important. The individual sources of detector uncertainty considered in the analysis are listed as follows:

- **Luminosity:** The luminosity uncertainty on the total Run 2 data is taken to be 1.7% [181] as recommended by the data preparation group and is taken into account by varying up and down by 1.7% the integrated luminosity that the MC is scaled to while performing the fit.
- **Jet Energy Scale (JES):** One of the two main sources of uncertainties for jets are uncertainties affecting the calibration of the energy scale (JES). The JES corrects the calorimeter's response to the true jet energy and the uncertainty on the JES is derived in bins of p_T and η as detailed in reference [90]. These variations, up and down, are estimated and included along with uncertainties arising from flavour composition and pile-up. Furthermore, to increase the efficiency of estimating the JES uncertainty, a reduced set of parameters are used.
- **Jet Energy Resolution (JER) for small-R jets:** The other of the two main sources of uncertainties for jets are uncertainties affecting the resolution (JER). JER is the uncertainty on the central value measured for the energy of a jet. The

JER can affect the jet multiplicity by varying the measured p_T of a given jet and thus leading to this jet not meeting the jet p_T requirements or vice-versa [90]. The JER uncertainties in this analysis is estimated by smearing all jets momenta in simulation events.

- **Jet Vertex Tagger:** This tagger is used remove central jets that arising from pile-up events and uncertainties in the JVT arises from mistakenly tagging hard scattering jets arising from pile-up events [182].
- **E_T^{miss} Soft-term Resolution and Scale:** The uncertainty on the E_T^{miss} is a consequence of uncertainties of individual objects such as the JES and JER systematics being propagated to all E_T^{miss} related variables. The uncertainty on the reconstructed E_T^{miss} is also dependent on the E_T^{miss} soft term derived by two different in-situ methods using $Z \rightarrow \mu\mu$ events [183].
- **b -tagging:** As the regions designed in this analysis require 2 b -jets, the uncertainties arising from b -tagging affects signal and backgrounds. These b -tagging uncertainties are accounted for by varying the p_T , η and flavour-dependent scale factors based on the kinematics of the jet and the jet flavour as described in this reference [184].
- **Lepton efficiencies:** Lepton reconstruction and identification efficiencies have contributions to the backgrounds. For electrons, the uncertainties originate from the e/γ resolution and scale and from the electron reconstruction efficiency. Similarly for muons the uncertainties originate from the muon resolution and reconstruction efficiency, the isolation and the momentum scale. The lepton trigger scale factors are also taken into consideration due to the usage of single lepton triggers in a three-lepton $t\bar{t}Z$ control region.
- **Pileup:** The uncertainty due to pileup re-weighting of the MC samples is accounted for by applying a scale factor to the MC simulations that considers the minimum-bias vertex data related to the number of pile-up interactions. And the uncertainty on the applied scale factor applied is calculated by varying the scale-factor within its uncertainties.

Due to the analysis final states and resulting selections, the most relevant detector uncertainties for the analysis are the uncertainties arising from the jets - the JER, JES and b -tagging uncertainties. The uncertainties coming from the leptons and E_T^{miss} are comparatively less relevant and is expected to only contribute a small amount to the overall total uncertainty.

Modelling Uncertainties

Theory uncertainties affecting the background normalisation and kinematic distribution impact significantly the background prediction in the signal regions, being in several cases the highest uncertainty in the signal regions. These uncertainties mainly stem from the non-arbitrary choices made when constructing a MC generator to model a physics process associated to either the MC generator, the parton shower and hadronisation model used, the simulation of ISR/FSR radiation and/or the PDF scale and or QCD scales used to predict the kinematics and cross-sections of the processes.

The uncertainties arising from the choices made when producing the signal MC are estimated when performing the model-dependent fit procedure as explained in the following

section.

4.4 Results and interpretation

The fitting procedure used in the analysis is implemented using the HistFitter [185] framework which performs a log likelihood fit using the number of expected MC events for each process, in each CR and SR; the number of data events in each region, and the errors on the number of expected MC events arising from the systematic uncertainties. This background estimation using this fitting procedure allows for partial cancellation of the systematic uncertainties. There are 3 types of fit: Background-only fit, Model-dependent or Exclusionfit and Model-Independent or Discovery fit.

The Background-only fit is done to get the normalisation parameters (μ_p) for each of the dominant backgrounds that have corresponding CRs defined. The purpose is to evaluate the total background expectation in the SRs (and VRs) without making any assumptions on the signal model under consideration ($\mu_{sig} = 0$). These normalisation parameters calculated by the fit procedure by using information only from the CRs. These normalisation parameters are then introduced into a different likelihood function, containing information from the CRs, VRs and SRs, to estimate the scaled backgrounds in the SRs and VRs. A background-only fit without systematics was performed to obtain the scaling factors for the dominant background contributions in region A. The normalisation factors obtained have been summarised in Table ?? and the both the background scaling factors were fitted simultaneously.

Table 4.18: Scaling factors for backgrounds obtained with separate background-only fits in region A and B

Region	Scaling Factor	Value
SRA	$\mu(\text{single top})$	0.8 ± 0.3
	$\mu(t\bar{t}Z)$	1.2 ± 0.2
SRB	$\mu(t\bar{t})$	0.8 ± 0.1
	$\mu(t\bar{t}Z)$	1.2 ± 0.3

After performing the background-only fit, a model dependent fit is performed to study the signal model. This fit calculates the normalisation or signal strength parameter (μ_{sig}) associated with the signal model under investigation. Also, this fit is known as an exclusion fit because with no observed significant excess of events in the SRs from the background-only fit results, exclusion limits can be applied to the SUSY signal. This fit is performed simultaneously on the CRs and SRs, adding the signal sample to the CRs to take into account possible signal contamination of the CRs. The results of the exclusion fit takes into consideration all of the signal mass scenarios in the considered mass plane such that an exclusion contour can be produced. If there is an observed excess of events, then this fit can be used to measure the signal strength of the model.

The model independent fit or discovery fit provides a model-independent limit on any additional number of events in the SRs beyond the expected number of background events such that the results of the analysis can be interpreted in the context of any generic model. This fit works in the same manner as the model independent fit. However

$tb+E_T^{\text{miss}}$ CRA	CRAst	CRttZ
Observed events	40	43
Fitted bkg events	40.10 ± 6.31	42.94 ± 6.54
Fitted Z events	0.23 ± 0.00	0.13 ± 0.00
Fitted W events	8.05 ± 0.14	0.00 ± 0.00
Fitted ttbar events	11.42 ± 0.19	0.27 ± 0.00
Fitted st events	17.65 ± 6.32	0.00 ± 0.00
Fitted ttZ events	1.88 ± 0.34	35.82 ± 6.54
Fitted other events	0.87 ± 0.01	6.72 ± 0.11
MC exp. SM events	43.28	37.76
MC exp. Z events	0.23	0.13
MC exp. W events	8.05	0.00
MC exp. ttbar events	11.42	0.27
MC exp. st events	21.10	0.00
MC exp. ttZ events	1.61	30.64
MC exp. other events	0.87	6.72

Table 4.19: Fit results for the background only-fit in the A-type control regions, for an integrated luminosity of 139 fb^{-1} . Nominal MC expectations (normalised to MC cross-sections) are given for comparison. The errors shown are statistical only. Uncertainties on the fitted yields are symmetric by construction, where the negative error is truncated when reaching to zero event yield

in this instance, a dummy signal is inserted instead of using an actual signal model and no signal contamination is allowed.

The background-only fit results for CRA, VRA and SRA are shown in Tables 4.19, 4.20 and 4.21 respectively. Generally a good overall agreement is found between the MC prediction and the observed data within uncertainties for all the regions. The combined VR for single-top and $t\bar{t}Z$ is further motivated by the pre- and post-fit yields as shown in Figure 4.22 and Table 4.20. Post fit, the background composition in the VRA fully validates the observed dominant backgrounds of single top followed by $t\bar{t}Z$ in the SRA.

The background-only fit results for CRB, VRB and SRB are shown in Tables 4.22, 4.23 and 4.24 respectively. Also for region B, the MC and data are in good agreement. The $t\bar{t}$ VRB post fit plots in Figure 4.23 validates the observed $t\bar{t}$ background observed in the SRB.

As no excess is observed from the background-only fit results, I performed a model dependent fit to place exclusion limits on the $tb+E_T^{\text{miss}}$ signal model under consideration. Figure 4.24 shows the expected limit plot and Figure 4.26 shows the expected limit plot with a flat 20% uncertainty applied produced for SRA. From this preliminary expected exclusion using SRA, it is observed that in comparison to the early Run 2 results as shown in Figure 4.27, there is an increased sensitivity. It is seen that upto $980 \text{ GeV} \tilde{t}/\tilde{b}$ mass can be excluded for $\tilde{\chi}_1^0$ mass of 110 GeV . This is already $\sim 150 \text{ GeV}$ gain in the expected exclusion limit in comparison to just the 1ℓ region shown by the red contour. and $\sim 60 \text{ GeV}$ gain in comparison to the combined $bb+E_T^{\text{miss}}$ and $tb+E_T^{\text{miss}}$ observed exclusion contour represented by the blue line.

$t\bar{b}+E_T^{\text{miss}}$ VRA	VRAs
Observed events	65
Fitted bkg events	65.93 ± 9.84
Fitted Z events	0.26 ± 0.00
Fitted W events	3.09 ± 0.05
Fitted $t\bar{t}$ events	15.63 ± 0.26
Fitted st events	26.55 ± 9.51
Fitted ttZ events	17.25 ± 3.15
Fitted other events	3.16 ± 0.05
MC exp. SM events	68.62
MC exp. Z events	0.26
MC exp. W events	3.10
MC exp. $t\bar{t}$ events	15.63
MC exp. st events	31.73
MC exp. ttZ events	14.75
MC exp. other events	3.16

Table 4.20: Validation region for single top: Fit results for the background only-fit in the A-type validation region, for an integrated luminosity of 139 fb^{-1} . Nominal MC expectations (normalised to MC cross-sections) are given for comparison. The errors shown are statistical only. Uncertainties on the fitted yields are symmetric by construction, where the negative error is truncated when reaching to zero event yield

$t\bar{b}+E_T^{\text{miss}}$ SRA	SRA
Observed events	5
Fitted bkg events	5.41 ± 1.15
Fitted Z events	0.02 ± 0.00
Fitted W events	0.67 ± 0.16
Fitted $t\bar{t}$ events	0.14 ± 0.03
Fitted st events	2.21 ± 0.97
Fitted ttZ events	2.19 ± 0.49
Fitted other events	0.18 ± 0.04
MC exp. SM events	5.54
MC exp. Z events	0.02
MC exp. W events	0.67
MC exp. $t\bar{t}$ events	0.14
MC exp. st events	2.65
MC exp. ttZ events	1.87
MC exp. other events	0.18

Table 4.21: SRA: Fit results for the background only-fit in the B-type validation region, for an integrated luminosity of 139 fb^{-1} . Nominal MC expectations (normalised to MC cross-sections) are given for comparison. The errors shown are statistical only. Uncertainties on the fitted yields are symmetric by construction, where the negative error is truncated when reaching to zero event yield.

Figure 4.25 shows the expected limits for SRB performed by the analysis team. Here too

$tb+E_T^{\text{miss}}$ CRA	CRBtt	CRttZ
Observed events	145	43
Fitted bkg events	144.79 ± 12.00	42.99 ± 6.53
Fitted Z events	0.06 ± 0.01	0.13 ± 0.03
Fitted W events	12.49 ± 2.47	0.00 ± 0.00
Fitted ttbar events	113.83 ± 13.21	0.23 ± 0.03
Fitted st events	12.32 ± 2.44	0.00 ± 0.00
Fitted ttZ events	3.11 ± 0.58	35.91 ± 6.67
Fitted other events	2.98 ± 0.59	6.72 ± 1.33
MC exp. SM events	166.60	37.76
MC exp. Z events	0.06	0.13
MC exp. W events	12.48	0.00
MC exp. ttbar events	136.10	0.27
MC exp. st events	12.32	0.00
MC exp. ttZ events	2.66	30.64
MC exp. other events	2.98	6.72

Table 4.22: Fit results for the background only-fit in the B-type control regions, for an integrated luminosity of 139 fb^{-1} . Nominal MC expectations (normalised to MC cross-sections) are given for comparison. The errors shown are statistical only. Uncertainties on the fitted yields are symmetric by construction, where the negative error is truncated when reaching to zero event yield

$tb+E_T^{\text{miss}}$ VRB	VRB-ttbar
Observed events	17
Fitted bkg events	26.32 ± 1.94
Fitted Z events	0.05 ± 0.01
Fitted W events	1.86 ± 0.37
Fitted ttbar events	18.08 ± 2.08
Fitted st events	3.24 ± 0.64
Fitted ttZ events	2.14 ± 0.44
Fitted other events	0.94 ± 0.19
MC exp. SM events	29.66
MC exp. Z events	0.05
MC exp. W events	1.86
MC exp. ttbar events	21.57
MC exp. st events	3.24
MC exp. ttZ events	2.00
MC exp. other events	0.94

Table 4.23: Validation region for $t\bar{t}$: Fit results for the background only-fit in the B-type validation region, for an integrated luminosity of 139 fb^{-1} . Nominal MC expectations (normalised to MC cross-sections) are given for comparison. The errors shown are statistical only. Uncertainties on the fitted yields are symmetric by construction, where the negative error is truncated when reaching to zero event yield

$t\bar{b}+E_T^{\text{miss}}$ SRB	SRB
Observed events	15
Fitted bkg events	15.84 ± 1.61
Fitted Z events	0.00 ± 0.00
Fitted W events	1.99 ± 0.41
Fitted $t\bar{t}$ events	3.94 ± 0.50
Fitted st events	2.49 ± 0.51
Fitted ttZ events	6.39 ± 1.23
Fitted other events	1.03 ± 0.21
MC exp. SM events	15.67
MC exp. Z events	0.00
MC exp. W events	1.98
MC exp. $t\bar{t}$ events	4.71
MC exp. st events	2.49
MC exp. ttZ events	5.45
MC exp. other events	1.03

Table 4.24: Fit results for the background only-fit in the B-type validation region, for an integrated luminosity of 139 fb^{-1} . Nominal MC expectations (normalised to MC cross-sections) are given for comparison. The errors shown are statistical only. Uncertainties on the fitted yields are symmetric by construction, where the negative error is truncated when reaching to zero event yield.

a marked improvement is observed in comparison to Figure 4.3 in the compressed region.

As mentioned at the start of the chapter, this is still an ongoing analysis at the time of writing this thesis. A few signal point have been added in the designed grid to produce a better limit contour around the $m_{\tilde{t}} = 700 \text{ GeV}$ and $m_{\tilde{\chi}_1^0} = 400 \text{ GeV}$. Overall, the preliminary results from the exclusion plot shown in Figures 4.24 and 4.27 motivates that the final exclusion contour produced in combination with the designed SRB for the compressed regions and with the latest $t\bar{b}+E_T^{\text{miss}}$ analysis will further exclude the limits of this signal model, thereby increasing the chances of finding SUSY beyond the excluded region.

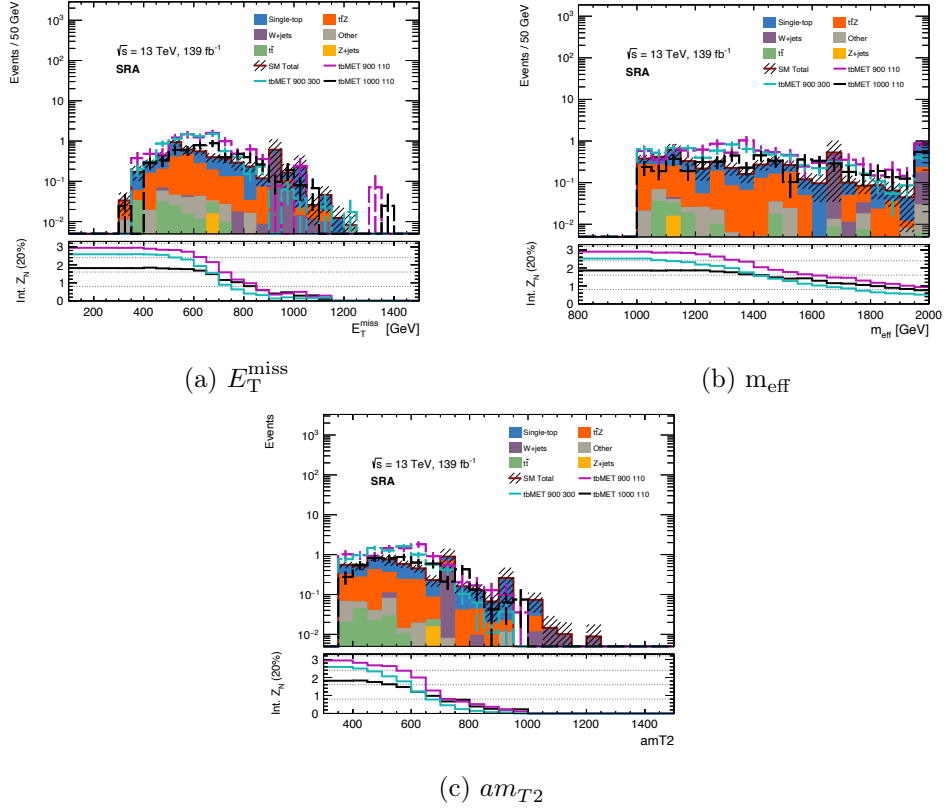


Figure 4.14: Three important variables are plotted after the conditions noted in Table 4.3 are applied to form SRA. The MC simulation is scaled to 139 fb^{-1} and a semi-log scale applied. The solid coloured histograms indicate the different SM background contributions. With the hashed area representing a total statistical uncertainty. The lines show the distributions from three different "representative" signal points. The lower panel displays the standard recommended ATLAS significance of each bin, Z_n , with a flat 20 % uncertainty applied. The plots show that in individual bins, it is dominated by the limited statistics in W+jets. However, this does not affect the SRA, as this phenomenon is related to the data generation in MC simulations and particularly noticeable when dealing with rare events. Furthermore, the observed main SM backgrounds are single-top and $t\bar{t}Z$.

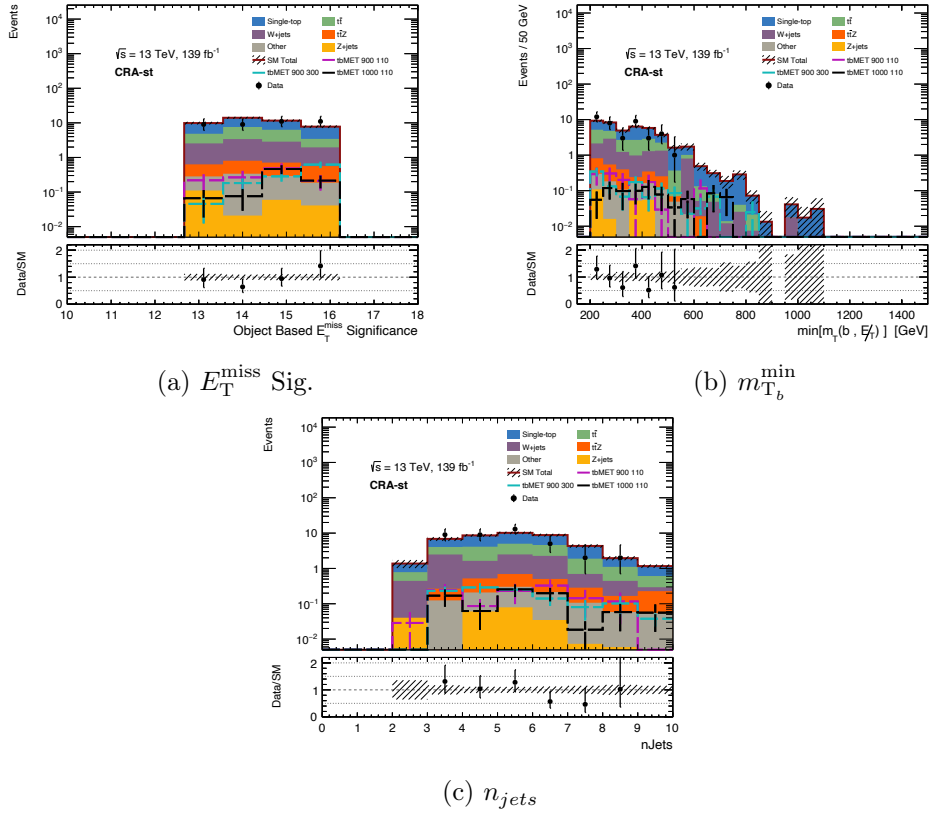


Figure 4.15: Distributions in single top CRA-st for different variables. In each sub-figure the coloured, solid histograms show the SM backgrounds scaled to 139 fb^{-1} . The hashed area represents the statistical error on the prediction. The black points show the data with statistical error bars. Overlaid are dashed lines of representative signal points. The lower panel contains the ratio of data over SM prediction.

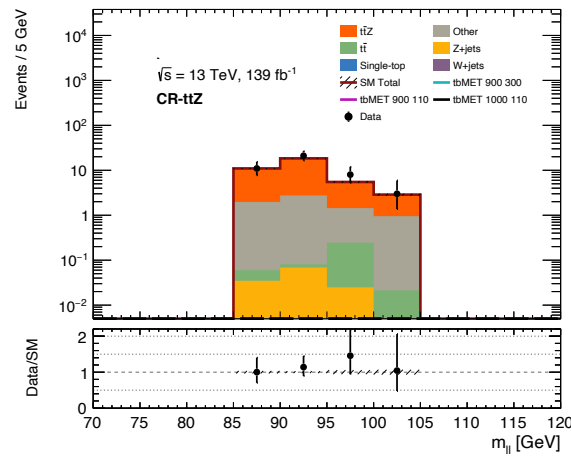


Figure 4.16: Distribution of invariant mass of the two leptons from Z-boson in the three lepton CR-ttZ. The coloured, solid histograms show the SM backgrounds scaled to 139 fb^{-1} . The hashed area represents the statistical error on the prediction. The black points show the data with statistical error bars. The lower panel contains the ratio of data over SM prediction.

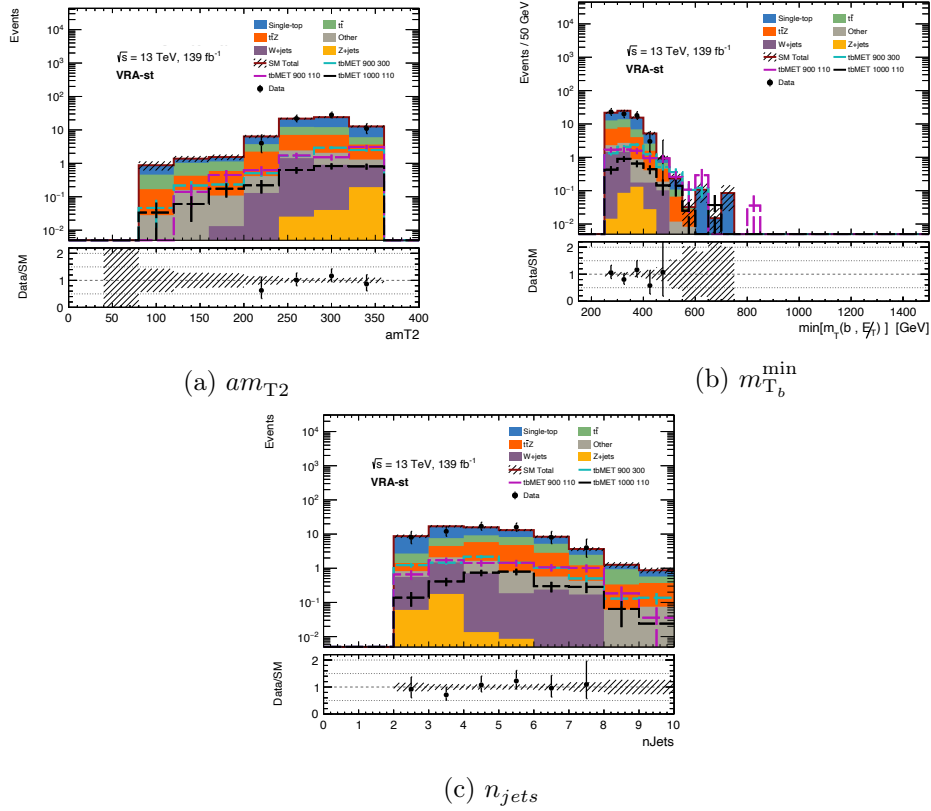


Figure 4.17: Distributions in single top VRA-st for different variables. In each sub-figure the coloured, solid histograms show the SM backgrounds scaled to 139 fb^{-1} . The hashed area represents the statistical error on the prediction. The black points show the data with statistical error bars. Overlaid are dashed lines of representative signal points. The lower panel contains the ratio of data over SM prediction.

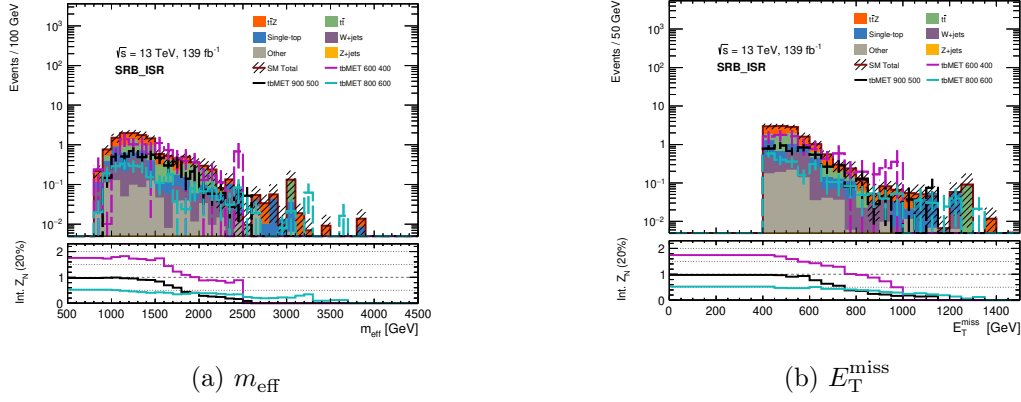


Figure 4.18: Two important variables are plotted after the conditions noted in Table ?? are applied to form SR. The MC simulation is scaled to 139 fb^{-1} and a semi-log scale applied. The solid coloured histograms indicate the different SM background contributions. With the hashed area representing a total statistical uncertainty. The lines show the distributions from three different "representative" signal points. The lower panel displays the standard recommended ATLAS significance of each bin, Z_n , with a flat 20 % uncertainty applied. The left hand figure shows the effective mass while the right presents the E_T^{miss} distribution.

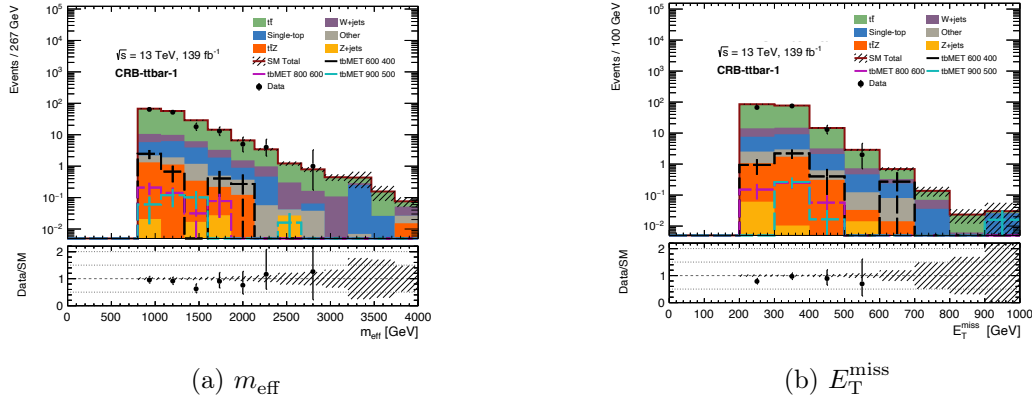


Figure 4.19: Distributions in CRB-ttbar for m_{eff} and E_T^{miss} variables. In each sub-figure the coloured, solid histograms show the SM backgrounds scaled to 139 fb^{-1} . The hashed area represents the statistical error on the prediction. The black points show the data with statistical error bars. Overlaid are dashed lines of representative signal points. The lower panel contains the ratio of data over SM prediction.

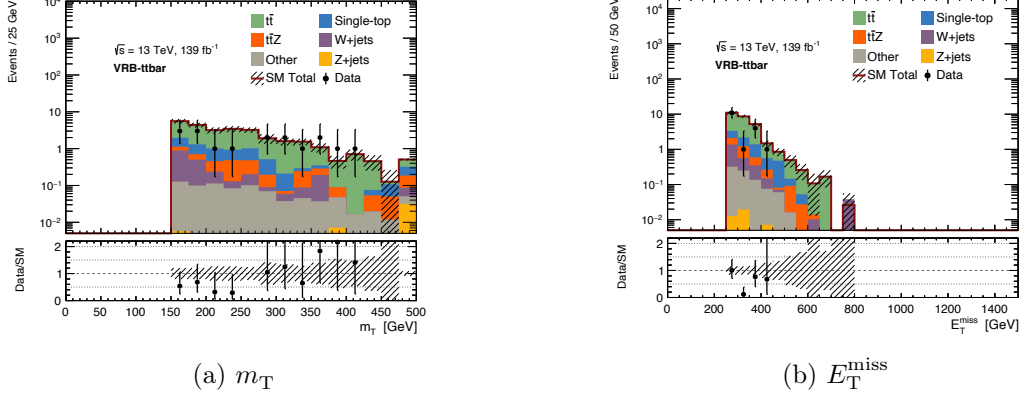


Figure 4.20: Distributions in VRB- $tt\bar{b}ar$ for m_T and E_T^{miss} variables. In each sub-figure the coloured, solid histograms show the SM backgrounds scaled to 139 fb^{-1} . The hashed area represents the statistical error on the prediction. The black points show the data with statistical error bars. Overlaid are dashed lines of representative signal points. The lower panel contains the ratio of data over SM prediction.

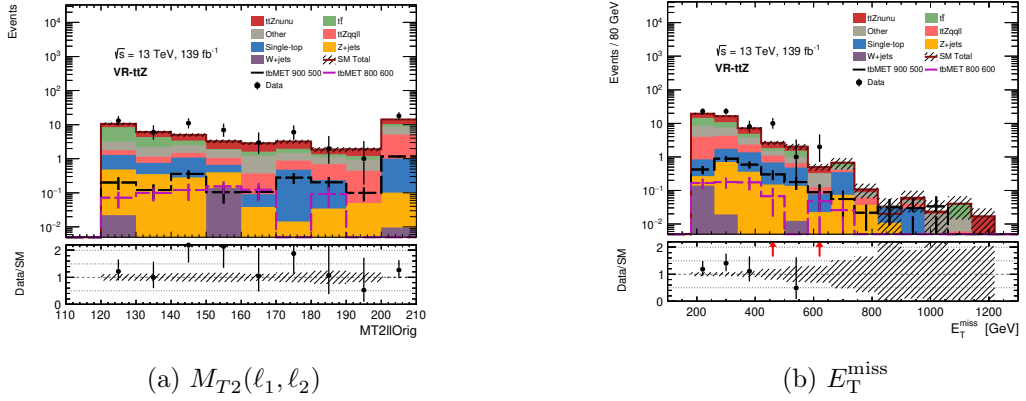


Figure 4.21: Distributions in two-lepton ttZ -VR for $M_{T2}(\ell_1, \ell_2)$ and E_T^{miss} variables. In each sub-figure the coloured, solid histograms show the SM backgrounds scaled to 139 fb^{-1} . The hashed area represents the statistical error on the prediction. The black points show the data with statistical error bars. Overlaid are dashed lines of representative signal points. The lower panel contains the ratio of data over SM prediction.

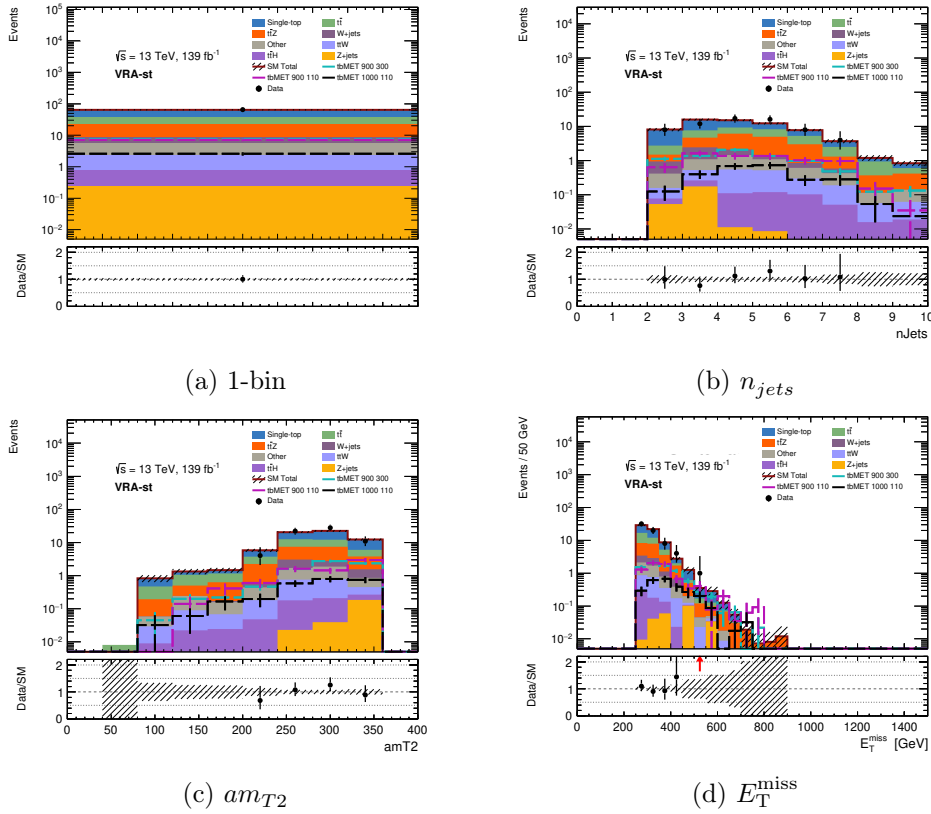


Figure 4.22: Post-fit one-bin plot and kinematic distributions in VRA-st. In each sub-figure the coloured, solid histograms show the SM backgrounds scaled to 139fb^{-1} . The hashed area represents the statistical error on the prediction. The black points show the data with statistical error bars. Overlaid are dashed lines of representative signal points. The lower panel contains the ratio of data over SM prediction.

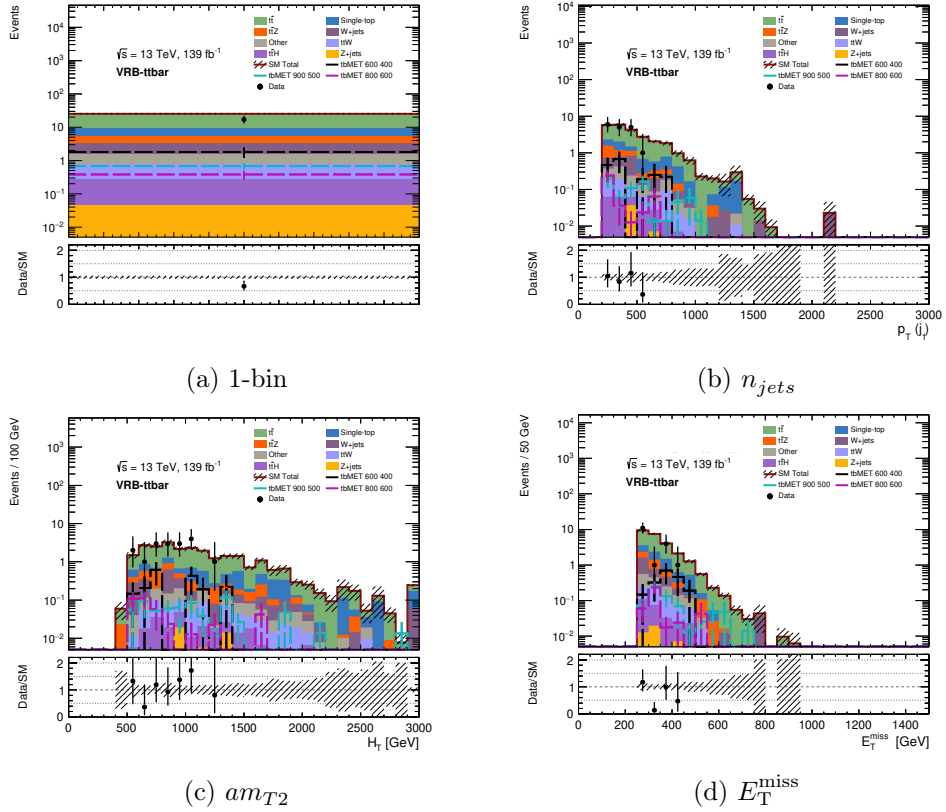


Figure 4.23: Post-fit one-bin plot and kinematic distributions in VRB- $t\bar{t}$ bar. In each sub-figure the coloured, solid histograms show the SM backgrounds scaled to 139fb^{-1} . The hashed area represents the statistical error on the prediction. The black points show the data with statistical error bars. Overlaid are dashed lines of representative signal points. The lower panel contains the ratio of data over SM prediction.

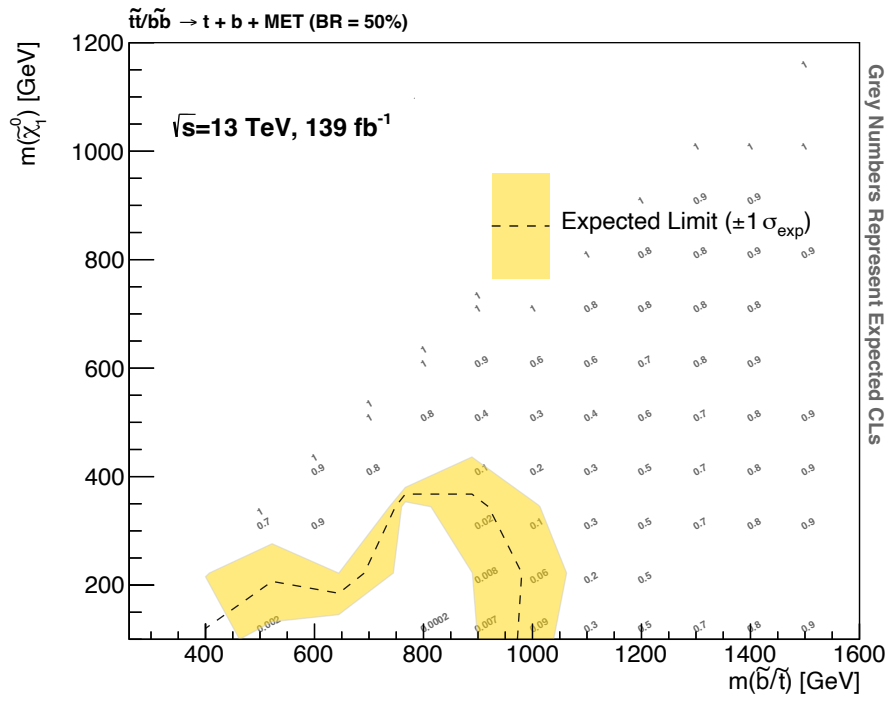


Figure 4.24: Expected model-dependent exclusion limits for SRA at 139 fb^{-1} without the inclusion of the systematic uncertainties. The limit is shown in the \tilde{b} mass (x-axis) and $\tilde{\chi}_1^0$ mass (y-axis) plane and the limit plot uses background normalisation factors obtained from background-only fits using associated single-top and $t\bar{t}Z$ CRAs for SRA.

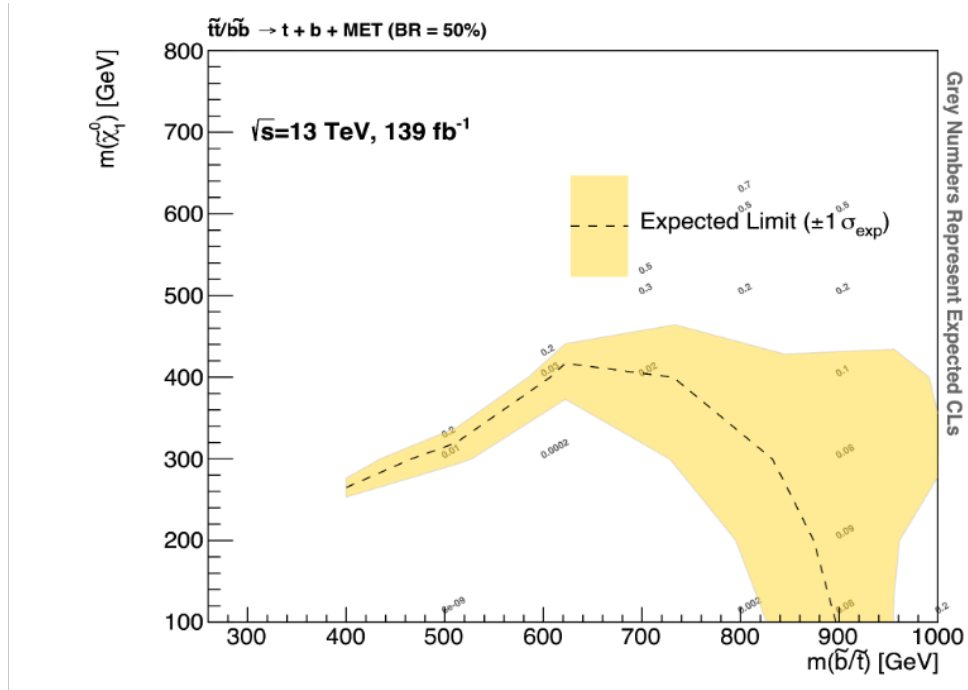


Figure 4.25: Expected model-dependent exclusion limits for SRB at 139 fb^{-1} , with no systematic uncertainties included. The limit is shown in the \tilde{b} mass (x-axis) and $\tilde{\chi}_1^0$ mass (y-axis) plane. The limit plot uses background normalisation factors obtained from background-only fits in $t\bar{t}$ and $t\bar{t}Z$ CRs for SRB.

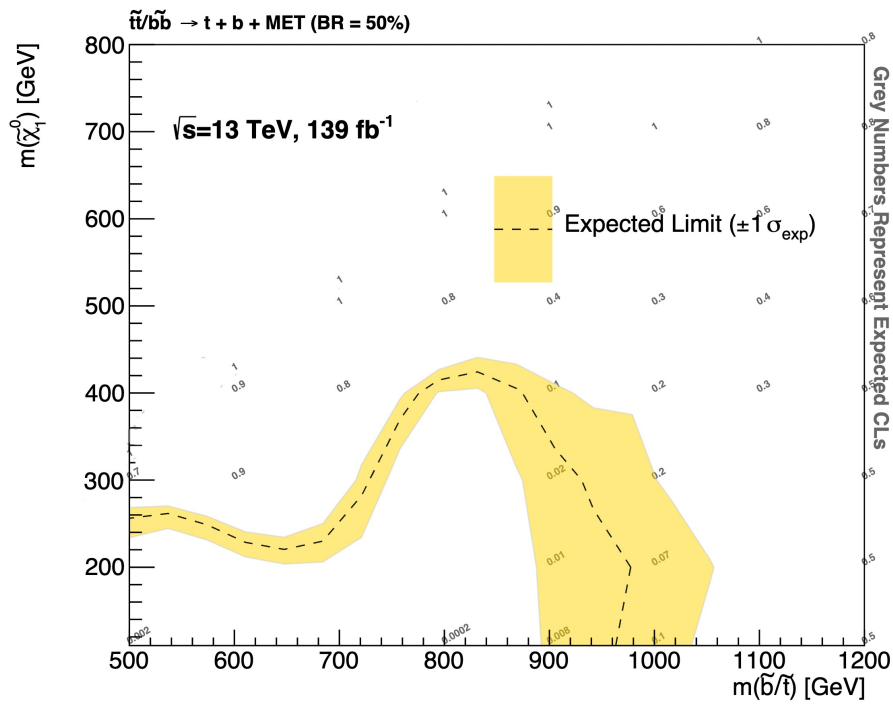


Figure 4.26: Expected model-dependent exclusion limits for SRA at 139 fb^{-1} , including a flat 20% systematic uncertainty. The limit is shown in the \tilde{b} mass (x-axis) and $\tilde{\chi}_1^0$ mass (y-axis) plane. The limit plot uses background normalisation factors obtained from background-only fits in single-top and $t\bar{t}Z$ CRs for SRA.

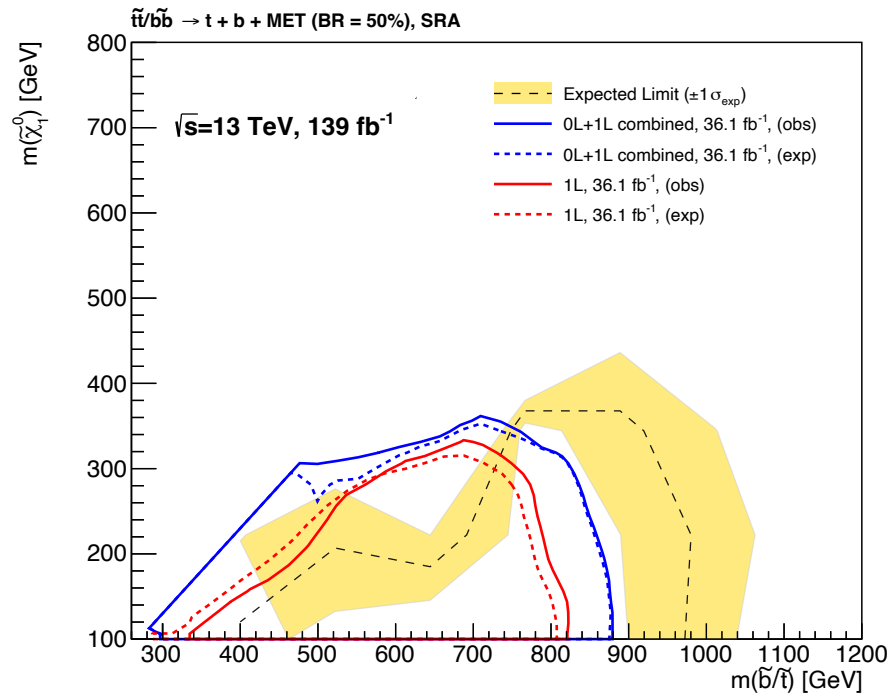


Figure 4.27: Comparing the previous combined $t\bar{t} + E_T^{\text{miss}}$ and $b\bar{b} + E_T^{\text{miss}}$ ($0\ell + 1\ell$) and the $t\bar{t} + E_T^{\text{miss}}$ limit (1ℓ) exclusion limits to the expected model-dependent exclusion limits obtained for SRA using full 139 fb^{-1} dataset. The limits are shown in the \tilde{b} mass (x-axis) and $\tilde{\chi}_1^0$ mass (y-axis) plane

Conclusions

This thesis documents the author's active engagement within the ATLAS Collaboration spanning from 2019 to 2023. During this period, the author has made significant contributions to the ATLAS Collaboration, co-authoring many publications and playing an equal role in two pivotal initiatives: the search for the pair production of 3rd generation squarks and the high-luminosity upgrade effort of the ATLAS detector whilst contributing directly to the following published work:

- J. Anders, et al., *A facility for radiation hardness studies based on a medical cyclotron*, Journal of Instrumentation 17 (2022) P04021 [186]
I contributed to pre- and post-irradiation characterisation of twin-axial electrical cables using the irradiation setup.

The SUSY search presented in this thesis is still ongoing and in its final stages. The initial plan had been to use machine learning techniques to design the analysis regions. However due to time constraints arising from long production time and limited duration of a Doctoral thesis a 'cut-and-count' method was employed. Since I started writing the thesis, there has been addition of new signal points around $m_{\tilde{t}} = 700 \text{ GeV}$ and $m_{\tilde{\chi}_1^0} = 400 \text{ GeV}$ in the signal grid. Also, the inclusion of the complete systematics in the fitting procedure is in progress. In this thesis the expected exclusion limits have been presented. Even if no significant excess is observed that would confirm the existence of SUSY, already the sensitivity shown in Figure 4.24 is such that it extends the limits as shown in Figure 4.3 by 60-150 GeV in the bulk region. The expected limits on $m_{\tilde{t}/\tilde{b}}$ exclude upto 980 GeV for $m_{\tilde{\chi}_1^0} = 110 \text{ GeV}$ assuming $\Delta m(\tilde{\chi}_1^0, \tilde{\chi}_1^\pm) = 1 \text{ GeV}$ to align with the last analysis. Moreover, this $\text{tb} + E_{\text{T}}^{\text{miss}}$ final state search results will also be combined with $\text{bb} + E_{\text{T}}^{\text{miss}}$ searches using the full 139 fb^{-1} Run 2 dataset. This is expected to further extend the exclusion contour well into the TeV mass scale. This is extremely promising and further motivates the need for the HL-LHC. With increased luminosity and consequently greater statistics, the possibility of finding the lightest SUSY particles is becoming very real.

The first two to almost three years of my Doctoral thesis was spent working in the Bern ATLAS laboratory, building and testing the first prototype of the ATLAS ITk Pixel data transmission chain associated to the HL-LHC upgrade of the ATLAS detector. I started with testing the GBCR1 using an Arduino micro-controller and then slowly building the chain adding one component at a time. Characterising each component in the chain and optimising the multiple registers in each of the components was at best a pleasure and at worst - particularly during the COVID era, very challenging. But I look upon this time of my thesis, where I learnt the most. I successfully managed to qualify the ITk Pixel

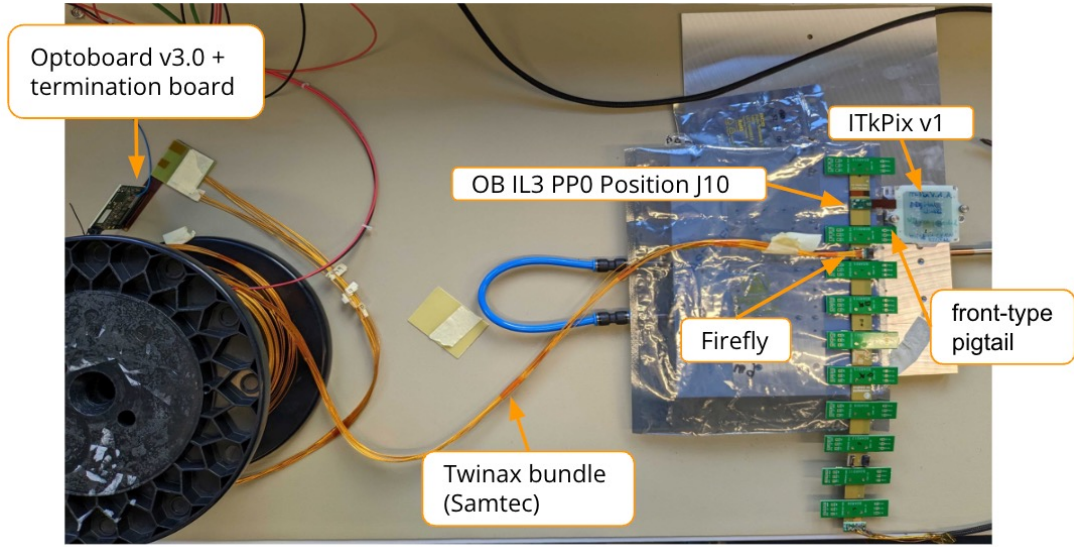


Figure 4.28: The complete functioning data transmission chain with the final ITk components.

electrical data transmission chain from the pixel modules to the optoboard. It is able to satisfy the requirements of $\text{BER} < 10^{-12}$ for a signal loss < 20 dB with lowest observed total jitter of ~ 110 ps. The lpGBT specifications have stated a jitter requirement of ≤ 100 ps. However, for properly configured components, the observed BER at 95% CL is $< 10^{-12}$.

When I moved from lab work to physics analysis, the transmission chain consisted of the RD53B clock-data-recovery (CDR) chip, 1 m flex and 6 m twinAx cables and optoboard prototype version 1, with GBCR2, lpGBT v0, and VTRx+ version 10. Instead of the FELIX, a customised KC705 board was used to communicate with the optoboard. Currently the transmission chain consists of the ITkPixV1 front-end (FE), patch panel 0, 6 m twinAx cables, optoboard prototype version 3, with GBCR2, lpGBT v1, and VTRx+ version 10 connected via optical fibres to the FELIX backend system. After a successful final design review, we are now in production phase.

Figures 4.29 and 4.28 show FELIX soft errors and BER limit results obtained by Bern ATLAS team members with the most up to date data transmission chain respectively.

I had dreamed of completing the ITk data transmission chain prototype inside the Bern laboratory and had hoped to conduct a source test and *watch* the particle being detected.

This too will soon be a reality.

My involvement in the ITk Pixel readout system highlighted the significance of not solely focusing on sensor and front-end attributes, but also adopting a comprehensive approach to detector design. This comprehensive perspective is indispensable for ensuring the successful development and functionality of a tracker. Elements like readout mechanisms, power supply, grounding strategies, and monitoring protocols must be considered early in the design phase. Anticipating these aspects from the outset is essential for example in the context of upcoming colliders like the Future Circular Collider (FCC) [187]

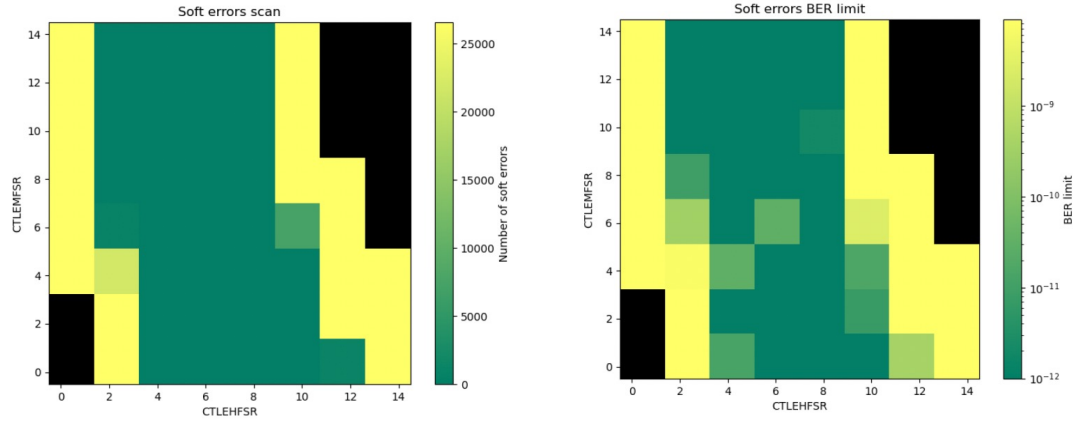


Figure 4.29: Soft error counter and BER limit measurements using FELIX system on the left and right respectively.

which examines scenarios for three different types of particle collisions: hadron (pp and heavy ion) collisions, like in the LHC (FCC-hh), electron-positron collisions (FCC-ee), as in the former LEP. Other options include proton-electron collisions or proton-heavy ion collisions. For example, detectors at FCC-ee [188] necessitate ultra-low material budgets, whereas those at FCC-hh [189] must meet unparalleled standards of radiation resistance. In this context, leveraging the insights gained from the design and operation of detectors at the High-Luminosity LHC is particularly invaluable, especially in addressing challenges related to material budget and radiation hardness. More research and development (R&D) is required and to this end, among the current experiments at the LHC, the ALICE experiment designed primarily for heavy-ion physics, focusing on the study of quark-gluon plasma, can contribute significantly to the understanding and building of the FCC project in comparison to the ATLAS and CMS experiments.

In conclusion, my work and time spent as a Doctoral candidate has contributed in testing and expanding the limits of particle physics and more importantly expanded my own exclusion limits.

Bibliography

- [1] S. L. Glashow, *The renormalizability of vector meson interactions*, [Nuclear Physics](#) **10** (1959) 107–117. Cited on page 1.
- [2] S. Weinberg, *A Model of Leptons*, [Phys. Rev. Lett.](#) **19** (1967) 1264–1266, <https://link.aps.org/doi/10.1103/PhysRevLett.19.1264>. Cited on pages 1 and 10.
- [3] A. Salam, *Weak and Electromagnetic Interactions*, [Conf. Proc. C](#) **680519** (1968) 367–377. Cited on pages 1 and 10.
- [4] A. Salam and J. Ward, *Electromagnetic and weak interactions*, [Physics Letters](#) **13** (1964) 168–171. Cited on page 1.
- [5] G. 't Hooft and M. Veltman, *Regularization and renormalization of gauge fields*, [Nuclear Physics B](#) **44** (1972) 189–213, <https://www.sciencedirect.com/science/article/pii/0550321372902799>. Cited on pages 1 and 10.
- [6] *LHC Machine*, [JINST](#) **3** (2008) S08001. Cited on pages 1 and 21.
- [7] ATLAS Collaboration, *Observation of a new particle in the search for the Standard Model Higgs boson with the ATLAS detector at the LHC*, [Physics Letters B](#) **716** (2012) 1–29. Cited on page 1.
- [8] CMS Collaboration, *Observation of a new boson at a mass of 125 GeV with the CMS experiment at the LHC*, [Physics Letters B](#) **716** (2012) 30–61. Cited on page 1.
- [9] S. Weinberg, *Implications of dynamical symmetry breaking*, [Physical Review D](#) **13** (1976) 974–996. Cited on page 1.
- [10] L. Susskind, *Dynamics of spontaneous symmetry breaking in the Weinberg-Salam theory*, [Physical Review D](#) **20** (1979) 2619–2625. Cited on page 1.
- [11] Particle Data Group Collaboration, M. Tanabashi, et al., *Review of Particle Physics*, [Phys. Rev. D](#) **98** (2018) 030001, <https://link.aps.org/doi/10.1103/PhysRevD.98.030001>. Cited on pages 1 and 8.
- [12] R. Barbieri and G. Giudice, *Upper bounds on supersymmetric particle masses*, [Nuclear Physics B](#) **306** (1988) 63–76. Cited on page 1.

- [13] B. de Carlos and J. Casas, *One-loop analysis of the electroweak breaking in supersymmetric models and the fine-tuning problem*, [Physics Letters B](#) **309** (1993) 320–328. Cited on page 1.
- [14] J. L. Feng, *Naturalness and the Status of Supersymmetry*, [Annual Review of Nuclear and Particle Science](#) **63** (2013) 351–382. Cited on page 1.
- [15] P. Ramond, *Dual Theory for Free Fermions*, [Physical Review D](#) **3** (1971) 2415–2418. Cited on page 1.
- [16] A. Neveu and J. Schwarz, *Factorizable dual model of pions*, [Nuclear Physics B](#) **31** (1971) 86–112. Cited on page 1.
- [17] J.-L. Gervais and B. Sakita, *Field theory interpretation of supergauges in dual models*, [Nuclear Physics B](#) **34** (1971) 632–639. Cited on page 1.
- [18] Y. A. Gelfand and E. P. Likhtman, *Extension of the algebra of Poincare group generators and violation of P invariance*, [JETP Lett.](#) **13** (1971) 323–325, <https://cds.cern.ch/record/433516>. Cited on page 1.
- [19] J. Wess and B. Zumino, *Supergauge invariant extension of quantum electrodynamics*, [Nuclear Physics B](#) **78** (1974) 1–13. Cited on page 1.
- [20] D. Volkov and V. Akulov, *Is the neutrino a goldstone particle?*, [Physics Letters B](#) **46** (1973) 109–110. Cited on page 1.
- [21] S. P. Martin, pp. , 1–153.
https://www.worldscientific.com/doi/pdf/10.1142/9789814307505_0001.
https://www.worldscientific.com/doi/abs/10.1142/9789814307505_0001.
Cited on pages 1, 13, 16, 17, 18, 19, and 20.
- [22] ATLAS Collaboration, *SUSY Summary Plots June 2021*, tech. rep., CERN, Geneva, Jun, 2021. <http://cds.cern.ch/record/2771785>. Cited on page 2.
- [23] CMS Collaboration, *CMS Supersymmetry Physics Results*, 2021.
<https://twiki.cern.ch/twiki/bin/view/CMSPublic/PhysicsResultsSUS>. last accessed 07.07.2021. Cited on page 2.
- [24] M. Aaboud, et al., *Search for supersymmetry in events with b-tagged jets and missing transverse momentum in pp collisions at $\sqrt{s} = 13$ TeV with the ATLAS detector*, [Journal of High Energy Physics](#) **2017** (2017) 195,
[https://doi.org/10.1007/JHEP11\(2017\)195](https://doi.org/10.1007/JHEP11(2017)195). Cited on pages 2, 93, and 94.
- [25] CERN Yellow Reports: Monographs, *CERN Yellow Reports: Monographs, Vol. 10 (2020): High-Luminosity Large Hadron Collider (HL-LHC): Technical design report*, 2020.
<https://e-publishing.cern.ch/index.php/CYRM/issue/view/127>. Cited on page 2.
- [26] A. Dainese, et al., *Report on the Physics at the HL-LHC, and Perspectives for the HE-LHC*, tech. rep., Geneva, Switzerland, 2019. Cited on page 2.
- [27] ATLAS Collaboration,, *Technical Design Report for the ATLAS Inner Tracker Strip Detector*, tech. rep., CERN, Geneva, 2017.
<https://cds.cern.ch/record/2257755>. Cited on pages 2, 47, and 48.

- [28] ATLAS Collaboration,, *Technical Design Report for the ATLAS Inner Tracker Pixel Detector*, tech. rep., CERN, Geneva, 2017. <https://cds.cern.ch/record/2285585>. Cited on pages 2, 47, 48, 49, 51, 52, and 54.
- [29] S. E. et al., *Technical Requirements / Specifications for the ATLAS ITk Pixel Services (AT2-IP-EP-0007)*, 8, 2017. https://indico.cern.ch/event/1213069/attachments/2556356/4407248/ITk_Pix-Services_Specifications_v6.pdf. CERN internal. Cited on pages 3 and 50.
- [30] D. Galbraith and C. Burgard, *Diagram of the Standard Model of particle physics, created at the CERN Webfest 2012*, 2012. <https://davidgalbraith.org/portfolio/ux-standard-model-of-the-standard-model>. last accessed 04.07.2023. Cited on page 6.
- [31] M. Thomson in *Modern Particle Physics*. Cambridge University Press, 2013. Cited on page 7.
- [32] P. A. M. Dirac, *Quantum theory of emission and absorption of radiation*, *Proc. Roy. Soc. Lond. A* **114** (1927) 243. Cited on page 7.
- [33] E. Fermi, *Quantum Theory of Radiation*, *Rev. Mod. Phys.* **4** (1932) 87–132, <https://link.aps.org/doi/10.1103/RevModPhys.4.87>. Cited on page 7.
- [34] M. Gell-Mann, *A schematic model of baryons and mesons*, *Physics Letters* **8** (1964) 214–215, <https://www.sciencedirect.com/science/article/pii/S0031916364920013>. Cited on page 7.
- [35] P. D. Group, et al., *Review of Particle Physics*, *Progress of Theoretical and Experimental Physics* **2020** (2020) 083C01, <https://academic.oup.com/ptep/article-pdf/2020/8/083C01/34673722/ptaa104.pdf>, <https://doi.org/10.1093/ptep/ptaa104>. Cited on pages 9 and 14.
- [36] S. L. Glashow, *Partial-symmetries of weak interactions*, *Nuclear Physics* **22** (1961) 579–588, <https://www.sciencedirect.com/science/article/pii/0029558261904692>. Cited on pages 9 and 10.
- [37] M. Peskin and D. Schroeder in *An Introduction To Quantum Field Theory*. Addison-Wesley, 1995. Cited on page 10.
- [38] P. Higgs, *Broken symmetries, massless particles and gauge fields*, *Physics Letters* **12** (1964) 132–133, <https://www.sciencedirect.com/science/article/pii/0031916364911369>. Cited on page 11.
- [39] F. Englert and R. Brout, *Broken Symmetry and the Mass of Gauge Vector Mesons*, *Phys. Rev. Lett.* **13** (1964) 321–323, <https://link.aps.org/doi/10.1103/PhysRevLett.13.321>. Cited on page 11.
- [40] G. S. Guralnik, C. R. Hagen, and T. W. B. Kibble, *Global Conservation Laws and Massless Particles*, *Phys. Rev. Lett.* **13** (1964) 585–587, <https://link.aps.org/doi/10.1103/PhysRevLett.13.585>. Cited on page 11.

- [41] A. Collaboration, *Summary plots from the ATLAS Standard Model physics group*, <https://atlas.web.cern.ch/Atlas/GROUPS/PHYSICS/CombinedSummaryPlots/SM/>. last accessed 04.07.2023. Cited on page 11.
- [42] *Dark matter*, <https://home.cern/science/physics/dark-matter>. last accessed 04.07.2023. Cited on page 12.
- [43] E. Corbelli and P. Salucci, *The extended rotation curve and the dark matter halo of M33*, *Monthly Notices of the Royal Astronomical Society* **311** (2000) 441–447, <https://academic.oup.com/mnras/article-pdf/311/2/441/2881340/311-2-441.pdf>, <https://doi.org/10.1046/j.1365-8711.2000.03075.x>. Cited on page 12.
- [44] *Rotation curve of spiral galaxy Messier 33*, https://commons.wikimedia.org/wiki/File:Rotation_curve_of_spiral_galaxy_Messier_33_%28Triangulum%29.png. last accessed 04.07.2023. Cited on page 12.
- [45] H. Georgi and S. L. Glashow, *Unity of All Elementary-Particle Forces*, *Phys. Rev. Lett.* **32** (1974) 438–441, <https://link.aps.org/doi/10.1103/PhysRevLett.32.438>. Cited on page 13.
- [46] A. Djouadi, et al., *The Minimal Supersymmetric Standard Model: Group Summary Report*, 1999. Cited on page 18.
- [47] H. Baer, et al., *LOW ENERGY SUPERSYMMETRY PHENOMENOLOGY*, 1995. Cited on page 18.
- [48] The Super-Kamiokande Collaboration Collaboration, C. Regis, et al., *Search for proton decay via $p \rightarrow \mu^+ K^0$ in Super-Kamiokande I, II, and III*, *Phys. Rev. D* **86** (2012) 012006, <https://link.aps.org/doi/10.1103/PhysRevD.86.012006>. Cited on page 18.
- [49] G. R. Farrar and P. Fayet, *Phenomenology of the production, decay, and detection of new hadronic states associated with supersymmetry*, *Physics Letters B* **76** (1978) 575–579, <https://www.sciencedirect.com/science/article/pii/0370269378908584>. Cited on page 18.
- [50] G. Steigman and M. S. Turner, *Cosmological constraints on the properties of weakly interacting massive particles*, *Nuclear Physics B* **253** (1985) 375–386, <https://www.sciencedirect.com/science/article/pii/0550321385905371>. Cited on page 18.
- [51] M. Papucci, J. T. Ruderman, and A. Weiler, *Natural SUSY endures*, *Journal of High Energy Physics* **2012** (2012) 35, [https://doi.org/10.1007/JHEP09\(2012\)035](https://doi.org/10.1007/JHEP09(2012)035). Cited on page 20.
- [52] S. Dimopoulos and D. Sutter, *The supersymmetric flavor problem*, *Nuclear Physics B* **452** (1995) 496–512, <https://www.sciencedirect.com/science/article/pii/055032139500421N>. Cited on page 20.

- [53] C. F. Berger, J. S. Gainer, J. L. Hewett, and T. G. Rizzo, *Supersymmetry without prejudice*, *Journal of High Energy Physics* **2009** (2009) 023, <https://dx.doi.org/10.1088/1126-6708/2009/02/023>. Cited on page 20.
- [54] M. W. Cahill-Rowley, et al., *The new look pMSSM with neutralino and gravitino LSPs*, *The European Physical Journal C* **72** (2012) 2156, <https://doi.org/10.1140/epjc/s10052-012-2156-1>. Cited on page 20.
- [55] M. W. Cahill-Rowley, J. L. Hewett, A. Ismail, and T. G. Rizzo, *More energy, more searches, but the phenomenological MSSM lives on*, *Phys. Rev. D* **88** (2013) 035002, <https://link.aps.org/doi/10.1103/PhysRevD.88.035002>. Cited on page 20.
- [56] E. Mobs, *The CERN accelerator complex in 2019. Complexe des accélérateurs du CERN en 2019*, <https://cds.cern.ch/record/2684277>, General Photo. Cited on pages 21 and 22.
- [57] ATLAS Collaboration, G. Aad et al., *The ATLAS Experiment at the CERN Large Hadron Collider*, *JINST* **3** (2008) S08003. Cited on pages 21, 22, 27, 28, 29, 30, 32, and 33.
- [58] CMS Collaboration, S. Chatrchyan et al., *The CMS Experiment at the CERN LHC*, *JINST* **3** (2008) S08004. Cited on page 22.
- [59] F. Carena, et al., *The ALICE data acquisition system*, *Nuclear Instruments and Methods in Physics Research Section A: Accelerators, Spectrometers, Detectors and Associated Equipment* **741** (2014) 130–162, <https://www.sciencedirect.com/science/article/pii/S0168900213016987>. Cited on page 22.
- [60] LHCb Collaboration, A. A. Alves, et al., *The LHCb Detector at the LHC*, *JINST* **3** (2008) S08005, <https://cds.cern.ch/record/1129809>, Also published by CERN Geneva in 2010. Cited on page 22.
- [61] TOTEM Collaboration, G. Anelli et al., *The TOTEM experiment at the CERN Large Hadron Collider*, *JINST* **3** (2008) S08007. Cited on page 22.
- [62] LHCf Collaboration, O. Adriani et al., *The LHCf detector at the CERN Large Hadron Collider*, *JINST* **3** (2008) S08006. Cited on page 22.
- [63] MoEDAL Collaboration, J. Pinfold, et al., *Technical Design Report of the MoEDAL Experiment*, tech. rep., 2009. <https://cds.cern.ch/record/1181486>. Cited on page 22.
- [64] F. Collaboration, et al., *Technical Proposal for FASER: ForwArd Search ExpeRiment at the LHC*, 2018. Cited on page 22.
- [65] SND@LHC Collaboration, A. Iuliano, *The Scattering and Neutrino Detector at the LHC*, in *30th International Workshop on Deep-Inelastic Scattering and Related Subjects*. 7, 2023. [arXiv:2308.00097 \[hep-ex\]](https://arxiv.org/abs/2308.00097). Cited on page 23.
- [66] ATLAS Collaboration, *Public ATLAS Luminosity Results for Run-3 of the LHC*, <https://atlas.web.cern.ch/Atlas/GROUPS/DATAPREPARATION/PublicPlots/2023/DataSummary/figs/intlumivsyyear.png>. Cited on page 24.

- [67] ATLAS Collaboration, *Public ATLAS Luminosity Results for Run-3 of the LHC*, https://atlas.web.cern.ch/Atlas/GROUPS/DATAPREPARATION/PublicPlots/2023/DataSummary/figs/mu_run123.png. Cited on page 24.
- [68] J. Pequeno, *Computer generated image of the whole ATLAS detector*, 2008. Cited on page 25.
- [69] A. P. O'Neill, *The Search for Supersymmetry in Complex Hadronic States Using the ATLAS Detector*, 2021. <https://cds.cern.ch/record/2845398>. Presented 2021. Cited on page 26.
- [70] ATLAS Collaboration, M. Capeans, et al., *ATLAS Insertable B-Layer Technical Design Report*, tech. rep., 2010. <https://cds.cern.ch/record/1291633>. Cited on page 27.
- [71] A. Vogel, *ATLAS Transition Radiation Tracker (TRT): Straw Tube Gaseous Detectors at High Rates*, tech. rep., CERN, Geneva, 2013. <https://cds.cern.ch/record/1537991>. Cited on page 28.
- [72] ATLAS Collaboration, *ATLAS magnet system: Technical Design Report, 1*. Technical design report. ATLAS. CERN, Geneva, 1997. <https://cds.cern.ch/record/338080>. Cited on page 33.
- [73] T. Kawamoto, et al., *New Small Wheel Technical Design Report*, tech. rep., 2013. <https://cds.cern.ch/record/1552862>. ATLAS New Small Wheel Technical Design Report. Cited on page 33.
- [74] G. Avoni, et al., *The new LUCID-2 detector for luminosity measurement and monitoring in ATLAS*, *JINST* **13** (2018) P07017, <https://cds.cern.ch/record/2633501>. Cited on page 34.
- [75] S. White, *The ATLAS zero degree calorimeter*, *Nucl. Instrum. Meth. A* **617** (2010) 126–128. Cited on page 34.
- [76] L. Adamczyk, et al., *Technical Design Report for the ATLAS Forward Proton Detector*, tech. rep., 2015. <https://cds.cern.ch/record/2017378>. Cited on page 34.
- [77] S. A. Khalek, et al., *The ALFA Roman Pot detectors of ATLAS*, *Journal of Instrumentation* **11** (2016) P11013–P11013, <https://doi.org/10.1088/1748-0221/11/11/P11013>. Cited on page 34.
- [78] M. Aaboud, et al., *Performance of the ATLAS trigger system in 2015*, *The European Physical Journal C* **77** (2017) 317, <https://doi.org/10.1140/epjc/s10052-017-4852-3>. Cited on pages 35 and 36.
- [79] J. Pequeno and P. Schaffner, *How ATLAS detects particles: diagram of particle paths in the detector*, 2013. Cited on page 37.
- [80] ATLAS Collaboration, *Performance of the reconstruction of large impact parameter tracks in the ATLAS inner detector*, tech. rep., CERN, Geneva, 2017.

- <https://cds.cern.ch/record/2275635>. All figures including auxiliary figures are available at <https://atlas.web.cern.ch/Atlas/GROUPS/PHYSICS/PUBNOTES/ATL-PHYS-PUB-2017-014>. Cited on pages 36 and 38.
- [81] ATLAS Collaboration,, *Performance of primary vertex reconstruction in proton-proton collisions at $\sqrt{s}=7$ TeV in the ATLAS experiment*, tech. rep., CERN, Geneva, 2010. <https://cds.cern.ch/record/1281344>. All figures including auxiliary figures are available at <https://atlas.web.cern.ch/Atlas/GROUPS/PHYSICS/CONFNOTES/ATLAS-CONF-2010-069>. Cited on page 38.
- [82] ATLAS Collaboration,, *Performance of the ATLAS Silicon Pattern Recognition Algorithm in Data and Simulation at $\sqrt{s}=7$ TeV*, tech. rep., CERN, Geneva, 2010. <https://cds.cern.ch/record/1281363>. All figures including auxiliary figures are available at <https://atlas.web.cern.ch/Atlas/GROUPS/PHYSICS/CONFNOTES/ATLAS-CONF-2010-072>. Cited on page 38.
- [83] G. Aad, et al., *Topological cell clustering in the ATLAS calorimeters and its performance in LHC Run 1*, *The European Physical Journal C* **77** (2017) 490, <https://doi.org/10.1140/epjc/s10052-017-5004-5>. Cited on pages 39 and 40.
- [84] G. Aad, et al., *Electron and photon performance measurements with the ATLAS detector using the 2015–2017 LHC proton-proton collision data*, *Journal of Instrumentation* **14** (2019) P12006, <https://dx.doi.org/10.1088/1748-0221/14/12/P12006>. Cited on pages 39, 40, and 103.
- [85] M. Aaboud, et al., *Measurement of the photon identification efficiencies with the ATLAS detector using LHC Run-1 data*, *The European Physical Journal C* **76** (2016) 666, <https://doi.org/10.1140/epjc/s10052-016-4507-9>. Cited on pages 39 and 40.
- [86] ATLAS Collaboration,, *Electron and photon reconstruction and performance in ATLAS using a dynamical, topological cell clustering-based approach*, tech. rep., CERN, Geneva, 2017. <https://cds.cern.ch/record/2298955>. All figures including auxiliary figures are available at <https://atlas.web.cern.ch/Atlas/GROUPS/PHYSICS/PUBNOTES/ATL-PHYS-PUB-2017-022>. Cited on page 39.
- [87] G. Aad, et al., *Muon reconstruction performance of the ATLAS detector in proton–proton collision data at $\sqrt{s}=13$ TeV*, *The European Physical Journal C* **76** (2016) 292, <https://doi.org/10.1140/epjc/s10052-016-4120-y>. Cited on page 40.

- [88] W. Lampl, et al., *Calorimeter Clustering Algorithms: Description and Performance*, tech. rep., CERN, Geneva, 2008.
<https://cds.cern.ch/record/1099735>. All figures including auxiliary figures are available at
<https://atlas.web.cern.ch/Atlas/GROUPS/PHYSICS/PUBNOTES/ATL-LARG-PUB-2008-002>. Cited on page 40.
- [89] A. Hrynevich, *ATLAS jet and missing energy reconstruction, calibration and performance in LHC Run-2*, *Journal of Instrumentation* **12** (2017) C06038, <https://dx.doi.org/10.1088/1748-0221/12/06/C06038>. Cited on pages 40 and 41.
- [90] M. Aaboud, et al., *Jet reconstruction and performance using particle flow with the ATLAS Detector*, *The European Physical Journal C* **77** (2017), <https://arxiv.org/abs/1703.10485>. Cited on pages 40, 41, 102, 118, and 120.
- [91] M. Cacciari, G. P. Salam, and G. Soyez, *The anti-kt jet clustering algorithm*, *Journal of High Energy Physics* **2008** (2008) 063, <https://dx.doi.org/10.1088/1126-6708/2008/04/063>. Cited on pages 41 and 102.
- [92] B. Isildak, *Measurement of the differential dijet production cross section in proton-proton collisions at $\sqrt{s} = 7\text{ TeV}$* , 2013. Cited on page 41.
- [93] M. Aaboud, et al., *Determination of jet calibration and energy resolution in proton-proton collisions at $\sqrt{s} = 8\text{ TeV}$ using the ATLAS detector*, *The European Physical Journal C* **80** (2020) 1104, <https://doi.org/10.1140/epjc/s10052-020-08477-8>. Cited on page 41.
- [94] *Tagging and suppression of pileup jets with the ATLAS detector*, tech. rep., CERN, Geneva, 2014. <https://cds.cern.ch/record/1700870>. All figures including auxiliary figures are available at
<https://atlas.web.cern.ch/Atlas/GROUPS/PHYSICS/CONFNOTES/ATLAS-CONF-2014-018>. Cited on page 41.
- [95] *Selection of jets produced in 13 TeV proton-proton collisions with the ATLAS detector*, tech. rep., CERN, Geneva, 2015.
<https://cds.cern.ch/record/2037702>. All figures including auxiliary figures are available at
<https://atlas.web.cern.ch/Atlas/GROUPS/PHYSICS/CONFNOTES/ATLAS-CONF-2015-029>. Cited on pages 42 and 107.
- [96] A. Collaboration, *Performance of b-jet identification in the ATLAS experiment*, *Journal of Instrumentation* **11** (2016) P04008, <https://dx.doi.org/10.1088/1748-0221/11/04/P04008>. Cited on page 42.
- [97] ATLAS Collaboration, *Optimisation and performance studies of the ATLAS b-tagging algorithms for the 2017-18 LHC run*, tech. rep., CERN, Geneva, 2017. <https://cds.cern.ch/record/2273281>. All figures including auxiliary figures

- are available at
<https://atlas.web.cern.ch/Atlas/GROUPS/PHYSICS/PUBNOTES/ATL-PHYS-PUB-2017-013>. Cited on pages 42 and 43.
- [98] G. Aad, et al., *Configuration and performance of the ATLAS b-jet triggers in Run 2*, *The European Physical Journal C* **81** (2021) 1087, <https://doi.org/10.1140/epjc/s10052-021-09775-5>. Cited on page 42.
- [99] ATLAS Collaboration,, *Optimisation of the ATLAS b-tagging performance for the 2016 LHC Run*, tech. rep., CERN, Geneva, 2016. <https://cds.cern.ch/record/2160731>. All figures including auxiliary figures are available at <https://atlas.web.cern.ch/Atlas/GROUPS/PHYSICS/PUBNOTES/ATL-PHYS-PUB-2016-012>. Cited on page 43.
- [100] ATLAS Collaboration,, *Secondary vertex finding for jet flavour identification with the ATLAS detector*, tech. rep., CERN, Geneva, 2017. <https://cds.cern.ch/record/2270366>. All figures including auxiliary figures are available at <https://atlas.web.cern.ch/Atlas/GROUPS/PHYSICS/PUBNOTES/ATL-PHYS-PUB-2017-011>. Cited on page 43.
- [101] ATLAS Collaboration,, *Topological b-hadron decay reconstruction and identification of b-jets with the JetFitter package in the ATLAS experiment at the LHC*, tech. rep., CERN, Geneva, 2018. <https://cds.cern.ch/record/2645405>. All figures including auxiliary figures are available at <https://atlas.web.cern.ch/Atlas/GROUPS/PHYSICS/PUBNOTES/ATL-PHYS-PUB-2018-025>. Cited on page 43.
- [102] *Expected performance of the ATLAS b-tagging algorithms in Run-2*, tech. rep., CERN, Geneva, 2015. <https://cds.cern.ch/record/2037697>. All figures including auxiliary figures are available at <https://atlas.web.cern.ch/Atlas/GROUPS/PHYSICS/PUBNOTES/ATL-PHYS-PUB-2015-022>. Cited on page 43.
- [103] ATLAS Collaboration,, *Calibration of light-flavour b-jet mistagging rates using ATLAS proton-proton collision data at $\sqrt{s} = 13$ TeV*, tech. rep., CERN, Geneva, 2018. <https://cds.cern.ch/record/2314418>. All figures including auxiliary figures are available at <https://atlas.web.cern.ch/Atlas/GROUPS/PHYSICS/CONFNOTES/ATLAS-CONF-2018-006>. Cited on pages 43 and 102.
- [104] M. Aaboud, et al., *Measurements of b-jet tagging efficiency with the ATLAS detector using $t\bar{t}$ events at $\sqrt{s} = 13$ TeV*, *Journal of High Energy Physics* **2018** (2018) 89, [https://doi.org/10.1007/JHEP08\(2018\)089](https://doi.org/10.1007/JHEP08(2018)089). Cited on page 43.

- [105] M. Aaboud, et al., *Performance of missing transverse momentum reconstruction with the ATLAS detector using proton-proton collisions at $\sqrt{s} = 13$ TeV*, *The European Physical Journal C* **78** (2018) 903, <https://doi.org/10.1140/epjc/s10052-018-6288-9>. Cited on page 43.
- [106] H. Damerau, et al., *LHC Injectors Upgrade, Technical Design Report*. 2014. <https://cds.cern.ch/record/1976692>. Cited on page 46.
- [107] L. Arnaudon, et al., *Linac4 Technical Design Report*, tech. rep., CERN, Geneva, 2006. <https://cds.cern.ch/record/1004186>. revised version submitted on 2006-12-14 09:00:40. Cited on page 46.
- [108] HL-LHC project group, *LHC/HL-LHC Plan (last update January 2021)*, 2021. <https://hilumilhc.web.cern.ch/sites/hilumilhc.web.cern.ch/files/images/HL-LHC-plan-2021-1.pdf>. last accessed 23.04.2021. Cited on page 47.
- [109] ATLAS Collaboration, *ITk Pixel Layout Updates*, Itk-2020-002, 04, 2020, <https://atlas.web.cern.ch/Atlas/GROUPS/PHYSICS/PLOTS/ITK-2020-002/>. Cited on page 49.
- [110] ATLAS Collaboration,, *Expected tracking and related performance with the updated ATLAS Inner Tracker layout at the High-Luminosity LHC*, tech. rep., CERN, Geneva, 2021. <https://cds.cern.ch/record/2776651>. All figures including auxiliary figures are available at <https://atlas.web.cern.ch/Atlas/GROUPS/PHYSICS/PUBNOTES/ATL-PHYS-PUB-2021-024>. Cited on pages 49, 50, and 53.
- [111] ATLAS Collaboration, *Public radiation simulation results, Phase II ITk Inclined Duals (April 2018)*, 2018. <https://twiki.cern.ch/twiki/bin/view/AtlasPublic/RadiationSimulationPublicResults>. last accessed 28.04.2021. Cited on page 51.
- [112] T. Böhlen, et al., *The FLUKA Code: Developments and Challenges for High Energy and Medical Applications*, *Nuclear Data Sheets* **120** (2014) 211–214, <https://www.sciencedirect.com/science/article/pii/S0090375214005018>. Cited on page 51.
- [113] RD53 Collaboration,, <https://rd53.web.cern.ch/>. Cited on page 51.
- [114] ATLAS Collaboration,, *Expected Tracking Performance of the ATLAS Inner Tracker at the HL-LHC*, tech. rep., CERN, Geneva, 2019. <https://cds.cern.ch/record/2669540>. All figures including auxiliary figures are available at <https://atlas.web.cern.ch/Atlas/GROUPS/PHYSICS/PUBNOTES/ATL-PHYS-PUB-2019-014>. Cited on page 51.
- [115] RD53 Collaboration, M. Garcia-Sciveres, *The RD53A Integrated Circuit*, tech. rep., CERN, Geneva, 2017. <https://cds.cern.ch/record/2287593>. Cited on page 52.

- [116] L. Gonella, et al., *A serial powering scheme for the ATLAS pixel detector at sLHC*, *Journal of Instrumentation* **5** (2010) C12002, <https://dx.doi.org/10.1088/1748-0221/5/12/C12002>. Cited on page 52.
- [117] ATLAS Collaboration, J. Long, *The ATLAS Inner Detector tracking trigger at 13 TeV in LHC Run-2 and new developments on standard and unconventional tracking signatures for the upcoming LHC Run-3*, tech. rep., CERN, Geneva, 2022. <https://cds.cern.ch/record/2813981>. Cited on page 52.
- [118] ATLAS Collaboration, *Latest Performance Studies of the ATLAS Inner Tracker (ITk) in the HL-LHC*, 2020. <https://atlas.web.cern.ch/Atlas/GROUPS/PHYSICS/PLOTS/IDTR-2019-009/>. IDTR-2019-009. Cited on page 53.
- [119] Panduro Vazquez, William, *FELIX: the new detector interface for ATLAS*, *EPJ Web Conf.* **245** (2020) 01037, <https://doi.org/10.1051/epjconf/202024501037>. Cited on page 52.
- [120] W. Zhang, et al., *Characterization and quality control test of a gigabit cable receiver ASIC (GBCR2) for the ATLAS Inner Tracker Detector upgrade*, *Journal of Instrumentation* **16** (2021) P08013, <https://dx.doi.org/10.1088/1748-0221/16/08/P08013>. Cited on pages 54, 64, and 79.
- [121] Telecommunications Industry Association et al., *Electrical Characteristics of Low Voltage Differential Signalling (LVDS) Interface Circuits*. Telecommunications Industry Association, 1996. Cited on page 54.
- [122] XILINX, *Aurora 64B/66B Protocol Specification*, 10, 2014. https://www.xilinx.com/support/documentation/ip_documentation/aurora_64b66b_protocol_spec_sp011.pdf. last accessed 05.05.2021. Cited on page 54.
- [123] J. K. Anders, et al., *ITk Pixel - Supporting documentation for PDR: The Optosystem*, 03, 2020. ATLAS internal document. Cited on page 55.
- [124] F. Faccio, et al., *The bPOL12V DCDC converter for HL-LHC trackers: towards production readiness*, in *Proceedings of Topical Workshop on Electronics for Particle Physics — PoS(TWEPP2019)*. Sissa Medialab, Mar., 2020. Cited on page 56.
- [125] R. Müller, *Characterisation of the optical-electrical data conversion system for the ATLAS ITk upgrade*, Master's thesis, Albert Einstein Center for Fundamental Physics, University of Bern, 2020. Cited on page 57.
- [126] J. A. Kunzmann, *Power distribution for the Optosystem of the ATLAS ITk Pixel Detector*, Bachelor Thesis, Albert Einstein Center for Fundamental Physics, University of Bern, 8, 2020. Cited on page 57.
- [127] L. O. J. Troska, C. Soos, *The Versatile Link⁺ Application Note*, 2021. <https://edms.cern.ch/ui/file/2149674/1/VTRxPlusApplicationNote.pdf>. last accessed 17.08.2023. Cited on pages 58, 60, and 61.

- [128] J. Troska, *Versatile Link⁺ Transceiver (VTRx⁺)*, revision v2.9, 2023.
https://edms.cern.ch/ui/file/1719329/1/VTRxPlus_spec.pdf. last accessed 17.08.2023. Cited on page 58.
- [129] P. Moreira, P. Gui, and M. Menouni, *The GBTIA, a 5 Gbit/s Radiation-Hard Optical Receiver for the SLHC Upgrades*, 2009.
<http://cds.cern.ch/record/1235833>. Cited on page 60.
- [130] Z. Zeng, et al., *LDQ10: a compact ultra low-power radiation-hard 4×10 Gb/s driver array*, *Journal of Instrumentation* **12** (2017) P02020–P02020. Cited on page 60.
- [131] NXP Semiconductors, *I²C-bus specification and user manual*, Rev. 6, 4, 2014.
<https://www.nxp.com/docs/en/user-guide/UM10204.pdf>. last accessed 17.08.2023. Cited on page 60.
- [132] P. Moreira, *The LpGBT project status and overview*, 2016.
<https://indico.cern.ch/event/468486/contributions/1144369/attachments/1239839/1822836/aces.2016.03.08.pdf>. ACES 2016 - Fifth Common ATLAS CMS Electronics Workshop for LHC Upgrades. Cited on page 61.
- [133] lpGBT Team, *Manual of the lpGBT*, 4, 2021.
<https://lpgbt.web.cern.ch/lpgbt/v0/lpgbt.pdf>. last accessed 10.07.2023, internal to CERN users. Cited on pages 61 and 62.
- [134] J. M. Mendez, S. Baron, S. Kulis, and J. Fonseca, *New LpGBT-FPGA IP: Simulation model and first implementation*, in *Proceedings of Topical Workshop on Electronics for Particle Physics — PoS(TWEPP2018)*. Sissa Medialab, May, 2019. Cited on page 61.
- [135] lpGBT Team, *lpGBT-FPGA Core repository*,
<https://gitlab.cern.ch/gbt-fpga/lpgbt-fpga>. last accessed 10.07.2023. Cited on page 61.
- [136] I. S. Reed and G. Solomon, *Polynomial Codes Over Certain Finite Fields*, *Journal of the Society for Industrial and Applied Mathematics* **8** (1960) 300–304. Cited on page 61.
- [137] RD53 Collaboration, M. Garcia-Sciveres, *RD53B Design Requirements*, tech. rep., CERN, Geneva, 2019. <https://cds.cern.ch/record/2663161>. Cited on page 62.
- [138] RD53 Collaboration, *RD53B users guide*, tech. rep., CERN, Geneva, 2020.
<https://cds.cern.ch/record/2754251>. Cited on page 62.
- [139] RD53collaboration Collaboration, M. Garcia-Sciveres, F. Loddo, and J. Christiansen, *RD53B Manual*, tech. rep., CERN, Geneva, 2019.
<https://cds.cern.ch/record/2665301>. Cited on page 62.
- [140] C. Chen, et al., *A gigabit transceiver for the ATLAS inner tracker pixel detector readout upgrade*, *JINST* **14** (2019) C07005, [arXiv:2009.06142](https://arxiv.org/abs/2009.06142),
<https://cds.cern.ch/record/2691882>. Cited on page 63.

- [141] C. Chen, et al., *1.28 and 5.12 Gbps multi-channel twinax cable receiver ASICs for the ATLAS Inner Tracker Pixel Detector Upgrade*, 2020. Cited on page 63.
- [142] K. Moustakas, et al., *A Clock and Data Recovery Circuit for the ATLAS/CMS HL-LHC Pixel Front End Chip in 65 nm CMOS Technology*, **PoS TWEPP2019 (2020) 046**. Cited on page 63.
- [143] Tektronix, *Understanding and Characterizing Timing Jitter*, https://download.tek.com/document/55W_16146_5_MR_Letter.pdf. Cited on pages 65 and 66.
- [144] A. Sridhar and G. Ayala, *Time-Domain Jitter Measurement Considerations for Low Noise Oscillators*, https://www.ti.com/lit/an/snaa285/snaa285.pdf?ts=1684543925998&ref_url=https%253A%252F%252Fwww.google.com%252F. Cited on page 66.
- [145] XILINX, *KC705 Evaluation Board for the Kintex-7 FPGA, v1.9*, 2019. https://www.xilinx.com/support/documentation/boards_and_kits/kc705/ug810_KC705_Eval_Bd.pdf. last accessed 18.08.2023. Cited on page 70.
- [146] XILINX, *Integrated Bit Error Ratio Tester 7 Series GTX Transceivers v3.0*, 6, 2016. https://www.xilinx.com/support/documentation/ip_documentation/ibert_7series_gtx/v3_0/pg132-ibert-7series-gtx.pdf. last accessed 18.08.2023. Cited on page 70.
- [147] CERN, *FEAST Radiation tolerant 10W Synchronous Step-Down Buck DC/DC converter*, <https://espace.cern.ch/project-DCDC-new/Shared%20Documents/FEAST%20datasheet.pdf>. FEAST datasheet – rev1.0 (CERN internal). Cited on page 73.
- [148] S. Kulis and lpGBT team, *A multi-channel multi-data rate eLinkreceiver circuit for the lpGBT*, https://espace.cern.ch/GBT-Project/LpGBT/Presentations/lpgbt_eportrx20190906.pdf. CERN internal. Cited on page 75.
- [149] XILINX, *Integrated Logic Analyzer v6.2: LogiCORE IP Product Guide*, 10, 2016. https://www.xilinx.com/support/documentation/ip_documentation/ila/v6_2/pg172-ila.pdf. last accessed 18.08.2023. Cited on page 79.
- [150] P. Fayet, *Supersymmetry and Weak, Electromagnetic and Strong Interactions*, **Phys. Lett. B** **64** (1976) 159. Cited on page 92.
- [151] P. Fayet, *Spontaneously Broken Supersymmetric Theories of Weak, Electromagnetic and Strong Interactions*, **Phys. Lett. B** **69** (1977) 489. Cited on page 92.
- [152] G. R. Farrar and P. Fayet, *Phenomenology of the Production, Decay, and Detection of New Hadronic States Associated with Supersymmetry*, **Phys. Lett. B** **76** (1978) 575–579. Cited on page 92.
- [153] E. Boos and V. Bunichev, *Differences in fully differential cross section of single top quark production and its subsequent decay process depending on various anomalous Wtb couplings.*, **EPJ Web of Conferences** **222** (2019) 04007. Cited on page 93.

- [154] G. Aad, et al., *ATLAS Run 1 searches for direct pair production of third-generation squarks at the Large Hadron Collider*, *The European Physical Journal C* **75** (2015), <https://arxiv.org/abs/1506.08616>. Cited on page 93.
- [155] J. K. Anders, *Searches for direct pair production of third generation squarks, and dark matter, in final states containing b -jets and E_T^{miss} using the ATLAS detector at the LHC*, 2017. Presented 07 Jun 2017. Cited on page 93.
- [156] and G. Aad, et al., *Performance of the missing transverse momentum triggers for the ATLAS detector during Run-2 data taking*, *Journal of High Energy Physics* **2020** (2020), <https://arxiv.org/abs/2005.09554>. Cited on pages 96 and 112.
- [157] CERN, *LHC SUSY Cross Section Working Group*, <https://twiki.cern.ch/twiki/bin/view/LHCPhysics/SUSYCrossSections>. CERN internal. Cited on page 100.
- [158] *Searches for supersymmetric particles in e^+e^- collisions up to 208 GeV and interpretation of the results within the MSSM*, *The European Physical Journal C* **31** (2003) 421–479, <https://link.springer.com/article/10.1140/epjc/s2003-01355-5>. Cited on page 99.
- [159] A. Collaboration, *Search for direct pair production of sleptons and charginos decaying to two leptons and neutralinos with mass splittings near the W -boson mass in $\sqrt{s} = 13$ TeV pp collisions with the ATLAS detector*, 2022. Cited on page 101.
- [160] T. Gleisberg, et al., *Event generation with SHERPA 1.1*, *JHEP* **02** (2009) 007, [arXiv:0811.4622](https://arxiv.org/abs/0811.4622) [hep-ph]. Cited on page 102.
- [161] S. Höche, F. Krauss, S. Schumann, and F. Siegert, *QCD matrix elements and truncated showers*, *JHEP* **05** (2009) 053, [arXiv:0903.1219](https://arxiv.org/abs/0903.1219) [hep-ph]. Cited on page 102.
- [162] T. Sjöstrand, et al., *An introduction to PYTHIA 8.2*, *Comput. Phys. Commun.* **191** (2015) 159, [arXiv:1410.3012](https://arxiv.org/abs/1410.3012) [hep-ph]. Cited on page 102.
- [163] J. Bellm et al., *Herwig 7.1 Release Note*, [arXiv:1705.06919](https://arxiv.org/abs/1705.06919) [hep-ph]. Cited on page 102.
- [164] ATLAS Collaboration, *Studies on top-quark Monte Carlo modelling for Top2016*, tech. rep., CERN, Geneva, 2016. <https://cds.cern.ch/record/2216168>. All figures including auxiliary figures are available at <https://atlas.web.cern.ch/Atlas/GROUPS/PHYSICS/PUBNOTES/ATL-PHYS-PUB-2016-020>. Cited on page 102.
- [165] J. Alwall, et al., *The automated computation of tree-level and next-to-leading order differential cross sections, and their matching to parton shower simulations*, *Journal of High Energy Physics* **2014** (2014), <https://doi.org/10.1007%2Fjhep07%282014%29079>. Cited on page 102.

- [166] H. Hartanto, B. Jäger, L. Reina, and D. Wackerroth, *Higgs boson production in association with top quarks in the POWHEG BOX*, *Physical Review D* **91** (2015), <https://doi.org/10.1103/PhysRevD.91.094003>. Cited on page 102.
- [167] G. Aad, et al., *Performance of pile-up mitigation techniques for jets in pp collisions at $\sqrt{s} = 8$ TeV using the ATLAS detector*, *The European Physical Journal C* **76** (2016) 581, <https://doi.org/10.1140/epjc/s10052-016-4395-z>. Cited on page 102.
- [168] M. Aaboud, et al., *Electron efficiency measurements with the ATLAS detector using 2012 LHC proton–proton collision data*, *The European Physical Journal C* **77** (2017) 195, <https://doi.org/10.1140/epjc/s10052-017-4756-2>. Cited on page 102.
- [169] G. Aad, et al., *Electron and photon energy calibration with the ATLAS detector using LHC Run 1 data*, *The European Physical Journal C* **74** (2014) 3071, <https://doi.org/10.1140/epjc/s10052-014-3071-4>. Cited on page 102.
- [170] ATLAS Collaboration, *Electron identification measurements in ATLAS using $\sqrt{s} = 13$ TeV data with 50 ns bunch spacing*, tech. rep., CERN, Geneva, 2015. <https://cds.cern.ch/record/2048202>. All figures including auxiliary figures are available at <https://atlas.web.cern.ch/Atlas/GROUPS/PHYSICS/PUBNOTES/ATL-PHYS-PUB-2015-041>. Cited on page 102.
- [171] G. Aad, et al., *Muon reconstruction and identification efficiency in ATLAS using the full Run 2 pp collision data set at $\sqrt{s} = 13$ TeV*, *The European Physical Journal C* **81** (2021) 578, <https://doi.org/10.1140/epjc/s10052-021-09233-2>. Cited on page 103.
- [172] ATLAS Collaboration, *SUSY Object Definitions (Rel 21)*, <https://twiki.cern.ch/twiki/bin/viewauth/AtlasProtected/SusyObjectDefinitions2113TeV#Electrons>. Cited on pages 103 and 104.
- [173] ATLAS Collaboration, *Performance of missing transverse momentum reconstruction with the ATLAS detector in the first proton–proton collisions at $\sqrt{s} = 13$ TeV*, ATL-PHYS-PUB-2015-027, 2015, <https://cds.cern.ch/record/2037904>. Cited on page 103.
- [174] ATLAS Collaboration, *Trigger Menu in 2017*, tech. rep., CERN, Geneva, 2018. <https://cds.cern.ch/record/2625986>. All figures including auxiliary figures are available at <https://atlas.web.cern.ch/Atlas/GROUPS/PHYSICS/PUBNOTES/ATL-DAQ-PUB-2018-002>. Cited on page 104.
- [175] A. J. Barr, B. Gripaios, and C. G. Lester, *Transverse masses and kinematic constraints: from the boundary to the crease*, *Journal of High Energy Physics* **2009** (2009) 096, <https://dx.doi.org/10.1088/1126-6708/2009/11/096>. Cited on page 106.

- [176] P. Konar, K. Kong, K. T. Matchev, and M. Park, *Dark matter particle spectroscopy at the LHC: generalizing MT2 to asymmetric event topologies*, *Journal of High Energy Physics* **2010** (2010) 86, [https://doi.org/10.1007/JHEP04\(2010\)086](https://doi.org/10.1007/JHEP04(2010)086). Cited on page 106.
- [177] ATLAS Collaboration,, *Data-Quality Requirements and Event Cleaning for Jets and Missing Transverse Energy Reconstruction with the ATLAS Detector in Proton-Proton Collisions at a Center-of-Mass Energy of $\sqrt{s} = 7$ TeV*, tech. rep., CERN, Geneva, 2010. <https://cds.cern.ch/record/1277678>. All figures including auxiliary figures are available at <https://atlas.web.cern.ch/Atlas/GROUPS/PHYSICS/CONFNOTES/ATLAS-CONF-2010-038>. Cited on page 107.
- [178] *Vertex Reconstruction Performance of the ATLAS Detector at $\sqrt{s} = 13$ TeV*, tech. rep., CERN, Geneva, 2015. <https://cds.cern.ch/record/2037717>. All figures including auxiliary figures are available at <https://atlas.web.cern.ch/Atlas/GROUPS/PHYSICS/PUBNOTES/ATL-PHYS-PUB-2015-026>. Cited on page 107.
- [179] G. Cowan, K. Cranmer, E. Gross, and O. Vitells, *Asymptotic formulae for likelihood-based tests of new physics*, *The European Physical Journal C* **71** (2011) 1554, <https://doi.org/10.1140/epjc/s10052-011-1554-0>. Cited on page 108.
- [180] G. Aad, et al., *Search for new phenomena in events with two opposite-charge leptons, jets and missing transverse momentum in pp collisions at $\sqrt{s} = 13$ TeV with the ATLAS detector*, *Journal of High Energy Physics* **2021** (2021) 165, [https://doi.org/10.1007/JHEP04\(2021\)165](https://doi.org/10.1007/JHEP04(2021)165). Cited on page 116.
- [181] ATLAS Collaboration,, *Luminosity determination in pp collisions at $\sqrt{s} = 13$ TeV using the ATLAS detector at the LHC*, tech. rep., CERN, Geneva, 2019. <https://cds.cern.ch/record/2677054>. All figures including auxiliary figures are available at <https://atlas.web.cern.ch/Atlas/GROUPS/PHYSICS/CONFNOTES/ATLAS-CONF-2019-021>. Cited on page 118.
- [182] ATLAS Collaboration,, *Forward Jet Vertex Tagging: A new technique for the identification and rejection of forward pileup jets*, tech. rep., CERN, Geneva, 2015. <https://cds.cern.ch/record/2042098>. All figures including auxiliary figures are available at <https://atlas.web.cern.ch/Atlas/GROUPS/PHYSICS/PUBNOTES/ATL-PHYS-PUB-2015-034>. Cited on page 120.
- [183] ATLAS Collaboration,, *E_T^{miss} performance in the ATLAS detector using 2015-2016 LHC p - p collisions*, tech. rep., CERN, Geneva, 2018. <https://cds.cern.ch/record/2625233>. All figures including auxiliary figures are available at

- <https://atlas.web.cern.ch/Atlas/GROUPS/PHYSICS/CONFNOTES/ATLAS-CONF-2018-023>. Cited on page 120.
- [184] G. Aad, et al., *ATLAS b-jet identification performance and efficiency measurement with $t\bar{t}$ events in pp collisions at $\sqrt{s} = 13$ TeV*, *The European Physical Journal C* **79** (2019), <https://doi.org/10.1140/epjc/s10052-019-7450-8>. Cited on page 120.
- [185] M. Baak, et al., *HistFitter software framework for statistical data analysis*, *The European Physical Journal C* **75** (2015) 153, <https://doi.org/10.1140/epjc/s10052-015-3327-7>. Cited on page 121.
- [186] J. Anders, et al., *A facility for radiation hardness studies based on a medical cyclotron*, *Journal of Instrumentation* **17** (2022) P04021, <https://doi.org/10.1088/1748-0221/17/4/P04021>. Cited on page 137.
- [187] FCC Collaboration, *FCC Physics Opportunities*, *The European Physical Journal C* **79** (2019), <https://doi.org/10.1140/epjc/s10052-019-6904-3>. Cited on page 138.
- [188] FCC Collaboration, *FCC-ee: The Lepton Collider*, *The European Physical Journal Special Topics* **228** (2019) 261–623. Cited on page 139.
- [189] FCC Collaboration, *FCC-hh: The Hadron Collider*, *The European Physical Journal Special Topics* **228** (2019) 755–1107. Cited on page 139.

Declaration of consent

on the basis of Article 18 of the PromR Phil.-nat. 19

Name/First Name: Chatterjee/Meghranjana

Registration Number: 18-132-050

Study program:

Bachelor ☐ Master ☐ Dissertation ☒

Title of the thesis: Prospects of Finding New Fundamental Physics and Upgrade Studies with the ATLAS detector at the LHC

Supervisor: Prof. Dr. Michele Weber

I declare herewith that this thesis is my own work and that I have not used any sources other than those stated. I have indicated the adoption of quotations as well as thoughts taken from other authors as such in the thesis. I am aware that the Senate pursuant to Article 36 paragraph 1 litera r of the University Act of September 5th, 1996 and Article 69 of the University Statute of June 7th, 2011 is authorized to revoke the doctoral degree awarded on the basis of this thesis.

For the purposes of evaluation and verification of compliance with the declaration of originality and the regulations governing plagiarism, I hereby grant the University of Bern the right to process my personal data and to perform the acts of use this requires, in particular, to reproduce the written thesis and to store it permanently in a database, and to use said database, or to make said database available, to enable comparison with theses submitted by others.

Bern, 06.09.2023

Place/Date


Signature